
THE MOLECULAR ISM OF QUASAR HOST GALAXIES IN THE EARLY UNIVERSE

Dominik Alexander Riechers
Max-Planck-Institut für Astronomie



MAX - PLANCK - GESELLSCHAFT

Heidelberg 2007

Dissertation in Astronomy
submitted to the
Combined Faculties for the Natural Sciences and for Mathematics
of the Ruperto–Carola University of Heidelberg, Germany
for the degree of
Doctor of Natural Sciences

presented by
Dipl.–Phys. *Dominik Alexander Riechers*
born in Hannover, Germany

Oral examination: **07.11.2007, 10:30 am**

THE MOLECULAR ISM OF
QUASAR HOST GALAXIES
IN THE EARLY UNIVERSE

Referees: Prof. Dr. Hans-Walter Rix
Dr. Fabian Walter

Zusammenfassung/Abstract

Detailed studies of the molecular gas phase in the host galaxies of the highest redshift quasars are important for our understanding of the formation and evolution of quasars and their bulges, since the molecular gas is the prerequisite material for star formation. This investigation capitalizes on state-of-the-art observations in the radio/millimeter wavelength regime to study the key properties of the molecular interstellar medium in some of the most distant, gas-rich quasars. To search for evolutionary, luminosity-dependent, or galaxy type-dependent trends in the conditions under which star formation takes place, results are interpreted in the context of studies of nearby galaxies and high redshift galaxy populations. From the first high-resolution CO($J=1\rightarrow 0$) spectroscopy of high- z quasars, the total molecular gas mass of their host galaxies is determined. By more than doubling the number of molecules known in the distant universe [from 2 (CO/HCN) to 5], it is found that multiple molecular probes of dense gas predict similar star formation rates within the dense molecular regions of high redshift galaxies, out to the first 2 Gyr after the Big Bang. Together with other studies, these results indicate an increase in star formation efficiency toward the most luminous distant gas-rich systems, possibly due to a higher median gas density. In a connected, time consuming interferometric study, the host galaxies of three $z>4$ quasars are resolved, for the first time, both spatially (at up to $0.15''$, or 1.0 kpc) and in velocity space, revealing that the molecular reservoirs show a wealth of morphologies. The derived dynamical masses are large enough to account for both the central supermassive black holes and the full reservoirs of molecular gas, but do not leave much room for a stellar bulge as predicted by the local relation between black hole mass and bulge velocity dispersion. Quasar host galaxies are thus prime laboratories to study the coevolution of supermassive black holes and the extreme starbursts hosted by the molecular environments at early cosmic epochs. The observations presented here thus provide an important foundation for future studies of normal galaxies at high redshifts with the Atacama Large Millimeter Array (ALMA).

Molekulares Gas ist der Treibstoff für Sternentstehung, weshalb es von großer Wichtigkeit für unser Bild von der Entstehung und Entwicklungsgeschichte von Quasaren ist, die molekulare Komponente in den Muttergalaxien der am weitesten entfernten Objekte im Detail zu untersuchen. In dieser Doktorarbeit werden die technologischen Neuerungen der größten Radio- und Millimeterteleskope genutzt um einige der wichtigsten Eigenschaften des molekularen interstellaren Mediums in hoch rotverschobenen Quasaren genauer zu studieren, und in einem evolutionären, galaxientyp- und leuchtkraftabhängigen Kontext der Sternentstehung zu begutachten. Die CO($J=1\rightarrow 0$) Linie wurde zum ersten Mal erfolgreich in hoch rotverschobenen Galaxien hochauflösend spektroskopiert, um die Gesamtmasse des molekularen Gases zu bestimmen. Eine Erweiterung dieser Studie auf andere molekulare Indikatoren führt zu mehr als einer Verdopplung der im frühen Universum bekannten Moleküle [5 statt bisher 2 (CO/HCN)]. Alle Indikatoren sagen miteinander konsistente Sternentstehungsraten in hoch rotverschobenen Quasaren voraus, und keines der Moleküle scheint ein klar bevorzugter Indikator zu sein. Im Zusammenwirken mit zwei anderen Studien ergibt sich der Befund daß Sternentstehung in weit entfernten, sehr gasreichen Galaxien mit einer höheren Effizienz vonstatten geht als in anderen Galaxien, was vermutlich mit einer höheren mittleren Dichte des Gases in diesen Systemen zusammenhängt. In einer auf diesen Ergebnissen aufbauenden, zeitaufwendigen Interferometerstudie ist es ausserdem zum ersten Mal gelungen die Muttergalaxien von Quasaren bei $z>4$ sowohl räumlich (auf Skalen von bis zu $0.15''$, oder 1.0 kpc) als auch dynamisch (in Geschwindigkeitsintervallen entlang einer molekularen Emissionslinie) aufzulösen. Die Karten zeigen daß die molekularen Reservoirs in diesen Galaxien reichhaltige Strukturen aufweisen. bestimmten dynamischen Massen sind in Einklang mit der Summe der Massen des zentralen schwarzen Lochs und der Gas- und Staubreservoirs, allerdings nicht groß genug um einen stellaren Bulge von der Masse zu enthalten, wie sie von der Beziehung zwischen der Masse des schwarzen Loches und der Geschwindigkeitsdispersion des Bulges in Galaxien im lokalen Universum vorausgesagt wird. Die Ergebnisse dieser Arbeit belegen, daß diese weit entfernten Galaxien erstklassige Laboratorien für Studien der Entstehung und Entwicklung supermassiver schwarzer Löcher und extremer Starbursts im frühen Universum sind. Die hier gezeigten Beobachtungen bilden die Grundlage für zukünftige Studien normaler Galaxien bei hohen Rotverschiebungen mit dem Atacama Large submillimeter/Millimeter Array (ALMA).

Danksagung/Acknowledgments

(Eine deutsche Fassung folgt in Anschluß an die englische Übersetzung)

There are a number of people that I would like to thank for contributing to the successful completion of this thesis. First, I would like to thank Fabian Walter and Hans-Walter Rix for agreeing to supervise my PhD thesis at MPIA. In particular, I want to express my gratitude toward Fabian for introducing me to this extremely exciting field of astronomy, and for always taking the time to explain things when necessary. I am also very grateful for the freedom that I had in carrying out my research over the past years, while still keeping the production of results in focus. This thesis, and the picture of science I have developed over the past few years, would not be the same without Fabian's support. Special thanks go to Chris Carilli for his ideas and always insightful, to the point comments on this work. I would also like to thank Axel Weiß for introducing me to the world of LVG modeling, to observing with the 30 m, and for many helpful comments on the different projects we worked on together. I also would like to take the opportunity to thank my other collaborators on the different research projects, in particular Frank Bertoldi, Pierre Cox, Roberto Neri, Kirsten K. Knudsen, Christian Henkel, Geraint Lewis, Brendon Brewer, Karl Menten, K. Y. Lo, Min Yun, Nick Scoville, Johannes Staguhn, Dominic Benford, Todd Hunter, Jaron Kurk, Xiaohui Fan, Laura Pentericci, Marianne Vestergaard, and Michael Strauss, for their contributions. I am also grateful for many helpful scientific discussions with a number of people, in particular Dennis Downes, Phil Solomon, Yu Gao, Rob Ivison, and Desika Narayanan.

I would like to thank a number of people for their hospitality during my visits to their institutions, in particular Glen Langston and Ron Maddalena at NRAO Green Bank, Jeff Wagg and Ran Wang at NRAO Socorro, Anneila Sargent, Andrew Blain, and Thomas Greve at Caltech, John Mulchaey, Francois Schweizer and Juna Kollmeier at Carnegie, Crystal Martin and Omer Blaes at UC Santa Barbara, Dave Sanders at IfA Honolulu, and David Wilner at CfA/Harvard-Smithsonian.

On a private side, I would like to thank my family for their continuous support and encouragement, in particular my parents, Annegret and Heinz-Hermann, and my brother, Patrick. I may move to the other end of the world, but I will always remember where I come from! I would like to thank Vernesa for a lot of things, but mostly for being who you are - hvala lijepa na svemu! It's more than good to know that you will be in Pasadena. There are a number of people whom I have met in the past three years that have grown

on me, in particular Isabel (Adiós, te voy a extrañar - remember summer 2004? Es war sehr schön,...), Antje (I guess dialing your number outspeeds ringing your doorbell now. Remember to come visit!), Monika (Thanks for having both a good taste in music and for the right kind of sports. Fingers crossed that everything runs smoothly for you at the beginning of next year!), MH (Drink a beer for me next Quebec day!), and Flo ("Vienna" is not only the name of a good song.). This is not to forget my old friends from Bonn and at the rest of the world, most importantly Kalle (One sentence on Tokyo: I'll be back!), Martin (Let's take a direct flight next time.), Tilo (Always fun to visit you guys!), Sven (What happened to DM parties?), and Woody (Hope I'll manage to come to Sydney before you finish...). You guys have to come visit!

Hiermit möchte ich mich bei allen Menschen bedanken die zum erfolgreichen Abschluß dieser Doktorarbeit beigetragen haben.

Als erstes möchte ich Fabian Walter und Hans-Walter Rix dafür danken, daß sie die Betreuung meiner Doktorarbeit am MPIA übernommen haben. Mein besonderer Dank gilt Fabian dafür, daß er mich an dieses extrem interessante Gebiet der Astronomie herangeführt hat, und sich die Zeit genommen hat Dinge zu erklären wann immer die Notwendigkeit bestand. Desweiteren bin ich sehr dankbar für die Freiräume die mir bei der Durchführung meiner wissenschaftlichen Arbeit gelassen wurden, wobei zugleich zu jedem Zeitpunkt das Ziel erkennbar blieb. Ohne Fabians Unterstützung wären diese Arbeit und mein Verständnis von Wissenschaft nicht auf dem gegenwärtigen Niveau. Hervorheben möchte ich auch die Zusammenarbeit mit Chris Carilli, da er stets mit guten Ideen und aufschlußreichen, präzisen Kommentaren zum Erfolg dieser Arbeit beigetragen hat. Mein Dank gilt auch Axel Weiß, der mir die Welt des LVG-Modellierens und das Beobachten mit dem 30m näher gebracht hat, und viele sehr hilfreiche Kommentare zu unseren gemeinsamen Projekten gegeben hat. An dieser Stelle möchte ich auch meinen anderen Kollegen danken, die in den verschiedenen Projekten involviert waren und zu ihrem Gelingen beigetragen haben, insbesondere Frank Bertoldi, Pierre Cox, Roberto Neri, Kirsten K. Knudsen, Christian Henkel, Geraint Lewis, Brendon Brewer, Karl Menten, K. Y. Lo, Min Yun, Nick Scoville, Johannes Staguhn, Dominic Benford, Todd Hunter, Jaron Kurk, Xiaohui Fan, Laura Pentericci, Marianne Vestergaard, und Michael Strauss. Sehr hilfreich waren auch die Diskussionen mit anderen Kollegen, insbesondere Dennis Downes, Phil Solomon, Yu Gao, Rob Ivison, and Desika Narayanan.

Als nächstes möchte ich einigen Personen für ihre Gastfreundschaft während meiner Aufenthalte an ihren Institutionen danken. Dies sind insbesondere Glen Langston und Ron Maddalena bei NRAO Green Bank, Jeff Wagg, und Ran Wang bei NRAO Socorro, Anneila Sargent, Andrew Blain, und Thomas Greve am Caltech, John Mulchaey, Francois Schweizer, und Juna Kollmeier bei Carnegie, Crystal Martin und Omer Blaes an der UC Santa Barbara, Dave Sanders am IfA Honolulu, und David Wilner am CfA/Harvard-Smithsonian Center.

Auf privater Seite möchte ich meiner Familie für ihre dauerhafte Unterstützung danken, insbesondere meinen Eltern Annegret und Heinz-Hermann und meinem Bruder Patrick. Ich werde zwar demnächst am anderen Ende der Welt wohnen, aber ich werde mich immer

meiner Wurzeln entsinnen. Ganz besonders möchte ich auch Vernesa danken - hvala lijepa na svemu, und bleib' wie du bist! Ich finde es schön und gut daß du auch nach Pasadena kommst. Ich möchte mich auch bei den anderen Menschen bedanken, die ich während der vergangenen drei Jahre kennen und schätzen gelernt habe, insbesondere bei Isabel (Adiós, te voy a extrañar - remember summer 2004? Es war sehr schön,...), Antje (Okay, anrufen geht jetzt schneller als klingeln. Denk' dran mich zu besuchen.), Monika (Thanks for having both a good taste in music and for the right kind of sports. Fingers crossed that everything runs smoothly for you at the beginning of next year!), MH (Drink a beer for me next Quebec day!), und Flo (Wien war wunderbar.). Natürlich möchte ich hier auch nicht meine alten Freunde aus Bonn und nicht unmittelbarer Umgebung vergessen. Aus diesem Kreis möchte ich insbesondere Kalle (Tokyo wird mich wiedersehen!), Martin (Nächstes Mal stimme ich für den Direktflug.), Tilo (Es ist immer wieder eine Freude euch zu besuchen!), Sven (Wir müssen mal wieder auf ne DM Party!), und Woody (Werde es hoffentlich nochmal nach Sydney schaffen...) danken - ich hoffe wir sehen uns bald mal wieder!

Contents

Abstract	v
Acknowledgments	vii
1 Introduction	1
1.1 The Interstellar Medium	2
1.1.1 Discovery of the ISM	2
1.1.2 Significance of the ISM	2
1.1.3 Properties of the ISM	5
1.2 The Molecular ISM	7
1.3 Molecular Gas in Galaxies	9
1.3.1 Molecular Gas in the Milky Way	9
1.3.2 Molecular Gas in Nearby Spiral Galaxies	11
1.3.3 Molecular Gas in Nearby Non-Spiral Galaxies	13
1.3.4 Molecular Gas in LIRGs and ULIRGs	13
1.3.5 Molecular Gas in Distant Galaxies	15
1.4 Relations between Molecular Gas Mass and Star Formation Rate	17
2 Diagnostics and Strategies	21
2.1 Molecular Line Spectroscopy	21
2.1.1 Molecular Line Frequencies	21
2.1.2 Minimum Excitation Temperature	23
2.2 Population of Rotational Molecular Transitions	24
2.2.1 Statistical Equilibrium and Radiative Transfer	24
2.2.2 Radiative Transfer in the LVG Approximation	27
2.2.3 LVG Calculations	28
2.3 Line Luminosity	29
2.3.1 Angular Size Distance and Luminosity Distance	30
2.3.2 Flux Density and Source Solid Angle	31
2.3.3 Rayleigh-Jeans Brightness Temperatures	32
2.3.4 Measured Brightness Temperature	32
2.3.5 Line Profiles	33
2.3.6 Line Luminosity	33

2.3.7	Negative K Correction	35
2.3.8	Gravitational Magnification	35
2.4	Telescopes	36
2.5	Discovery Space	41
2.6	Selection Criteria	43
2.6.1	Selection Criteria for CO Observations	43
2.6.2	Selection Criteria for Observations of Dense Gas Tracers	45
3	Masses of Molecular Gas Reservoirs in $z \gtrsim 4$ Quasar Host Galaxies	53
3.1	Context	53
3.2	Abstract	54
3.3	Introduction	54
3.4	Observations	56
3.4.1	Green Bank Telescope	56
3.4.2	Effelsberg	57
3.4.3	Combined Spectra	58
3.5	Results	58
3.5.1	BR 1202–0725	58
3.5.2	PSS J2322+1944	62
3.5.3	APM 08279+5255	65
3.6	Analysis and Discussion	66
3.6.1	Large Velocity Gradient Modeling	66
3.6.2	Correlations of High- and Low-Redshift Galaxies	68
3.7	Summary	71
4	Dense Molecular Gas I: Search for HCN at $z=6.42$	73
4.1	Context	73
4.2	Abstract	74
4.3	Introduction	74
4.4	Observations	75
4.5	Results	77
4.6	Analysis	78
4.6.1	‘Dense Gas Fraction’: The $L'_{\text{HCN}}/L'_{\text{CO}}$ Ratio	78
4.6.2	‘Star Formation Law’: The $L_{\text{FIR}}/L'_{\text{HCN}}$ Ratio	79
4.7	Discussion	81
4.7.1	Median Gas Density and Star Formation Efficiency	81
4.7.2	The Role of AGN Heating for L_{FIR}	81
4.7.3	Implications for Future Studies	82
5	Dense Molecular Gas II: HCO⁺ in a $z=2.56$ Quasar Host Galaxy	83
5.1	Context	83
5.2	Abstract	84
5.3	Introduction	84

5.4	Observations	85
5.5	Results	87
5.6	Discussion	88
6	Dense Molecular Gas III: CN in a $z=2.56$ Quasar Host Galaxy	93
6.1	Context	93
6.2	Abstract	93
6.3	Introduction	94
6.4	Observations	95
6.5	Theoretical Considerations	96
6.6	Results	99
6.6.1	CN Maps and Spectrum	99
6.6.2	Line Luminosities	100
6.7	Discussion	101
7	Dense Molecular Gas IV: CS in a $z=2.56$ Quasar Host Galaxy	105
7.1	Context	105
7.2	Abstract	105
7.3	Introduction	106
7.4	Observations	107
7.5	Results	108
7.6	Discussion	109
8	Dense Molecular Gas V: Search for H₂O at $z=3.2$	113
8.1	Context	113
8.2	Abstract	113
8.3	Introduction	114
8.4	Observations	115
8.5	Results	116
8.6	Discussion	118
8.6.1	Intrinsic Line Brightness Temperatures	118
8.6.2	Area Filling Factor	119
8.6.3	Comparison with Other Extragalactic Studies	119
8.6.4	Possible Interpretations of the Nondetection	120
9	Molecular Line Mapping I: A Compact Quasar Host Galaxy at $z=3.91$	123
9.1	Context	123
9.2	Abstract	124
9.3	Introduction	124
9.4	Observations	126
9.4.1	VLA Data	126
9.4.2	GBT Data	130
9.5	Results	130

9.5.1	CO(1–0) Line and 23.5 GHz Continuum Emission	130
9.5.2	CO(2–1) Line Emission	133
9.5.3	The Search for CN(1–0) Line Emission	137
9.5.4	Continuum Emission at 1.4 GHz	137
9.5.5	Continuum Emission at 4.5 GHz	137
9.5.6	Continuum Emission at 8.4 GHz	139
9.5.7	Continuum Emission at 14.9 GHz	139
9.6	Analysis	140
9.6.1	Spectral Energy Distribution	140
9.6.2	Comparison to Previous CO(1–0) Imaging	144
9.6.3	On the 46.9 GHz Continuum Emission	145
9.6.4	A Limit for the CN Luminosity	146
9.6.5	Radio Luminosity	148
9.6.6	Morphology at X-Ray to Radio Wavelengths	149
9.7	Gravitational Lensing	151
9.7.1	Direct Constraints on the Lensing Properties from CO Observations	151
9.7.2	Lens Modeling: Previous Models	154
9.7.3	Lens Modeling: New Model	158
9.8	Black Hole, Gas and Dynamical Masses	158
9.8.1	Black Hole Mass	158
9.8.2	Molecular Gas Mass	159
9.8.3	Dynamical Mass	160
9.8.4	Stellar Bulge Mass Limit	160
9.8.5	Limitations of this Analysis	161
9.9	On the Radio–Far-Infrared Correlation	161
9.10	Discussion	162
9.11	Summary	166
10	Molecular Line Mapping II: Zoom-In Through a $z=4.12$ Einstein Ring	169
10.1	Context	169
10.2	Abstract	169
10.3	Introduction	170
10.4	Observations	171
10.5	Results	171
10.6	Gravitational Lens Inversion	174
10.6.1	Method: Bayesian Inference	174
10.6.2	Application to Interferometric Data	177
10.6.3	Modeling Results	177
10.7	Discussion	180

11 Molecular Line Mapping III: Formation of a $z=4.41$ Quasar Host	183
11.1 Context	183
11.2 Abstract	183
11.3 Introduction	184
11.4 Observations	185
11.5 Results	185
11.5.1 Morphology of the Molecular Gas Reservoir	185
11.5.2 Dynamical Structure of the CO Distribution	188
11.6 Discussion	191
12 Summary and Outlook	193
12.1 Summary	193
12.1.1 Masses of Molecular Gas Reservoirs in Distant Quasars	193
12.1.2 Composition of Molecular Gas Reservoirs in Distant Quasars	195
12.1.3 Mapping the Molecular Gas in Distant Quasars	198
12.2 Outlook	204
12.2.1 Molecular Gas Masses at High Redshift	204
12.2.2 Molecular Tracers of Star Formation at High Redshift	207
12.2.3 Dynamical Properties of Distant Star-Forming Galaxies	209
12.2.4 A Bright Future for ISM Studies of Galaxies in the Early Universe	211
A Existing Molecular Line Observations at High Redshift	215
A.1 Inventory of Observations	215
A.2 Statistical Analysis and Source Classification	221
List of Abbreviations	225
Units, Constants, and Conversions	229
Curriculum Vitae	254
List of Publications	259

List of Figures

1.1	CO/Optical Overlay of the Antennae	4
1.2	Molecular Lines and Model for Orion	8
1.3	Molecular Disk of the Milky Way	10
1.4	CO($J=1\rightarrow 0$) Map of M51	12
1.5	CO($J=2\rightarrow 1$) Map of Arp 220	14
1.6	CO($J=3\rightarrow 2$) Map of J1148+5251	15
1.7	Relation between Gas Density and SFR Density	18
1.8	Relations between CO and HCN Luminosity and Infrared Luminosity	19
2.1	Temperature-Density Plot	27
2.2	LVG Models	28
2.3	Single Dish Radio/Millimeter Telescopes	38
2.4	Radio/Millimeter Interferometers	39
2.5	Computer-Rendered Image of ALMA	41
2.6	Redshift Discovery Space	44
2.7	High Resolution CO Observations of BR 1202–0725 ($z=4.69$)	46
2.8	Kinetic Temperature-Critical Density Diagram	48
2.9	CO and Radio Continuum Emission in the Cloverleaf Quasar	50
3.1	CO($J=1\rightarrow 0$) Spectra of BR 1202–0725	59
3.2	CO($J=1\rightarrow 0$) Spectra of PSS J2322+1944	60
3.3	CO($J=1\rightarrow 0$) Spectrum of APM 08279+5255	61
3.4	LVG model of BR 1202–0725	67
3.5	$L'_{\text{CO}}-L_{\text{FIR}}$ Correlation toward High Redshift	69
4.1	HCN($J=2\rightarrow 1$) Observations of SDSS J1148+5251	76
4.2	HCN Luminosity Relations	80
5.1	HCO ⁺ ($J=1\rightarrow 0$) Line Map in the Cloverleaf	86
5.2	HCO ⁺ ($J=1\rightarrow 0$) Velocity Channel Maps in the Cloverleaf	87
5.3	HCO ⁺ Luminosity Relations	89
6.1	CN($N=3\rightarrow 2$) Model Spectrum of the Cloverleaf	97
6.2	CN($N=3\rightarrow 2$) Line Map in the Cloverleaf	98

6.3	CN($N=3\rightarrow 2$) Velocity Channel Maps in the Cloverleaf	99
6.4	CN($N=3\rightarrow 2$) Spectrum in the Cloverleaf	100
6.5	CN Luminosity Relations	102
7.1	CS($J=3\rightarrow 2$) Line Map in the Cloverleaf	108
7.2	CS Luminosity Relations	110
8.1	43.6 GHz Maps of MG 0751+2716	117
9.1	CO($J=1\rightarrow 0$) Line Map of APM 08279+5255	131
9.2	CO($J=1\rightarrow 0$) Velocity Channel Maps of APM 08279+5255	133
9.3	Smoothed CO($J=1\rightarrow 0$) Line Map of APM 08279+5255	134
9.4	CO($J=1\rightarrow 0$) Spectrum of APM 08279+5255	135
9.5	CN($N=1\rightarrow 0$) Spectrum of APM 08279+5255	136
9.6	Radio Continuum Maps of APM 08279+5255	138
9.7	High Resolution 8.4 GHz Map of APM 08279+5255	140
9.8	SED of APM 08279+5255	141
9.9	CN($N=1\rightarrow 0$) Model Spectrum of APM 08279+5255	147
9.10	NIR/X-Ray Overlays of APM 08279+5255	149
9.11	Lensing Properties of APM 08279+5255	152
9.12	Lensing Model of APM 08279+5255	157
10.1	CO($J=2\rightarrow 1$) Line Map of PSS J2322+1944 (0.3'')	172
10.2	CO($J=2\rightarrow 1$) Line Map of PSS J2322+1944 (0.5'')	173
10.3	CO($J=2\rightarrow 1$) Velocity Channel Maps of PSS J2322+1944 (0.3'')	175
10.4	CO($J=2\rightarrow 1$) Velocity Channel Maps of PSS J2322+1944 (0.5'')	176
10.5	Lensing Model of PSS J2322+1944	178
10.6	Color Composite of the Lens Model of PSS J2322+1944	179
11.1	CO($J=2\rightarrow 1$) Line Map of BRI 1335-0417 (1.4 kpc)	186
11.2	CO($J=2\rightarrow 1$) Line Map of BRI 1335-0417 (1.0 kpc)	187
11.3	CO($J=2\rightarrow 1$) Velocity Channel Maps of BRI 1335-0417	189
11.4	CO($J=2\rightarrow 1$) Color Composite Map of BRI 1335-0417	190
12.1	CO($J=1\rightarrow 0$) Measurements – Mass Estimates	194
12.2	Dense Molecular Gas Tracers at High Redshift	196
12.3	Schmidt-Kennicutt Law for Different Molecular Tracers	198
12.4	Molecular Gas Emission in the $z=3.91$ Quasar APM 08729+5255	199
12.5	Molecular Gas Emission in the $z=4.12$ Quasar PSS J2322+1944	200
12.6	Molecular Gas Emission in the $z=4.41$ Quasar BRI 1335-0417	202
12.7	CO($J=1\rightarrow 0$) Search in PSS J1418+4449 ($z=4.35$)	205
12.8	HCO ⁺ Excitation in the Cloverleaf	208
12.9	Computer-Rendered Image of ALMA and ACA	212
A.1	Source Counts	222

A.2 Source Counts by Galaxy Type	223
A.3 Detected CO/HCN Transitions	223
A.4 Commonly observed CO/HCN Transitions	224

List of Tables

1.1	Characteristics of the Different ISM Phases	6
2.1	Minimum Excitation Temperatures for CO, HCN, HCO ⁺ , and CS	25
2.2	Critical Densities for Selected Transitions of CO, HCN, HCO ⁺ , and CS	26
2.3	Properties of Current and Future (Sub)mm/Radio Facilities	42
3.1	Observed CO($J=1\rightarrow 0$) Line Parameters	61
3.2	Luminosities, Gas Masses and Star Formation Rates	63
3.3	CO Detections in the Quasar Hosts of Our Targets in the Literature	64
4.1	Line Luminosities in SDSS J1148+5251	77
4.2	Luminosity Ratios at High z and Average Values	78
5.1	CO, HCN, and HCO ⁺ Line Luminosities in the Cloverleaf	88
6.1	Molecular Line Luminosities in the Cloverleaf	101
7.1	Molecular Line Luminosities in the Cloverleaf	109
8.1	Extragalactic para-H ₂ O($3_{13}\rightarrow 2_{20}$) Emission	118
9.1	New (2005) and Archival (1998–2001) VLA Observations Summary	127
9.2	CO/CN Line Peak and Continuum Fluxes	132
9.3	Continuum Fluxes of VLA J083141+524514	139
9.4	Line Intensities, Luminosities, and Ratios	146
9.5	Mass Budget in the Central Region of APM08279+5255	159
A.1	All $z>1$ CO Detections in the Literature ($1.06\leq z\leq 2.56$)	217
A.2	All $z>1$ CO Detections in the Literature ($2.56\leq z\leq 4.69$)	218
A.3	All $z>1$ CO Detections in the Literature ($4.69\leq z\leq 6.42$)	219
A.4	All $z>1$ Detections of Dense Molecular Gas in the Literature	220
A.5	All $z>1$ Detections of Millimeter Carbon Lines in the Literature	220

Chapter 1

Introduction

The focus of this thesis lies on understanding the molecular gas properties of gas-rich galaxies at high redshift. This study has the potential to answer a number of important questions about star formation and galaxy evolution in the early universe. The main questions in this context are: What are the masses of the molecular gas reservoirs in these distant galaxies, and how do they compare to the dynamical mass? How do these gas masses compare to present day galaxies? How are the molecular gas reservoirs composed, and is this composition different from what is observed at $z=0$? In particular, do the local relations between total and dense gas mass and the star formation rate in a galaxy hold out to high redshift, and thus trace universal properties of star formation? Are the distant, gas-rich galaxies centrally concentrated like most local ultra-luminous infrared galaxies (ULIRGs, the closest counterparts to the gas-rich high redshift systems), or are they extended protogalaxies that host substantially more molecular gas than nearby galaxies? How long can the bursts of star formation observed toward these distant systems be maintained? What is the evolutionary state of these high redshift galaxies? These and more questions are addressed in the framework of this PhD thesis. This study is aimed at providing a foundation for selecting and interpreting observations of distant galaxies with future facilities, in particular the Atacama Large submillimeter/Millimeter Array (ALMA). Even though the galaxies currently detected in molecular gas emission at high redshift are extreme, it is important to understand these systems in more detail to focus future studies of more typical galaxies in the early universe.

To provide some general context, the introduction starts with a historical perspective, and with describing the general properties of the interstellar medium (ISM), in particular its connection to star formation. The molecular component of the ISM is described in the following, and some properties of the molecular ISM in galaxies at different redshifts, in particular the variations in molecular mass and its distribution, are discussed. The introduction closes by quantifying the relation between molecular gas and star formation rate as a diagnostic of galaxy properties (and a tracer of star formation efficiency), and the role of different molecules as probes of these properties.

1.1 The Interstellar Medium

1.1.1 Discovery of the ISM

The concept of interstellar space has been discussed on a philosophical level early on. References are found in the literature as early as in the 17th century (e.g., F. Bacon 1626, in “*Sylva Sylvarum, or a Naturall Historie in ten Centuries*”, § 354-5).¹ The idea that some medium may fill this region between the stars in our Galaxy has been introduced in the 19th century in the context of aether theory (Patterson 1862, *Ess. Hist. & Art* 10). Before the theory of electromagnetism was developed, such an invisible, luminiferous aether was thought to be the carrier of light waves (at the time, it was considered necessary to have a mediator to transfer energy, such as radiation). Due to the fact that stellar light can be observed on Earth, this aether was thought to fill the interstellar regime. Although the aether theory was dropped only a few decades later, the concept of an interstellar medium prevailed.² However, the ISM was not directly observed until the early 20th century. First images of “dark nebulae” (i.e., dust and gas-rich interstellar regions) were obtained by Barnard (1919), silhouetted against the background star field of the galaxy. However, the first direct detection of cold, diffuse interstellar matter was obtained through absorption line spectroscopy of δ Ori by Hartmann (1904). He realized that a Calcium-K line observed toward this star did not share the characteristics of other lines within the spectrum. It thus was unlikely to originate from the atmosphere of the star himself, but rather from an isolated cloud between the star and Earth.

Today, more than a century after its initial discovery (and the development of quantum mechanics), we have a quite detailed picture of the ISM and its properties within the Milky Way. Moreover, it has been studied in numerous external galaxies, and even been detected out to the highest observable redshifts, less than a Gigayear after the Big Bang ($z=6.42$). In the following, the general properties of the ISM are described, and the importance of its molecular component is elaborated on.

1.1.2 Significance of the ISM

In principle, the ISM is a minor constituent of large spiral galaxies like the Milky Way. In our Galaxy, it only encompasses a few per cent of the total amount of the stellar mass. However, the ISM is important for basically every astrophysically relevant process, and holds information about the properties of a galaxy on all scales, starting at individual stars. The ISM (in particular its molecular component) is the prerequisite material out of which stars form. It thus delivers the overall framework for star formation to take place. The ISM is also by no means stationary. Gravitational forces squeeze the interstellar matter, and lead

¹The passage reads: “And the Interstellar Sky, (though the Opinion be vaine, that the Starre is the Denser Part of his Orbe,) hath notwithstanding so much Affinity with the Starre, that there is a Rotation of that, as well as of the Starre.”

²Note that, ironically, our modern concept of vacuum and the cosmological constant is at times reminiscent of the aether theory.

to a fragmentation of its initial condensations. These strong forces act on the vast scales of giant molecular clouds, but persist down to individual stars. These forces are strong enough to initiate nuclear fusion, the most energetic process known on microscopic scales, and thus to actually bring stars to life. Star formation itself is a complex process, and still a prime discipline of astrophysical studies. This process, together with the multifaceted life cycle of the various types of stars resulting from it, has numerous intermediate stages and byproducts, leading to a richness of ISM components. Nested within the ISM, we find a range of hot and cold condensations. Around newborn stars, accretion disks represent a special form of structured interstellar matter, which may even lead to the formation of planetary systems in some cases (e.g., van Dishoeck 2004). Different classes of young stars show jets and bipolar outflows, energetic stellar winds, or even shocks (e.g., Bachiller 1996). All these processes have a feedback effect on the surrounding ISM, and determine the global properties under which star formation can take place. Also, the significant, sometimes violent impact that these processes have on the ISM is responsible for the overall low efficiency of star formation itself, and only a few per cent of the total amount of material available for star formation actually ends up in stars in a typical star formation cycle (e.g., Shu et al. 1987; Evans 1999).

The physical properties, chemical composition, and global mass of the ISM in a galaxy thus are largely determined by its interaction with stars, which causes the richness, but also the peculiarity of the ISM phase. This does not only concern the formation of new stars as described above. In particular during the final stages of a stellar lifecycle, a number of phenomena exist that heavily impact the ISM. When an intermediate mass star ($2 M_{\odot} \leq M_{\star} \leq 7 M_{\odot}$, i.e., nuclear fusion does not proceed beyond the production of C and O) climbs up the asymptotic giant branch (AGB), it blows away its outer layers in thermal pulses, leading to strong winds (e.g., Lattanzio & Boothroyd 1997). Depending on their effective temperature, some of these stars ionize their expanding, blown-off hull material during their post-AGB phase, leading to the formation of spectacular planetary nebulae. An even stronger feedback is caused by the most massive stars, when they end their stellar life in a highly energetic supernova blast, being a very effective way to enrich the ISM with the metals that they produced in the earlier stages of their life cycle. The remnants of such supernovae can even create magnetohydrodynamic waves, which also impact the ISM (e.g., Chevalier et al. 1992). In addition to intense ultraviolet (UV) radiation from massive young stars, winds and explosions, highly energetic radiation strongly influences the structure and composition of the ISM. Light emitted in the X-ray and γ -ray wavelength regimes, and cosmic rays of even higher energies strongly interact with the atoms and molecules of the ISM. The range of interactions taking place leads to a partial ionization of the ISM, favors the occurrence of magnetic fields, and the creation of turbulence and shocks.

The feedback of star formation on the ISM (whose dynamics triggered it in the first place), and the interactions between stars and ISM that occur due to stellar evolution also govern the overall chemical evolution of the galaxy that hosts both the stars and the medium. It thus is essential to understand these processes in detail for studies of galaxy formation and evolution throughout cosmic times.

A range of phenomena connected to the ISM can be observed on galactic scales. The

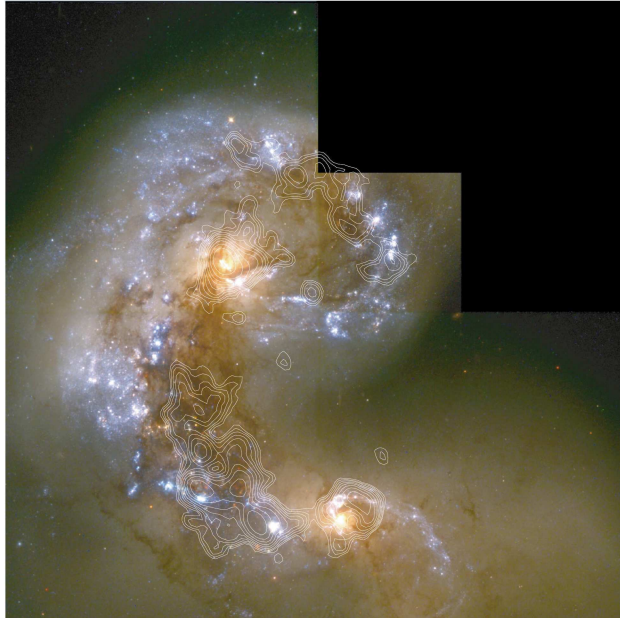


Figure 1.1: Map of the molecular ISM (here: CO) in the central region of the Antennae (NGC 4038/39), a nearby merger, overlaid on a true color HST image (Wilson et al. 2000). The molecular gas is largely aligned with the dust lanes, and peaks around the galactic nuclei and in the “overlap” region.

ISM is a self-interacting, dissipating medium. It is commonly found at the origin of galactic disk formation, showing that it plays an important role in studies of the formation of disk galaxies. It also is subject to strong interactions in galaxy collisions and major merger events (see, e.g., Figure 1.1). Mergers are often observed to occur coevally with major starbursts, which gives rise to the interpretation that the compression of several ISM components on larger scales due to the merger event triggers and feeds such starbursts. Also, the same material may feed supermassive black holes (SMBHs) in the centers of the merging galaxies in the same event, being to a significant fraction responsible for their growth and active galactic nucleus (AGN)/quasar activity (e.g., Di Matteo et al. 2007). This may then also explain the locally observed correlation between black hole mass and stellar bulge velocity dispersion (as a tracer of stellar mass) in galaxies ($M_{\text{BH}}-\sigma_v$), which is interpreted as a coeval growth of SMBHs and stellar bulges (e.g., Magorrian et al. 1998; Ferrarese & Merritt 2000; Gebhardt et al. 2000).

The mass of the ISM does not only increase via mergers, but also through accretion of extragalactic gas. Gas is also found in connection with galactic bars, which may play a role in the inflow of gas to the center of a galaxy (e.g., Bournaud & Combes 2002). The ISM is also strongly affected and compressed by spiral density waves that lead to the formation of spiral arms. The influence of the density waves on the ISM can then also lead to star formation in spiral structures (e.g., Binney & Tremaine 1987). Due to

the pressure-driven effects in star formation mentioned previously, some starburst galaxies show huge outflows of ISM material from the starburst center into the galactic halo. The scales of such an outflow may even extend beyond the galaxy, and can be responsible for the enrichment of the intergalactic medium (IGM) with heavy elements (e.g., Ellison et al. 2000). The processes taking place in the ISM thus are fundamental to the understanding of astrophysics on a large range of scales.

1.1.3 Properties of the ISM

There are a number of physical parameters that are important to describe the ISM (see, e.g., Tielens 2005). It has different phases, described by a range of temperatures and densities. The ISM is subject to different sources of heating and cooling. Many processes taking place in the ISM are highly dynamic. The interplay of heating, cooling, and dynamical processes imprints some special thermodynamical properties on the ISM, such as the existence of major instabilities, and the occurrence of frequent shocks and peculiar turbulence. A range of chemical reactions takes place within the ISM. Apart from gas, the ISM also hosts dust (typically <1% of the gas mass) and nanoparticles [most importantly polycyclic aromatic hydrocarbons (PAHs)]. Radiative transfer processes thus play a major role in the determination of its properties, such as its energy balance, and its overall, multiwavelength spectral energy distribution (SED).

Phases of the ISM

The ISM is described well by three-phase medium models (McKee & Ostriker 1977). Such models assume that the ISM has a cold, dense phase ($T < 300$ K) that consists mostly of clouds of neutral and molecular hydrogen (H I and H₂), a warm intercloud phase ($T \simeq 10^3$ K), consisting of rarefied neutral and ionized gas, and a dynamic third phase representing the very hot ($T = 10^6$ K) gas that was shock heated by supernovae. This third phase may constitute most of the volume of the ISM (see Table 1.1).

Heating of the ISM

There is a range of different processes that contribute to heating the ISM. Apart from the processes that heat the ISM on a macroscopic level (gravitational collapse of a cloud, expansion of H II regions, winds, supernova explosions), a number of processes takes place on a microscopic level. Cosmic rays heat the ISM by transferring energy to the gas via ionization and excitation, and to free electrons via Coulomb interactions. Photoionization dominates the heating in H II regions. Photoelectrons from X-ray light are strong enough to cause secondary ionization, causing X-ray heating to be efficient in the warm, atomic medium.

However, one of the most important sources of heating is the intense UV radiation from newly formed, massive young stars (and AGN). UV photons cause photoelectric ejections of electrons (and, in the vicinity of an intense UV source, atoms) from dust grains. However,

Table 1.1: Characteristics of the Different ISM Phases

Phase	n_0 (cm^{-3})	T_0 (K)	f_V (%)	State
Molecular Clouds	>200	10	0.05	molecular
Cold Neutral Medium	50	80	1	neutral
Warm Neutral Medium	0.5	8000	30	neutral
Warm Ionized Medium	0.1	8000	25	ionized
H II Regions	1–10 ⁵	10 ⁴	~5	ionized
Hot Ionized Medium (Coronal Gas)	0.003	10 ⁶	~50	highly ionized

Notes—Symbols are: n_0 – Typical density. T_0 – Typical temperature. f_V – Volume fraction. Values adopted from Tielens (2005). Note that the relative proportions of the phases and their subdivisions are a matter of considerable contention.

part of the energy of the UV photon is transferred into lattice energy, effectively heating the dust grains. This process is the main source of dust obscuration of UV/optical light. The dust channels a substantial fraction of the energy created in star formation into the infrared (IR) to far-infrared (FIR) wavelength regime, where it shines brightly. Depending on the amount of dust in a galaxy, this may fully deplete the UV/optical radiation from stars, and create a huge bump in the infrared region of its SED (so-called infrared-luminous galaxies). While the heating of large dust grains create this strong continuum bump in the FIR (e.g., Draine & Lee 1984), nanoparticles create strong, broad PAH bands in the mid-IR region of the SED (e.g., Désert et al. 1990). The dust that is heated by this process can also heat the gas via dust grain-gas particle collisions, locking the temperature of the gas to that of the dust. However, this process only dominates the gas heating deep in dense molecular clouds (which are optically thin to far-infrared radiation, but very opaque to all light at shorter wavelengths).

There is one other process that is important for both dust and gas heating, and also closely connected to the formation of molecular gas, which sublimates on dust grains: Molecular hydrogen can be formed on the surface of a dust grain from two hydrogen atoms. This process yields an energy of 4.48 eV, which is partly used to heat the dust grain, and partly to heat the gas (via collisions of the formed H₂ molecule, which also receives a certain kinetic energy).

Note that, even though some of the processes taking place in the interstellar gas are quite energetic, it still is only a small fraction of the overall energy generated in stars and active galactic nuclei.

Cooling of the ISM

The most basic cooling process in the ISM is adiabatic expansion. A second important process is cooling of dust, mostly in the mid-to-far-infrared continuum. This process is effective in all but the densest regions of the ISM. The third process, which is important in most regions of the ISM (except regions of hot gas where atoms are highly ionized, and molecular clouds), is the cooling via fine structure lines of atoms and ions. Fine structure cooling is most efficient via atoms/ions that a) are highly abundant, and b) have fine structure levels close to the fundamental level (as cooling via forbidden lines is most effective in cold gas where allowed transitions cannot be excited). In the neutral medium, these are mostly C II and O I. In H II regions, these are mostly O II, O III, N II, N III, Ne II, and Ne III. The transitions in these atoms/ions are usually collisionally excited, and will then de-excite radiationally.

The fourth process is cooling via non-forbidden atomic lines. For these lines to be collisionally excited, the temperature has to be relatively high (few times 10^3 K). The most important case is the $n=2$ level of hydrogen, which emits a Lyman- α photon at 121.6 nm upon de-excitation. However, the efficiency of this process drops above 10^5 K, as most species (except Fe) are highly ionized and retain only few bound electrons³.

The fifth process, which is dominant in molecular clouds, is the collisional excitation of rotational molecular transitions, in particular CO (note that H₂ does not have ‘basic’ rotational transitions; see Chapter 2). These transitions have low energies and radiate typically at millimeter wavelengths (see Figure 1.2). Due to the low energies, this cooling process is very efficient, causing molecular clouds to be very cool⁴. They however require relatively high densities to be collisionally excited (typically 10^3 – 10^5 cm⁻³). Due to its high abundance, ¹²CO dominates the cooling at the lowest densities. At higher densities, the contribution from ¹³CO becomes significant, sometimes comparable to that of ¹²CO⁵. At high densities, other abundant molecules, such as H₂O, HCN, HCO⁺, and CS, dominate the cooling budget.⁶

1.2 The Molecular ISM

The gaseous ISM is mostly of low density ($< 10^3$ cm⁻³). However, this is only true outside of star-forming regions, which have considerably higher densities (few times 10^4 to 10^5 cm⁻³). As described in the previous section, material in star-forming regions has to contract to actually form stars, which makes them likely to have densities above the average. However, another perspective to this is that stars form out of molecular clouds. This is due to the fact that efficient molecular line cooling to low temperatures is required to support the gravitational collapse (which, by the laws of thermodynamics, would stall without cooling).

³However, hydrogen cooling becomes efficient again above 10^7 K via the free-free channel.

⁴The cooling timescale of a dense core of 10^4 cm⁻³ is only of order 10^4 yr.

⁵The ¹²C/¹³C isotope ratio in the Galaxy is ~ 65 , however, lines from ¹²CO, in contrast to those of ¹³CO, are typically optically thick, and thus tend to saturate in the densest parts of molecular clouds.

⁶Depending on temperature.

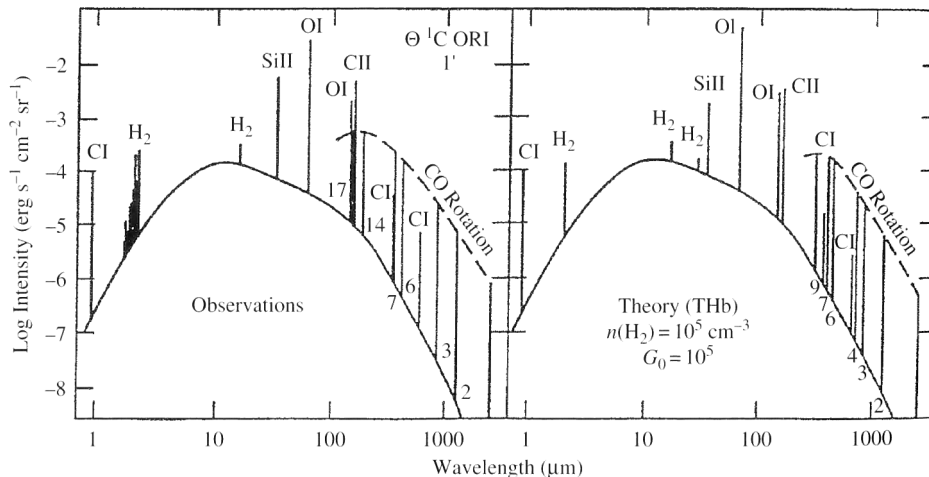


Figure 1.2: Observed IR spectrum (*left*) and model calculations (*right*) for Orion, a dense, star-forming region (Hollenbach & Tielens 1999). The most prominent emission lines are those of CO, C I, C II, and O I, responsible for the cooling of the neutral atomic and molecular ISM.

Molecular gas is also an essential constituent of proto-planetary disks around young stars, which form out of the remainder material that got caught into the gravitational collapse, but did not lose enough angular momentum to accrete onto the star. However, due to a number of violent processes and penetrating, highly energetic radiation, the ISM is in general hostile to molecules, as they are relatively easily photodissociated by the interstellar radiation field. In order to survive, molecules need to find shelter in dense, less affected environments, where they are shielded (by dust grains and self-shielding) from highly energetic radiation (typically effective at densities in excess of 10^2 cm^{-3} ; e.g., Solomon & Wickramasinghe 1969). Also, molecules are formed at higher rates in denser regions. Molecules thus typically trace the denser, cooler regions of the ISM. In the dense cores of the molecular gas phase, star formation takes place. This is why a) the total amount of molecular gas in a galaxy is considered the prerequisite material for star formation, and b) dense molecular gas is considered a direct tracer for star formation (see discussion in Section 1.4 and Chapters 2, and 4–7). The abundance of molecules is determined by the balance between formation (dominantly sublimation on dust grains) and destruction (mostly UV radiation) processes. Due to the high abundance of hydrogen, H_2 is by far the most abundant molecule (by at least 3-4 orders of magnitude), followed by CO (the main tracer of the molecular ISM, due to its high abundance and low electric dipole moment of $\mu_D^{\text{CO}}=0.112$) and H_2O . Less than 1% of the mass of a molecular cloud is found in dust grains, which are intimately mixed with the gas particles and, together with cosmic rays, are responsible for most of the heating. As this heating is rather inefficient, the molecular ISM is mostly cold (10-50 K), but can be significantly warmer (~ 100 K) due to intense starbursts or proximity to an AGN (or, on small scales, individual stars).

Due to its importance for star formation, its rich physical properties, and the implications of its chemical composition, studies of molecular gas are a key topic of observational astronomy and theoretical astrophysics. Observing molecular gas in galaxies at different redshifts helps to understand the formation, evolution, and interaction of different kinds of galaxies out to the times when most stars in galaxies formed, and even beyond, into the epoch when the first galaxies themselves formed. In particular, they have the potential to reveal the connection between AGN and their host galaxies. This is an important aspect in unifying the “zoo” of galaxies detected at different epochs, and thus in obtaining a more comprehensive picture of the structures that populate and evolve in the universe.

1.3 Molecular Gas in Galaxies

It is important to study interstellar gas on galactic scales to understand the structure and dynamics of galaxies, as well as to understand the global properties of star formation. The standard tracer of neutral atomic gas, even in molecular clouds, is the 21 cm spin-flip transition of H I. The H I kinematics can be used to study the rotation and global mass of galaxies, including their dark matter content (e.g., Walter et al. 2005). Due to its high abundance and brightness (and the difficulty of direct observations of H₂), CO is the standard tracer of molecular gas. The studies of molecular gas in our own and external galaxies has proven to be the key to understanding how stars form in galaxies. Studying the amount, distribution, and dynamics of molecular gas thus are vital to our picture of star formation and galaxy evolution in a more general framework. Not surprisingly, the properties of star formation are closely tied to those of the molecular gas, and appear to be subject to similar variations among galaxies. The global star formation rate in a galaxy appears to strongly depend on feeding by extragalactic gas. It also seems to be pronounced in interacting galaxies and major mergers, where intense starbursts are observed to occur. The total amount of molecular gas is by far the largest in spiral galaxies, and varies strongly among galaxy types. In the central regions of galaxies, the properties of the molecular ISM are often different from the outer regions, and shows strong concentrations and sites of starbursts in some galaxies. Also, there appears to be a connection with bars, and even AGN activity. The observed properties of molecular gas for different types of galaxies are briefly discussed in the following (see Solomon & Vanden Bout 2005 and Omont 2007 for reviews).

1.3.1 Molecular Gas in the Milky Way

CO is the brightest molecule in basically all molecular clouds in our Galaxy (due to the lack of rotational transitions of H₂, see Chapter 2), as well as in any other galaxy, even out to the highest redshifts. It thus is systematically used to determine the total molecular gas mass in a galaxy.

In the Milky Way, about 90% of the molecular mass appear to be in massive structures that are distributed in clumps - the giant molecular clouds (GMCs, e.g., Dame et al. 1987,

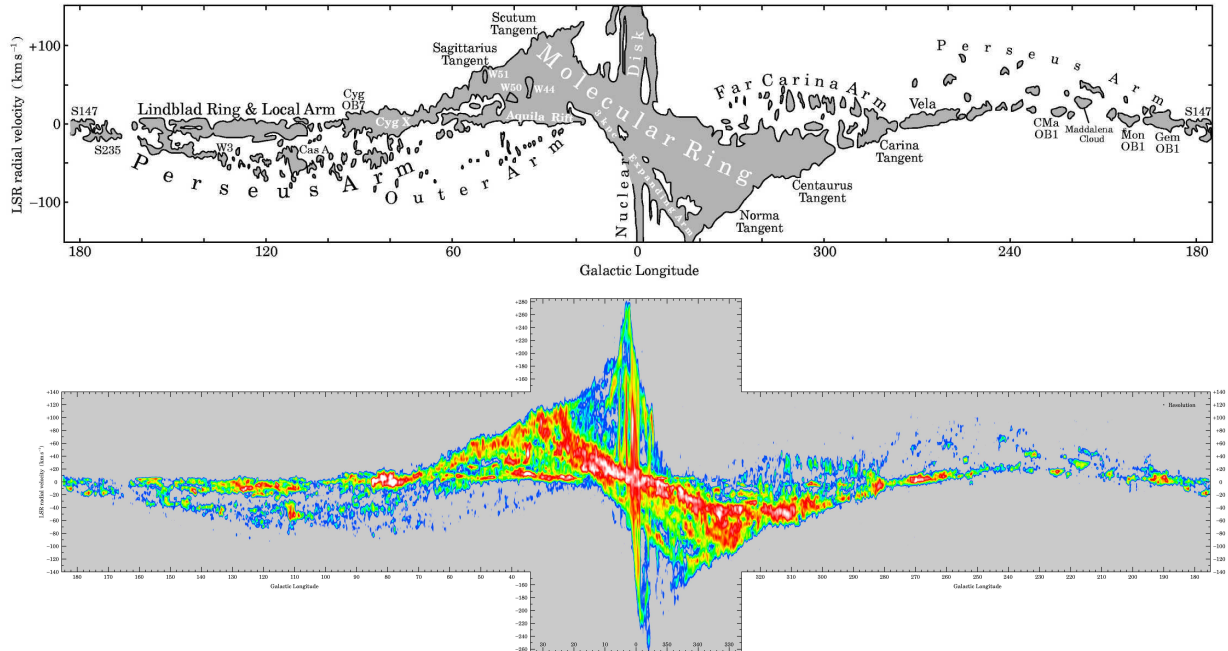


Figure 1.3: Longitude-velocity diagram of the molecular disk of the Milky Way, as traced by CO emission (Dame et al. 2001). *Top*: Labeled sketch of the distribution. *Bottom*: Map of the CO($J=1\rightarrow 0$) intensity.

2001, see Figure 1.3). The practically complete CO($J=1\rightarrow 0$) survey of GMCs in the Milky Way by Dame et al. (2001) has shown that almost all GMCs (and thus, molecular mass) are concentrated within or very close to the Galactic plane. This is not surprising, as this is also where most of the stars form. GMCs are typically 50 pc in diameter, host $\sim 10^5 - 10^6 M_{\odot}$ of material, and have average densities of order 10^2 cm^{-3} (e.g., Scoville & Solomon 1974; Evans 1999; Williams et al. 2000). The line widths, sizes, and masses of these GMCs are strongly correlated, indicating that they have a constant average surface density and are close to virial equilibrium (Larson 1981).

Due to the fact that the CO($J=1\rightarrow 0$) line is usually optically thick and requires a comparatively low density to be excited, it is considered a good tracer of the large-scale envelopes which contain most of the mass of GMCs, i.e., a tracer of the total molecular gas mass in a galaxy. However, in spite of being the most sensitive qualitative tracer of molecular gas, the fact that the CO($J=1\rightarrow 0$) line is optically thick makes it difficult to derive the actual mass from such observations. In principle, the abundance of CO, its excitation, and radiative transfer with random cloud sizes and velocity distributions all have to be taken into account to obtain the H₂ mass from the CO($J=1\rightarrow 0$) line intensity. It however has been found empirically that the velocity-integrated CO($J=1\rightarrow 0$) line intensity quantitatively traces molecular gas quite well. This is probably due to velocity/turbulent broadening, and the fact that the velocity width depends on mass. The connection between

CO intensity and molecular gas mass is usually quantified by the “X-factor”, a conversion between the H_2 column density (which can then be converted to mass), and the integrated CO line intensity I_{CO} :

$$X = N_{H_2}/I_{CO}, \quad (1.1)$$

given in units of $\text{cm}^{-2} (\text{K km s}^{-1})^{-1}$. The variation of X derived based on different estimators (e.g., diffuse γ -ray emission, FIR and 21 cm surveys, extinction in the optical/X-ray regime; Combes 1991; Dame et al. 2001; Lequeux 2005) shows little variation, indicating that the I_{CO} -based H_2 column density estimate is relatively solid. Based on studying the correlation of γ -ray flux (produced by cosmic ray interactions with protons) with CO line flux in the Galactic molecular ring, Hunter et al. (1997) find:

$$X = (1.56 \pm 0.05) \times 10^{20} \text{ cm}^{-2} (\text{K km s}^{-1})^{-1}. \quad (1.2)$$

The uncertainty of the total H_2 mass is the same as that of X . The conversion factor α between H_2 mass and CO line luminosity is defined as:

$$\alpha = M_{H_2}/L'_{CO}, \quad (1.3)$$

given in units of $M_{\odot} (\text{K km s}^{-1} \text{ pc}^2)^{-1}$. Note that this definition typically includes both H_2 and He to encompass the total gas mass for molecular clouds (where H is almost completely molecular). Different methods have been used to determine α in the Galaxy, such as studying the correlation of optical extinction with ^{13}CO flux (Dickman 1978), the CO- γ ray correlation in the Galactic molecular ring (Bloemen et al. 1986; Strong et al. 1988), and the relations between virial mass and CO line luminosity in GMCs (Solomon et al. 1987). Based on these diagnostics, Solomon & Barrett (1991) have found for the Milky Way that:

$$\alpha = 4.6 M_{\odot} (\text{K km s}^{-1} \text{ pc}^2)^{-1}. \quad (1.4)$$

Blitz (1996) has derived an H_2 mass of the Milky Way of $\sim 1 \times 10^9 M_{\odot}$, which is about 20% of the H I mass (Wouterloot et al. 1990).

1.3.2 Molecular Gas in Nearby Spiral Galaxies

Molecular gas observations in galaxies different from the Milky Way are limited by the same main problem: to convert CO intensities into H_2 masses. However, assuming that, to first order, the techniques used for studies in the Galaxy hold for other environments, our knowledge about molecular gas in other galaxies is quite detailed (see Figure 1.4 for an illustrative example), with about 1000 CO-detected galaxies of different types to date. It has been found that, in the local universe, molecular gas is by far the most prominent in massive, early-type spiral galaxies. However, even within homogenous samples of massive spiral galaxies, the variations in the molecular content are quite large (e.g., Bettoni et al. 2003). The ratio of molecular to atomic gas mass (i.e., $H_2/H\text{I}$) shows variations over two

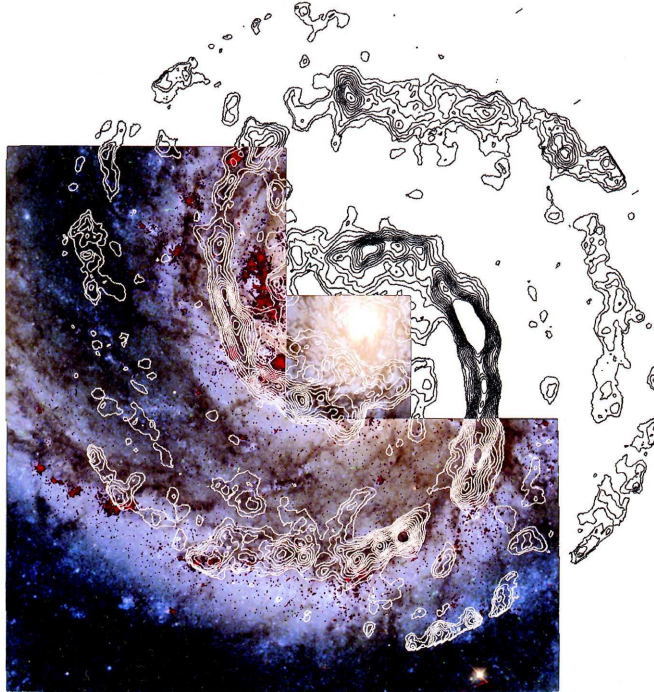


Figure 1.4: CO($J=1\rightarrow 0$) intensity distribution in the disk of the nearby spiral galaxy M51, overlaid on a Hubble Space Telescope image (Aalto et al. 1999).

orders of magnitude with standard diagnostics such as the blue and FIR luminosities, L_B and L_{FIR} . Part of this scatter may be due to the uncertainty of the X factor. However, on average, the ratio clearly correlates with parameters such as metallicity, dynamical mass, L_B , and L_{FIR} .

The X factor itself is calibrated either based on the Milky Way value, or based on other, simplified methods. The two most common methods are to calculate the conversion under the assumption that the GMCs in a galaxy are in virial equilibrium (Young & Scoville 1991), or to extrapolate the gas mass from the cold dust mass observed in the FIR, assuming a metallicity-dependent gas-to-dust ratio (Guélin et al. 1995). Based on such methods, it has been found that the X factor of nearby spiral galaxies seems to agree with that of the Milky Way within a factor of 2 (e.g., Boselli et al. 2002). With this result, the molecular-to-atomic gas mass ratio can be determined for nearby spirals. Different authors have found ratios in the range of 0.2-0.4 (Casoli et al. 1998; Boselli et al. 2002; Bettoni et al. 2003), i.e., similar to that of the Milky Way. It thus appears to be a global property of nearby spiral galaxies to host significantly more atomic than molecular gas.

Looking at the distribution of the molecular gas in spiral galaxies, it has been found that the radial profiles are centrally peaked, showing an exponential falloff toward the outskirts. The structure and dynamics of molecular gas in the inner regions of barred spiral galaxies suggests that the stellar bars may aid the molecular gas in losing angular

momentum, leading to infall toward the nuclear region in the central kiloparsec (e.g., Lee et al. 2006). This could explain the elevated surface densities of molecular gas and nuclear starbursts in the center of some barred spiral galaxies.

1.3.3 Molecular Gas in Nearby Non-Spiral Galaxies

Molecular gas has also been observed in galaxies different from spirals, such as dwarf galaxies (including the Magellanic Clouds), low surface brightness galaxies (LSBs), ellipticals (in particular central cluster galaxies), and interacting galaxies.

Dwarf galaxies are weak CO emitters, and show X factors that are typically within a factor of a few of that in the Milky Way (e.g., Wilson 1995; Walter et al. 2001). Also, it was found that the molecular material mostly resides in photodissociation regions (PDRs; e.g., Lequeux et al. 1994; Leroy et al. 2005).

LSBs typically have low metallicities and low mean gas surface densities; however, some of them are detected in CO emission and show molecular to atomic gas mass ratios similar to galaxies of higher surface brightness (e.g., Matthews et al. 2005).

A fraction of elliptical galaxies is also detected in CO (note that most are not), and shows molecular to atomic gas mass ratios that are by a factor of 2-5 times lower than in normal spirals. Also, the molecular gas masses do not appear to correlate with the properties of the stellar population inside those galaxies, and thus may have accumulated after most of the stars formed (e.g., Knapp & Rupen 1996). This is compatible with the finding that CO is part of cooling flows in massive central ellipticals in clusters (e.g., Edge & Frayer 2003).

Additionally, CO is detected in the tidal debris of interacting galaxies (e.g., Walter & Heithausen 1999; Lisenfeld et al. 2004).

1.3.4 Molecular Gas in LIRGs and ULIRGs

A particularly interesting case in studies of molecular gas in galaxies are luminous infrared galaxies (LIRGs; $L_{\text{FIR}} > 10^{11} L_{\odot}$) and ultra-luminous infrared galaxies (ULIRGs; $L_{\text{FIR}} > 10^{12} L_{\odot}$), which are by one or two orders of magnitude more luminous in the FIR than normal galaxies. These galaxies are typically very dust-rich, which means that most of the energy produced by star formation gets re-processed into the FIR. Indeed, to produce such high L_{FIR} , tens to hundreds of $M_{\odot} \text{ yr}^{-1}$ are required, indicating that there are large starbursts in these systems. ULIRGs often show a perturbed morphology, indicating that the starbursts in these systems are triggered by strong interactions and mergers (see, e.g., Downes & Eckart 2007, Figure 1.5). ULIRGs are relatively rare in the local universe, but (assuming that submillimeter galaxies are their distant counterparts) highly abundant at higher redshift, in particular close to the peak of star formation in the universe at redshifts of 2–3. The molecular gas as traced by CO in these galaxies is commonly found in rotating circumnuclear disks or rings, which also hosts the starbursts (Downes & Solomon 1998). A fraction of the ULIRGs also show indication for AGN activity, which is also fueled by the (molecular) gas in these systems. Even though the neutral gas in the central CO-emitting

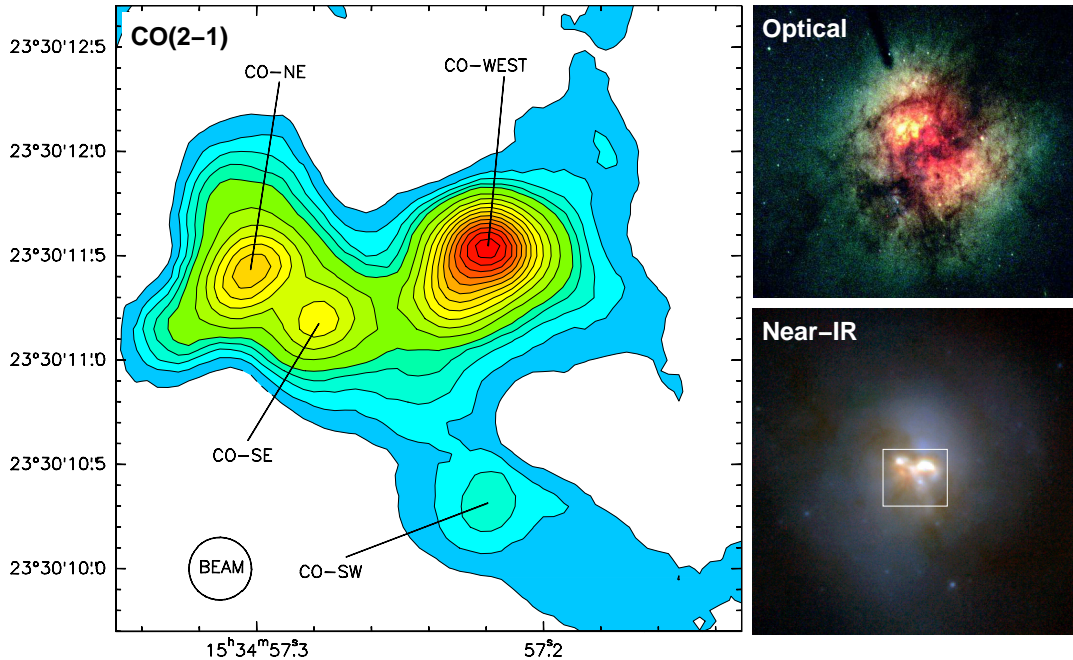


Figure 1.5: *Left*: CO($J=2\rightarrow 1$) intensity distribution of the central region of Arp 220, a nearby merging ULIRG (Downes & Eckart 2007). *Right*: Three-color optical (Wilson et al. 2006) and near-infrared (NIR; Scoville et al. 1998) composite images of Arp 220. The white box overlaid on the NIR image indicates the size of the CO map.

regions of ULIRGs is almost entirely molecular, using a Milky Way X factor overestimates the molecular mass in ULIRGs, which then sometimes even exceeds the dynamical masses in these systems (i.e., by assuming $\Delta V^2 = GM_{\text{dyn}}/R$; e.g., Sanders et al. 1986; Solomon et al. 1997). This is probably due to the fact that the molecular disks and rings in ULIRGs have a different structure and temperature than individual, virialized clouds in the disks of normal spiral galaxies. Kinematic modeling accounting for rotation curves, density distribution, size, turbulent velocity, and mass of the molecular rings shows that the bulk of the CO emission originates from a moderately dense, warm intercloud medium (Downes & Solomon 1998). Downes & Solomon find a conversion factor of:

$$X \simeq 0.4 \times 10^{20} \text{ cm}^{-2} (\text{K km s}^{-1})^{-1}, \quad (1.5)$$

a few times lower than the Milky Way value. This corresponds to a mass conversion factor of:

$$\alpha = 0.8 M_{\odot} (\text{K kms}^{-1} \text{ pc}^2)^{-1}. \quad (1.6)$$

This leads to typical molecular gas masses of $5 \times 10^9 M_{\odot}$, i.e., about five times that found in the Milky Way, however, still five times lower than what would have been estimated based on the Milky Way conversion factor.

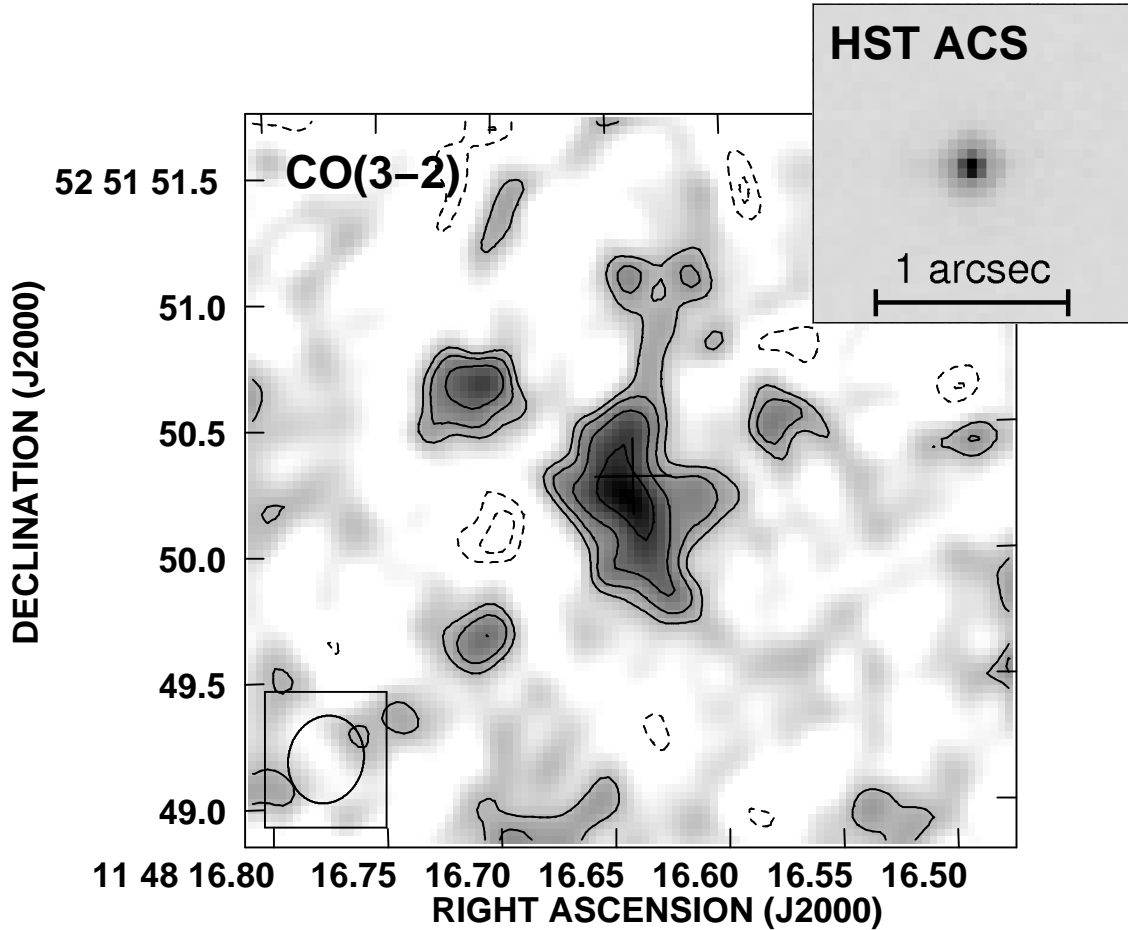


Figure 1.6: CO($J=3\rightarrow 2$) map of the $z=6.42$ quasar J1148+5251 at a linear resolution of $0.3''$ (Walter et al. 2004). The inset shows the optical quasar (White et al. 2005), as indicated by the cross.

1.3.5 Molecular Gas in Distant Galaxies

Despite the fact that a number of major initiatives over the past decade were aimed at finding molecular gas in the most distant galaxies, it has been detected in 43 galaxies at high redshift ($z > 1$) to date. This is mostly due to the faintness of the emission lines, which only permits to detect them in the most gas- and dust-rich systems in the early universe, and due to the limited bandwidth of the telescopes that can be used for such studies, requiring precise *systemic* redshifts (which may differ significantly from redshifts derived from broad optical emission lines; see Appendix A for a summary, and Solomon & Vanden Bout 2005 for a review). The distance of these galaxies and the faintness of the lines makes it difficult to resolve the molecular line emission (although sometimes aided by gravitational magnification). In the few cases where structure can at least be marginally resolved, there

is possible evidence for interaction or even merging (Omont et al. 1996; Carilli et al. 2002b; Walter et al. 2004, see Figures 1.6 and 2.7), but also compact molecular disks, reminiscent of local ULIRGs (e.g., Downes & Solomon 2003). Due to detection at other wavelengths, these objects are known to encompass a range of galaxy types, such as quasars (QSOs), submillimeter galaxies (SMGs), radio galaxies (RGs), few Lyman-break galaxies (LBGs), and one extremely red object (ERO). The one property all those galaxies have in common (except for being detected in CO) is their extreme brightness in the FIR. Even though only SMGs are considered the high redshift counterparts of today's ULIRGs (although they are typically even more FIR-luminous than ULIRGs), the ULIRG conversion factor α of Downes & Solomon (1998) is usually adapted to derive molecular masses for all these galaxies. This leads to molecular gas masses within the range of ULIRGs for some of these galaxies, but to masses in excess of those of ULIRGs in more than half of the galaxies in the sample. Typical molecular gas masses are few times $10^{10} M_{\odot}$ (e.g., Chapter 3/Riechers et al. 2006a), which is higher than in nearby ULIRGs (typically $5 \times 10^9 M_{\odot}$; Downes & Solomon 1998). Due to the fact that only upper limits are known for the sizes of the CO-emitting regions in most of these galaxies, this approach has to be treated with caution, as it is difficult to calibrate with dynamical masses. Moreover, most of the high- z galaxies are only observed in higher J CO transitions (which may trace only part of the total CO luminosity), whereas ULIRGs are typically studied in the ground-state ($J=1$) CO transition (see Chapter 3 for a detailed investigation). In one of the few cases where a conversion factors could be derived for a high- z galaxy, it exceeds the ULIRG conversion factor by far ($\alpha = 5M_{\odot} (\text{K kms}^{-1} \text{pc}^2)^{-1}$; Weiß et al. 2007). However, note that the galaxy in the study by Weiß et al. is known to be extreme, even within the high z sample. The ultimate goal of molecular gas studies in these early systems is to resolve the emission (see Chapters 9 to 11 for a detailed investigation), as only this will provide insight on the nature of these galaxies, and help to understand how their integrated properties (e.g., molecular excitation, chemical composition) can be compared to particular types of nearby galaxies. Most importantly, such observations can reveal how the starbursts (and AGN, if present) in these systems are fueled, and thus provide insight on how the evolution of central supermassive black holes connects to that of the stellar bulge (such a connection is suggested by the locally observed relation between black hole mass and velocity dispersion of the stellar bulge, e.g., Ferrarese & Merrit 2000; Gebhardt et al. 2000).

In summary, molecular gas was detected in a range of galaxies of different types, and in different environments. The observed variations are largely due to variations in mass, luminosity, and metallicity, among those galaxies, which is reflected in the correlations between molecular gas mass and those quantities (e.g., Boselli et al. 2002). The fraction of molecular vs. atomic gas is highest in spiral galaxies, and shows values similar to those found in the Milky Way. There is about an order of magnitude of scatter between different types of galaxies, which reflects both the uncertainties in obtaining molecular masses, and the variations of the molecular environments among galaxy types. However, some fundamental correlations exist between the amount of molecular gas in a galaxy and other properties. The key relation is that between molecular gas mass and star formation rate, as it offers significant insight on the nature and evolution of gas-rich galaxies.

1.4 Relations between Molecular Gas Mass and Star Formation Rate

Due to the necessary fragmentation and collapse of clumps, star formation is a process that takes place in the densest parts of the ISM. In these parts, most of the matter is found in molecular form. The amount of molecular gas in a galaxy thus is also some form of measure of the star formation rate. The standard measure of star formation in nearby galaxies is the UV continuum luminosity, or the $H\alpha$ luminosity. Both measure the light emitted by newly formed massive stars, and thus are a measure for the rate of massive star formation. The total star formation rate (SFR) can then be derived assuming a certain stellar initial mass function (IMF). However, star formation is known to take place in dust- and gas-rich environments. This means that the measured UV and $H\alpha$ luminosities are usually reduced due to dust obscuration (extinction). The dust-processed light is re-emitted in the FIR. If a galaxy is not significantly obscured by dust, the FIR luminosity is a measure for the correction factor of the UV/optical SFRs. If a galaxy is heavily dust-obscured, the FIR luminosity itself is a better tracer of the SFR than the UV/optical indicators altogether. In those galaxies, the SFR can be inferred directly based on L_{FIR} (Kennicutt 1998a):

$$\text{SFR} \simeq 1.5 \times 10^{-10} L_{\text{FIR}} . \quad (1.7)$$

In the Milky Way and nearby galaxies, it is known that most star formation takes place in GMCs that have the necessary mass to form massive stars. The size of GMCs thus can be considered the fundamental scale for star formation, and the mass of and number of these clouds in a galaxy can be considered a measure for the global amount of star formation.

In a general form, the relation between gas mass and SFR can be expressed in several ways. Following the original formulation of Schmidt (1959), Kennicutt (1998a) suggested that the total amount of gas (i.e., $H_2+H\text{I}$) surface density is the fundamental quantity for determining the SFR, at least averaged over the whole timescale on which a galaxy forms stars. The SFR and gas surface densities are then expressed in units of $M_{\odot} \text{ pc}^{-2}$, and $M_{\odot} \text{ yr}^{-1} \text{ kpc}^{-2}$. Figure 1.7 shows such a Schmidt-Kennicutt law of star formation for normal galaxies and starburst galaxies. Clearly, all galaxies follow a common relation, which is fitted best by a power law with a slope of $N=1.40 \pm 0.05$ (note that this slope varies throughout the literature depending on the sample that is studied, but usually close to 1.5).

If the subject of interest is the SFR at a certain time, it is more common to examine the relation between SFR and total molecular (H_2) gas mass, expressed in units of M_{\odot} , and $M_{\odot} \text{ yr}^{-1}$. This diagnostic is particularly useful for high redshift galaxies, where only total luminosities can be measured in most cases. The most common quantity to determine the total molecular gas mass is L'_{CO} . The most common quantity to determine the SFR is the FIR luminosity, in particular in gas-rich galaxies (however, note that for non-starburst galaxies, L_{FIR} usually has to be corrected based on other SFR tracers, see above). The $L'_{\text{CO}}-L_{\text{FIR}}$ relation has been the subject of many studies (see, e.g., Solomon & Sage 1988;

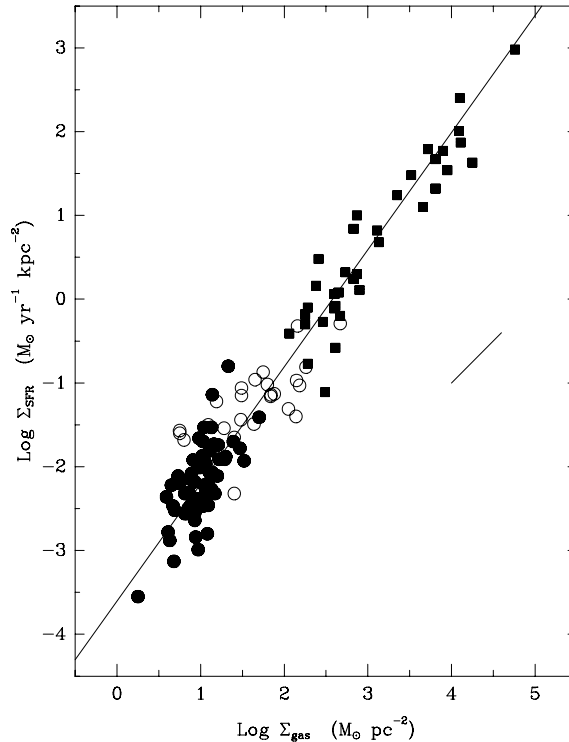


Figure 1.7: Relation between gas density and SFR density for normal disk (filled circles) and starburst (squares) galaxies (Kennicutt 1998a, 1998b). Open circles show the SFRs and gas densities for the centers of the normal disk galaxies. The line is a least-squares fit with a power-law index of $N=1.40$.

Solomon et al. 1997; Yao et al. 2003; Gao & Solomon 2004a, 2004b, see Figure 1.8, left; Riechers et al. 2006a, see Chapter 3), and typically leads to power laws with a slope of $N=1.4-1.7$, which is very similar to the Schmidt-Kennicutt law. This is not surprising, as the galaxies in Kennicutt's sample are predominantly molecular over the examined dynamical range. There is a number of possible explanations for a power-law slope close to 1.5. The SFR per unit gas mass is expected to be proportional to the amount of molecular gas available for star formation. However, the free-fall, or dynamical time scale for a molecular cloud to contract depends on the square root of the density of the medium. If a constant fraction of the molecular gas in a cloud is converted into stars each free-fall time, the star formation rate per unit volume thus is expected to grow with mass density to the power 1.5 (Madore 1977). The CO luminosity per unit volume, on the other hand, is roughly proportional to the mass density. As discussed by Krumholz & Thompson (2007), this would explain a power-law slope close to 1.5 in the $L'_{\text{CO}}-L_{\text{FIR}}$ relation (assuming that gas scale heights in galaxies do not vary strongly).

In general, the ratio of the SFR and the amount of gas that is available for star formation defines some sort of efficiency of star formation. In the above definition, this star formation

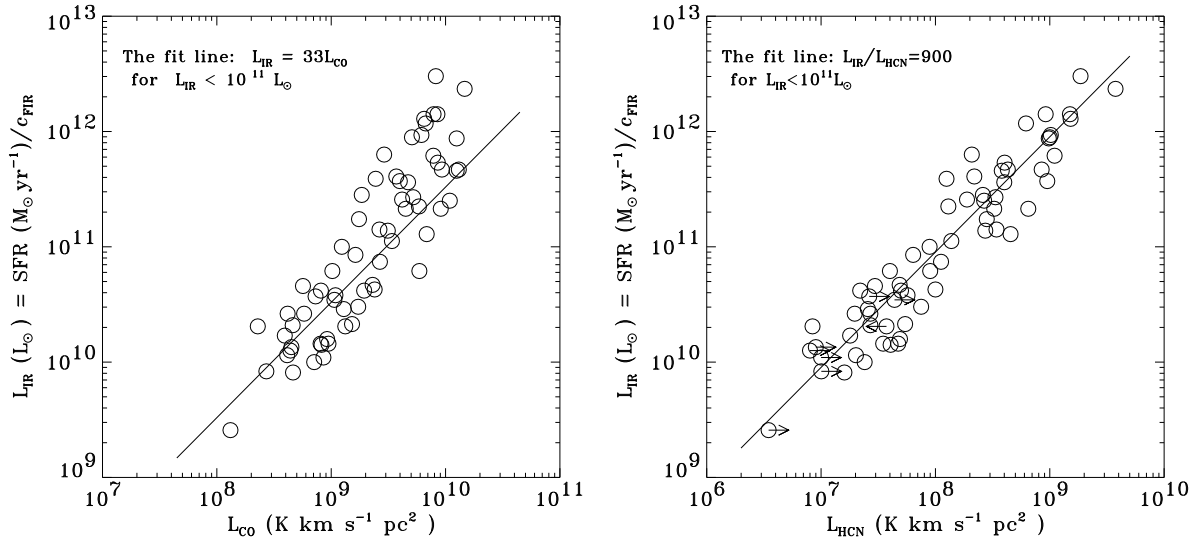


Figure 1.8: Relations between CO (*left*) and HCN (*right*) luminosity and infrared luminosity for 65 nearby galaxies, encompassing normal spiral galaxies, LIRGs, and ULIRGs (Gao & Solomon 2004a). The solid lines are fits to the least luminous galaxies, with a slope fixed to unity.

efficiency (SFE) rises roughly with gas density as $\text{SFE} \propto n^{1.5}$. However, note that this is only the case because the median density in molecular clouds is higher than the critical density necessary to excite the ground-state transition of CO (see Chapter 2 for a more detailed description), which is most commonly observed. Due to this non-linear dependence on the SFR, the CO luminosity is in general not considered a good direct tracer of star formation. However, the clearly defined $L'_{\text{CO}}-L_{\text{FIR}}$ relation still is a good indicator for the SFE (in terms of the total amount of molecular gas converted into stars).

A good molecular tracer of star formation has to relate linearly to the SFR. If the median molecular gas density in a galaxy is lower than the critical density of a molecular transition, this transition primarily traces the dense peaks of the molecular clouds that are close to its critical density (i.e., the luminosity does not scale with density/free-fall time). If the critical density of this transition is close to the median density of the dense cores where star formation takes place, it thus is a good tracer of these dense cores, and the SFR (see Krumholz & Thompson 2007 for a model). The HCN($J=1 \rightarrow 0$) transition is such a tracer of dense cores. Indeed, observations show that the $L'_{\text{HCN}}-L_{\text{FIR}}$ relation scales linearly (Gao & Solomon 2004a, see Figure 1.8, right). It has even been shown that this relation stays linear down to individual dense cores (Wu et al. 2005), confirming the validity of this relation. Note that this is somewhat surprising, as we have seen that the circumnuclear rings in ULIRGs host conditions that are quite different from those in the disks of spiral galaxies, and implies that the conditions for star formation itself are actually

not that different. If we define the SFE as SFR per unit of *dense* (HCN) molecular gas mass, it stays constant, and does not rise toward higher luminosity (or, in a simplified picture, toward higher median gas density, which would imply that there is a limit where this is not valid anymore - see Chapter 4).

In practice, the SFE depends on many variables, in particular the gas temperature, and the structure of the molecular ISM in a galaxy, as well as the obvious variations between galaxies. In addition, L_{FIR} may be biased by dust heating of active galactic nuclei instead of (in addition to) star formation. However, due to the fact that the observed $L'_{\text{CO}}-L_{\text{FIR}}$ and $L'_{\text{HCN}}-L_{\text{FIR}}$ relations are quite tight over many orders of magnitude in luminosity, they are two of the main diagnostics in studies of star formation in galaxies, with the implications that 1) the FIR luminosity is a good tracer of the SFR, 2) the CO luminosity is a good tracer for the total amount of molecular gas in a galaxy, and 3) the HCN luminosity is a good tracer of dense, star-forming cores. Also, due to the fact that these relations are described by integrated luminosities, they are particularly useful for studies at high redshift. It thus has been attempted to extend these relations to galaxies at high redshift (see Chapter 3 for CO, and Gao et al. 2007 and Chapter 4 for HCN). Also, it has been attempted to extend these studies to other molecules which trace different environments (see Chapters 5-7 for HCO^+ , CN, and CS, and Chapter 2 for a description how “good” molecular tracers are selected).

The penultimate goal in studies of the star formation reservoirs in high redshift galaxies is to actually resolve the emission, which allows us to infer a number of physical properties that cannot be obtained in any other way. The first results of such a study are shown in Chapters 9-11.

Chapter 2

Diagnostics and Strategies

The main diagnostic in studies of the molecular ISM is the luminosity of emission lines of different molecules in the interstellar matter field. This chapter will start with an outline of how the main observables, the frequency and intensity of an emission line, connect to the main properties describing the physical conditions in the molecular ISM of a galaxy, namely the temperature, density, and composition of the gas. In practice, it is not useful to use the intensity of an emission line (mainly due to its dependency on scales) to study generalized relations, but rather the integrated line luminosity. Afterwards, a description of how to obtain the line luminosity from observables is given, and the implications for observations at high redshift are elaborated. The chapter closes with a description of the current and future facilities used for such observations, including their limitations. This information is vital to understand how the targets and emission lines for the studies in this thesis were chosen, and to elaborate on future prospects.

2.1 Molecular Line Spectroscopy

Due to their rotational ladders, molecular lines are ideal probes of the physical properties of the gas that gives rise to them. Different rotational transitions of a molecule originate from levels at different energies and have different critical densities. The relative intensities of different rotational lines of the same molecule thus can be used to derive both the temperature and the density of the gas. In the following, it is first described how to determine the frequencies and minimum excitation temperatures of the rotational transitions of some of the most common interstellar molecules. Afterwards, a brief outline of how to derive the physical properties of the gas based on models of the population of the different rotational transitions is given.

2.1.1 Molecular Line Frequencies

The free rotation of a molecule is quantized according to quantum mechanical selection rules. This means that the emission from rotational transitions of molecules occurs in

discrete lines, typically in the millimeter wavelength regime. The moment of inertia of a molecule is defined as:

$$I = \sum_i m_i r_i^2, \quad (2.1)$$

where m_i is the mass of atom i at distance r_i from the center of mass. In general, molecules have three moments of inertia I_1 , I_2 , and I_3 , one for each spatial dimension (i.e., rotational axis originating at its center of mass), and thus a wealth of emission lines. A special case are “linear”, i.e., cylindrically symmetric molecules. In these molecules, one moment of inertia is much smaller than the others (e.g., $I_1 \ll I_2 = I_3$).

The diatomic (linear) molecule H_2 is by far the most abundant molecule in the universe, but does not exhibit millimeter rotational line emission. This is simply due to the fact that H_2 is a perfectly symmetric molecule, and thus does not have a permanent electric dipole moment μ_D (which would be caused by an asymmetric charge distribution).¹ Asymmetric linear molecules such as CO or HCN are significantly less abundant than H_2 , but have a non-zero permanent electric dipole moment. Such molecules are called polar, and exhibit observable millimeter line emission from rotational transitions. An electric dipole rotating at constant angular velocity ω varies sinusoidally at that angular frequency, and thus radiates at its rotation frequency.

The quantized orbital angular momentum of a polar molecule can then simply be expressed as (e.g., Townes & Schawlow 1975):

$$L = n\hbar. \quad (2.2)$$

The corresponding rotational energy implied by this angular momentum is:

$$E_{\text{rot}} = \frac{L^2}{2I} = \frac{n^2\hbar^2}{2I}, \quad (2.3)$$

implying that E_{rot} is also quantized.² The corresponding energy eigenvalues of the Schrödinger equation thus are:

$$E_{\text{rot}} = \frac{J(J+1)\hbar^2}{2I}, \quad \text{where } J = 0, 1, 2, \dots \quad (2.4)$$

Selection rules require that $\Delta J = \pm 1$ for all rotational transitions. For a transition $J \rightarrow J-1$, the energy

$$\Delta E_{\text{rot}} = [J(J+1) - (J-1)J] \frac{\hbar^2}{2I} = \frac{\hbar^2 J}{I}, \quad (2.5)$$

is released. The energy of the corresponding photon is given by $\Delta E_{\text{rot}} = h\nu_{\text{line}}$. We thus obtain a line frequency of:

¹ H_2 still has rotation-vibration and pure rotational transitions in the near- and mid-IR, which however need high temperatures to be excited. They thus can only be excited by UV light, or by shocks.

²The Born-Oppenheimer approximation is used, i.e., higher-order contributions due to electronic and vibrational motions are neglected.

$$\nu_{\text{line}} = \frac{\hbar J}{2\pi I}, \quad \text{where} \quad J = 0, 1, 2, \dots \quad (2.6)$$

The rotational spectrum of a linear molecule thus appears as a ladder with steps that are harmonics of the fundamental frequency. This frequency is determined solely by the moment of inertia. However, note that this is a simplification for several reasons. First, the centrifugal force increases with J ,³ so the bond will stretch and the distance between the nuclei will slightly increase. In addition, the atoms vibrate around their equilibrium positions.⁴ Spectral lines emitted by more rapidly rotating molecules thus will have frequencies slightly lower than the harmonics. Second, there may be fine structure and hyperfine structure overlaid on this main rotational structure, depending on the molecule under consideration. Such additional line splittings and shifts are induced by magnetic and electrostatic interactions inside the molecule. The main interactions are due to 1) electron spin-electron spin coupling (interaction between two magnetic dipoles, only occurs in molecules with two or more unpaired electrons), 2) electron spin-molecular angular momentum coupling (as the latter also corresponds to a magnetic dipole), 3) electron spin-nuclear spin coupling (if the nuclei have a magnetic dipole moment), 4) electric field gradient-nuclear electric quadrupole coupling, and 5) nuclear spin-nuclear spin coupling.

Note that 2) and 3) are of particular importance for radicals like CN, where the unbound electron causes a relatively wide splitting, whereas all these effects are rather minor in linear molecules without unpaired electrons, such as CO.

2.1.2 Minimum Excitation Temperature

The observed relative intensities of lines in the rotational ladder depend (in particular) on the temperature of the cloud. This is due to the fact that molecules are excited into higher level states by ambient radiation and by collisions in a gas. The minimum gas temperature $T_{\text{ex,min}}$ needed for significant collisional excitation is given by the rotational energy:⁵

$$T_{\text{ex,min}} \simeq \frac{E_{\text{rot}}}{k} = \frac{h\nu_{\text{line}}}{k}. \quad (2.7)$$

Inserting above equations for E_{rot} and ν_{line} , the moment of inertia I can be eliminated, leading to:

$$T_{\text{ex,min}} \simeq \frac{J(J+1)h^2}{2 \cdot 4\pi^2 I k} \quad (2.8)$$

$$= \frac{\nu h(J+1)}{2k}. \quad (2.9)$$

³Actually, the centrifugal distortion grows $\propto J^4$, and thus is much more significant for higher-order transitions.

⁴These corrections only become necessary due to the fact that we applied the (first order) Born-Oppenheimer approximation earlier.

⁵The actual excitation temperatures strongly depend on the density of the medium.

Table 2.1 lists the values for the first 15 transitions of CO, HCN, HCO⁺, and CS. The actual excitation conditions depend on a number of physical properties, in particular the density (see next section).

2.2 Population of Rotational Molecular Transitions

The population of the rotational levels of a molecule and the resulting intensities of its emission lines are coupled through the equations of statistical equilibrium and radiative transfer. To determine the physical properties of the surrounding medium from the observed intensities of multiple rotational transitions from one or more molecules, both have to be solved.

2.2.1 Statistical Equilibrium and Radiative Transfer

The simplest case to be considered is that of local thermodynamic equilibrium (LTE). If collisional excitation dominates over radiative excitation, the population of the different levels in LTE can be described by a Boltzmann distribution, which is determined by only one excitation temperature T_{ex} . Moreover, T_{ex} equals the kinetic temperature T_{kin} of the gas in LTE.

Due to the comparatively low average density of the ISM, LTE can only be considered a limiting case in general. However, when the density of the medium crosses a certain critical value, the conditions approach those in LTE. This critical density n_{crit} is determined by the ratio of the Einstein (A_{ul}) coefficient for spontaneous emission and the collision rate coefficient (γ_{ul}), which is defined as:

$$\gamma_{ul} = \frac{4}{\sqrt{\pi}} \left(\frac{m_{\text{red}}}{2k_B T} \right)^{3/2} \int_0^\infty \sigma_{ul} v^3 \exp \left[-\frac{m_{\text{red}} v^2}{2k_B T} \right] dv, \quad (2.10)$$

where m_{red} is the reduced mass of the system, σ_{ul} the collisional de-excitation cross section at the relative velocity v of the collision partners. Note that

$$A_{ul} = \frac{64\pi^4}{3hc^3} \nu_{ul}^3 |\mu_{ul}|^2, \quad (2.11)$$

i.e., $A_{ul} \propto \mu_{\text{D}}^2 \nu_{\text{line}}^3$. This leads to a higher critical density for high dipole moment molecules.

Also, note that

$$|\mu_{J+1 \rightarrow J}|^2 = \frac{\mu_{\text{D}}^2 (J+1)}{(2J+3)}. \quad (2.12)$$

Assuming a constant γ_{ul} , and considering $\nu_{J+1 \rightarrow J} \approx (J+1) \nu_{1 \rightarrow 0}$ gives:

$$n_{J+1 \rightarrow J}^{\text{crit}} \approx \frac{3(J+1)^4}{(2J+3)} n_{1 \rightarrow 0}^{\text{crit}}. \quad (2.13)$$

Table 2.1: Minimum Excitation Temperatures for CO, HCN, HCO⁺, and CS

Transition	ν_r (GHz)	$T_{\text{ex,min}}$ (K)	Transition	ν_r (GHz)	$T_{\text{ex,min}}$ (K)
CO($J=1\rightarrow 0$)	115.271	5.53	HCO ⁺ ($J=1\rightarrow 0$)	89.189	4.28
CO($J=2\rightarrow 1$)	230.538	16.56	HCO ⁺ ($J=2\rightarrow 1$)	178.375	12.84
CO($J=3\rightarrow 2$)	345.796	33.19	HCO ⁺ ($J=3\rightarrow 2$)	267.558	25.68
CO($J=4\rightarrow 3$)	461.041	55.32	HCO ⁺ ($J=4\rightarrow 3$)	356.734	42.80
CO($J=5\rightarrow 4$)	576.268	82.97	HCO ⁺ ($J=5\rightarrow 4$)	445.903	64.20
CO($J=6\rightarrow 5$)	691.473	116.15	HCO ⁺ ($J=6\rightarrow 5$)	535.062	89.88
CO($J=7\rightarrow 6$)	806.652	154.85	HCO ⁺ ($J=7\rightarrow 6$)	624.209	119.83
CO($J=8\rightarrow 7$)	921.800	199.08	HCO ⁺ ($J=8\rightarrow 7$)	713.342	154.06
CO($J=9\rightarrow 8$)	1036.912	248.82	HCO ⁺ ($J=9\rightarrow 8$)	802.458	192.56
CO($J=10\rightarrow 9$)	1151.985	304.08	HCO ⁺ ($J=10\rightarrow 9$)	891.558	235.33
CO($J=11\rightarrow 10$)	1267.014	364.84	HCO ⁺ ($J=11\rightarrow 10$)	980.637	282.38
CO($J=12\rightarrow 11$)	1381.995	431.11	HCO ⁺ ($J=12\rightarrow 11$)	1069.694	333.69
CO($J=13\rightarrow 12$)	1496.923	502.89	HCO ⁺ ($J=13\rightarrow 12$)	1158.728	389.27
CO($J=14\rightarrow 13$)	1611.794	580.15	HCO ⁺ ($J=14\rightarrow 13$)	1247.735	449.11
CO($J=15\rightarrow 14$)	1726.603	662.91	HCO ⁺ ($J=15\rightarrow 14$)	1336.714	513.22
HCN($J=1\rightarrow 0$)	88.632	4.25	CS($J=1\rightarrow 0$)	48.991	2.35
HCN($J=2\rightarrow 1$)	177.261	12.76	CS($J=2\rightarrow 1$)	97.981	7.05
HCN($J=3\rightarrow 2$)	265.886	25.52	CS($J=3\rightarrow 2$)	146.969	14.11
HCN($J=4\rightarrow 3$)	354.505	42.53	CS($J=4\rightarrow 3$)	195.954	23.51
HCN($J=5\rightarrow 4$)	443.116	63.80	CS($J=5\rightarrow 4$)	244.936	35.27
HCN($J=6\rightarrow 5$)	531.716	89.31	CS($J=6\rightarrow 5$)	293.912	49.37
HCN($J=7\rightarrow 6$)	620.304	119.08	CS($J=7\rightarrow 6$)	342.883	65.82
HCN($J=8\rightarrow 7$)	708.877	153.09	CS($J=8\rightarrow 7$)	391.847	84.63
HCN($J=9\rightarrow 8$)	797.434	191.35	CS($J=9\rightarrow 8$)	440.803	105.78
HCN($J=10\rightarrow 9$)	885.971	233.86	CS($J=10\rightarrow 9$)	489.751	129.27
HCN($J=11\rightarrow 10$)	974.488	280.61	CS($J=11\rightarrow 10$)	538.689	155.12
HCN($J=12\rightarrow 11$)	1062.983	331.60	CS($J=12\rightarrow 11$)	587.616	183.31
HCN($J=13\rightarrow 12$)	1151.452	386.83	CS($J=13\rightarrow 12$)	636.532	213.84
HCN($J=14\rightarrow 13$)	1239.895	446.29	CS($J=14\rightarrow 13$)	685.435	246.72
HCN($J=15\rightarrow 14$)	1328.308	509.99	CS($J=15\rightarrow 14$)	734.324	281.94

Table 2.2: Critical Densities for Selected Transitions of CO, HCN, HCO⁺, and CS

Transition	n_{crit} (10^4 cm^{-3})
CO($J=1 \rightarrow 0$)	0.11
CO($J=2 \rightarrow 1$)	0.67
CO($J=3 \rightarrow 2$)	2.1
CO($J=4 \rightarrow 3$)	4.4
CO($J=5 \rightarrow 4$)	7.8
CO($J=6 \rightarrow 5$)	13
CO($J=7 \rightarrow 6$)	20
HCN($J=1 \rightarrow 0$)	260
HCN($J=3 \rightarrow 2$)	7800
HCN($J=4 \rightarrow 3$)	15000
HCO ⁺ ($J=1 \rightarrow 0$)	170
HCO ⁺ ($J=3 \rightarrow 2$)	4200
HCO ⁺ ($J=4 \rightarrow 3$)	9700
CS($J=1 \rightarrow 0$)	4.6
CS($J=2 \rightarrow 1$)	30
CS($J=3 \rightarrow 2$)	130
CS($J=5 \rightarrow 4$)	880
CS($J=7 \rightarrow 6$)	2800

Notes— n_{crit} depends on temperature. The given values are typical for the conditions in Galactic molecular clouds.

This means that high J transitions of low critical density molecules have high critical densities (but also high minimum excitation temperatures). Table 2.2 lists the critical densities for several transitions of CO, HCN, HCO⁺, and CS. Note that, e.g., the critical density of the CO($J=6 \rightarrow 5$) transition is one tenth of that of CS($J=3 \rightarrow 2$), or one twentieth of HCN($J=1 \rightarrow 0$). However, its minimum excitation temperature is ~ 10 – 30 times higher than that of CS($J=3 \rightarrow 2$) and HCN($J=1 \rightarrow 0$) (see Table 2.1). This is why the CO rotational ladder may be considered primarily a temperature probe, while those of high dipole moment, low excitation temperature molecules like HCN, HCO⁺, and CS may rather be considered density probes (however, note that optical depth effects like line trapping pose a certain limitation to the direct interpretation of line fluxes). This demonstrates that the different molecules and transition indeed probe regions with different physical properties (see also Figure 2.1).

In practice, radiative trapping limits the overall decay rate of optically thick emission lines. This means that the critical density to maintain LTE can be considerably lower than given above. The critical density for the CO($J=1 \rightarrow 0$) transition is $\sim 300 \text{ cm}^{-3}$, while that of the $J=1 \rightarrow 0$ transition of high dipole moment molecules like HCN, HCO⁺, or CS is a few times 10^4 cm^{-3} .

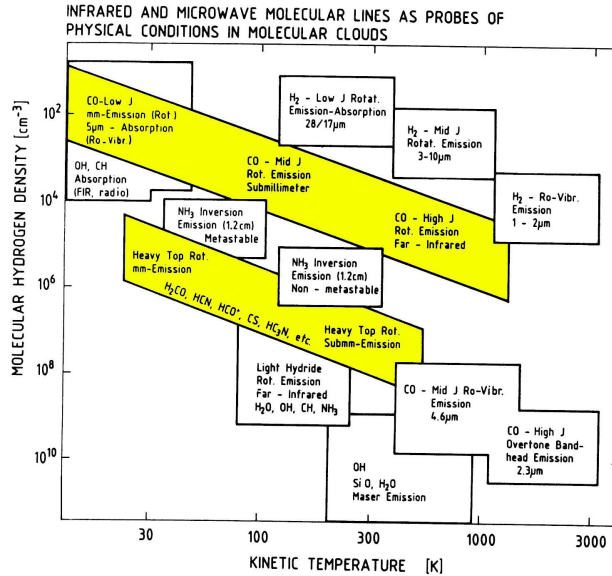


Figure 2.1: An overview over the importance of different kinds of molecular lines for a range of physical conditions (Genzel 1991). CO is an effective probe over a range of T_{kin} , but only for rather low densities, while high dipole moment molecules like HCN, HCO^+ , and CS trace much higher densities.

2.2.2 Radiative Transfer in the LVG Approximation

In principle, it is necessary to solve the coupled equations of statistical equilibrium and radiative transfer. The Einstein coefficients are known for most molecules. Also, the collision rates of the rotational transitions can be obtained from quantum mechanical calculations. However, the full problem strongly depends on the geometry of the (non-linear) radiative transfer problem: the level populations depend on the radiation field, which in turn depends on the level populations everywhere. The most common approach to this complex problem is to use the large velocity gradient (LVG) approximation (Scoville & Solomon 1974; Goldreich & Kwan 1974). This is a method that considers local photon trapping and introduces the concept of an escape probability (i.e., photons produced locally can only be absorbed locally) resulting from a strong velocity gradient to solve the problem, and is very useful due to the fact that it can be described by few parameters. It is particularly useful for high redshift studies, where only few information about the physical properties of the studied systems is available. In the LVG limit, A_{ul} is replaced by $\beta_{\text{esc}} A_{ul}$, where β_{esc} quantifies the escape probability. To calculate an optical depth, the method assumes that local-level populations hold globally. For optically thick lines (i.e., $\tau_{\text{line}} \gg 1$), this means that $\beta_{\text{esc}} \propto \tau_{\text{line}}^{-1}$. For optically thin lines, β_{esc} approaches a constant value (e.g., 1/2 for a semi-infinite slab).

In the following, we will briefly describe how to use an LVG code to obtain molecular excitation ladders, or ‘‘Spectral Line Energy Distributions’’ (SLEDs).

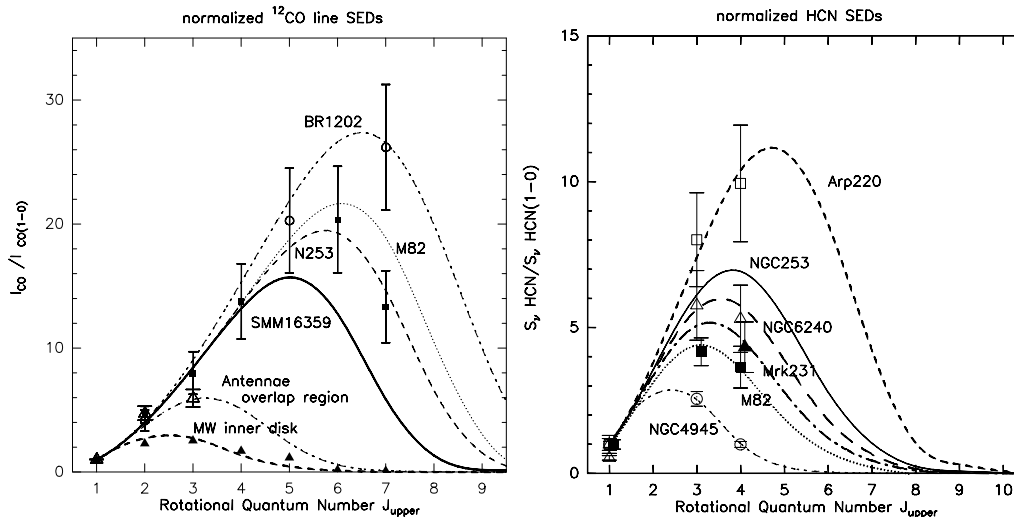


Figure 2.2: LVG-predicted SLEDs for different nearby galaxies for CO (*left*; Weiß et al. 2005a) and HCN (*right*; Knudsen et al. 2007). For CO, the $z=2.5$ SMG SMM J16359+6612 and the $z=4.7$ quasar BR1202-0725 are added for comparison (see Chapter 3 for the modeling of this source; no SLED different from CO was measured at high z to date). The upper rotational quantum number of the transition is plotted versus normalized line intensity (the absolute 1–0 intensities of HCN are by at least an order of magnitude lower than those of CO). Due to the lower critical density, the excitation of CO is significantly higher than that of HCN in all galaxies.

2.2.3 LVG Calculations

The LVG calculations presented in this thesis are based on a modified version of the LVG code developed by Christian Henkel. Apart from the molecule(s) under consideration and the tabulated collision coefficients for those molecules, only few input parameters have to be specified. First, an ortho-to-para ratio for H_2 has to be given (typically 3:1)⁶. Second, the redshift of the source under consideration has to be specified. This is required to calculate the temperature of the cosmic microwave background (T_{CMB}) for the observed source, which has to be considered for all calculations of gas the temperatures (plus, all observations are made relative to the CMB). Third, a H_2 abundance has to be specified. As we are obtaining calculations for molecules different from H_2 , it is required to define the abundance of the molecules under consideration relative to H_2 . The last assumption is the actual velocity gradient (in $\text{km s}^{-1} \text{pc}^{-1}$). For high redshift studies, the chemical abundances and velocity gradients are typically fixed to values (or at least extrapolated based on values) for nearby starburst galaxies like M82 or NGC 253, where these quantities

⁶This is due to the relative statistical weights of the symmetrical (ortho) and antisymmetrical (para) eigenstates of the wavefunction: there are three symmetrical combinations of the spins of both H nuclei, but there is only one antisymmetrical combination.

can be determined in more detail (based on spatial information, isotopomeric ratios, etc.). The parameter space is then spanned by pairs of the molecular hydrogen density $n(\text{H}_2)$, and the kinetic temperature of the gas, T_{kin} . The main output of the LVG calculations are the occupation numbers of different transitions, the excitation temperatures T_{ex} and optical depths τ for those transitions, as well as the (Rayleigh-Jeans) brightness temperatures T_b (note that these would be identical for all transitions if they were thermalized, i.e., in LTE). Based on the velocity gradient and the observed line profile, the size of an equivalent disk containing all observed molecular gas can be defined. The most important result, however, are the predicted line intensities, which scale with $\nu^2 T_b$ (see derivation in Section 2.3). Note that, for LTE, the $2 \rightarrow 1/3 \rightarrow 2/4 \rightarrow 3/\dots$ rotational transitions thus have $4/9/16/\dots$ times higher line fluxes than the $1 \rightarrow 0$ transition. Depending on galaxy type, the observed SLEDs deviate from LTE at lower (e.g., above $2 \rightarrow 1$ for CO in the Milky Way) or higher (e.g., typically above $4 \rightarrow 3$ for CO in ULIRGs) transitions (see Figure 2.2 for examples). This demonstrates the importance to observe multiple transitions of one molecule to constrain the physical properties of a source.

Multiple molecules (e.g., low-density tracers like CO and high-density tracers like HCN, HCO^+ , and CS) would have to fulfill the same general requirements in terms of $n(\text{H}_2)$ and T_{kin} . Observing the ladders for multiple molecules thus gives independent measures for these parameters, narrowing down the uncertainties. Also, they have the power to reveal density/temperature structure within the molecular ISM without obtaining spatially resolved observations. In particular, it has the power to trace the filling factor of dense cores within the molecular gas reservoir, i.e., the actual sites of star formation.

Modeling different isotopomers of the same molecule (e.g., ^{12}CO and ^{13}CO) is of particular importance due to the fact that ^{12}CO is usually optically thick, but ^{13}CO tends to be optically thin (at least the lower- J transitions) even in starburst galaxies. Combining the SLEDs for both isotopomers thus is a direct measure for the CO mass (another quantity that is usually extrapolated to high z from observations of nearby starbursts and ULIRGs), and with information about the relative CO abundance, a measure for the total H_2 mass.

In conclusion, it is found that, in order to derive the physical properties (i.e., masses, temperatures, densities, optical depths, and spatial structure/filling factors) and chemical composition (i.e., relative abundances) of the ISM in a galaxy, it is desirable to observe multiple 1) transitions, 2) molecules, and 3) isotopomers. These are given in order of difficulty for observations of high redshift galaxies, and are all (to some extent) addressed in the framework of this thesis. This, of course, can only be a complement to observations at high spatial resolution, which do not only provide integrated fluxes, but also direct information about the spatial distribution of the molecular gas (and, to first order, differentiate between mergers and disk galaxies).

2.3 Derivation of the Line Luminosity

To obtain the intrinsic properties of a source, and in order to compare it to other galaxies, it is desirable to obtain a quantity that, in contrast to the observed intensity, does not depend

on the source's distance. The main quantity used in molecular line observations is the line luminosity. There are two main ways to express the line luminosity. The first quantity, L_{CO} , is expressed via the source's flux density, and typically given in units of L_{\odot} . The second quantity, L'_{CO} , is expressed via the source's brightness temperature, and typically given in units of $\text{K km s}^{-1} \text{pc}^2$. Both expressions are connected by a simple conversion factor, as shown below. In the following, two definitions of the distance to a cosmological source are introduced. Then, it is described how to obtain the flux density of a source from observations, before introducing its connection to the actual brightness temperature of a source. Afterwards, the connection between the peak flux density and the integrated line flux is given. With these tools, the line luminosity is derived.

2.3.1 Angular Size Distance and Luminosity Distance

The angular size distance D_A is defined as the ratio between the transverse size R of an object, and the angle θ (in radians) that it subtends on the sky (e.g., Peacock 1999):

$$D_A \equiv R/\theta. \quad (2.14)$$

The solid angle Ω_S of a source on the sky then corresponds to the area:

$$\Omega_S = \pi(R/D_A)^2. \quad (2.15)$$

The luminosity L is defined as the surface integral of the flux F . Assuming that a source radiates into a spherical volume, this integral can be carried out directly (from zero to radial distance r) and gives:

$$L = 4\pi r^2 F. \quad (2.16)$$

The luminosity distance D_L is defined via this equation by assuming that the observer sits at a distance $r=D_L$. We thus find:

$$D_L^2 \equiv \frac{L}{4\pi F}. \quad (2.17)$$

As the cosmic microwave background corresponds to an (almost) perfect blackbody, we can derive a universal relation between D_A and D_L (as the characteristics of a blackbody do not appear to change between $z=0$ and $z \simeq 1100$, just the observed brightness temperature). The luminosity of a blackbody is defined as:

$$L \equiv 4\pi R^2 \sigma_{\text{SB}} (T_b^{\text{r}})^4, \quad (2.18)$$

where R is the radius, σ_{SB} is the Stephan-Boltzmann constant, and T_b^{r} is the rest-frame brightness temperature of the emitting blackbody. The measure flux of this blackbody is:

$$F \equiv \theta^2 \sigma_{\text{SB}} (T_b^{\text{obs}})^4, \quad (2.19)$$

where T_b^{obs} is the observed brightness temperature, which relates to T_b^{r} via:

$$T_b^{\text{obs}} = T_b^{\text{r}}/(1+z). \quad (2.20)$$

Combining these equations, we find:

$$D_L^2 = \frac{L}{4\pi F} \quad (2.21)$$

$$= \frac{4\pi R^2 \sigma_{\text{SB}} (T_b^{\text{r}})^4}{4\pi \theta^2 \sigma_{\text{SB}} (T_b^{\text{obs}})^4} \quad (2.22)$$

$$= \frac{R^2 (T_b^{\text{r}})^4}{\theta^2 (T_b^{\text{obs}})^4} \quad (2.23)$$

$$= D_A^2 (1+z)^4, \text{ i.e.,} \quad (2.24)$$

$$D_L = D_A (1+z)^2. \quad (2.25)$$

2.3.2 Flux Density and Source Solid Angle

Assuming that an energy $dE_\nu d\nu$ flows through a surface $d\sigma$ in a time dt in the frequency range $[\nu; \nu + d\nu]$ within a solid angle $d\Omega$ along a ray at an angle ξ relative to the surface normal, one finds (e.g., Chandrasekhar 1960):

$$dE_\nu d\nu = I_\nu \cos \xi d\sigma d\Omega dt d\nu. \quad (2.26)$$

This corresponds to a power dP of:

$$dP = I_\nu \cos \xi d\sigma d\Omega d\nu. \quad (2.27)$$

The specific intensity I_ν is then defined as:

$$I_\nu \equiv \frac{dP}{\cos \xi d\sigma d\nu d\Omega}. \quad (2.28)$$

This can be re-written as:

$$\frac{dP}{d\sigma d\nu} = I_\nu \cos \xi d\Omega. \quad (2.29)$$

For a discrete source (i.e., a source subtending a well-defined solid angle), the spectral power received by a detector of unit area is called the source flux density S_ν . This simply requires to integrate the previous equation over the source solid angle:

$$S_\nu \equiv \int_{\text{source}} I_\nu \cos \xi d\Omega. \quad (2.30)$$

For a source of an angular extent of $\ll 1$ rad (i.e., $\cos \xi \simeq 1$), this equation simplifies to:

$$S_\nu \approx \int_{\text{source}} I_\nu d\Omega. \quad (2.31)$$

In the following, we will work with the source solid angle Ω_S , which is given by:

$$S_\nu = I_\nu \Omega_S. \quad (2.32)$$

2.3.3 Rest-Frame Rayleigh-Jeans Brightness Temperatures

The temperature of a blackbody is given by the Planck function:

$$B_\nu = \frac{2h\nu^3}{c^2} \cdot \frac{1}{\exp\left(\frac{h\nu}{k_B T}\right) - 1}, \quad (2.33)$$

where B_ν is the specific intensity of blackbody radiation, h is Planck's constant, c is the speed of light, and k_B is Boltzmann's constant. In the low frequency limit ($h\nu \ll k_B T$), this equation simplifies to the Rayleigh-Jeans equation:

$$B_\nu = \frac{2k_B T \nu^2}{c^2} \quad (2.34)$$

In radio astronomy, source temperatures are approximated mostly well by the Rayleigh-Jeans limit. An observed Rayleigh-Jeans brightness temperature T_b^{obs} thus is given by (note that for optically thick emission $B_\nu = I_\nu$):

$$T_b^{\text{obs}} = \frac{c^2}{2k_B \nu_{\text{obs}}^2} I_\nu. \quad (2.35)$$

Inserting the flux density, we thus find the rest-frame Rayleigh-Jeans brightness temperature T_b^{r} to be:

$$T_b^{\text{r}} = (1+z) \frac{c^2}{2k_B \nu_{\text{obs}}^2 \Omega_S} S_\nu. \quad (2.36)$$

In the following, we will refer to Rayleigh-Jeans brightness temperatures simply as “brightness temperatures”. Note that at high frequencies approaching the peak of a source's SED, the Rayleigh-Jeans approximation is not valid anymore, and have to be corrected to represent Planck temperatures (this is accounted for where appropriate).

2.3.4 Measured Brightness Temperature

In general, the source solid angle Ω_S is different from that measured by the telescope, as it is diluted by the observing beam, which covers a solid angle Ω_B (e.g., Rohlfs & Wilson 1996):

$$\Omega_B \equiv \int_{4\pi} P_n d\Omega, \quad (2.37)$$

where P_n is the power pattern of the antenna, normalized to its maximum.

The temperature T_A observed by the antenna is related to the true brightness temperature via the beam-diluted source solid angle Ω_{S^*B} :

$$T_A \Omega_{S^*B} = T_b \Omega_S. \quad (2.38)$$

If the source is much smaller than the beam, $\Omega_{S^*B} \approx \Omega_S$. In the following derivation of the line luminosity, we thus consider T_b a directly observed quantity.

2.3.5 Line Profiles

A rotationally broadened emission line originating from a uniformly brightened, rotating disk shows a simple Doppler Gaussian profile. In reality, molecular line profiles in galaxies are more complex than that, mainly due to local variations and inhomogeneities of the temperatures, densities, molecular abundances, and velocity fields. Due to the fact that molecular line detections at high redshift often lack the signal-to-noise to examine the line profiles in more detail, the line properties are usually still parameterized by the peak flux and full width at half maximum (FWHM) of one or more Gaussian fits to the line. Note that, due to very small Einstein A coefficients, the Lorentz wings of millimeter molecular lines are in general negligible, justifying the use of a simple Gaussian.

Consider a Gaussian function of the form:

$$G(x; \sigma) = A \frac{e^{-(x-x_0)^2/(2\sigma)^2}}{\sigma\sqrt{2\pi}}. \quad (2.39)$$

For an emission line, x corresponds to velocity v or frequency ν , x_0 corresponds to the velocity (frequency) offset v_0 (ν_0) relative to a defined zero point, A corresponds to the line peak flux density S_ν , and σ is the width of the Gaussian. The FWHM is then given by:

$$\Delta v_{\text{FWHM}} = 2\sqrt{2 \ln 2} \sigma \simeq 2.35 \sigma. \quad (2.40)$$

The integral of the Gaussian function then corresponds to:

$$\int_{-\infty}^{+\infty} G(x) dx = \int_{\text{line}} S_\nu dv = S_\nu \Delta v_{\text{FWHM}} \frac{\sqrt{\pi}}{2\sqrt{\ln 2}} \simeq 1.06 S_\nu \Delta v_{\text{FWHM}}. \quad (2.41)$$

The integrated line flux thus is almost equal to the product of the peak flux and the line FWHM.

2.3.6 Line Luminosity

From energy conservation, one can derive that the rest-frame monochromatic luminosity L_ν^r relates to the observed flux density S_ν via:

$$L_\nu^r d\nu_r = 4\pi D_L^2 S_\nu d\nu_{\text{obs}} \quad (2.42)$$

The direct definition of the luminosity of an emission line is found by integrating L_ν^r over the width of the emission line. Substituting $c d\nu_{\text{obs}} = \nu_{\text{obs}} dv$ (where v is the linewidth in km s^{-1}), we find:

$$L_{\text{line}} = \int_{\text{line}} L_\nu^r d\nu_r \quad (2.43)$$

$$= \int_{\text{line}} 4\pi D_L^2 S_\nu d\nu_{\text{obs}} \quad (2.44)$$

$$= 4\pi D_L^2 \nu_{\text{obs}}/c \int_{\text{line}} S_\nu dv \quad (2.45)$$

$$= 4\pi D_L^2 (1+z)^{-1} \nu_r/c \int_{\text{line}} S_\nu dv. \quad (2.46)$$

In convenient units, the line luminosity (in L_\odot) can be expressed as:

$$L_{\text{line}} = 1.04 \times 10^{-3} S_{\text{line}} \Delta v \frac{D_L^2}{(1+z)} \nu_r \quad (2.47)$$

$$= 1.04 \times 10^{-3} S_{\text{line}} \Delta v D_L^2 \nu_{\text{obs}}, \quad (2.48)$$

where the velocity-integrated line flux $S_{\text{line}} \Delta v$ is given in Jy km s^{-1} , D_L is given in Mpc, and ν_r is given in GHz (see, e.g., Solomon et al. 1992a).

However, a sometimes more practical definition of the line luminosity is used relatively often, which depends on the measured rest-frame brightness temperature T_b^r and its size on the sky. The luminosity can be given by the velocity-integrated source brightness temperature integrated over its area on the sky. As shown above, the source area on the sky can be expressed as $\Omega_S D_A^2$. We thus find:

$$L'_{\text{line}} = \int_{\text{line}} T_b^r dv \Omega_S D_A^2 \quad (2.49)$$

$$= \int_{\text{line}} T_b^r dv \Omega_S D_L^2 (1+z)^{-4} \quad (2.50)$$

$$= (1+z) \frac{c^2}{2k_B \nu_{\text{obs}}^2 \Omega_S} \int_{\text{line}} S_\nu dv \Omega_S D_L^2 (1+z)^{-4} \quad (2.51)$$

$$= \frac{c^2}{2k_B \nu_{\text{obs}}^2} \frac{D_L^2}{(1+z)^3} \int_{\text{line}} S_\nu dv \quad (2.52)$$

$$= \frac{c^2}{2k_B \nu_r^2} \frac{D_L^2}{(1+z)} \int_{\text{line}} S_\nu dv. \quad (2.53)$$

In convenient units, the line luminosity (in $\text{K km s}^{-1} \text{pc}^2$) can be expressed as:

$$L'_{\text{line}} = 3.25 \times 10^7 S_{\text{line}} \Delta v \frac{D_L^2}{(1+z)\nu_r^2} \quad (2.54)$$

$$= 3.25 \times 10^7 S_{\text{line}} \Delta v \frac{D_L^2}{(1+z)^3 \nu_{\text{obs}}^2}, \quad (2.55)$$

where the velocity-integrated line flux $S_{\text{line}} \Delta v$ is given in Jy km s⁻¹, D_L is given in Mpc, and ν_r is given in GHz (see, e.g., Solomon et al. 1992a).

Note that L_{line} and L'_{line} are directly related via:

$$L_{\text{line}} = \frac{8\pi k_B \nu_r^3}{c^3} L'_{\text{line}}. \quad (2.56)$$

2.3.7 Negative K Correction

L'_{line} is directly proportional to T_b ; thus, the L'_{line} ratio of two lines in the same source simply equals the ratio of their intrinsic, source-averaged T_b . For thermalized, optically thick emission, both ratios are always 1 between all transitions of a molecule.

As shown above, $L'_{\text{line}} \propto D_L^2 (1+z)^{-3}$ in the observed frame. This means that, for a constant L'_{line} , the integrated line flux scales $\propto D_L^{-2} (1+z)^3$. The emission lines thus do not simply dim with distance squared, but much less strongly. This so-called negative K correction (Solomon et al. 1992a) is one of the main reasons why (mid- to high J) molecular emission lines at high redshift are observable in the millimeter observing windows, which were initially designed for observations of low- J CO transitions of $z=0$ galaxies. However, this observational limitation currently is also one of the main biases of CO-detected samples at high redshift (note that all except one of the initial high redshift CO detections were obtained in the 3 mm observing window, which corresponds to the CO($J=3 \rightarrow 2$) frequency at $z \simeq 2.5$), as the mid- to high- J emission lines have to be excited to be able to detect these sources. This is not the case in “normal” galaxies like the Milky Way, which is clearly subthermally excited in the CO($J=3 \rightarrow 2$) transition. This is the main reason why it is desirable to be able to obtain high- z galaxy samples selected via the CO($J=1 \rightarrow 0$) transition, and in a first step, to obtain CO($J=1 \rightarrow 0$) observations of high- z galaxies at all (see Chapter 3).

2.3.8 Gravitational Magnification

A large fraction of the galaxies that have been detected in molecular gas emission at high redshift is gravitationally lensed. The peak brightness temperature is a conserved quantity under gravitational lensing, but emitted over an enhanced area when lensed. This increase in (projected) area leads to an effective increase in the line luminosity. The ratio between apparent and intrinsic luminosities is known as the lensing magnification factor μ_L , and basically directly expresses the increase in area. However, note that it is quite difficult to derive μ_L , as (in principle) the exact geometry of the lensing system has to be known, as well as its mass and dynamics.

2.4 Telescopes

There currently are a number of telescopes that can observe molecular lines in the submillimeter to centimeter wavelength regime at high redshift, as required for the observations in this thesis. For currently existing facilities, there are two main categories: millimeter telescopes typically observing higher J molecular line transitions at high z (typically in bands at 1, 2, and 3 mm), and centimeter (“radio”) telescopes that are capable of observing low J transitions (typically at 0.7 and 1.3 cm). This can be split up into two further categories: single-dish telescopes, consisting of only one antenna, and interferometers, consisting of multiple antennas.

The main advantage of millimeter telescopes is that they usually have a higher sensitivity relative to the brightness of the observed line. The intensity of molecular transitions in thermal equilibrium scale with ν^2 (due to the fact that they have the same brightness temperature)⁷, while due to technological differences, the sensitivity scales with less than ν^2 between millimeter and centimeter observing windows. The main advantage of centimeter telescopes is the fact that observations of low J , in particular ground-state transitions, do not depend on the excitation conditions, and thus are a more direct measure for physical properties like masses, and the full size of the regions that emit line radiation.

The main advantage of single-dish telescopes is that they usually have comparatively large collecting areas relative to all interferometers but the largest, and offer high spectral bandwidths and velocity resolutions (which is more difficult to realize in interferometers due to the fact that signals of the different antennas have to be correlated). There are two main advantages of interferometers. First, the so-called spectral baselines (i.e., defined zero flux levels of the spectral bandpass) are much more stable than for single-dish telescopes due to the fact that fluctuations of these levels recorded by the single antennas get subtracted out in the correlated signal (although the precision of the correlation signal largely depends on the stability of the atmosphere, which is mainly measured by the rms of the phases of the incoming antenna signals, and defines some sort of “seeing”). This means that interferometers can measure faint signals with higher reliability. It also means that interferometers can measure line and continuum signals with spectrometers, while single-dish telescopes can only measure line signals at faint levels (this limitation is overcome by the use of wide-band bolometers, which in turn cannot measure line signals). Second, due to the longer baselines between the single antennas, interferometers offer significantly higher spatial resolution (generally diffraction-limited) than single-dish telescopes. This enables spectroscopic imaging, and allows us to trace kinematics and velocity structure within spectral lines (comparable to the so-called integral field spectroscopy in the optical/infrared).

On the down side, interferometers only record signals at distinct positions in the fourier plane instead of “real” images in the image plane. Images thus have to be created by applying a discrete fourier transformation, reflecting the fact that the fourier (“ $u-v$ ”) plane

⁷It is important to mention that, even in the most favourable case (i.e., for a low dipole moment molecule), only the lower few transitions of a molecule are in thermal equilibrium.

is not sampled perfectly, which creates artifacts (that however can be reduced significantly applying specially designed algorithms). However, interferometers like the VLA with 27 antennas sample the $u - v$ plane much better than two- or three-element interferometers, leading to high image quality. Another limitation of interferometers is that they are blind to structure on scales that are larger than that sampled by their shortest baseline (such structure is “outresolved”), while structure smaller than that sampled by their longest baseline gets smeared in a fashion similar to single-dish telescopes and only limits the spatial resolution. Outresolved structure can be recovered by parallel observations with a single-dish telescope, which are added in as so-called zero spacings. Due to the small angular scales of distant sources, this is usually unnecessary in studies of molecular gas at high redshift, where the main concern is to be able to resolve structure at all, even with interferometers in their long baseline configurations.

Table 2.3 lists the most important current and future facilities for high redshift molecular line observations in the submillimeter to centimeter regime. Note that only the wavebands usable for high redshift line observations are listed for the radio telescopes and the SMA. For the studies presented in this thesis, the Green Bank Telescope, the Effelsberg 100 m telescope, the Very Large Array, and the Plateau de Bure Interferometer were used (I also used the IRAM 30 m telescope for studies that complement those presented here). These facilities and their importance for high redshift molecular line observations are briefly discussed in the following. To put the capabilities of these telescopes into context, the other existing and planned large facilities in this wavelength regime [except the Square Kilometre Array (SKA), which is still in a relatively early design phase] are also shortly discussed. This is necessary to show how this particular field of science will be impacted by the advent of the Atacama Large submillimeter/Millimeter Array, but also the VLA expansion project (EVLA). It may be useful to compare this summary of the capabilities of existing facilities to the existing observations listed in Appendix A.

Green Bank Telescope (GBT): The Robert C. Byrd Green Bank Telescope (Figure 2.3, left) is a single-dish radio telescope located in Green Bank, WV, USA, and commenced science operations in 2000. It is operated by the NRAO. Its adaptive surface is a 100 by 110 m section of a rotationally symmetric 208 m figure. The observing bands that are useful for high- z molecular line observations are the 1.3 cm (22 GHz, K band) and 7 mm (43 GHz, Q band) bands, and potentially the 1.0 cm (30 GHz, Ka band) band opened to science observations in winter 2007/2008. Only the K band receiver has been used to detect highly redshifted molecular gas to date (see Section 3/Riechers et al. 2006a; Hainline et al. 2006 for the first reported studies).⁸ The K band receiver offers a maximum dual polarization⁹ bandwidth of 1.6 GHz, corresponding to a redshift coverage of $\Delta z/z=10\%$ at $z=4$.

⁸Test observations earlier this year have led to tentative detections in both the Ka and Q band, but are not published to date.

⁹In radio astronomy, “dual polarization” means two orthogonal single polarization receivers.



Figure 2.3: Single dish radio/millimeter telescopes. *Left*: GBT. *Middle*: Effelsberg. *Right*: IRAM 30 m (see text for further description). Image courtesy of NRAO/AUI, Curtis Saxton, and IRAM Spain.

Effelsberg: The Effelsberg 100 m telescope (Figure 2.3, middle) is a single-dish radio telescope located in Effelsberg near Bonn, Germany, and commenced science operations in 1972. It is operated by the MPIfR in Bonn. The 1.3 cm observing band has been successfully used for observations of high redshift molecular gas (see Section 3/Riechers et al. 2006a for the first reported study). A maximum bandwidth of 500 MHz can be used, corresponding to a redshift coverage of $\Delta z/z=3\%$ at $z=4$.

(Expanded) Very Large Array [(E)VLA]: The VLA (Figure 2.4, left) is a radio interferometer located near Socorro, NM, USA, and is operated by the NRAO. It was completed in 1980, and consists of 27 antennas of 25 m diameter each, which are arranged in a Y-shaped configuration that optimizes the $u-v$ coverage. The antennas can be arranged in four different configurations. The most extended configuration, A, covers baselines between 0.68 and 36.4 km. The most compact configuration, D, covers baselines between 0.035 and 1.03 km. The observing bands useful for high redshift molecular line observations are the 1.3 cm and 7 mm bands. As part of the EVLA upgrade (to be finished by 2013), all EVLA antennas will be equipped with 1.0 cm receivers that will (almost) completely cover the gap between the former two bands. In practice, high redshift sources are too faint to be observed in A array where the atmospheric phase noise is highest. With a substantial time investment (even compared to the observation times of high redshift detection projects), observations in B array are feasible and offer maximum resolutions of $0.3''$ and $0.15''$ in the 1.3 cm and 7 mm bands. Note that $0.15''$ corresponds to 1 kpc at $z=4$, and thus reaches the critical scale to resolve distant galaxies (see Carilli et al. 2002b; Walter et al. 2004, and Sections 9–11 for the first such studies). The VLA’s sensitivity and resolution is superior to that of the GBT and Effelsberg, however, the main limitation is the width of the spectral bandpass, which is only 50 MHz dual polarization. This barely covers the width of a molecular emission line in a typical high redshift gas-rich galaxy. This main limitation of the VLA for such observations will be overcome with the EVLA upgrade, which will offer 8 GHz instantaneous bandwidth at better spectral resolution, corresponding to $\Delta z/z=50\%$



Figure 2.4: Radio/millimeter interferometers. *Left:* VLA. *Middle:* PdBI. *Right:* CARMA (see text for further description). Image courtesy of NRAO/AUI, IRAM France, and Kevin P. Rauch.

at $z=4$ in the 1.3 cm band.

IRAM 30 m: The IRAM 30 m telescope (Figure 2.3, right) is located near Pico Veleta in the Sierra Nevada in southern Spain. It is a single-dish millimeter telescope operating in the 1, 2, and 3 mm (230, 150, and 100 GHz) observing bands (reaching down to almost 4 mm). It has played a significant role in detections of CO lines at high redshift from the beginning (e.g., Solomon et al. 1992a). Due to the fact that it covers a large fraction of the wavelength regions between 1 and 4 mm, it is very useful to expand the range of detected CO transitions in a source, whereas initial detection is usually achieved with interferometers (due to the better stabilities of the spectral baselines). Currently, the maximum dual polarization bandwidth is 512 MHz at 3 mm, and 1 GHz at 2 and 1 mm. This corresponds to $\Delta z/z=1\%$ at $z=4$ in the 2 mm band.

Plateau de Bure Interferometer (PdBI): The IRAM PdBI (Figure 2.4, middle) is a millimeter interferometer located on the Plateau de Bure in the French Alps. As of winter 2007/2008, it will cover the 1, 2, and 3 mm observing bands. It consists of 6 antennas of 15 m diameter each, which can be arranged in four cross-shaped configurations. In the most extended configuration (A), the longest baseline on the east-west arm is 760 m, and that on the north-south arm is 368 m. This provides resolutions of up to $0.3''$ at 1 mm. Since winter 2006/2007, this can be used for studies of CO emission in distant galaxies at high resolution, achieving up to half of the maximum resolution of the VLA, albeit in higher J transitions that are not necessarily highly excited (and may not trace the same physical regions). This capability will be an important complement to the high-resolution CO studies with the VLA. To date, the PdBI is by far the most sensitive millimeter facility in the world, and thus the standard facility to search for redshifted molecular gas. Currently, all receivers can be used with a maximum dual polarization bandwidth of 1 GHz, which will be extended to 4 GHz in the near future. 1 GHz corresponds to $\Delta z/z=1.5\%$ at $z=4$ in the 3 mm band.

Combined Array for Research in Millimeter-wave Astronomy (CARMA): CARMA (Figure 2.4, right) is a merger of the Owens Valley Radio Observatory (OVRO) millimeter array and the Berkeley-Illinois-Maryland Association (BIMA) millimeter array, and became operational in late 2006 (OVRO used to be a key player in high- z CO observations). CARMA is located on Cedar Flat near Big Pine, CA, USA. It consists of nine 6.1 m antennas and six 10.4 m antennas. The collecting area of CARMA is smaller than that of the PdBI, but its $u - v$ coverage is more complete. Starting winter 2007/2008, CARMA operates in both the 1 mm and 3 mm wavebands. Five telescope configurations are planned (A-E), of which three (B-D) are currently offered (B configuration includes baselines of 82-813 m). This currently limits the maximum resolution to $\sim 0.3''$ at 1 mm, similar to the maximum resolution of the PdBI. The CARMA receivers are single polarization, and offer a maximum bandwidth of 1.5 GHz, which will be extended to 4 GHz in the near future. 1.5 GHz corresponds to $\Delta z/z=2\%$ at $z=4$ in the 3 mm band.

Nobeyama Millimeter Array (NMA): The NMA is a millimeter interferometer near Nobeyama, Nagano in Japan, operated by the National Astronomical Observatory of Japan (NAOJ). It consists of six 10 m antennas that can be arranged in three configurations. It can be interferometrically linked to the NRO 45 m telescope to improve resolution and sensitivity. The interferometer operates in the 1, 2, and 3 mm bands. The maximum resolution is $1''$, which is achieved in the 2 mm band. Only few high- z CO detections with the NMA are reported in the literature. The maximum bandwidth of the single polarization receivers is 1 GHz.

Submillimeter Array (SMA): The SMA is a submillimeter and millimeter interferometer located on Mauna Kea, HI, USA. It consists of eight 6 m antennas that can be arranged in four configurations. The eSMA project aims at interferometrically linking the SMA to the CSO 10.4 m and the JCMT 15 m telescopes to extend the sensitivity and maximum resolution. As of 2007, the SMA operates in the 1 mm (230 GHz), $850 \mu\text{m}$ (345 GHz), $750 \mu\text{m}$ (400 GHz), and $450 \mu\text{m}$ (690 GHz) bands, the latter of which is significantly less sensitive than the former three. Due to the comparatively small collecting area, no high- z CO line has been detected with the SMA to date. The SMA has a maximum bandwidth of 2 GHz. Dual polarization receivers are only available in the $750 \mu\text{m}$ band.

Atacama Large submillimeter/Millimeter Array (ALMA): ALMA (Figure 2.5) is currently being constructed at Llano de Chajnantor in the Atacama desert in northern Chile. Upon completion in 2013, it will consist of 50 12 m antennas. Its extension, the ALMA Compact Array (ACA) will consist of four 12 m antennas and twelve 7 m antennas. ALMA will almost completely cover the wavelength range between 3 mm and $300 \mu\text{m}$, and possibly even extend down to 1 cm (not funded yet). ALMA will offer four interferometer configurations, the most extended of which is aimed to include baselines up to 14 km. One design goal of ALMA is to achieve a resolution of $0.015''$ at $850 \mu\text{m}$, and a sensitivity far superior to current submillimeter and millimeter facilities. Also, ALMA receivers are aimed to have a bandwidth of 8 GHz (possibly 16 GHz).

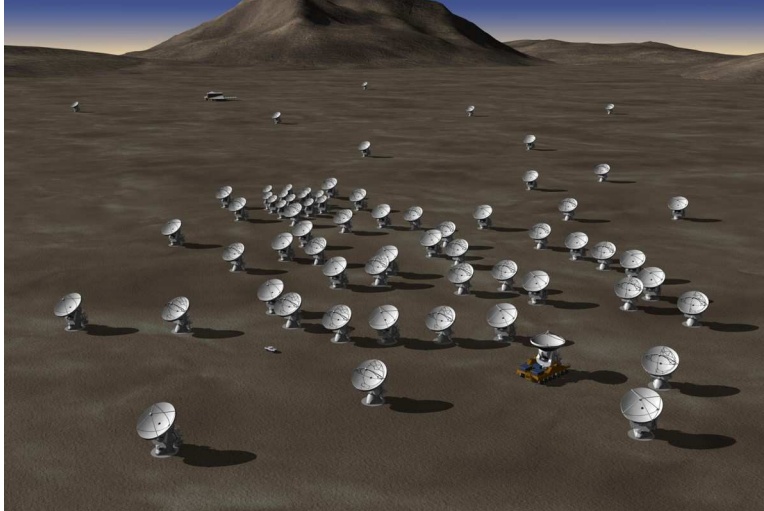


Figure 2.5: Computer-rendered image of ALMA. Image courtesy of NRAO/AUI, and Computer Graphics by ESO

2.5 Discovery Space

There are several factors that limit studies of molecular lines at high redshift. First, the bandwidth of millimeter/radio telescopes is limited. Even if a source has a good spectroscopic redshift in the optical wavelength regime, there may be a systemic offset between optical atomic/ionic emission lines, tracing hot gas, and the cold gas traced by molecular lines. This offset may be larger than the full bandwidth of the millimeter/radio telescope, and thus shift the emission line out of the bandpass. Although the bandwidth of most millimeter/radio facilities has recently been improved, this is still an issue. Future very wide-band spectrometers, so-called z -Machines, are being developed to overcome this limitation, and allow for “blind” redshift searches. Note, however, that such instruments are only feasible for single-dish telescopes, whereas interferometers are the main discovery instruments for molecular lines (see Outlook for further discussion).

Second, redshifted molecular lines are very faint, and require substantial integration times (typically 10 h per line, but up to 80 h depending on line and instrument). Such observations are currently only feasible in the most luminous galaxies - even ULIRGs are detectable at $z > 2$ in molecular line emission only if they are magnified by gravitational lensing. A necessary criterion to search for molecular line emission thus is that the galaxy is bright in the FIR continuum. This limits studies to the most dust-rich starbursting galaxies, and excludes “normal” L_* galaxies at any redshift > 0 . Note however that the most recent studies have allowed to detect very strongly lensed LBGs, which shows that it is possible to probe at least somewhat down the luminosity function. Note that this

Table 2.3: Properties of Current and Future (Sub)mm/Radio Facilities

Telescope	Collecting Area (m ²)	Diameter/ Longest Baseline (m)	Configurations	Waveband (GHz)	Resolution (arcsec)
GBT	8640	110		18.0-26.5 26.0-36.0 38.2-49.8	32 23 16
Effelsberg	7850	100		17.9-26.2	40
(E)VLA ^a	13,255	36,400	A/B/C/D	18.1-26.5 40-50	0.08/0.3/0.9/2.8 0.05/0.15/0.5/1.5
30m	710	30		80-115.5 129-183 197-266 241-281	22 15 10 10
PdBI	1060	760	A/B/C/D	81-116 128-169 201-256	0.8/1.2/2.7/5.0 0.5/0.8/1.8/3.3 0.3/0.5/1.2/2.2
CARMA ^b	780	1,600 ^c	A/B/C/D/E	85-116 215-270	0.3/0.8/2.0/5.0/10.0 0.15/0.3/0.9/2.2/4.4
NMA	470	351	AB/C/D D only	85-116 126-152 213-237	2/3/5 1/2/4 2
Rainbow ^d	2060	410		(no 1 mm)	
SMA	225	509	1/2/3/4 ^e	186-242 271.5-349.5 320-420	0.4/1.0/2.9/3.5 0.3/0.7/1.9/2.3 0.25/0.6/1.7/2.0 (0.17 at 400 GHz)
eSMA ^f	490	780			
ALMA	5655	14,000	four	84-116 125-169 163-211 ^g 211-275 275-373 385-500 602-720 787-950	0.05 0.03 0.025 0.02 0.015 ^h 0.01 0.007 0.005
ALMA+ACA	6570				
SKA	1,000,000	3,000,000		up to 25	<0.001

Notes—^aThe EVLA will also be equipped with 26-40 GHz receivers in a few years from now.

^bCARMA is a combination of the former OVRO mm array and BIMA, and consists of six 10.4 m antennas and nine 6.1 m antennas.

^cNot de-commissioned yet, longest baseline operative in Fall 2007: 813 m.

^dThe Rainbow interferometer is the NMA in its AB configuration linked with the NRO 45 m telescope.

^eConfigurations are called subcompact, compact, extended, and very extended.

^fThe eSMA is the SMA interferometrically linked to the CSO 10.4 m and the JCMT 15 m telescopes.

^gNot fully funded yet.

^hDesign goal.

all applies to CO emission lines, which are by at least an order of magnitude brighter than those of other molecular tracers. Studies of dense gas (e.g., through HCN, HCO⁺, or CS) thus are even stronger biased towards the most luminous and often strongly lensed systems. Also, this applies to studies of integrated emission - projects aiming at resolving the emission are even more expensive in terms of observing time.

Third, studies are limited by the passbands of different receivers, which only cover certain molecular line transitions of a certain molecule at a certain redshift. Figure 2.6 illustrates this limitation for the four most commonly used current facilities (note that CARMA basically covers two out of the three bands of the PdBI), and for ALMA. Diagrams are shown for a range of transitions of CO (frequencies similar to CN), HCN (frequencies similar to HCO⁺ and HNC), CS, and millimeter atomic tracers such as C I, C II, O I, and N II (note that only C I and C II were observed at significant redshift to date). For HCN, HCO⁺, and HNC, transitions higher than 4→3 are typically not highly excited due to their very high critical densities, and thus very faint. The same applies for CS transitions higher than 8→7, and probably CN transitions higher than 6→5. Also, note that this is inferred from local studies, as for none of these molecules, transition ladders could be observed at high redshift to date. For CO, the only molecule where this could be tested in practice for a number of sources, the 7→6 and lower transitions have proven to be the brightest tracers, which however strongly depends on galaxy type (A. Weiß et al., in prep.). Although very faint, detection of the high order transitions is also important, as their faintness strongly constrains the excitation conditions. Still, due to the sensitivity limits of current telescopes, most observations focus on the highly excited low to mid order transitions. Apart from the holes in redshift coverage, Figure 2.6 illustrates that observations of redshifted CO with millimeter (and submillimeter) facilities get increasingly difficult at the highest redshifts, in particular beyond $z=6$, due to the fact that only transitions that are not highly excited can be covered. This means that observations of atomic and ionic lines, in particular C II, N II, and O I, may become increasingly important in studies of galaxies at even higher redshift. Also, these lines can be studied at $z=0$ with the upcoming HERSCHEL satellite. Note that the fine structure lines of C II and O I are the main cooling lines within the neutral (not highly dense) ISM. In particular, C II lines are very bright, usually much brighter than CO lines, and thus a valuable tracer of the neutral medium, particularly at the highest redshifts (see Maiolino et al. 2005 for the first high- z detection of C II, which is in the highest redshift quasar at $z=6.42$).

2.6 Selection Criteria

2.6.1 Selection Criteria for CO Observations

As shown in Figure 2.6, depending on transition, CO can basically be studied over the whole redshift range by current millimeter telescopes, such as the PdBI. However, for the observations presented in this thesis, two main selection criteria apply:

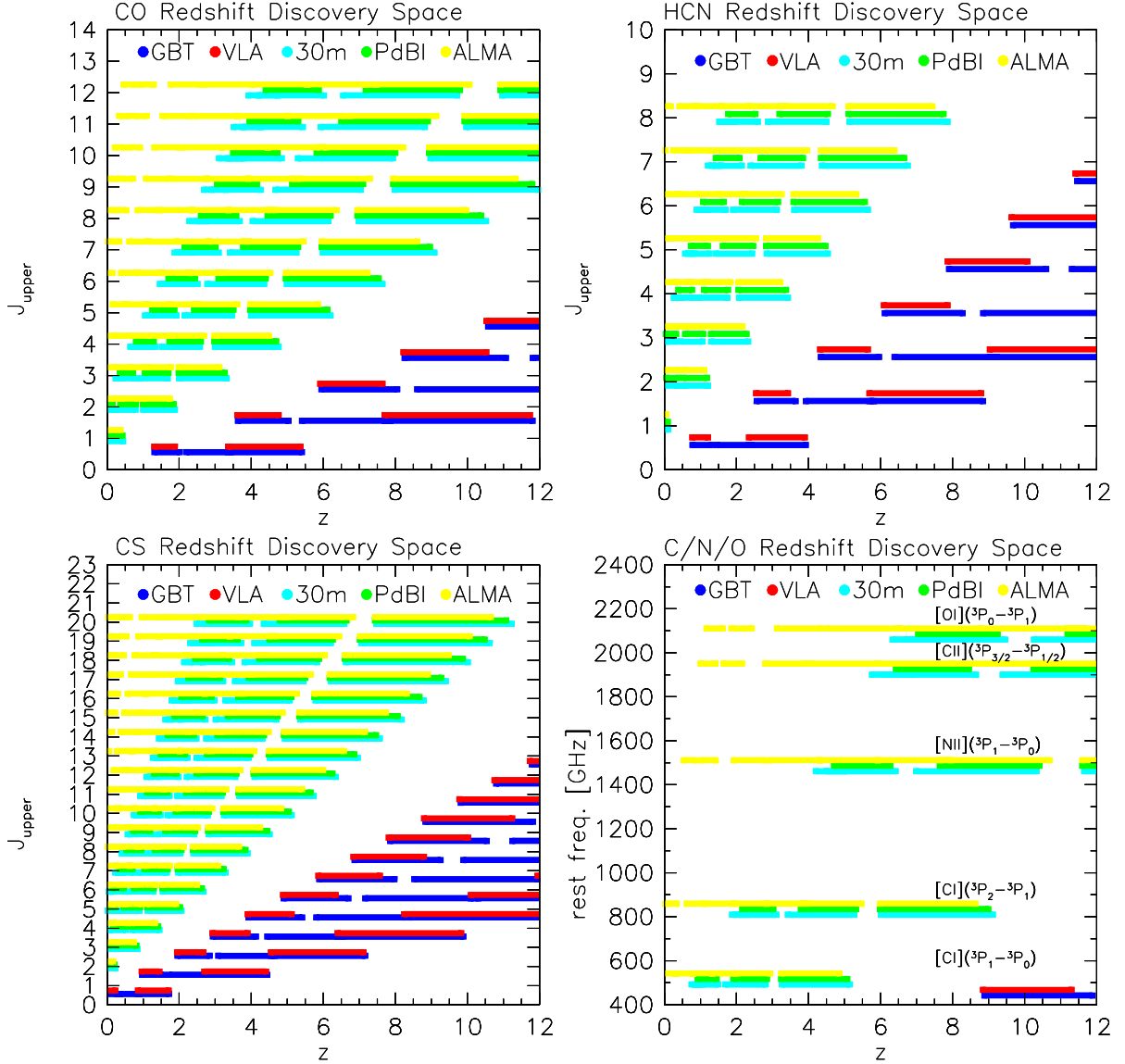


Figure 2.6: Redshift discovery space for different atomic/ionized and molecular lines with current and future radio/(sub)millimeter facilities. Representative diagrams for all species bright enough to be currently (or in the near future) observable in at least one $z > 1$ source are shown. The stripes indicate the frequency coverage of the receiver bands of the different telescopes [including the new Ka band (currently 26–36 GHz) at the GBT, the new EVLA K band (18.1–26.5 GHz) at the VLA, the new band 2 at PdBI (128–169 GHz) and band 5 for ALMA (163–211 GHz) which is not yet fully funded]. *Top left*: Redshift coverage for observations of CO rotational lines. As an indication for the frequency, the upper J -quantum number of the transition is plotted (frequency is roughly 115 GHz times J_{upper}) versus redshift. The coverage is similar to that for observations of CN (roughly multiples of 113 GHz). *Top right*: Same, but for HCN (frequency is roughly 89 GHz times J_{upper}). The coverage is similar to that for observations of HCO⁺ and HNC. *Bottom left*: Same, but for CS (frequency is roughly 49 GHz times J_{upper}). *Bottom right*: The rest frequency of forbidden transitions of [C I], [O I], [C II], and [N II] is plotted versus redshift.

- 1) At which redshifts greater than 2 can CO($J=1\rightarrow 0$) be observed?

As the 1.0 cm receiver at the GBT is only becoming available in winter 2007/2008, the only observing band currently covering the CO($J=1\rightarrow 0$) line at $z>2$ is the 1.3 cm K band. This corresponds to a redshift range of $3.35<z<5.40$. The project presented in the next chapter requires that the sources to be observed have to already be detected in higher J CO transitions, and it concentrates on quasar host galaxies. As of winter 2004/2005, the time at which the observations were carried out, this sample was limited to five sources (a sixth source was detected in 2007). One out of these five sources is much fainter than the rest of the sources, rendering CO($J=1\rightarrow 0$) observations with a single-dish telescope currently unfeasible. The sample presented in the next chapter consists of three out of the remaining four sources, encompassing about 20% of the CO-detected quasars at high redshift. Note that, if the 1.0 cm receiver proves to have sufficient sensitivity, this enlarges the CO($J=1\rightarrow 0$) discovery space down to $z=2.20$, giving access to another eight quasars (and 12 galaxies of other types).

- 2) At which redshifts can we observe CO at the highest possible resolution?

The SMA does not have sufficient collecting area (i.e., sensitivity) to enable high-resolution molecular gas studies at high redshift (note that no redshifted CO emission line has been detected with the SMA to date). The PdBI obtained its highest resolution capabilities only in winter 2006, and studies of redshifted CO emission at $0.3''$ are now under way. CARMA will obtain similar capabilities this winter. However, millimeter CO observations at 1 kpc ($0.15''$) resolution at the highest redshifts are challenging, and will remain difficult until the advent of ALMA. The only telescope that can currently observe CO emission at $z>4$ at 1 kpc linear resolution is the VLA in the 7 mm band. This observing band covers the CO($J=2\rightarrow 1$) transition at $3.61<z<4.76$, and the CO($J=3\rightarrow 2$) transition at $5.92<z<7.64$. As it is a requirement that the integrated CO flux is known to evaluate the feasibility of such high-resolution observations, a sample will also be selected out of those galaxies that are already detected in CO emission. Limiting ourselves again to quasar host galaxies, this leaves six candidates. One of these sources (the same as above) is too faint to render high-resolution observations feasible. One of the sources was observed by Carilli et al. (2002b, see Figure 2.7), the second by Walter et al. (2004, see Figure 1.6). High resolution CO observations of the remaining three sources at up to $0.15''$ linear resolution are shown in Chapters 9-11.

2.6.2 Selection Criteria for Observations of Dense Gas Tracers

Choosing Molecules

As shown above, due its relative brightness, CO is the main tracer of molecular gas in galaxies. It has been detected toward of order 10^3 nearby galaxies and 43 galaxies at high redshift (see, e.g., Appendix A, and references therein). HCN is the main tracer of dense molecular gas, i.e., the fraction of molecular gas that is more intimately associated with

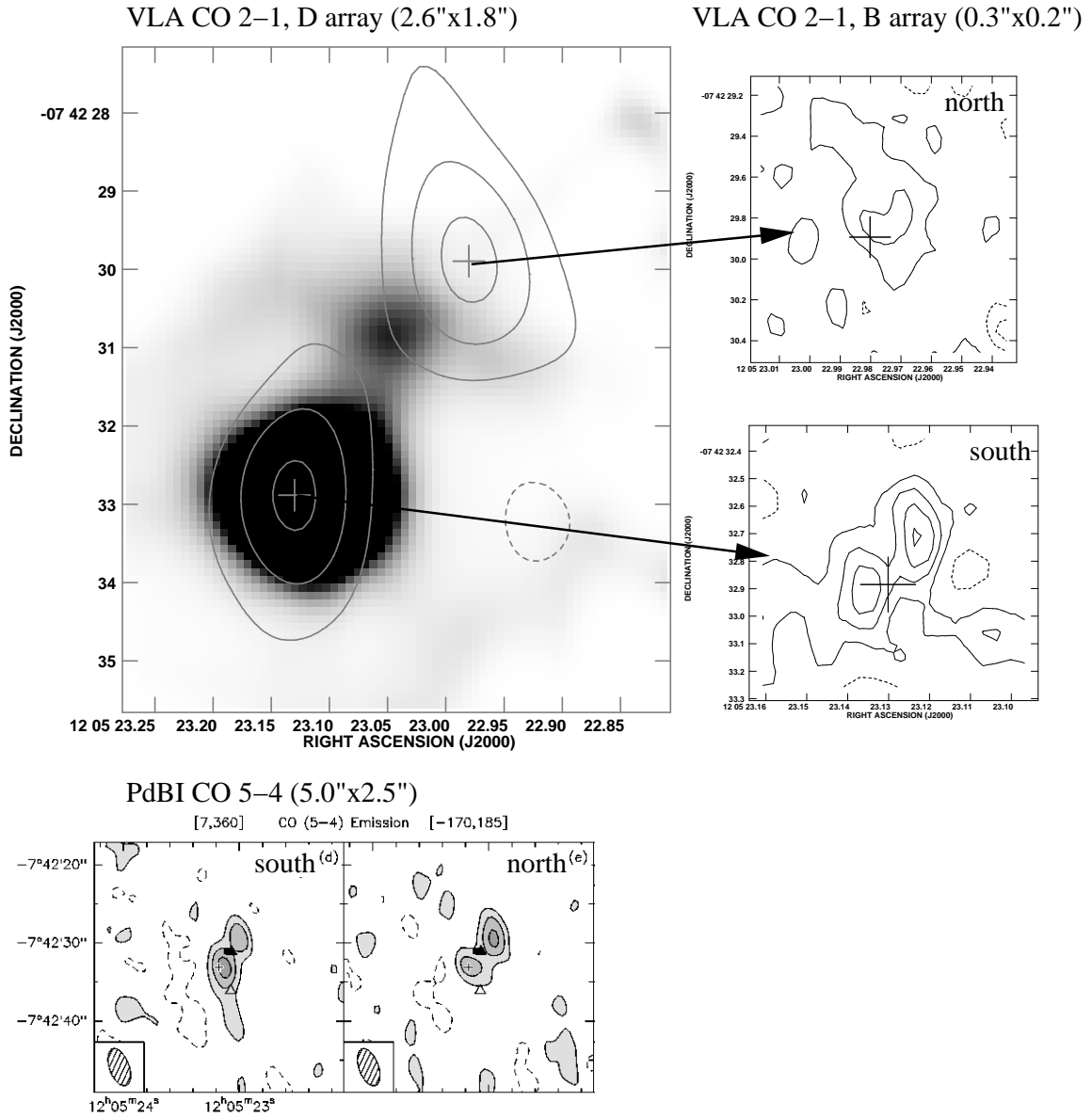


Figure 2.7: High Resolution CO Observations of BR 1202-0725 ($z=4.69$; Carilli et al. 2002b). *Top left*: Medium resolution CO($J=2\rightarrow 1$) contour map at $2.6''\times 1.8''$ resolution, overlaid on a Ly α emission line map. The two CO components are separated by ~ 28 kpc. *Top right*: Zoom-in on the two components. Although the signal-to-noise is only moderate, both components appear to be resolved at a resolution of $0.3''\times 0.2''$. These maps are $\sim 1.2''$ on a side. *Bottom*: CO($J=5\rightarrow 4$) map, obtained with the PdBI (Omont et al. 1996), at $5.0''\times 2.5''$ resolution. The blue and red parts of the CO emission are shown separately, showing that the two peaks are at slightly different redshifts, and thus likely to be two different galaxies (possibly in the process of merging).

star formation than the more diffuse fraction of the CO. HCN has been detected in of order 10^2 galaxies in the nearby universe, and in five galaxies at high redshift.

Until November 2005, these were the only two molecules from which emission has been detected at $z > 1$. As described in Chapters 5–7, we have now detected emission from three more molecules, HCO^+ , CN, and CS, in a $z=2.56$ quasar host galaxy. In addition, we have searched for H_2O emission toward a $z=3.2$ quasar host galaxy, which however has not yielded a detection yet (see Chapter 8). In addition, Guélin et al. (2007) have reported a possible detection of HNC in a $z=3.9$ quasar host galaxy. Due to line blending, this detection is likely to be HNC, but remains to be confirmed through another HNC transition.

There are two main motivations to search for additional molecular tracers. The first motivation is simply a technical one: if there is a tracer of dense molecular gas that is brighter than HCN and thus easier to observe, the sample of high- z galaxies toward which a search of dense molecular gas is feasible might dramatically improve. This was a particular reason to search for H_2O emission, which may be greatly enhanced by maser amplification, but also part of the reason to search for the other molecules, which are sometimes brighter than HCN in nearby galaxies.

The second reason is the more important one, and does not only apply to galaxies at high redshift: different molecules probe different physical conditions. Also, knowing the excitation conditions, line ratios of different molecules can actually probe chemical abundance ratios, revealing how and to what extent molecular clouds are chemically enriched at high redshift. Note that this is an important issue, as optical studies of atomic/ionic lines are often biased towards particular regions of galaxies that do not necessarily probe the material that forms new stars. In particular in quasars, these lines usually probe the central regions associated with the AGN rather than the regions that determine the properties for star formation.

The most useful molecules to probe the physical properties of distant galaxies are obviously those that are understood locally. In particular, it is only possible to obtain a flux integrated over the whole galaxy at high redshift, i.e., the most useful tools will be luminosity relations (apart from multi-molecule LVG modeling, where possible). In the local universe, the most commonly used dense molecular gas tracers after HCN are HCO^+ and CS. Apart from their relatively high dipole moment (and thus, critical density), this is mainly due to the fact that they are usually quite abundant, and thus likely to be bright.

HCN and HCO^+ have similar dipole moments, and thus are, in principle, tracers of regions of similar density (and thus should show similar brightness). In the simplest case, HCO^+ thus should be found to have the same qualities as HCN in terms of tracing dense gas, and determining star-formation rates and efficiencies. However, there are a number of reasons why this might not be the case. First, the HCN/ HCO^+ ratio obviously depends on the relative abundance of nitrogen and oxygen. If there is some process that depletes one or the other, it influences which of the molecules is the better tracer of dense cores in a certain galaxy. More importantly, HCO^+ is an ion. Its abundance thus greatly depends on the ionizing field and abundance of free electrons. If a galaxy, such as a bright quasar, has a strong ionizing field, it may impact the HCN/ HCO^+ brightness ratio, and thus bias

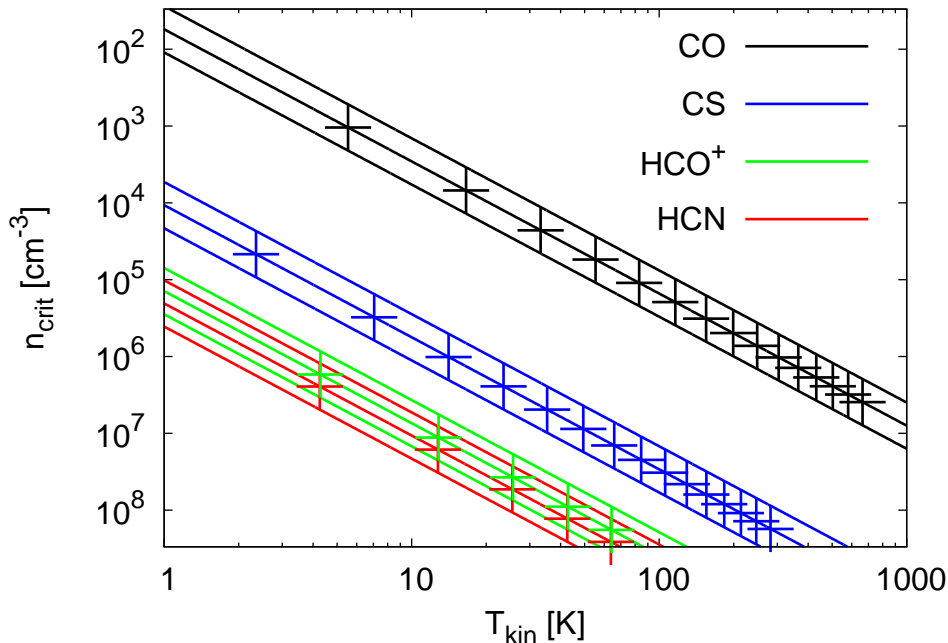


Figure 2.8: Relation between kinetic temperature (expressed as minimum excitation temperature here) and critical density for CO, HCN, HCO⁺, and CS. The crosses indicate different rotational levels, starting with $J=1$ for the lowest temperatures. As the exact value of n_{crit} is temperature dependent, typical ranges instead of discrete values are shown. Also, note that n_{crit} is reduced by radiative trapping, typically by a factor of a few.

the dense gas-star formation relation. In short, the study of both HCN and HCO⁺ is an important diagnostic in determining how reliable one or the other is as a tracer of dense molecular clouds.

Simply put, CS is a valuable tracer due to the fact that it traces intermediate densities between CO and HCN/HCO⁺, or, more precisely, that it covers the intermediate region in the $T_{\text{kin}}-n_{\text{crit}}$ plane (see Figure 2.8). It thus comprises an independent estimate of the conditions in the galaxy, or, spoken in terms of modeling, gives an independent constraint to determine the conditions. Also, a $L'_{\text{CS}}-L_{\text{FIR}}$ relation should lie in the region between the CO and HCN/HCO⁺ laws if chemical and excitation biases are accounted for properly. On a sidenote, CS implicitly probes the abundance of sulphur, i.e., a species much heavier than H, C, N, and O. It thus is not a result of element synthesis in low- or intermediate mass stars, but just in massive stars. From a more technical perspective, the rotational transitions of CS have about half the spacing of that of CO, HCN, and HCO⁺, and thus are accessible at larger ranges in redshift within a certain wavelength range.

Although more reasons to observe HCN, HCO⁺, and CS can be found based on their distribution in resolved nearby starburst galaxies such as M82 and NGC 253, the main reasons are their positions in the $T_{\text{kin}}-n_{\text{crit}}$ plane (excitation conditions are fairly well-

constrained once two transitions per molecule are available in addition to a measured CO ladder), and their Schmidt-Kennicutt laws.

A main difficulty in such studies is that HCO⁺ and CS studies are even more limited than those of HCN. Once comprehensive samples are picked from the literature, only few more than 10 galaxies are available. However, the situation in the local universe is about to improve in the near future, in particular for LIRGs and ULIRGs (e.g., Gracia-Carpio et al. 2007). There are few other molecular gas tracers observed comprehensively in at least 10 galaxies. One particularly interesting of those few remaining tracers is the CN radical.

Probing dense, star-forming regions in the Galaxy, CN is observed to be highly abundant in the dense interfaces between molecular clouds and ionization fronts (e.g., Orion, Rodruíguez-Franco et al. 1998). It also is observed to be highly abundant in the central regions of starburst galaxies like M82 (Fuente et al. 2005), in particular relative to HCN, the main tracer of dense gas (note that CN is a major dissociation product of HCN). In short, CN is known to reside in regions that are strongly affected by stellar UV radiation, and thus in particular regions within star-forming environments (but possibly also in regions where UV radiation from an AGN may be strong enough to dissociate HCN, but not CN). CN thus is also found to be very abundant in the outer layers of photodissociation regions¹⁰ (PDRs, e.g., Fuente et al. 1993; Sternberg & Dalgarno 1995). Although the critical density of CN is by a factor of about 5 lower than that of HCN, it thus is dominant in regions of density where HCN would be expected to be dominant in terms of density, but (in reality) is not due to dissociating radiation. In other words, CN is biased relative to HCN, and thus provides an important test as a dense gas tracer. In particular in starbursting quasars, where UV radiation from both the starburst and the AGN may be important for the composition of the molecular clouds, CN may play a different role compared to normal galaxies or even ULIRGs. Due to the fact that CN is a significantly different probe of dense gas from HCN, it thus may show a different Schmidt-Kennicutt law (and different excitation than expected from the excitation of other dense gas tracers once such studies can be done). On a sidenote, the brightness ratios of CO, CN, and CS may provide a zeroth-order limit on the relative abundance of O, N, and S in molecular clouds.

In short, numerous molecules have been detected in external galaxies (about 50 including isotopes, see Martín et al. 2006, their Table 3). Most of these are rare isotopes, isotopomers, or ionized species, leaving 10-15 relatively abundant molecules. Out of these, few are regularly observed in nearby galaxies and thus understood well enough for potential high redshift studies, leaving basically only CO, HCN, HCO⁺, CS, CN, HNC, H₂O, H₂CO, OH, NH₃, and SiO. Looking for molecules that have simple rotational ladders with observable transitions in the millimeter/centimeter regime leaves us with the first six of these molecules (H₂O is a special interest case due to its high abundance and possible maser bonus,¹¹ however rarely observed at $z=0$ due to the strong atmospheric water lines).

¹⁰Note that PDRs also stand out in the main atomic cooling lines of the ISM, in particular C II, O I, and C I.

¹¹Other molecules such as OH and SiO are also masing.

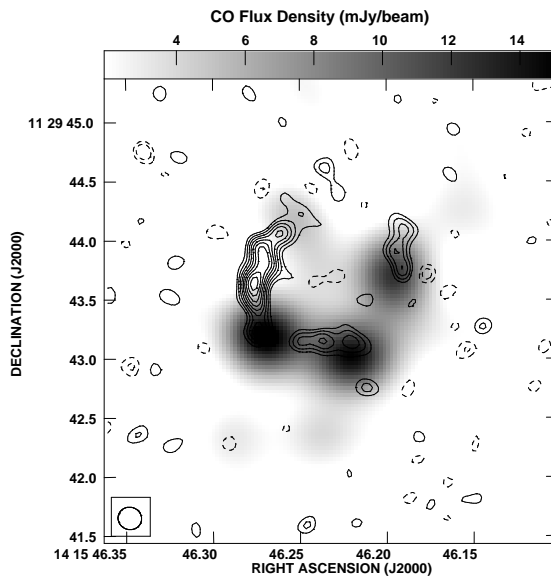


Figure 2.9: CO and radio continuum emission in the Cloverleaf quasar, a quadruple lens at $z=2.56$. Contours of the 8.4 GHz radio continuum at $0.20'' \times 0.19''$ resolution (Kayser et al. 1990; Riechers et al. 2008, in prep.) overlaid on a map of the CO($J=7 \rightarrow 6$) emission line at $0.77'' \times 0.44''$ resolution (Alloin et al. 1997; Kneib et al. 1998).

Showing interest in the first five of these,¹² the question occurs if they provide insight on the physical properties we are interested in. CO probes cold and warm gas that is not particularly dense. CS probes cold and moderately warm gas of medium density. HCN, HCO⁺, and CN probe cold dense gas. The HCN/CO and HCN/HCO⁺ line ratios are common diagnostics in the local universe, and thus promise to provide insight on the extreme systems observed at high redshift. CN, on the other hand, is a particular tracer of dense environments that are impacted by strong UV radiation, and that thus are not dominated by the more common dense gas tracers HCN and HCO⁺.

Choosing Targets

Obviously, it is most useful to observe different molecular probes in the same galaxies to be able to study line ratios and coupled excitation conditions, and to compare the different Schmidt-Kennicutt laws. There are three main selection criteria:

- 1) Which sources are bright enough in CO emission to enable studies of molecular lines that are by at least a factor of 10 fainter?

¹²HNC tends to be overluminous in ULIRGs relative to HCN and thus also is a potentially interesting probe; Cernicharo et al. (2006); Aalto et al. (2007), but not part of the study described here.

2) Which sources have CO SLEDs that indicate the presence of excited dense gas (i.e., with a significant brightness temperature), or alternatively, are already detected in HCN?

3) Which sources have suitable transitions of the molecular probes of interest that fall into the observing windows of the most sensitive telescopes (i.e., currently the VLA and the PdBI)?

For observations of HCO^+ , CS, and CN, one obvious candidate occurs: the Cloverleaf quasar, a strongly lensed galaxy at $z=2.56$ (Figure 2.9). It is the brightest $z>2$ source ever to be detected in CO emission (Barvainis et al. 1994), it is already detected in HCN emission (Solomon et al. 2003), and it is observable in both low- and high order transitions of all five molecules. It thus has proven to be a virtual goldmine for molecular line studies (see Chapters 5-7 and Outlook).

For the search for water masers, the third brightest CO source at high redshift, the lensed quasar MG 0751+2716 at $z=3.2$, has proven to be the most suitable source (see Chapter 8).

Chapter 3

Masses of Molecular Gas Reservoirs in $z \gtrsim 4$ Quasar Host Galaxies

3.1 Context

As shown in the previous chapters, two of the main diagnostics in studies of galaxy properties, formation and evolution are the total molecular gas mass and the star formation rate (and their ratio, the star formation efficiency). Determining molecular gas masses at $z=0$ is difficult due to its dependence on the conversion from molecular line luminosity (typically CO) to molecular gas mass (i.e., H_2). Assuming that this conversion factor is defined properly locally, it is possible to extrapolate this conversion factor to systems at high redshift. This is a non-trivial task, as the systems currently detected in molecular line emission at $z>1$ are almost exclusively more luminous in molecular line emission than all galaxies known at $z=0$, which already demonstrates that there is significant evolution. Assuming that these limitations can be accounted for by using local ULIRGs as templates for the high redshift systems, there is one main limitation of high- z molecular gas studies: Due to redshift, CO in distant galaxies cannot be observed in the ground-state $CO(J=1\rightarrow 0)$ transition with millimeter telescopes typically used for studies of molecular gas, but rather in higher J transitions such as $CO(J=3\rightarrow 2)$, $CO(J=4\rightarrow 3)$, and $CO(J=5\rightarrow 4)$. In normal spiral galaxies, such transitions are not highly excited, and thus have lower line luminosities than the $CO(J=1\rightarrow 0)$ transition. This means that they only trace a fraction of the total CO luminosity in a galaxy, and thus, by extension, only a fraction of the total molecular mass. Studies of star formation efficiency at high redshift thus may be systematically biased due to an underestimation of the total molecular mass, which would mimic an excessive efficiency. This is why the Schmidt-Kennicutt law is a standard diagnostic in the local universe, but, so far, had to be treated with great caution when extrapolated toward higher redshift. The driving force behind establishing a study of $CO(J=1\rightarrow 0)$ emission in $z \gtrsim 4$ quasar host galaxies that were already detected in higher J CO transitions, as described here, was to better understand these issues. The redshift of this study was limited to $z > 3.5$ due to available observing windows at the time the project was carried out. This leaves

only very few potential targets. Due to the frequencies of the redshifted CO($J=1\rightarrow 0$) lines, this study also had to rely on classical radio telescopes rather than the standard millimeter observing facilities. From a technical perspective, these observations thus can also be considered a feasibility study to detect redshifted CO emission with classical single-dish radio telescopes. In spite of considerable efforts, such studies were not successful previously.

3.2 Abstract

We present CO($J=1\rightarrow 0$) observations of the high-redshift quasi-stellar objects (QSOs) BR 1202–0725 ($z = 4.69$), PSS J2322+1944 ($z = 4.12$), and APM 08279+5255 ($z = 3.91$) using the NRAO Green Bank Telescope (GBT) and the MPIfR Effelsberg 100 m telescope. We detect, for the first time, the CO ground-level transition in BR 1202–0725. For PSS J2322+1944 and APM 08279+5255, our observations result in line fluxes that are consistent with previous NRAO Very Large Array (VLA) observations, but they reveal the full line profiles. We report a typical lensing-corrected velocity-integrated intrinsic CO($J=1\rightarrow 0$) line luminosity of $L'_{\text{CO}} = 5 \times 10^{10} \text{ K km s}^{-1} \text{ pc}^2$ and a typical total H₂ mass of $M(\text{H}_2) = 4 \times 10^{10} M_{\odot}$ for the sources in our sample. The CO/FIR luminosity ratios of these high- z sources follow the same trend as seen for low- z galaxies, leading to a combined solution of $\log(L_{\text{FIR}}) = (1.39 \pm 0.05) \log(L_{\text{CO}}) - 1.76$. It has previously been suggested that the molecular gas reservoirs in some quasar host galaxies may exhibit luminous, extended CO($J=1\rightarrow 0$) components that are not observed in the higher J CO transitions. Using the line profiles and the total intensities of our observations and large velocity gradient (LVG) models based on previous results for higher J CO transitions, we derive that emission from all CO transitions is described well by a single gas component in which all molecular gas is concentrated in a compact nuclear region. Thus, our observations and models show no indication of a luminous extended, low surface brightness molecular gas component in any of the high-redshift QSOs in our sample. If such extended components exist, their contribution to the overall luminosity is limited to at most 30%.

3.3 Introduction

Understanding when and how galaxies form is one of the primary objectives in both observational and theoretical astrophysics. The mere fact that active galaxies, such as radio galaxies, quasi-stellar objects (QSOs), and emission-line galaxies are observed up to redshifts of $z = 6.6$ (e.g., Fan et al. 2001; Rhoads & Malhotra 2001; Hu et al. 2002; Kodaira et al. 2003; Taniguchi et al. 2005), less than 1 Gyr after recombination, implies that galactic-scale ($\sim 10 \text{ kpc}$), gravitationally bound structures exist at this early epoch. The study of the masses and dynamical state of these young systems serves as a direct constraint to the models describing the growth of large-scale structures since the epoch of recombination.

Studies of the molecular and dusty interstellar medium (ISM) in these galaxies are of fundamental importance, since it is this medium out of which stars form; accurate determi-

nation of the molecular gas mass could therefore serve as an indicator of the evolutionary state of a galaxy. The detection of carbon monoxide (CO) is also a strong confirmation that star formation is going on in some of the highest redshift systems. In fact, the combination of molecular gas and dust detections with large far-infrared (FIR) luminosities provides the strongest evidence that a significant fraction of high- z galaxies are undergoing starbursts at prodigious rates ($> 10^3 M_{\odot} \text{yr}^{-1}$), consistent with the formation of a large elliptical galaxy on a dynamical timescale of $\sim 10^7$ – 10^8 yr.

Over the past decade, more than 30 galaxies at $z > 2$ have been detected in CO emission (Solomon & Vanden Bout 2005) out to a redshift of $z = 6.42$ (Walter et al. 2003, 2004; Bertoldi et al. 2003b), confirming the presence of intense starbursts in numerous high- z galaxies. As most of these observations were obtained using millimeter interferometers, these detections were typically achieved by observing high- J CO($J \rightarrow J - 1$) transitions ($J \geq 3$). Although these high- J lines exhibit in general higher peak flux densities than the ground-state ($J = 1$) transition, it is possible that the higher order transitions are biased to the excited gas close to a central starburst and do not necessarily trace the entire molecular gas reservoir seen in CO($J=1 \rightarrow 0$). In addition, the conversion factor (α) to derive molecular (H_2) masses from measured CO luminosities has mostly been estimated for the CO($J=1 \rightarrow 0$) line (e.g., Downes & Solomon 1998; Weiß et al. 2001). Observing CO($J=1 \rightarrow 0$) has the additional advantage that properties of the highly redshifted sources can be *directly* compared to the molecular gas properties of nearby (starburst) galaxies that are predominantly mapped in the CO($J=1 \rightarrow 0$) transition.

These are main motivations for observing the CO($J=1 \rightarrow 0$) ground-state transition. However, due to the faintness of the line and the bandwidth limitations of current radio telescopes, such high- z CO($J=1 \rightarrow 0$) observations only exist for two QSOs and two radio galaxies to date. All of these observations have been obtained with radio interferometers operating at centimeter wavelengths: the NRAO Very Large Array (VLA; Papadopoulos et al. 2001; Carilli et al. 2002a; Greve et al. 2004) and the Australia Telescope Compact Array (ATCA; Klamer et al. 2005). In particular, due to the bandwidth limitations of the VLA, obtaining better constraints on the spectral line shape and total flux of the CO($J=1 \rightarrow 0$) transition is desirable even for already detected sources. Today’s largest single-dish telescopes, such as the NRAO Green Bank Telescope (GBT)¹ and the MPIfR Effelsberg telescope,² can eliminate some of those issues due to their larger spectral bandwidths.

Here we report on first observations of CO($J=1 \rightarrow 0$) in three CO-bright high- z QSOs, which also exhibit ultraluminous IR emission, using the GBT and the Effelsberg telescope. In Section 2, we describe our observations. Section 3 summarizes our results on the individual objects (BR 1202–0725 at $z = 4.69$, PSS J2322+1944 at $z = 4.12$, and APM 08279+5255 at $z = 3.91$). Section 4 provides an analysis and discussion, and Section 5 closes with a summary of our results. We assume a standard Λ CDM cosmology

¹The Green Bank Telescope is a facility of the National Radio Astronomy Observatory (NRAO), operated by Associated Universities, Inc., under a cooperative agreement with the National Science Foundation.

²The Effelsberg telescope is a facility of the Max-Planck-Gesellschaft (MPG), operated by the Max-Planck-Institut für Radioastronomie (MPIfR).

throughout, with $H_0 = 71 \text{ km s}^{-1} \text{ Mpc}^{-1}$, $\Omega_M = 0.27$, and $\Omega_\Lambda = 0.73$ (Spergel et al. 2003).

3.4 Observations

3.4.1 Green Bank Telescope

Observations of the three targets were carried out with the GBT during 12 observing runs between 2004 October and 2005 April with a total observing time of 89.5 hr. The total/on-source observing times were 31.5/20 hr for BR 1202–0725, 23/15 hr for PSS J2322+1944, and 35/22 hr for APM 08279+5255. During all runs, 3C 147 and 3C 286 were used as primary/flux calibrators. For spectral line calibration, we observed IRC+10216, DR 21, Orion IRc2, Orion HC, and W3OH H₂O. As secondary/pointing calibrators, 3C 273, J1256–0547 (for BR 1202–0725), J2253+1608 (for PSS J2322+1944), J0753+538, and J0824+5552 (for APM 08279+5255) were used. The pointing accuracy, determined by continuum cross scans of nearby sources, was typically $\sim 3''$ (reaching $\lesssim 1''$ under the best conditions). We estimate the calibration to be accurate to 10%–15%. As the CO($J=1 \rightarrow 0$) transition at 115.2712 GHz is redshifted into the K band for all three targets (BR 1202–0725: $\nu_{\text{obs}} = 20.2450 \text{ GHz}$; PSS J2322+1944: $\nu_{\text{obs}} = 22.5258 \text{ GHz}$; APM 08279+5255: $\nu_{\text{obs}} = 23.4663 \text{ GHz}$), the dual-beam, dual-polarization 18–26 GHz receiver was used for all observations. The beam size of the GBT at our observing frequencies is $\sim 32\text{--}36''$ ($\sim 225\text{--}250 \text{ kpc}$ at $z \simeq 4$), i.e., much larger than our targets. The two beams have a fixed separation of $178.8''$ in the azimuth direction. Two different spectrometer setups were used; half of the observing runs were executed in the first mode, and the other half of the runs in the second mode. The first mode features two simultaneous intermediate frequencies (IFs) with a bandwidth of 800 MHz ($\sim 10,000\text{--}12,000 \text{ km s}^{-1}$ at our observing frequencies) and 2048 channels each, resulting in a spectral resolution of 391 kHz ($\sim 5 \text{ km s}^{-1}$). The CO($J=1 \rightarrow 0$) line was always centered in the first 800 MHz IF. The second mode has one IF with 200 MHz ($\sim 2500\text{--}3000 \text{ km s}^{-1}$) and 16,384 channels, resulting in a spectral resolution of 12 kHz ($\sim 0.15 \text{ km s}^{-1}$). BR 1202–0725 and APM 08279+5255 were observed with both setups, while PSS J2322+1944 was only observed during runs that used the second setup. The spectra taken in each mode were examined separately and then combined. The ON-OFF position switching mode was used; i.e., the target was observed alternately with the two telescope beams, and the off-source beam was always monitoring the sky background in parallel. The beam switching frequency was once every 60–120 s depending on the observing run. The weather was excellent for the winter nights with typical zenith system temperatures of $T_{\text{sys}} = 22 - 35 \text{ K}$ on a T_A^* scale. On 2005 April 19 and 20 the system temperatures were significantly higher (typically $T_{\text{sys}} = 50 - 60 \text{ K}$).

For data reduction, the AIPS++³ package and the new GBT IDL software⁴ were used, providing consistent results. The spectra of BR 1202–0725, PSS J2322+1944, and APM 08279+5255 were binned to 2.00 MHz (30 km s^{-1}), 1.80 MHz (24 km s^{-1}), and 5.86 MHz

³See <http://aips2.nrao.edu>.

⁴See <http://gbtidl.sourceforge.net>.

(75 km s^{-1}), reaching rms noise values of ~ 75 , ~ 140 , and $\sim 65 \mu\text{Jy}$, respectively. A linear baseline was subtracted from the PSS J2322+1944 spectrum to remove continuum fluxes and atmospheric/instrumental effects. For BR 1202–0725 and APM 08279+5255, polynomials of order 2 have been used to remove a very wide ($\gg 100 \text{ MHz}$, i.e., much broader than the width of the CO line) “bending” of the baselines. Only the frequency range that was used to define the spectral baselines is used for the final GBT spectra. APM 08279+5255 was observed using both the 200 and 800 MHz bandwidth setups. While the CO($J=1\rightarrow 0$) line was clearly detected with both setups, the spectrum obtained with the narrowband high-resolution 200 MHz setup shows significant baseline problems, as the continuum level is significantly different on the red and blue sides of the line. Therefore, we only use the results obtained with the wide 800 MHz bandwidth setup (corresponding to 15 hr on-source, and covering a velocity range of $\sim 8000 \text{ km s}^{-1}$) for the final spectrum. In addition to simple ON-OFF combinations and subtraction of low-order polynomial spectral baselines, we also followed the scheme proposed by Vanden Bout et al. (2004) for reconstructing the temporal baseline variations; however, we found that this did not improve our final results. The reduced spectra were read into GILDAS/CLASS⁵ to write out the final combined spectrum tables. The final spectra are shown in the top panels of Figures 3.1 and 3.2 and in Figure 3.3. We note that the spectrum of BR 1202–0725 is limited to the central $\sim 150 \text{ MHz}$ due to the fact that about half of the data were taken with the narrower 200 MHz setting.

3.4.2 Effelsberg

Observations were carried out towards BR 1202–0725 and PSS J2322+1944 in 2003 January and February with a total observing time of $\sim 40 \text{ hr}$ (20 hr per source, corresponding to 8 hr on-source each). At $40''$ beam size, the pointing accuracy, as determined by continuum cross scans of nearby sources, was better than $10''$, with typical values of $\sim 5''$. Calibrations for the gain as well as the variation of the atmospheric opacity and zenith distance were obtained from observations of 3C 286 and NGC 7027 (see Ott et al. 1994 for reference fluxes), leading to a total formal calibration uncertainty of $\sim 15\%$. We observed in beam switching mode using a rotating horn with a beam throw of $2'$ and a switching frequency of $\sim 1 \text{ Hz}$. We have used a dual polarization HEMT receiver for all observations. The autocorrelator backend was split into eight bands of 160 MHz bandwidth and 128 channels each that could individually be shifted in frequency by up to $\pm 250 \text{ MHz}$ relative to the recessional velocity of the targets. The final spectra cover a velocity range of $\sim 6000 \text{ km s}^{-1}$ with channel spacings of $\sim 16 \text{ km s}^{-1}$. We achieved single channel system temperatures of 65 and 85 K on a T_A^* scale. After combination of both orthogonal linear polarizations, this leads to T_{sys} of 47 and 60 K.

The GILDAS/CLASS package was used for data reduction. All spectral baselines are of good quality and only first-order polynomial baselines had to be subtracted. The final spectra of BR 1202–0725 and PSS J2322+1944 are shown in the middle panels of Figures 3.1 and 3.2. These spectra were binned to 5.97 MHz (88 km s^{-1}) and 3.60 MHz (48 km s^{-1}),

⁵See <http://www.iram.fr/IRAMFR/GILDAS/>.

reaching rms noise values of ~ 150 and $\sim 380 \mu\text{Jy}$, respectively. We note that the latter do not show the full ranges used for spectral baseline fitting. Those ranges (~ 380 MHz for BR 1202–0725 and ~ 180 MHz for PSS J2322+1944) are illustrated by the insets in the same figures.

3.4.3 Combined Spectra

As BR 1202–0725 and PSS J2322+1944 were observed with both telescopes, we also created combined spectra of both results to increase the signal-to-noise ratio and average out part of the calibrational uncertainties. The GILDAS/CLASS package was used to reprocess and combine the final spectra of both telescopes. The final unbinned GBT and Effelsberg spectra were regridded to a common velocity resolution and baseline-subtracted before combination. In the combination, spectra were weighted with their respective rms. The combined spectra of BR 1202–0725 and PSS J2322+1944, as shown in the bottom panels of Figures 3.1 and 3.2, were binned to a resolution of 2.00 MHz (30 km s^{-1}) and 1.80 MHz (24 km s^{-1}), reaching rms noise values of ~ 70 and $\sim 125 \mu\text{Jy}$, respectively.

3.5 Results

The sources in our study are the three CO-brightest high-redshift QSOs that can currently be observed in the CO($J=1 \rightarrow 0$) transition. We obtained detections for all our targets. CO line luminosities L'_{CO} (in $\text{K km s}^{-1} \text{pc}^2$) were derived using

$$L'_{\text{CO}} = 3.25 \times 10^7 [I \nu_{\text{obs}}^{-2} D_L^2 (1+z)^{-3}] , \quad (3.1)$$

where I is the velocity-integrated CO($J=1 \rightarrow 0$) line flux in Jy km s^{-1} , D_L is the luminosity distance in Mpc, and ν_{obs} is the observed frequency in GHz (Solomon et al. 1992b). For the systems with known lensing magnification factor μ_L^{CO} , L'_{CO} has to be divided by that factor in order to get the intrinsic CO luminosity of the discussed target. A conversion factor $\alpha = 0.8 M_{\odot} (\text{K km s}^{-1} \text{pc}^2)^{-1}$ to convert $L'_{\text{CO}(1-0)}$ to $M_{\text{gas}}(\text{H}_2)$ is assumed throughout, as applicable for local ultraluminous infrared galaxies (ULIRGs)/starbursts (Downes & Solomon 1998). All observational results are summarized in Table 3.1. Derived CO luminosities and gas masses as well as FIR luminosities from the literature are given in Table 3.2.

3.5.1 BR 1202–0725

Previous Results

BR 1202–0725 ($z = 4.69$) was detected in multiple CO transitions before (see Table 3.3) but not in CO($J=1 \rightarrow 0$). This optically bright, radio-quiet QSO has the curious property that the optical QSO is a single source, but the millimeter continuum and CO line observations show a double source with a separation of about $4''$ (Omont et al. 1996; Guilloteau et al.

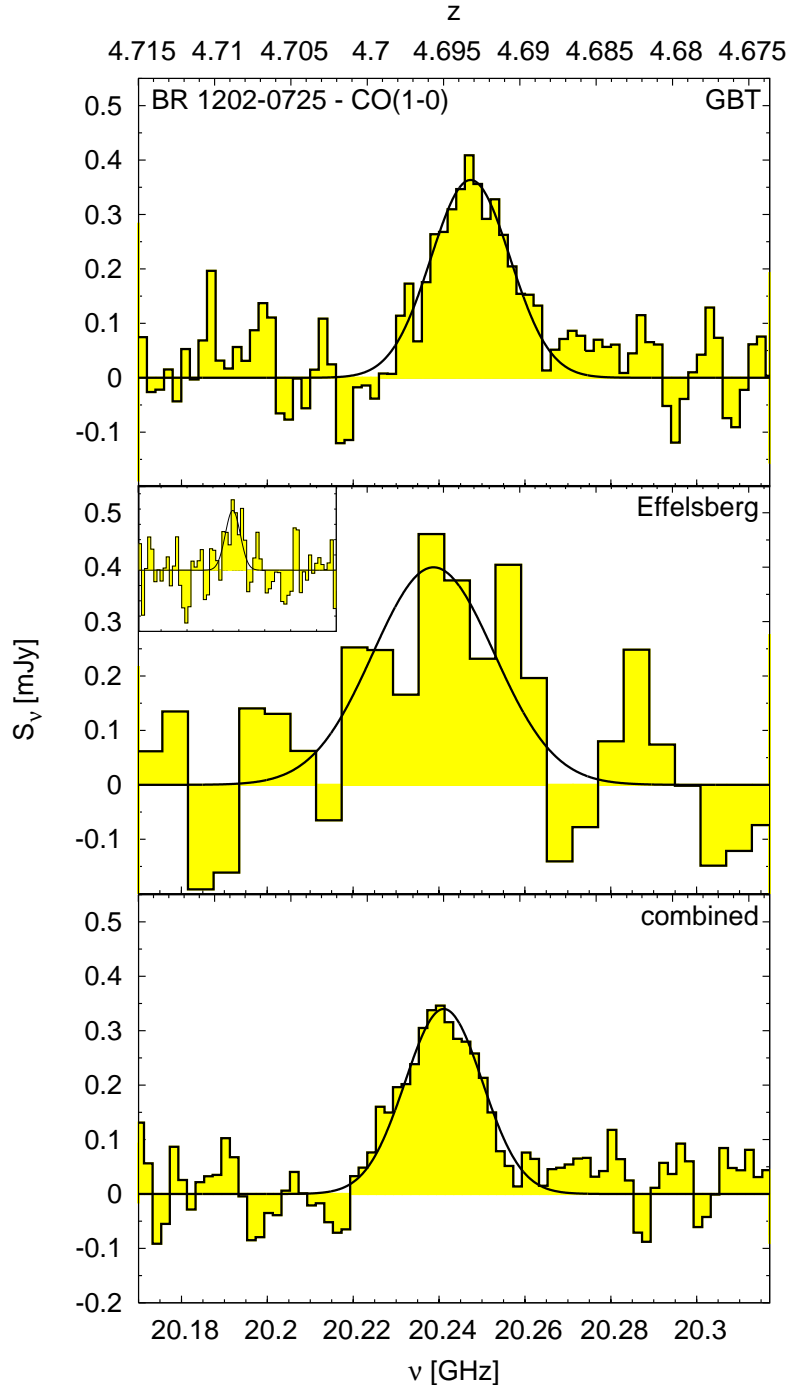


Figure 3.1: GBT (*top*) and Effelsberg (*middle*) spectra of CO($J=1\rightarrow 0$) emission from BR 1202–0725. The bottom panel shows the combined spectrum. The GBT spectrum has been smoothed to a resolution of 2.00 MHz (30 km s^{-1}). The rms per channel is $\sim 75 \mu\text{Jy}$. The Effelsberg spectrum has been smoothed to a resolution of 5.97 MHz (88 km s^{-1}). The rms per channel is $\sim 155 \mu\text{Jy}$. For illustration, the inset shows the full spectral range of the Effelsberg spectrum that was used for spectral baseline fitting (width ~ 380 MHz). The combined spectrum has been smoothed to a resolution of 2.00 MHz (30 km s^{-1}). The rms per channel is $\sim 70 \mu\text{Jy}$. The thin black lines show Gaussian fits to the data (see Table 3.1).

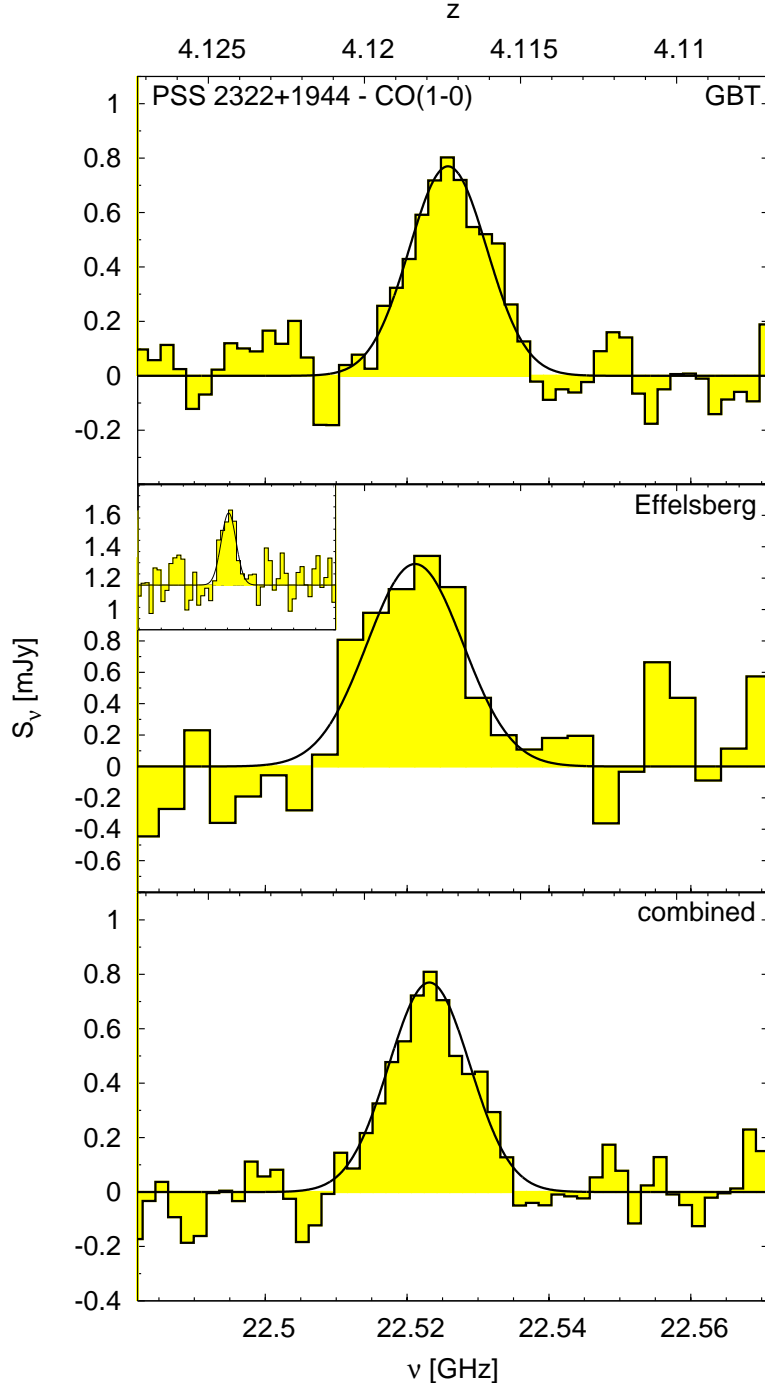


Figure 3.2: GBT (*top*) and Effelsberg (*middle*) spectra of CO($J=1 \rightarrow 0$) emission from PSS J2322+1944. The bottom panel shows the combined spectrum. The GBT spectrum has been smoothed to a resolution of 1.80 MHz (24 km s^{-1}). The rms per channel is $\sim 140 \mu\text{Jy}$. The Effelsberg spectrum has been smoothed to a resolution of 3.60 MHz (48 km s^{-1}). The rms per channel is $\sim 380 \mu\text{Jy}$. For illustration, the inset shows the full spectral range of the Effelsberg spectrum that was used for spectral baseline fitting (width ~ 180 MHz). The combined spectrum has been smoothed to a resolution of 1.80 MHz (24 km s^{-1}). The rms per channel is $\sim 125 \mu\text{Jy}$. The thin black lines show Gaussian fits to the data (see Table 3.1).

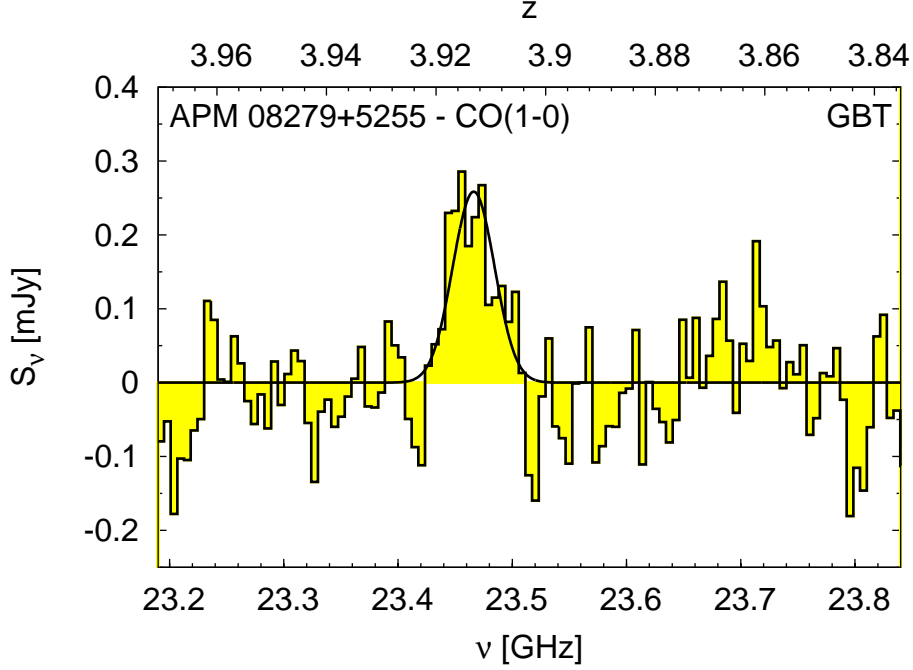


Figure 3.3: GBT spectrum of CO($J=1\rightarrow 0$) emission from APM08279+5255. The spectrum has been smoothed to a resolution of 5.86 MHz (75 km s^{-1}). The rms per channel is $\sim 65 \mu\text{Jy}$. The thin black line shows a Gaussian fit to the data (see Table 3.1).

Table 3.1: Observed CO($J=1\rightarrow 0$) Line Parameters

Source	z	ν_{obs} (GHz)	S_{ν}^a (mJy)	ΔV_{FWHM} (km s^{-1})	I (Jy km s^{-1})	Telescope
BR 1202-0725	4.6932 ± 0.0004	20.2450	0.36 ± 0.03	329 ± 36	0.124 ± 0.012	GBT
	4.6956 ± 0.0012	20.2388	0.40 ± 0.11	522 ± 146	0.22 ± 0.06	Effelsberg
	4.6949 ± 0.0003	20.2411	0.34 ± 0.03	333 ± 30	0.120 ± 0.010	Combined
PSS J2322+1944	4.1173 ± 0.0003	22.5258	0.77 ± 0.07	202 ± 17	0.165 ± 0.014	GBT
	4.1184 ± 0.0008	22.5211	1.29 ± 0.26	184 ± 46	0.25 ± 0.06	Effelsberg
	4.1179 ± 0.0002	22.5231	0.77 ± 0.07	190 ± 14	0.155 ± 0.013	Combined
APM 08279+5255	3.9122 ± 0.0007	23.4663	0.26 ± 0.04	556 ± 55	0.152 ± 0.020	GBT

Notes—All given uncertainties are formal (correlated) errors from the Gaussian fit. The z error was derived from a full three-parameter fit. In the error estimates for S_{ν} and ΔV_{FWHM} , the correlation with the error in z is neglected, as the relative uncertainty in z is ~ 3 orders of magnitude less than that of the other two quantities. The error estimate for I takes the correlation of the errors of S_{ν} and ΔV_{FWHM} into account.

^aA $T_{\text{A}}^*(\text{K})/S(\text{Jy})$ conversion factor of 1.5 was assumed for the GBT.

1999; Carilli et al. 2002b). This double morphology may indicate a pair of interacting objects separated by only 28 kpc (Yun et al. 2000; Carilli et al. 2002b). An alternative explanation would be a double-starburst system composed of a QSO (southern source) and a dust-obscured, Ly α -emitting companion (northern source; Hu et al. 1996), which is ionized by the strong QSO. Recently, Klamer et al. (2004) suggested that the nature of the double source might be due to jet-induced star formation, in which the northern component corresponds to a radio hot spot. It has been discussed that the quasar activity in this system may be triggered by gravitational interaction with the companion. Using typical conversion factors for a ULIRG (Downes & Solomon 1998), the total molecular gas mass derived from the CO luminosity exceeds the dynamical mass of the system (Carilli et al. 2002b), and as a remedy for this inconsistency, gravitational lensing has been suggested. However, the same authors argue that masses and velocity widths of the components are very different; therefore, it appears unlikely that the multiple components are different lensed images of one source.

New Observations

The final CO($J=1 \rightarrow 0$) spectra of BR 1202–0725 are shown in Figure 3.1 (*top*, GBT; *middle*, Effelsberg; *bottom*, combined spectrum). Gaussian fitting to the line profile of the combined spectrum results in a peak flux density of 0.34 ± 0.03 mJy and a FWHM of 333 ± 30 km s $^{-1}$. The integrated CO($J=1 \rightarrow 0$) line flux is 0.120 ± 0.010 Jy km s $^{-1}$. This agrees well with the extrapolated value of 0.123 ± 0.013 Jy km s $^{-1}$ derived from the CO($J=2 \rightarrow 1$) flux (Carilli et al. 2002b) under assumption of fully thermalized and optically thick CO emission (see also discussion in Sect. 4.1). The width of the CO($J=1 \rightarrow 0$) line is consistent within the error bars with an average of the higher J transitions in the literature (~ 290 km s $^{-1}$; see Table 3.3). The derived redshift of 4.6949 ± 0.0003 is in good agreement with the CO($J=5 \rightarrow 4$) redshift (Omont et al. 1996; northern and southern components combined). The structure of this source is unresolved at the resolution of our measurements; all line parameters are in good agreement with the higher J lines adding up both components. The derived CO line luminosity of 1.0×10^{11} K km s $^{-1}$ pc 2 results in an H $_2$ gas mass of 8.1×10^{10} M $_{\odot}$ (see also Table 3.2).

3.5.2 PSS J2322+1944

Previous Results

The $z = 4.12$ QSO PSS J2322+1944 is an IR-luminous high-redshift source (see Table 3.2) that is known to exhibit strong CO line emission in multiple transitions (see Table 3.3). Optical imaging and spectroscopy reveal a double-source structure, and the two components are separated by about $1.5''$. The spectra of both peaks are essentially identical, consistent with strong gravitational lensing (optical magnification factor $\mu_L^{\text{opt}} = 3.5$) by an intervening foreground galaxy (Carilli et al. 2003). In high-resolution VLA images, Carilli et al. (2003) find a molecular Einstein ring with a diameter of $1.5''$ in CO($J=2 \rightarrow 1$)

Table 3.2: Luminosities, Gas Masses and Star Formation Rates

Source	D_L (Gpc)	μ_L^{CO}	L_{FIR}^a ($10^{12} L_\odot$)	$L'_{\text{CO}(1-0)}^a$ ($10^{10} \text{ K km s}^{-1} \text{ pc}^2$)	$L_{\text{FIR}}/L'_{\text{CO}(1-0)}$ ($L_\odot/\text{K km s}^{-1} \text{ pc}^2$)	$M_{\text{gas}}(\text{H}_2)^b$ ($10^{10} M_\odot$)	SFR ^c ($10^3 M_\odot \text{ yr}^{-1}$)
BR 1202-072	44.2	1 ^d	60 ^e /60	10.1/10.1	596	8.1	9.0
PSS J2322+1944	37.8	2.5 ^f	23 ^g /9.2	10.5/4.2	219	3.4	1.4
APM 08279+5255	35.6	7 ^h	200 ⁱ /28.6	9.6/1.4	2090	1.1	4.3

^a Apparent luminosities (not corrected for lensing)/intrinsic luminosities (lensing corrected).

^b Assuming a conversion factor of $\alpha = 0.8 M_\odot (\text{K km s}^{-1} \text{ pc}^2)^{-1}$ from $L'_{\text{CO}(1-0)}$ to $M_{\text{gas}}(\text{H}_2)$ as appropriate for ULIRGs (see Downes & Solomon 1998).

^c Assuming a Schmidt-Kennicutt law (Kennicutt 1998a, 1998b): $SFR(M_\odot \text{ yr}^{-1}) = 1.5 \times 10^{-10} L_{\text{FIR}}(L_\odot)$, i.e., $\delta_{\text{MF}} \delta_{\text{SB}} = 1.5$ following the notation of Omont et al. (2001), where δ_{MF} describes the dependence on the mass function of the stellar population and δ_{SB} gives the fraction of L_{FIR} that is actually powered by the starburst and not the AGN.

^d Carilli et al. (2002b).

^e Carilli et al. (2005).

^f Carilli et al. (2003).

^g Cox et al. (2002).

^h Lewis et al. (2002a).

ⁱ Beelen et al. (2006).

line emission, which can be modeled as a circumnuclear star-forming disk with a radius of 2.2 kpc (CO magnification factor $\mu_L^{\text{CO}} \sim 2.5$). The derived intrinsic star formation rate (SFR) is of the order of $900 M_\odot \text{ yr}^{-1}$. PSS J2322+1944 exhibits strong, nonthermal (synchrotron) radio continuum emission at 1.4 GHz, and the rest-frame radio-to-IR spectral energy distribution (SED) resembles that of local nuclear starburst galaxies such as M82 (Cox et al. 2002). This QSO is the fourth high- z CO emitter to be detected in [C I] emission (Pety et al. 2004), providing additional evidence for the presence of active star formation in the host galaxy.

New Observations

The final CO($J=1 \rightarrow 0$) spectra of PSS J2322+1944 are shown in Figure 3.2 (*top*, GBT; *middle*, Effelsberg; *bottom*, combined spectrum). From Gaussian fitting to the combined spectrum, the peak line flux density is found to be $0.77 \pm 0.07 \text{ mJy}$, the line FWHM is $190 \pm 14 \text{ km s}^{-1}$, and the integrated line flux is $0.155 \pm 0.013 \text{ Jy km s}^{-1}$. These values are in good agreement with the CO($J=1 \rightarrow 0$) detection of Carilli et al. (2002a; $S_\nu = 0.89 \pm 0.22 \text{ mJy}$, $\Delta V_{\text{FWHM}} = 200 \pm 70 \text{ km s}^{-1}$, $I = 0.19 \pm 0.08 \text{ Jy km s}^{-1}$), although results for the higher J CO transitions indicate a larger linewidth ($\Delta V_{\text{FWHM}} > 250 \text{ km s}^{-1}$; see Table 3.3). The Gaussian fit gives a redshift of 4.1179 ± 0.0002 . The derived lensing-corrected CO line luminosity of $4.2 \times 10^{10} \text{ K km s}^{-1} \text{ pc}^2$ results in an H_2 gas mass of $3.4 \times 10^{10} M_\odot$ (see also Table 3.2).

Table 3.3: CO Detections in the Quasar Hosts of Our Targets in the Literature

Source	Component	z	Transition	S_ν (mJy)	I (Jy km s ⁻¹)	ΔV_{FWHM} (km s ⁻¹)	References
BR 1202-0725	N	4.692	2-1	0.44 ± 0.07	0.26 ± 0.05		1
	S	4.695	2-1	0.77 ± 0.10	0.23 ± 0.04		1
	NS		4-3	~ 5.1	1.50 ± 0.3	280 ± 30	2
	N	4.6916	5-4	~ 3.5	1.3 ± 0.2	350	2
	S	4.6947	5-4	~ 5.5	1.1 ± 0.3	190	2
	NS	4.695	5-4	9.3 ± 2.1	2.7 ± 0.41	220 ± 74	3
	NS	4.6915	7-6	~ 10.6	3.1 ± 0.86	~ 275	2
PSS J2322+1944		4.1192	1-0	0.89 ± 0.22	0.19 ± 0.08	200 ± 70	4
		4.1192	2-1	2.70 ± 0.24	0.92 ± 0.30	280 ± 42	4,5
		4.1199	4-3	10.5	4.21 ± 0.40	375 ± 41	6
		4.1199	5-4	12	3.74 ± 0.56	273 ± 50	6
			6-5				7
APM 08279+5255		3.9	1-0		0.150 ± 0.045^a	575	8
			1-0		0.22 ± 0.05	575	9
			1-0				10
		3.9	2-1		$\sim 0.81^b$		8
		3.9114	4-3	7.4 ± 1.0	3.7 ± 0.5	480 ± 35	11
		3.9115	4-3	7.3 ± 1.9	3.7 ± 0.4	500 ± 17^c	12
		3.9118	4-3	7.5 ± 0.56	3.8 ± 0.4		12
		3.9113	6-5	14.3 ± 3.1	7.3 ± 0.7	500 ± 17^c	12
		3.9109	9-8	17.9 ± 1.4	9.1 ± 0.8		11
		3.9111	9-8	21.9 ± 4.9	11.1 ± 2.2	500 ± 17^c	12
		3.9119	9-8	24.2 ± 1.3	12.5 ± 2.4		12
		3.9101	10-9	23.3 ± 4.0	11.9 ± 2.4	500 ± 17^c	12
	3.9110	11-10	20.5 ± 4.1	10.4 ± 2.1	500 ± 17^c	12	

Notes—For BR 1202-0725, N and S indicate the northern and southern components, respectively, and NS indicates an integrated measurement over both components.

^aApparent luminosities (not corrected for lensing)/intrinsic luminosities (lensing corrected).

^bAssuming a velocity-averaged brightness temperature ratio between CO($J=2 \rightarrow 1$) and CO($J=1 \rightarrow 0$) of 1.35 ± 0.55 (Papadopoulos et al. 2001).

^cDerived from a line profile averaged over all transitions.

References—(1) Carilli et al. 2002b; (2) Omont et al. 1996; (3) Ohta et al. 1996; (4) Carilli et al. 2002a; (5) Carilli et al. 2003; (6) Cox et al. 2002; (7) A. Weiß et al. 2006, in prep.; (8) Papadopoulos et al. 2001; (9) Lewis et al. 2002a; (10) D. Riechers et al. 2006, in prep.; (11) Downes et al. 1999; (12) Weiß et al. 2007.

3.5.3 APM 08279+5255

Previous Results

APM 08279+5255 is a strongly lensed, radio-quiet broad absorption line (BAL) QSO at $z = 3.91$. Gravitational lens models of the QSO continuum source suggest magnification by a factor of $\mu_L^{\text{opt}} \sim 100$, and the image breaks up into three components with a maximum separation of $0.4''$ (Ledoux et al. 1998; Ibata et al. 1999; Egami et al. 2000). APM 08279+5255 has been detected in the millimeter and submillimeter dust continuum, revealing an apparent bolometric luminosity of $\sim 5 \times 10^{15} L_\odot$ (Lewis et al. 1998). A multitransition CO study (see Table 3.3) in combination with detailed lens models appears to reveal a spatially extended structure on a scale of at least 400 pc (Lewis et al. 2002a), which is gravitationally magnified by a factor of $\mu_L^{\text{CO}} = 7$. The strength of the CO($J=9 \rightarrow 8$) emission indicates the presence of hot dense gas with a kinetic temperature of approximately 200 K (Downes et al. 1999).

From VLA imaging of the CO ground-state transition at a linear resolution of $2.25''$, Papadopoulos et al. (2001) report the detection of an extended, low-excitation molecular gas reservoir around the compact nucleus that extends over a scale of $7''$ (~ 30 kpc). The integrated brightness temperature of this extended domain appears to be of the same order of magnitude as that of the nuclear region. This extended reservoir would be well within our $32''$ GBT beam. Papadopoulos et al. (2001) do not derive the total flux in the extended reservoir. For the central $\sim 1''$ (corresponding to ~ 7.2 kpc at the source redshift), which they call “the nuclear CO($J=1 \rightarrow 0$) emission,” they find an integrated flux of $0.150 \pm 0.045 \text{ Jy km s}^{-1}$. The VLA bandpass used by Papadopoulos et al. (2001) has an effective bandwidth of ~ 45 MHz, or $\sim 575 \text{ km s}^{-1}$ at the CO($J=1 \rightarrow 0$) line frequency. Therefore, assuming that the peak in their Figure 1c is $6.5\sigma = 260 \mu\text{Jy beam}^{-1}$ ($\sigma = 40 \mu\text{Jy beam}^{-1}$), we consistently derive an integrated flux over the peak of $0.15 \text{ Jy km s}^{-1} \text{ beam}^{-1}$. However, Papadopoulos et al. (2001) suggest that this peak of “nuclear emission” sits on a broad, extended plateau (see their Figure 1c). If we assume that the extended reservoir component is traced by their 2σ ($80 \mu\text{Jy beam}^{-1}$) contour, it has a width of $\sim 8'' \times 3''$, or ~ 4.7 beam areas at the given resolution of $2.25'' \times 2.25''$. This corresponds to a flux of $0.22 \text{ Jy km s}^{-1}$ for the extended emission. The same estimate for their 3σ ($120 \mu\text{Jy beam}^{-1}$) contour gives a width of $\sim 7'' \times 2.25''$, or ~ 3.1 beam areas. This again corresponds to a flux of $0.22 \text{ Jy km s}^{-1}$ (note that both these estimates are lower limits for the extended emission). The total flux in the CO($J=1 \rightarrow 0$) map of Papadopoulos et al. (2001) is therefore estimated to be $\gtrsim 0.37 \text{ Jy km s}^{-1}$. The same authors also suggest that this reservoir breaks up into multiple components at higher resolution; in their CO($J=2 \rightarrow 1$) observations at $0.5''$ resolution, they claim to find two emitting regions $2\text{--}3''$ distant from the central region; if real, these could be companion galaxies that are not individually resolved in the extended CO($J=1 \rightarrow 0$) reservoir.

New Observations

The final CO($J=1 \rightarrow 0$) spectrum of APM08279+5255 is shown in Figure 3.3. We derive a CO($J=1 \rightarrow 0$) peak flux of 0.26 ± 0.04 mJy and a FWHM of 556 ± 55 km s⁻¹ from our Gaussian fit. This results in an integrated line flux of 0.152 ± 0.020 Jy km s⁻¹, which is in good agreement with the value of 0.150 ± 0.045 Jy km s⁻¹ found by Papadopoulos et al. (2001) for the central $\sim 1''$ [“the nuclear CO($J=1 \rightarrow 0$) emission”]. However, our result is inconsistent with the integrated flux of 0.37 Jy km s⁻¹ given by our estimate of their full CO($J=1 \rightarrow 0$) reservoir (see previous subsection). Such a high flux is clearly ruled out by our GBT observations. We thus find no evidence for a luminous extended halo, which would be well within our $32''$ beam, and cannot confirm the existence of bright companion galaxies. The derived FWHM velocity width of our CO($J=1 \rightarrow 0$) detection is in agreement with single-dish observations of the CO($J=6 \rightarrow 5$), CO($J=10 \rightarrow 9$), and CO($J=11 \rightarrow 10$) transitions obtained with the IRAM 30 m telescope (~ 500 km s⁻¹; Weiß et al. 2007) and IRAM Plateau de Bure interferometer observations of the CO($J=4 \rightarrow 3$) transition (480 ± 35 km s⁻¹; Downes et al. 1999; see Table 3.3). Our derived CO($J=1 \rightarrow 0$) redshift of 3.9122 ± 0.0007 is in good agreement with previous results (3.9114 ± 0.0003 for the $4 \rightarrow 3$ transition). The derived lensing-corrected CO line luminosity of 1.4×10^{10} K km s⁻¹ pc² results in an H₂ gas mass of $1.1 \times 10^{10} M_{\odot}$ (see also Table 3.2).

3.6 Analysis and Discussion

3.6.1 Large Velocity Gradient Modeling

To investigate how much of the CO($J=1 \rightarrow 0$) emission in our target QSOs is associated with the molecular gas reservoirs detected in the higher J CO transitions, we have used spherical, one-component large velocity gradient (LVG) models. All these LVG calculations use the collision rates from Flower (2001) with an ortho/para H₂ ratio of 3 and a CO abundance per velocity gradient of $[\text{CO}]/(dv/dr) = 1 \times 10^{-5}$ pc (km s⁻¹)⁻¹ (e.g. Weiß et al. 2005c). Models were fitted to those lines *above* the CO($J=1 \rightarrow 0$) transition listed in Table 3.3 for each source. The turnover of the CO line SED (and therefore the slope beyond the turnover) is not well determined. Thus, a large degeneracy exists between the kinetic gas temperature T_{kin} and density $\rho_{\text{gas}}(\text{H}_2)$, the two main free parameters in our study. As an example, Figure 3.4 shows data of all transitions and three representative models for BR 1202–0725: Model 1 (*solid line*) assumes $T_{\text{kin}} = 60$ K and $\rho_{\text{gas}}(\text{H}_2) = 10^{4.1}$ cm⁻³ and gives the overall best fit to all transitions. Models 2 (*dashed line*) and 3 (*dotted line*) are shown as a representation of the parameter space allowed by the data within the error bars. Model 2 assumes $T_{\text{kin}} = 120$ K and $\rho_{\text{gas}}(\text{H}_2) = 10^{3.7}$ cm⁻³, while model 3 assumes $T_{\text{kin}} = 30$ K and $\rho_{\text{gas}}(\text{H}_2) = 10^{4.6}$ cm⁻³. The LVG predicted CO($J=1 \rightarrow 0$) flux of the different models based on the $J > 1$ CO transitions is fairly well constrained by the solutions. Most of our calculated models suggest that the CO emission is close to thermalized up to the CO($J=4 \rightarrow 3$) transition and optically thick ($\tau \gtrsim 5$), which implies that the LVG predicted CO($J=1 \rightarrow 0$) line fluxes are similar to those we would derive by assuming a ν^2 scaling

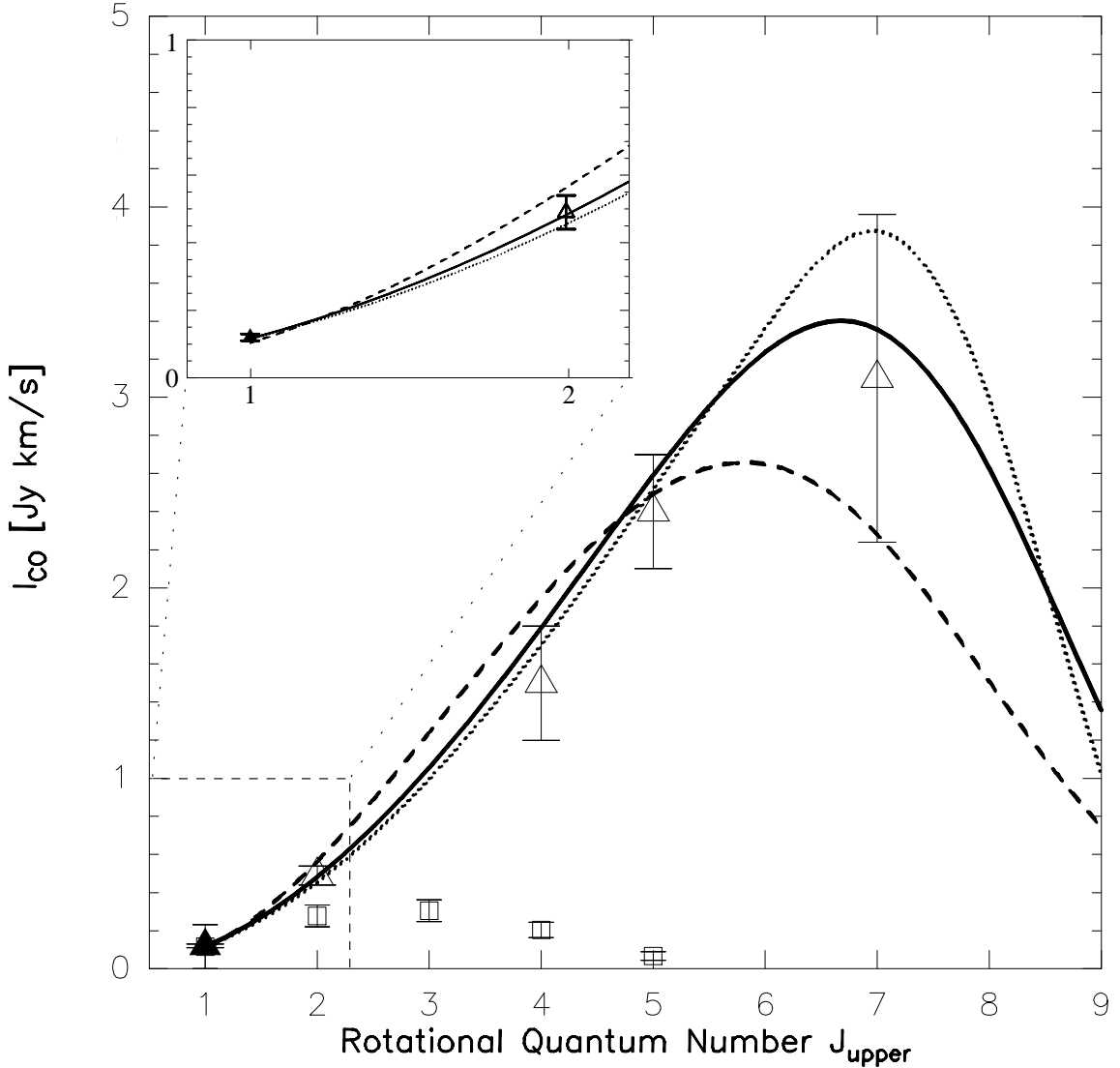


Figure 3.4: CO ladder and LVG models (based on all $J > 1$ transitions) for BR 1202–0725. The inset shows a zoomed-in version of the $J = 2, 1$ region (as indicated by the dashed box). The filled triangle is the CO($J=1 \rightarrow 0$) data point based on the combined spectrum. Data for the higher J CO transitions (*open triangles*) are taken from the literature (see Table 3.3). For comparison, we also show data for the inner disk of the Milky Way (*open squares*; Fixsen et al. 1999), normalized to the CO($J=1 \rightarrow 0$) flux of BR 1202–0725. The kinetic temperature T_{kin} and gas density $\rho_{\text{gas}}(\text{H}_2)$ are treated as free parameters in this study. Three representative models are shown: Model 1 (*solid line*) assumes $T_{\text{kin}} = 60$ K and $\rho_{\text{gas}}(\text{H}_2) = 10^{4.1} \text{ cm}^{-3}$ and gives the overall best fit to all transitions. Model 2 (*dashed line*) assumes $T_{\text{kin}} = 120$ K and $\rho_{\text{gas}}(\text{H}_2) = 10^{3.7} \text{ cm}^{-3}$, while model 3 (*dotted line*) assumes $T_{\text{kin}} = 30$ K and $\rho_{\text{gas}}(\text{H}_2) = 10^{4.6} \text{ cm}^{-3}$.

of the line flux densities from the mid- J CO transitions. The predicted LVG integrated flux ranges of the CO($J=1\rightarrow 0$) transition are 0.10–0.12 Jy km s⁻¹ (BR 1202–0725), 0.20–0.23 Jy km s⁻¹ (PSS J2322+1944), and 0.13–0.20 Jy km s⁻¹ (APM 08279+5255) and are in good agreement with our observations for all sources. As described in Sect. 3.2.2, the observed CO($J=1\rightarrow 0$) line width in our new observations and in the VLA spectrum (Carilli et al. 2002a) of PSS J2322+1944 is lower than that of the higher J transitions; thus, the integrated model fluxes are a bit higher than our result. If we compare the peak fluxes only, we obtain a good agreement.

Our observations and models are in agreement with the assertion that *all* observed CO($J=1\rightarrow 0$) flux density is associated with the highly excited molecular gas seen in the high- J CO lines. We thus find no evidence for an additional luminous, more extended low surface brightness gas component surrounding the central region of our target QSOs, in contrast to what has been suggested previously for APM 08279+5255 (Papadopoulos et al. 2001). Given the accuracy of our measurements, we conclude that at most 20%–30% of the CO($J=1\rightarrow 0$) luminosity may be associated with such a diffuse component. We note, however, that if the L'_{CO} to $M_{\text{gas}}(\text{H}_2)$ conversion factor (α) for a faint extended component were higher (e.g. Galactic), a higher H₂ mass may be hidden in such an extended component.

3.6.2 Correlations of High- and Low-Redshift Galaxies

CO results for our three high-redshift IR-luminous QSOs are summarized in Tables 3.1 and 3.2. Our sample consists of all three high- z QSOs for which the CO ground-state transition has been detected to date and covers $\sim 20\%$ of the CO-detected $z > 2$ quasars. As discussed above, the CO($J=1\rightarrow 0$) transition provides the best information of the total amount of molecular gas in a system, quantified by $L'_{\text{CO}(1-0)}$. For most QSOs/galaxies detected in CO at high z , CO($J=3\rightarrow 2$) and CO($J=4\rightarrow 3$) are the lowest transitions that have been detected to date. Based on our results in the previous paragraph, however, we can now estimate their $L'_{\text{CO}(1-0)}$ by assuming constant brightness temperature for all transitions from CO($J=1\rightarrow 0$) to CO($J=4\rightarrow 3$) (i.e., L'_{CO} is the same for those transitions). This assumption is also in agreement with observations towards the radio galaxy 4C 60.07 (Greve et al. 2004). However, it is important to note that all high- z sources were selected via higher J CO transitions, which could, in principle, introduce a bias towards highly excited starburst environments.

Following Sanders et al. (1991), Gao & Solomon (2004a) found a nonlinear relation between the logarithms of the FIR luminosity L_{FIR} and the CO($J=1\rightarrow 0$) line luminosity L'_{CO} for a sample of local spiral galaxies, luminous infrared galaxies, and ultraluminous infrared galaxies. Their sample consists mostly of galaxies whose FIR luminosity is powered by star formation only. Our CO($J=1\rightarrow 0$) observations and LVG models suggest that L'_{CO} can be estimated for all CO-detected high- z sources with some degree of confidence, even if only observations of higher J CO transitions exist for most of these sources. To put this result into context, we now aim to discuss the $L'_{\text{CO}}-L_{\text{FIR}}$ relation and its implications for

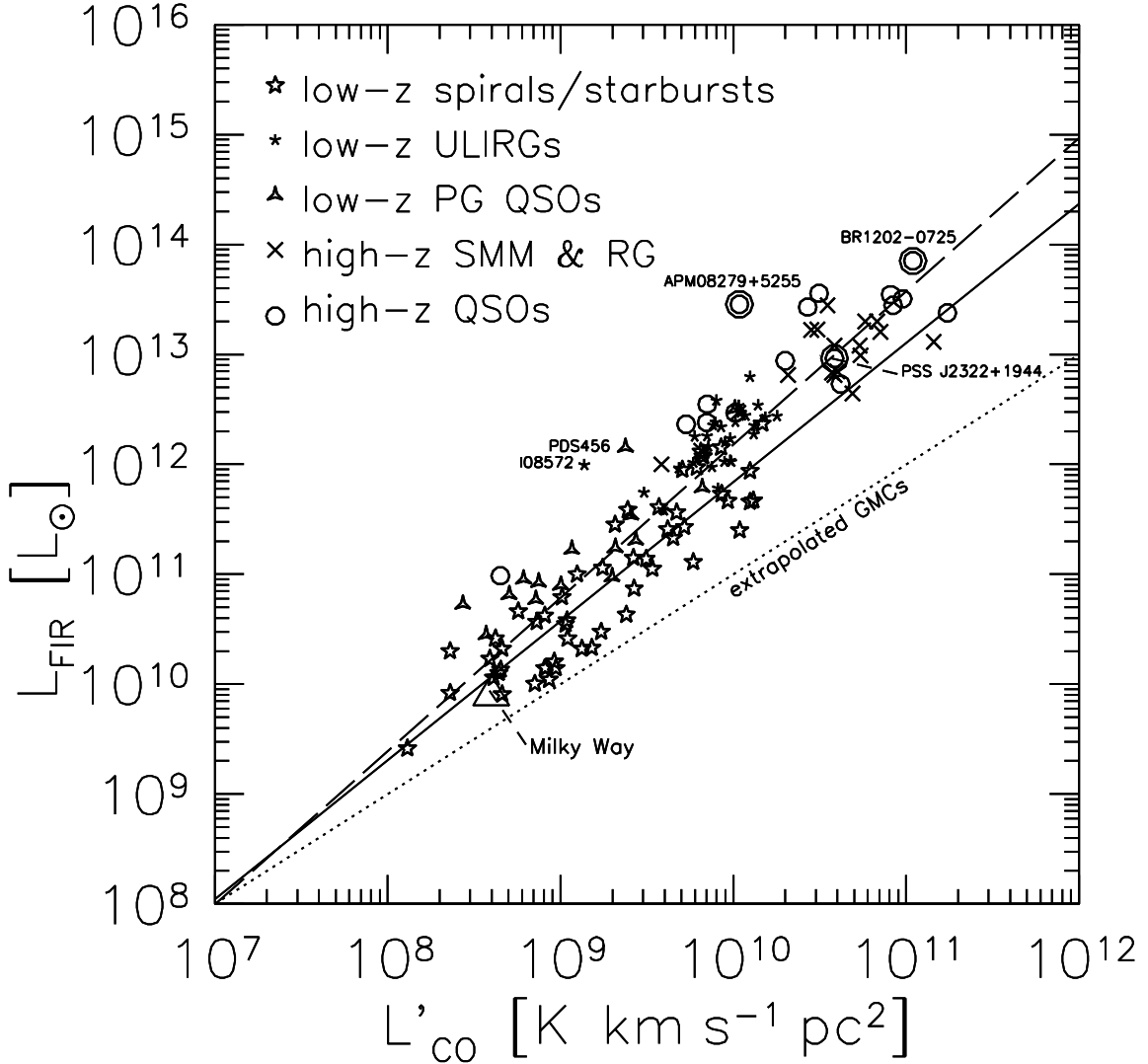


Figure 3.5: Comparison of velocity-integrated CO line luminosity with FIR luminosity for a sample of low- z spiral and starburst galaxies from Gao & Solomon (2004a), the ULIRGs from Solomon et al. (1997), $z < 0.2$ PG QSOs from Alloin et al. (1992), Evans et al. (2001), and Scoville et al. (2003), extrapolated Galactic molecular clouds (GMCs) from Mooney & Solomon (1988), the Milky Way (Fixsen et al. 1999), and high- z submillimeter galaxies, radio galaxies, and QSOs from the literature (see Solomon & Vanden Bout 2005) with respect to our new results. All FIR luminosities are rederived as described in Carilli et al. (2005). All data are corrected for gravitational lensing. The solid line is a straight-line least-squares fit to the Gao & Solomon (2004a) sample, corresponding to $\log(L_{\text{FIR}}) = (1.26 \pm 0.08) \log(L_{\text{CO}}) - 0.81$. The dotted line shows the fit to the GMCs from Mooney & Solomon (1988), corresponding to a power-law index of 0.96 ± 0.08 . The dashed line is a fit to all high- z sources, the Gao & Solomon (2004a) data, the Solomon et al. (1997) ULIRGs, and the PG QSOs, corresponding to $\log(L_{\text{FIR}}) = (1.39 \pm 0.05) \log(L_{\text{CO}}) - 1.76$.

some selected samples of galaxies at low and high redshift.

Figure 3.5 shows the relationship between $\log(L_{\text{FIR}})$ and $\log(L'_{\text{CO}})$ for our three targets, all other high- z CO detections (except TN J0924–2201, which does not have a measured FIR luminosity), the $z < 0.2$ Palomar-Green (PG) QSOs from Alloin et al. (1992), Evans et al. (2001), and Scoville et al. (2003) including PDS 456 (Yun et al. 2004), local ($z < 0.3$) ULIRGs from Solomon et al. (1997), and the local galaxy sample ($z < 0.1$) of Gao & Solomon (2004a). All FIR luminosities for the high- z sources are rederived as described by Carilli et al. (2005) unless stated otherwise. Lensing magnification factors were taken into account. In addition, data for the Milky Way disk (Fixsen et al. 1999) and an (extrapolated) relation for Galactic molecular clouds (Mooney & Solomon 1988) are given for comparison. The solid line is a straight-line least-squares fit to the Gao & Solomon (2004a) sample, corresponding to $\log(L_{\text{FIR}}) = (1.26 \pm 0.08) \log(L_{\text{CO}}) - 0.81$ (the power-law index is 1.25 ± 0.08 in the original publication). Fitting the high- z sources, the Gao & Solomon (2004a) data, the Solomon et al. (1997) ULIRGs, and the PG QSOs together, we find the relation $\log(L_{\text{FIR}}) = (1.39 \pm 0.05) \log(L_{\text{CO}}) - 1.76$. Both relations are clearly nonlinear, as their power-law indexes are significantly larger than unity (see also the corresponding discussion in Gao & Solomon 2004a). We recover a Schmidt-Kennicutt law (power-law index of 1.4; Kennicutt 1998a, 1998b) for the larger, more heterogeneous sample. More importantly, the high- z sources seem to follow the same slope (within the errors) as seen at low z , even though most high- z sources harbor central active galactic nuclei (AGNs). In addition, the high- z QSOs and high- z submillimeter (likely lacking a luminous AGN) and radio galaxies statistically occupy the same area in the plot. The same behaviour is found for the PG QSOs in comparison to the low- z spiral galaxies, LIRGs, and ULIRGs. It is in general not clear that the FIR emission comes mostly from star formation, i.e. that it is not strongly biased by active nuclei or the interstellar radiation field. For example, SED modeling of the $z = 2.6$ quasar H1413+117 (the Cloverleaf) reveals that only $\sim 20\%$ of its FIR luminosity is powered by star formation (Solomon et al. 2003), but it is not an outlier in the $L'_{\text{CO}}-L_{\text{FIR}}$ diagram. In this context, the elevated $L_{\text{FIR}}/L'_{\text{CO}}$ ratio in APM08279+5255 may be explained by a combination of differential lensing and a relatively high contribution of the AGN to L_{FIR} (see Rowan-Robinson 2000 for models of the IR SED). Outliers such as APM08279+5255 are also found at low z (e.g. the QSO PDS 456 and the warm ULIRG IRAS 08572+3915; see Fig. 3.5). As the relative number of such outliers is very small, this may also be explained by a brief FIR-bright AGN phase (Yun et al. 2004). However, it is likely that the dominant energy source in most ULIRGs is an extreme starburst rather than heating by a dust-enshrouded AGN (e.g., Solomon et al. 1997; Downes & Solomon 1998). This picture is supported by the finding that ULIRGs harbor large quantities of *dense* molecular gas, which is more intimately involved with star formation than the major fraction of the mostly diffuse CO (Gao & Solomon 2004a). It has to be kept in mind that the high- z sources are highly selected and probably fulfill the Malmquist bias (i.e., the apparent increase in the average L'_{CO} and L_{FIR} towards high redshift is probably a consequence of the flux limitation in the sample, e.g. Sandage 1994). As an additional consequence of flux limitation in the sample, lensing influences the results (i.e., stronger lensing magnification allows us to probe deeper, and therefore the intrinsic CO luminosity

drops).

We can also set an approximate lower limit on the duration of the intense starburst phase. Considering the total H_2 masses and star formation rates in Table 3.2, the depletion timescale of the molecular gas is of the order of 10^7 yr for all three QSOs under the assumption of a constant SFR and 100% star-forming efficiency. This implies that the starburst itself can be relatively short-lived (and compact, as the dynamical time must be less than the starburst lifetime), unless the molecular gas in which the star formation occurs can be resupplied on timescales of $\sim 10^7$ yr.

3.7 Summary

We have detected $\text{CO}(J=1\rightarrow 0)$ emission in three QSOs at redshifts $3.9 < z < 4.7$ with the NRAO GBT and the MPIfR Effelsberg telescope. From our analysis of the resulting spectra of BR 1202–0725, PSS 2322+1944, and APM 08279+5255, we obtain the following results:

1. We derived lensing-corrected $\text{CO}(J=1\rightarrow 0)$ line luminosities of $1.0 \times 10^{11} \text{ K km s}^{-1} \text{ pc}^2$ for BR 1202–0725, $4.2 \times 10^{10} \text{ K km s}^{-1} \text{ pc}^2$ for PSS 2322+1944, and $1.4 \times 10^{10} \text{ K km s}^{-1} \text{ pc}^2$ for APM 08279+5255. These results are in good agreement (within a factor of 2) with previous estimates of the total CO luminosities based on the higher J CO transitions, consistently providing very large $M_{\text{gas}}(\text{H}_2)$ of $> 10^{10} M_{\odot}$.

2. $\text{CO}(J=1\rightarrow 0)$ fluxes predicted by one-component LVG models are in good agreement with our observations. Considering our modeling results, the CO emission appears to be close to thermalized up to the $4\rightarrow 3$ transition in all cases. Thus, our observations show no indication of a luminous extended, low surface brightness molecular gas component in any of the high-redshift QSOs in our sample (cf. Papadopoulos et al. 2001). In fact, all CO transitions are described very well by a single gas component in which all molecular gas is concentrated in a compact circumnuclear region. If such extended components were to exist, our observations and models would limit their contribution to the overall luminosity to at most 20–30%.

3. There appears to be a correlation between $\log(L_{\text{FIR}})$ and $\log(L'_{\text{CO}})$ for low-redshift galaxies including (U)LIRGs over orders of magnitude in L_{FIR} , and the significantly brighter sources found at high z appear to follow the same general trend (see also Solomon & Vanden Bout 2005). In particular, we find that the correlation shows no significant difference between QSOs and systems without a luminous AGN.

The observations presented herein demonstrate the feasibility of detecting high- z CO with 100 m single-dish radio telescopes and highlight the physical implications of observing the ground-state transition of this molecule towards massive galaxies at redshifts greater than 4.

It is a pleasure to thank my collaborators on this project:

Fabian Walter (MPIA), Chris Carilli (NRAO), Kirsten K. Knudsen (MPIA), Fred Lo

(NRAO), Dominic Benford and Johannes Staguhn (NASA Goddard), Todd Hunter (CfA), Frank Bertoldi (AIfA), Christian Henkel, Karl Menten and Axel Weiß (MPIfR), Min Yun (UMASS), and Nick Scoville (Caltech).

CHAPTER PUBLISHED AS:

Riechers, D. A., Walter, F., Carilli, C. L., Knudsen, K. K., Lo, K. Y., Benford, D. J., Staguhn, J. G., Hunter, T. R., Bertoldi, F., Henkel, C., Menten, K. M., Weiß, A., Yun, M. S., & Scoville, N. Z., ‘*CO(1–0) in $z \gtrsim 4$ Quasar Host Galaxies: No Evidence for Extended Molecular Gas Reservoirs*’, 2006, ApJ, 650, 604

Chapter 4

Dense Molecular Gas I: Search for HCN at $z=6.42$

4.1 Context

In the previous chapters, it was shown that the total molecular gas mass and the star formation rate as traced by L'_{CO} and L_{FIR} are two of the main diagnostics in studies of galaxy properties, formation and evolution. Clearly, these properties correlate. Interestingly, the relation between both properties appears to define a global law, which does not change with galaxy type, luminosity, or redshift. However, the relation is also clearly non-linear and shows considerable scatter, which implies that both properties do not trace the same physical regions. This is not a surprise, as we have seen that star formation only takes place in the dense cores within the molecular ISM, whereas the more diffuse regions (that are also traced by L'_{CO}) just play a passive role. One may thus expect that, if only the dense fraction of the molecular gas in a galaxy is considered, the relation should show less scatter and be more linear. The main tracer of dense gas in nearby galaxies is HCN. After CO, HCN thus is the second most commonly observed molecule in the nearby universe. However, the first systematic survey of HCN in the nearby universe was carried out only recently by Gao & Solomon (2004a, 2004b), and encompasses 65 galaxies (the most comprehensive sample to date). Their survey was extended down to individual Galactic GMCs by Wu et al. (2005). These observations indeed show that L'_{HCN} correlates with L_{FIR} in a linear fashion, indicating that dense molecular gas is indeed a good tracer for star formation. This is why the $L'_{\text{HCN}}-L_{\text{FIR}}$ correlation has recently also become a subject of study at high redshift, where the huge star formation rates of several $1000 M_{\odot} \text{ yr}^{-1}$ derived from FIR observations have led to discussions concerning the reliability of L_{FIR} as a star formation tracer. This discussion is in part driven by the fact that many of the high- z FIR-detected galaxies host an AGN, which may power (at least in part) the FIR luminosity, leading to an overestimate of the SFR. Due to the fact that molecules get dissociated close to an AGN, L'_{HCN} is believed to not have such a bias. Due to the fact that HCN emission is typically by an order of magnitude fainter than CO emission (which

is already difficult to detect at high z), only few redshifted galaxies were detected in HCN emission to date. A recent study by Gao et al. (2007) summarizes the results obtained so far, and shows that, indeed, the high redshift galaxies are systematically offset from the local $L'_{\text{HCN}}-L_{\text{FIR}}$ relation towards higher L_{FIR} . The results presented here provide further evidence for decreasing L'_{HCN} as a function of L_{FIR} for large luminosities.

4.2 Abstract

We report a sensitive search for the HCN($J=2\rightarrow 1$) emission line towards SDSS J114816.64+525150.3 (hereafter: J1148+5251) at $z=6.42$ with the Very Large Array (VLA). HCN emission is a star formation indicator, tracing dense molecular hydrogen gas ($n(\text{H}_2) \geq 10^4 \text{ cm}^{-3}$) within star-forming molecular clouds. No emission was detected in the deep interferometer maps of J1148+5251. We derive a limit for the HCN line luminosity of $L'_{\text{HCN}} < 3.3 \times 10^9 \text{ K km s}^{-1} \text{ pc}^2$, corresponding to a HCN/CO luminosity ratio of $L'_{\text{HCN}}/L'_{\text{CO}} < 0.13$. This limit is consistent with a fraction of dense molecular gas in J1148+5251 within the range of nearby ULIRGs (median value: $L'_{\text{HCN}}/L'_{\text{CO}} = 0.17^{+0.05}_{-0.08}$) and HCN-detected $z > 2$ galaxies ($0.17^{+0.09}_{-0.08}$). Due to their linear correlation in the nearby universe, the relationship between L'_{HCN} and L_{FIR} is considered a sensitive probe for the conditions of star formation. In J1148+5251, we find $L_{\text{FIR}}/L'_{\text{HCN}} > 6600$. This is significantly higher than the average ratios for normal nearby spiral galaxies ($L_{\text{FIR}}/L'_{\text{HCN}} = 580^{+510}_{-270}$) and ULIRGs (740^{+505}_{-50}), confirming a trend seen for other $z > 2$ galaxies (predominantly quasars; 1525^{+1300}_{-475}). This trend is not easily explained with a large contribution of AGN heating to L_{FIR} alone, and may hint at an elevated star-formation efficiency toward the more luminous high-redshift systems. There is marginal evidence that the $L_{\text{FIR}}/L'_{\text{HCN}}$ ratio in J1148+5251 may exceed the trend set by other $z > 2$ galaxies; however, only future facilities with large collecting areas such as the Square Kilometre Array will offer the sensitivity required to further investigate this question.

4.3 Introduction

High redshift galaxy populations are now being detected back to 780 million years after the Big Bang (spectroscopically confirmed: $z=6.96$; Iye et al. 2006), probing into the epoch of cosmic reionization (e.g., Fan et al. 2006; Hu & Cowie 2006). Many of these very distant galaxies show evidence for star formation activity (e.g., Taniguchi et al. 2005). Some are even found to be hyperluminous infrared galaxies (HLIRGs; Bertoldi et al. 2003a; Wang et al. 2007) with far-infrared (FIR) luminosities exceeding $10^{13} L_{\odot}$, suggesting vigorous star formation and/or AGN activity. To probe the earliest stages of galaxy formation and the importance of AGN in this process, it is necessary to study the star formation characteristics of these galaxies.

A good diagnostic to examine the star-forming environments in distant HLIRGs are observations of molecular gas, the fuel for star formation. The by far brightest and most

common indicator of molecular gas in galaxies is line emission from the rotational transitions of carbon monoxide (CO), which was detected in ~ 40 galaxies at high redshift ($z > 1$) (see Solomon & Vanden Bout 2005 for a review). These observations have revealed molecular gas reservoirs with masses of $> 10^{10} M_{\odot}$ in these galaxies, even in the very distant quasar J1148+5251 at $z=6.42$ (Walter et al. 2003, 2004; Bertoldi et al. 2003b).

Although CO is a good tracer of the total amount of molecular gas in a galaxy, due to the relatively low critical density of $n_{\text{H}_2} \sim 10^2 - 10^3 \text{ cm}^{-3}$ required to collisionally excite its lower J transitions, it is not a reliable tracer of the dense molecular cloud cores where the actual star formation takes place. Recent studies of nearby actively star-forming galaxies have shown that hydrogen cyanide (HCN) is a far better tracer of the dense ($n_{\text{H}_2} \sim 10^5 - 10^6 \text{ cm}^{-3}$) molecular gas where stars actually form (e.g. Gao & Solomon 2004a, 2004b, hereafter: GS04ab). In the local universe it was found that the HCN luminosity (L'_{HCN}) scales linearly (unlike L'_{CO}) with the FIR luminosity (L_{FIR}) over 7–8 orders of magnitude, ranging from Galactic dense cores to ultraluminous infrared galaxies (ULIRGs, Wu et al. 2005). As L_{FIR} traces the massive star formation rate (unless AGN heating is significant), this implies that HCN is also a good tracer of star formation.

HCN has now also been detected in five galaxies at $z > 2$ (Solomon et al. 2003; Vanden Bout et al. 2004; Carilli et al. 2005, hereafter: C05; Wagg et al. 2005; Gao et al. 2007, hereafter: G07). Adding a number of upper limits obtained for other high- z galaxies, these observations indicate that the linear $L'_{\text{HCN}}-L_{\text{FIR}}$ correlation found in the local universe is systematically different for the more luminous, higher redshift systems (G07). To further investigate this apparent trend, our aim has been to extend the range of existing HCN observations beyond redshift 6 and to higher L_{FIR} .

In this chapter, we report sensitive VLA¹ observations of HCN($J=2 \rightarrow 1$) emission towards the $z=6.42$ quasar J1148+5251, the highest redshift source detected in CO. A previous, less sensitive search for HCN($J=2 \rightarrow 1$) emission in this source has yielded no detection (C05). We use a concordance, flat Λ CDM cosmology throughout, with $H_0=71 \text{ km s}^{-1} \text{ Mpc}^{-1}$, $\Omega_{\text{M}}=0.27$, and $\Omega_{\Lambda}=0.73$ (Spergel et al. 2003, 2007).

4.4 Observations

We observed the HCN($J=2 \rightarrow 1$) transition line ($\nu_{\text{rest}} = 177.2612230 \text{ GHz}$) towards J1148+5251 using the VLA in D configuration in 10 tracks on 2004 June 21 and 26 (these observations were discussed by C05), and between 2007 May 01 and 13. At the target redshift of 6.419, the line is shifted to 23.892873 GHz (11.96 mm). The total integration time amounts to 80 hr. Observations were performed in fast-switching mode using the nearby source 11534+49311 (at 3.4° distance to J1148+5251) for secondary amplitude and phase calibration. Observations were carried out under very good weather conditions with 26 antennas (including 9 EVLA antennas in 2007): the phase stability was excellent

¹The Very Large Array is a facility of the National Radio Astronomy Observatory, operated by Associated Universities, Inc., under cooperative agreement with the National Science Foundation.

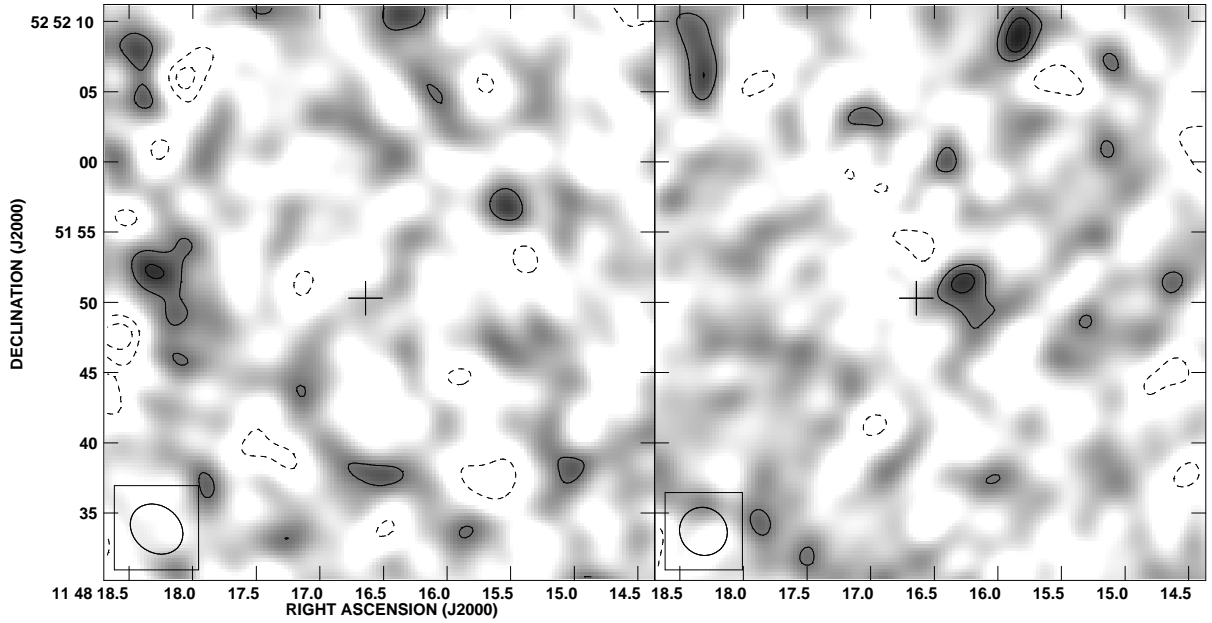


Figure 4.1: VLA observations of HCN($J=2\rightarrow 1$) (*left*) and 23.9 GHz continuum emission (*right*) towards J1148+5251 at a resolution of $4.0''\times 3.3''$ (*left*) and $3.5''\times 3.3''$ (*right*; as indicated in the bottom left corner of both panels). The HCN($J=2\rightarrow 1$) line map is integrated over the full 25 MHz IF. No emission is detected in both maps. The cross indicates the geometrical center of the CO emission. Contours are shown at $(-3, -2, 2, 3)\times\sigma$ ($1\sigma = 15\ \mu\text{Jy beam}^{-1}$ for the line map, and $14\ \mu\text{Jy beam}^{-1}$ for the continuum map).

Table 4.1: Line Luminosities in SDSS J1148+5251

	S_ν	L'	Ref.
	[μJy]	[$10^9 \text{ K km s}^{-1} \text{ pc}^2$]	
HCN($J=2\rightarrow 1$)	(7 ± 15)	<3.3	1
CO($J=1\rightarrow 0$)	<360	<142	2
CO($J=3\rightarrow 2$)	570 ± 57	26.4 ± 2.6	3
CO($J=6\rightarrow 5$)	2450	26.9 ± 2.4	2
CO($J=7\rightarrow 6$)	2140	17.3 ± 2.4	2

Notes—Bracketed number indicates nondetection.

References—(1) This work; (2) Bertoldi et al. 2003b; (3) Walter et al. 2003.

(typically $<15^\circ$ rms for the longest baselines). The QSO 3C286 was observed as a primary flux calibrator. The resulting flux scale is accurate within the standard 15% uncertainty.

In 2004, two 25 MHz wide intermediate frequency bands (IFs) with seven 3.125 MHz channels each were observed simultaneously, one centered at the HCN($J=2\rightarrow 1$) line frequency (23.8929 GHz), and one centered at 24.0430 GHz for continuum monitoring². This leads to an effective bandwidth of 21.875 MHz for both the line and continuum observations, corresponding to 274 km s^{-1} at 23.9 GHz. For lines as broad as CO (279 km s^{-1} FWHM; Bertoldi et al. 2003b), this setup would miss only $\lesssim 15\%$ flux in the line wings. In 2007, observations were carried out in continuum mode, with one 25 MHz wide IF centered at the HCN($J=2\rightarrow 1$) line frequency (23.8929 GHz), and one 50 MHz wide IF centered at 23.7649 GHz to monitor the source’s continuum³.

For data reduction and analysis, the *AIPS* package was used. All data were mapped using the CLEAN algorithm and ‘natural’ weighting; this results in synthesized beams of $4.0'' \times 3.3''$ for the line map and $3.5'' \times 3.3''$ ($\sim 20 \text{ kpc}$ at $z = 6.42$) for the continuum map (see Fig. 4.1). The final rms in the integrated HCN($J=2\rightarrow 1$) line map is $15 \mu\text{Jy beam}^{-1}$, and $14 \mu\text{Jy beam}^{-1}$ in the continuum map. Averaging both uv datasets to a ‘high-sensitivity’ continuum map leads to an rms of $11 \mu\text{Jy beam}^{-1}$.

4.5 Results

No HCN($J=2\rightarrow 1$) emission is detected in J1148+5251 (Fig. 4.1, left). We derive a peak flux density of $(7 \pm 15) \mu\text{Jy beam}^{-1}$ at the source’s CO position (see Table 4.1), setting an upper limit⁴ of $30 \mu\text{Jy}$ to the emission line peak flux. No continuum emission is detected at and/or close to the HCN($J=2\rightarrow 1$) line frequency (Fig. 4.1, right). From the ‘high-sensitivity’ continuum map, we derive a peak flux density of $(11 \pm 11) \mu\text{Jy beam}^{-1}$ at the source’s position, setting an upper limit of $22 \mu\text{Jy}$ to the 23.9 GHz continuum flux density. This is consistent with the model-predicted continuum level of $\lesssim 8 \mu\text{Jy}$ (Beelen et al. 2006).

²In fact, this is the center frequency of the $\text{HCO}^+(J=2\rightarrow 1)$ line, which however was not detected. Neither was the continuum.

³This frequency avoids other potentially bright emission lines near the HCN($J=2\rightarrow 1$) frequency, such as $\text{HCO}^+(J=2\rightarrow 1)$, $\text{HNC}(J=2\rightarrow 1)$, and $\text{C}_2\text{H}(N=2\rightarrow 1)$.

⁴In this chapter, we quote 2σ limits; however, note that all conclusions hold for 3σ limits.

Table 4.2: Luminosity Ratios at High z and Average Values

Source	$L_{\text{FIR}}/L'_{\text{HCN}}$ [L_{\odot}/L_l]	$L'_{\text{HCN}}/L'_{\text{CO}}$	Refs.
SDSS J1148+5251	>6600	<0.13	1,2,3
Cloverleaf	1305±360	0.10±0.02	4,5,6
IRAS F10214+4724	2835±855	0.18±0.05	7,8,9
VCV J1409+5628	2615±860	0.09±0.03	9,10,3
APM 08279+5255 ^a	1000	0.27	11,12,13
SMM J16359+6612	1550±550	0.18±0.04	14,15,16
avg. ‘normal’ spiral (33)	580 ⁺⁵¹⁰ ₋₂₇₀	0.04 ^{+0.01} _{-0.02}	17,14
avg. $z \simeq 0$ LIRG (23)	650 ⁺³⁶⁰ ₋₂₉₀	0.07 ^{+0.02} _{-0.02}	17,14
avg. $z \simeq 0$ ULIRG (9)	740 ⁺⁵⁰⁵ ₋₅₀	0.17 ^{+0.05} _{-0.08}	17,14
avg. $z \simeq 0$ ‘all’ (33+23+9)	680 ⁺⁴⁰⁰ ₋₃₆₀	0.05 ^{+0.05} _{-0.02}	17,14
avg. $z > 2$ galaxy (5)	1525 ⁺¹³⁰⁰ ₋₄₇₅	0.17 ^{+0.09} _{-0.08}	4–16

Notes—Line luminosity unit is $L_l = K \text{ km s}^{-1} \text{ pc}^2$. Bracketed numbers are sample sizes (‘all’ corresponds to the full Gao & Solomon sample). For the averaged samples, median values and 1σ statistical errors of the cumulative distribution are given. Where not quoted in the literature, 25% error are assumed for L_{FIR} .

^aWe adopt the extrapolated HCN($J=1 \rightarrow 0$) luminosity from Weiß et al. (2007), derived by assuming collisional excitation only (uncertainties are model-dominated). Also, we only consider the ‘cold, dense’ gas and dust component in their model, which is assumed to give rise to the HCN emission.

References—(1) This work; (2) Walter et al. 2003; (3) Beelen et al. 2006; (4) Solomon et al. 2003; (5) Weiß et al. 2003; (6) Riechers et al. 2006b; (7) Vanden Bout et al. 2004; (8) D. Downes & P. M. Solomon, in prep.; (9) Carilli et al. 2005; (10) Beelen et al. 2004; (11) Wagg et al. 2005; (12) Riechers et al. 2006a; (13) Weiß et al. 2007; (14) Gao et al. 2007; (15) Kneib et al. 2005; (16) Kneib et al. 2004; (17) Gao & Solomon 2004a.

From our observations, we derive a limit to the HCN($J=2 \rightarrow 1$) line luminosity of $L'_{\text{HCN}} < 3.3 \times 10^9 \text{ K km s}^{-1} \text{ pc}^2$ (assuming a HCN/CO linewidth ratio of 0.67, i.e., the average value for the four $z > 2$ HCN-detected quasars⁵; see Table 4.2 for references), corresponding to 13% of the CO luminosity (Walter et al. 2003). Using the FIR luminosity derived by Beelen et al. (2006)⁶, we find $L_{\text{FIR}}/L'_{\text{HCN}} > 6600$.

4.6 Analysis

4.6.1 ‘Dense Gas Fraction’: The $L'_{\text{HCN}}/L'_{\text{CO}}$ Ratio

The nondetection of HCN($J=2 \rightarrow 1$) in J1148+5251 at the depth of our observations has several implications. For the following comparison with other galaxies (for which L'_{CO} and L'_{HCN} are given in the ground-state transition), we assume that the HCN($J=2 \rightarrow 1$) and CO($J=3 \rightarrow 2$) lines are thermalized, so that $L'_{\text{HCN}(J=2-1)} = L'_{\text{HCN}(J=1-0)}$ and $L'_{\text{CO}(J=3-2)} = L'_{\text{CO}(J=1-0)}$. Considering the high CO excitation in this source (Bertoldi et al.

⁵This ratio lies between 57% and 80% for the $z > 2$ sample, but is up to 100% in nearby starburst galaxies like NGC 253 (e.g., Knudsen et al. 2007).

⁶FIR luminosities estimated from modeling the sparsely sampled FIR SEDs of high- z galaxies are only accurate within a factor of 2.

2003b) and the fact that both lines arise from low J transitions, this is likely a valid assumption.

The critical density of the CO($J=1\rightarrow 0$) transition and its excitation threshold temperature of $T_{\text{ex}}=5.5$ K are low compared to the median gas density and temperature in most galaxies. This is one of the reasons why CO($J=1\rightarrow 0$) emission is considered a good tracer for the total amount of molecular gas in a galaxy. The critical density of the HCN($J=1\rightarrow 0$) transition [$T_{\text{ex}}=4.3$ K, similar to CO($J=1\rightarrow 0$)] is significantly higher than the median density in most galaxies (e.g., Downes & Solomon 1998). HCN($J=1\rightarrow 0$) emission thus is considered a good tracer for the dense peaks of the molecular mass distribution.

The $L'_{\text{HCN}}/L'_{\text{CO}}$ ratio thus is considered a measure for the dense fraction of molecular gas in a galaxy⁷. On average, this ratio is about four to five times higher in local ULIRGs compared to normal, nearby spiral galaxies [median value of $0.17^{+0.05}_{-0.08}$ (ULIRGs) vs. $0.04^{+0.01}_{-0.02}$ (spirals); see Table 4.2]. However, there does not appear to be a further increase toward the even more FIR-luminous systems at $z>2$ ($0.17^{+0.09}_{-0.08}$ on average) within the statistical uncertainties (all values rederived from GS04ab; G07). The upper limit for $L'_{\text{HCN}}/L'_{\text{CO}}$ in J1148+5251 is 0.13, placing it below the median but within the range of values measured for ULIRGs and $z>2$ galaxies (Fig. 4.2a). Our observations thus confirm the finding of G07 that galaxies brighter than $L_{\text{FIR}}=10^{12} L_{\odot}$ appear to have a higher fraction of dense molecular gas than normal spiral galaxies; however, there is no indication that this fraction rises further toward the highest L_{FIR} , or that it changes with redshift.

4.6.2 ‘Star Formation Law’: The $L_{\text{FIR}}/L'_{\text{HCN}}$ Ratio

The FIR luminosity is thought to originate dominantly from dust-reprocessed light of young massive stars, and thus to be a good tracer of the star-formation rate (SFR) in a galaxy. Star formation in galaxies takes place in dense molecular clouds that are traced well by HCN emission, resulting in a linear correlation between the FIR and HCN luminosities (Wu et al. 2005). However, G07 have found a mild increase of $L_{\text{FIR}}/L'_{\text{HCN}}$ with increasing FIR luminosity between normal spiral galaxies and ULIRGs [$L_{\text{FIR}}/L'_{\text{HCN}}=580^{+510}_{-270}$ (spirals) vs. 740^{+505}_{-50} (ULIRGs) on average; see Table 4.2]. This trend is found to get stronger toward the even more FIR-luminous $z>2$ systems ($L_{\text{FIR}}/L'_{\text{HCN}}=1525^{+1300}_{-475}$ on average). The lower limit of $L_{\text{FIR}}/L'_{\text{HCN}}>6600$ obtained for J1148+5251 clearly confirms this trend, and extends it toward higher redshift (Fig. 4.2b). Due to the fact that the high- z sources also have systematically higher L_{FIR} than the nearby galaxies, it remains unclear whether we observe a trend with redshift or with L_{FIR} , or both.

⁷Note that Graciá-Carpio et al. (2006) have questioned the validity of $L'_{\text{HCN}}/L'_{\text{CO}}$ as a tracer of the dense gas fraction.

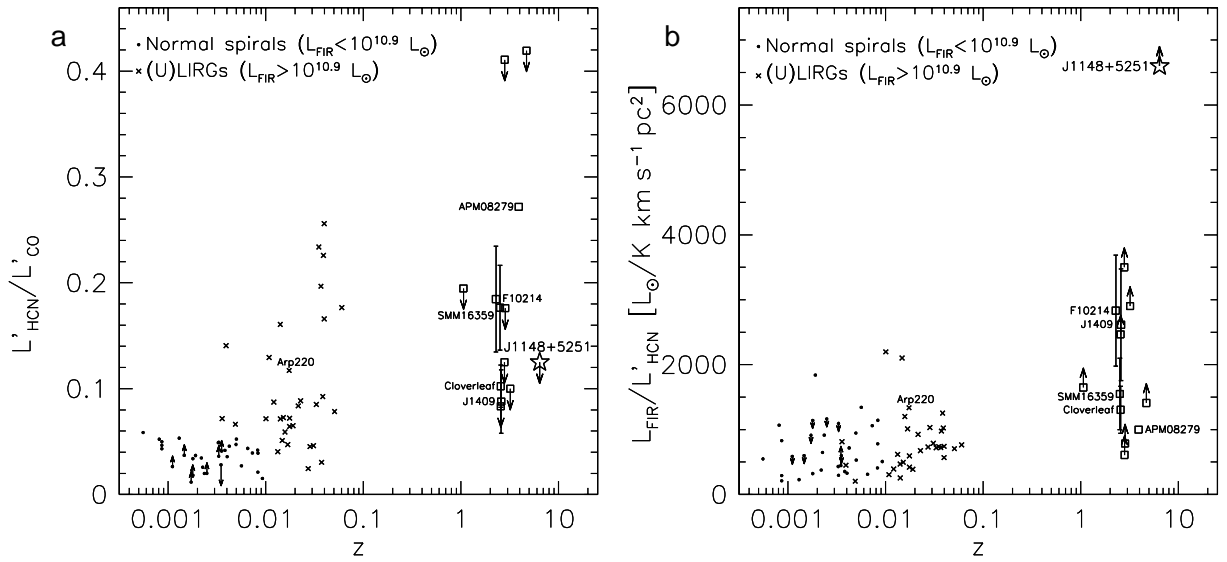


Figure 4.2: Trend of the $L'_{\text{HCN}}/L'_{\text{CO}}$ (‘dense gas fraction’) and $L_{\text{FIR}}/L'_{\text{HCN}}$ (‘star formation law’) ratios with redshift. Data for nearby spirals ($L_{\text{FIR}} < 10^{10.9} L_{\odot}$ i.e., $L_{\text{IR}} < 10^{11} L_{\odot}$) and (U)LIRGs ($L_{\text{FIR}} > 10^{10.9} L_{\odot}$; GS04ab; G07), and high- z galaxies including J1148+5251 are shown (detections labeled, see Table 4.2 for references). In the *left* panel, down-arrows indicate upper limits for HCN, and up-arrows indicate that HCN was detected, but not mapped throughout the whole galaxy. In the *right* panel, this is indicated vice versa.

4.7 Discussion

4.7.1 Median Gas Density and Star Formation Efficiency

Krumholz & Thompson (2007) argue that $L_{\text{FIR}}/L'_{\text{HCN}}$ is expected to be higher for galaxies with a median gas density n_{med} close to or higher than the critical density $n_{\text{crit}}^{\text{HCN}}$ of the observed HCN transition than for galaxies with lower n_{med} . In their case, they define star formation efficiency as the fraction of the mass that is converted into stars per dynamical time of the system. Note that this is different than the star formation rate per unit total gas mass. They argue that the non-linear relation between FIR and CO luminosity arises due to the fact that CO traces all the gas, and the star formation rate is then dictated by the density divided by the free fall time (free fall time $\propto n^{-0.5}$), giving the standard Schmidt-law: star formation rate $\propto n^{1.5}$, or $L_{\text{FIR}} \propto (L'_{\text{CO}})^{1.5}$. For molecules like HCN, which only trace the small fraction of dense gas clouds directly associated with star formation in normal galaxies, the free-fall time is roughly fixed by the critical density for excitation. Hence the star formation rate shows a linear relationship with density, or $L_{\text{FIR}} \propto (L'_{\text{HCN}})^{1.0}$. However, in extreme galaxies, where the median molecular gas density in the ISM approaches the critical density for excitation of HCN, the free-fall time again becomes relevant (i.e., HCN emission no longer selects just the rare, dense peaks whose density is fixed by the HCN critical density, but instead traces the bulk of the ISM, whose density can vary from galaxy to galaxy, and thus the variation of the density and the free-fall time re-enter the calculation), and the relationship approaches: $L_{\text{FIR}} \propto (L'_{\text{HCN}})^{1.5}$. Interestingly, current data show a marginal trend for a changing power-law index at the highest luminosities of the type proposed by Krumholz & Thompson. This change in power-law index from 1 to 1.5 would suggest that, in these extreme luminosity systems, the median ISM gas density approaches the critical density for excitation of HCN. More systems at high luminosity are required to confirm this changing power-law index.

4.7.2 The Role of AGN Heating for L_{FIR}

Like most of the $z > 2$ HCN-detected galaxies, J1148+5251 is a quasar. Based on radiative transfer models of the dust SED of J1148+5251, Li et al. (2007) thus argue that this source may currently undergo a ‘quasar phase’, in which AGN heating of the hot and warm dust contributes significantly to L_{FIR} . This may be an alternative explanation for the elevated $L_{\text{FIR}}/L'_{\text{HCN}}$ in this galaxy. The (rest-frame) IR properties (tracing emission from hot dust) of J1148+5251 are similar to those of other $z > 6$ quasars with much lower L_{FIR} (tracing emission from warm dust), and even to local quasars (Jiang et al. 2006). This supports the assumption that the hot dust in J1148+5251 is dominantly heated by the AGN; however, the lack of a $L_{\text{IR}}-L_{\text{FIR}}$ correlation indicates that the warm dust may still be dominantly heated by a different mechanism. Moreover, J1148+5251 follows the radio-FIR correlation for star-forming galaxies (Carilli et al. 2004), which may suggest a starburst origin for the dominant fraction of L_{FIR} .

Also, one of the $z > 2$ HCN detections and some of the meaningful limits are submillime-

ter galaxies without a known luminous AGN, but are still offset from the local relation. It thus is not straight forward to assume that AGN heating can fully account for the higher average $L_{\text{FIR}}/L'_{\text{HCN}}$ in the high- z galaxy sample.

4.7.3 Implications for Future Studies

The depth of our observations is sufficient to detect a galaxy with the highest $L_{\text{FIR}}/L'_{\text{HCN}}$ in the HCN-detected sample ($L_{\text{FIR}}/L'_{\text{HCN}}=2835\pm 855$) at the redshift of J1148+5251 ($z=6.42$) in HCN emission at a signal-to-noise ratio of >5 . To first order, our lower limit thus confirms previous suggestions (G07) that $L_{\text{FIR}}/L'_{\text{HCN}}$ ratios in high redshift sources lie systematically above those for nearby galaxies. The scatter in this trend is still significant, and will primarily be improved by increasing the number of HCN-detected galaxies at high z , but also by extending studies to different dense gas tracers such as HCO^+ and CS. In addition, it will be important to improve on the main sources of error for the individual high- z detections (e.g., signal-to-noise limited HCN/CO linewidth ratio, accuracy of the FIR SED fit, AGN bias of L_{FIR} , see above). The statistical and individual results, so far, may even imply that the trend in $L_{\text{FIR}}/L'_{\text{HCN}}$ increases further toward J1148+5251. Clearly, it is desirable to obtain more sensitive observations of this source. Although J1148+5251 is the most CO- and FIR-luminous $z>6$ galaxy known, 80 hr of VLA observations were necessary to obtain the current limit. In a favourable case, the HCN($J=2\rightarrow 1$) line may have a strength of about 1.5 times the current rms. To obtain a solid 5σ detection of such a line, about 1000 hr of observations with the VLA would be required. Due to improved receivers and antenna performance, the fully operational Expanded Very Large Array (EVLA) will be by a factor of two more sensitive to the comparatively narrow spectral lines in sources like J1148+5251, and thus will still require long integration times. Studies of dense gas at $z>6$ thus appear to require an order of magnitude increase in collecting area, such as offered by future facilities like the Square Kilometre Array (SKA) phase I demonstrator (e.g., Carilli 2006) and the Atacama Large Millimeter/submillimeter Array (ALMA).

It is a pleasure to thank my collaborators on this project:

Fabian Walter (MPIA), Chris Carilli (NRAO), and Frank Bertoldi (AIfA).

CHAPTER PUBLISHED AS:

Riechers, D. A., Walter, F., Carilli, C. L., & Bertoldi, F., ‘*Observations of Dense Molecular Gas in a Quasar Host Galaxy at $z=6.42$: Further Evidence for a Trend in the $L_{\text{FIR}}/L'_{\text{HCN}}$ Star Formation Diagnostic*’, 2007, ApJL, submitted

Chapter 5

Dense Molecular Gas II: HCO^+ in a $z=2.56$ Quasar Host Galaxy

5.1 Context

Motivated by early indications that the $L'_{\text{HCN}}-L_{\text{FIR}}$ relation does not appear to hold toward high redshift, and that the properties of star formation rather than AGN heating may be the key to explain this offset, a program was started to study the composition in the molecular ISM in distant galaxies in more detail. In practice, there are two main approaches. The first approach is to study the excitation of both CO and HCN to understand the overall density and temperature structure in these galaxies by those two tracer molecules. The second approach is to study additional molecular tracers, which, from local studies, are known to probe different environments. Due to the fact that CO and HCN are almost always the brightest emission lines in galaxies, this means that even fainter levels have to be probed. The most useful tracers will be other tracers of the dense peaks of the molecular ISM, which then can be examined through their relation to the FIR and HCN luminosities. In the local universe, the most common tracers of dense molecular gas are HCN, HCO^+ , and CS. The main difficulty apart from detecting even fainter molecular lines is the fact that sample sizes in the local universe get increasingly smaller (note that even HCN is detected in only of order 100 nearby galaxies). In the following chapters, our observations are described, which have lead to the first high redshift detections of emission from molecules different from CO (discovered in 1991) and HCN (discovered in 2003), namely those of HCO^+ , CS, and CN (plus an upper limit for H_2O). Conclusions are drawn from the Schmidt-Kennicutt relations for those molecules, and relations to CO and HCN¹ In this chapter, the discovery of HCO^+ in the distant universe is described.

¹Note that in the following three chapters, the HCN-FIR relation is treated as ‘linear’, as the significance of and reason for the nonlinearity of the HCN-FIR relation in the high redshift systems is still subject to debate (see Chapter 4). The Schmidt-Kennicutt relations of other molecules are examined in comparison to HCN, which requires this simplification at present.

5.2 Abstract

We report the detection of HCO⁺($J=1\rightarrow 0$) emission towards the Cloverleaf quasar ($z = 2.56$) through observations with the Very Large Array. This is the first detection of ionized molecular gas emission at high redshift ($z > 2$). HCO⁺ emission is a star formation indicator similar to HCN, tracing dense molecular hydrogen gas [$n(\text{H}_2) \simeq 10^5 \text{ cm}^{-3}$] within star-forming molecular clouds. We derive a lensing-corrected HCO⁺ line luminosity of $L'_{\text{HCO}^+} = 3.5 \times 10^9 \text{ K km s}^{-1} \text{ pc}^2$. Combining our new results with CO and HCN measurements from the literature, we find an HCO⁺/CO luminosity ratio of 0.08 and an HCO⁺/HCN luminosity ratio of 0.8. These ratios fall within the scatter of the same relationships found for low- z star-forming galaxies. However, an HCO⁺/HCN luminosity ratio close to unity would not be expected for the Cloverleaf if the recently suggested relation between this ratio and the far-infrared luminosity were to hold. We conclude that a ratio between HCO⁺ and HCN luminosity close to 1 is likely due to the fact that the emission from both lines is optically thick and thermalized and emerges from dense regions of similar volumes. The CO, HCN, and HCO⁺ luminosities suggest that the Cloverleaf is a composite active galactic nucleus–starburst system, in agreement with the previous finding that about 20% of the total infrared luminosity in this system results from dust heated by star formation rather than heating by the active nucleus. We conclude that HCO⁺ is potentially a good tracer for dense molecular gas at high redshift.

5.3 Introduction

One important goal in studies of galaxy formation is to determine star formation characteristics through observations of molecular gas in the early universe. Molecular gas in high-redshift galaxies is commonly traced by CO emission and has been found in more than 30 galaxies at $z > 2$ to date. The observed molecular gas with masses of $\geq 10^{10} M_{\odot}$ provides the requisite material for star formation (see review by Solomon & Vanden Bout [2005 and references therein]).

CO is a good indicator for the total molecular gas content of a system, as it can be excited at relatively low densities; its low dipole moment of $\mu_{\text{D}}^{\text{CO}} = 0.11$ implies a critical density of only $n_{\text{H}_2} \sim 10^2\text{--}10^3 \text{ cm}^{-3}$ for the lower J transitions. Hence, emission from low- J CO transitions is a relatively poor tracer of the denser gas that is more intimately associated with star formation. The most common tracers of the dense molecular gas phase are HCN and HCO⁺. Both molecules have much higher dipole moments ($\mu_{\text{D}}^{\text{HCN}} = 2.98$, $\mu_{\text{D}}^{\text{HCO}^+} = 3.30$) than CO. The critical density to collisionally thermalize their lower J transitions is therefore much higher than for CO, $n_{\text{H}_2} \sim 10^5\text{--}10^6 \text{ cm}^{-3}$ (e.g., Gao & Solomon 2004a, 2004b; Brouillet et al. 2005).

Recent studies of the dense molecular gas phase in nearby ($z < 0.3$) luminous and ultraluminous infrared galaxies (LIRGs and ULIRGs) have shown that the HCN and HCO⁺ luminosities correlate with the star formation rate as traced by the far-infrared (FIR) luminosity. These correlations are tighter than the correlation between the CO and FIR

luminosities (Solomon et al. 1992c; Gao & Solomon 2004a, 2004b; Graciá-Carpio et al. 2006). Because of the relative faintness of the emission lines, HCN has only been detected in four objects at high z to date, and all the detections are in the host galaxies of quasars (Solomon et al. 2003; Vanden Bout et al. 2004; Carilli et al. 2005; Wagg et al. 2005).

It has recently been argued that galaxies dominated by active galactic nuclei (AGNs) have higher HCN/HCO⁺ and HCN/CO luminosity ratios than starburst-dominated galaxies (Kohno et al. 2001; Kohno 2005; Imanishi et al. 2006). In this context, it has been suggested that the presence of X-ray emission emerging from a dust-enshrouded AGN may significantly enhance the chemical abundance of HCN relative to HCO⁺ (Lepp & Dalgarno 1996; Kohno et al. 2001; Usero et al. 2004). Also, the excitation of the HCN molecule may be affected by IR-pumping through a 14 μm vibrational band (Aalto et al. 1995). Based on these considerations and their HCO⁺ survey of low- z (U)LIRGs, Graciá-Carpio et al. (2006) suggest that the HCO⁺-to-HCN intensity ratio toward FIR-bright ($L_{\text{FIR}} > 10^{12} L_{\odot}$) objects (such as the Cloverleaf) are likely low. Measurements of HCO⁺ emission in high-redshift objects would thus lead to new constraints on their dense interstellar medium and, potentially, on the radiation field pervading it.

In this chapter, we report the first high- z detection of HCO⁺ ($J=1\rightarrow 0$) emission, which was observed toward the Cloverleaf quasar ($z = 2.56$) with the NRAO Very Large Array (VLA).² Because of its strong gravitational magnification (magnification factor $\mu_L = 11$; Venturini & Solomon 2003), the Cloverleaf is the brightest CO source at high redshift, and it also exhibits bright HCN ($J=1\rightarrow 0$) emission (Solomon et al. 2003) and emission from both C I fine structure lines (Weiß et al. 2003, 2005b). A previous search for HCO⁺ ($J=4\rightarrow 3$) emission in this source was unsuccessful, setting an upper limit of 14 mJy on the line peak flux density (Wilner et al. 1995). We use a standard concordance cosmology throughout, with $H_0 = 71 \text{ km s}^{-1} \text{ Mpc}^{-1}$, $\Omega_m = 0.27$, and $\Omega_{\Lambda} = 0.73$ (Spergel et al. 2003, 2007).

5.4 Observations

We observed the HCO⁺ ($J=1\rightarrow 0$) transition line ($\nu_{\text{rest}} = 89.1885230 \text{ GHz}$) towards H 1413+117 (the Cloverleaf quasar) using the VLA in its D configuration between 2005 November 26 and 2006 January 13. At the target z of 2.55784, the line is redshifted to 25.068166 GHz (11.96 mm). The total integration time amounts to 25.5 hr. Observations were performed in fast-switching mode using the nearby source 14160+13204 (distance to the Cloverleaf: 1.8°) for secondary amplitude and phase calibration. Observations were carried out under excellent weather conditions with 23 antennas. The phase stability in all runs was excellent (typically less than 15° rms for the longest baselines). For primary flux calibration, 3C 286 was observed during each run.

Two 25 MHz wide intermediate-frequency bands (IFs) with seven 3.125 MHz channels each were observed simultaneously in the so-called spectral line mode centered at the

²The National Radio Astronomy Observatory is a facility of the National Science Foundation, operated under cooperative agreement by Associated Universities, Inc.

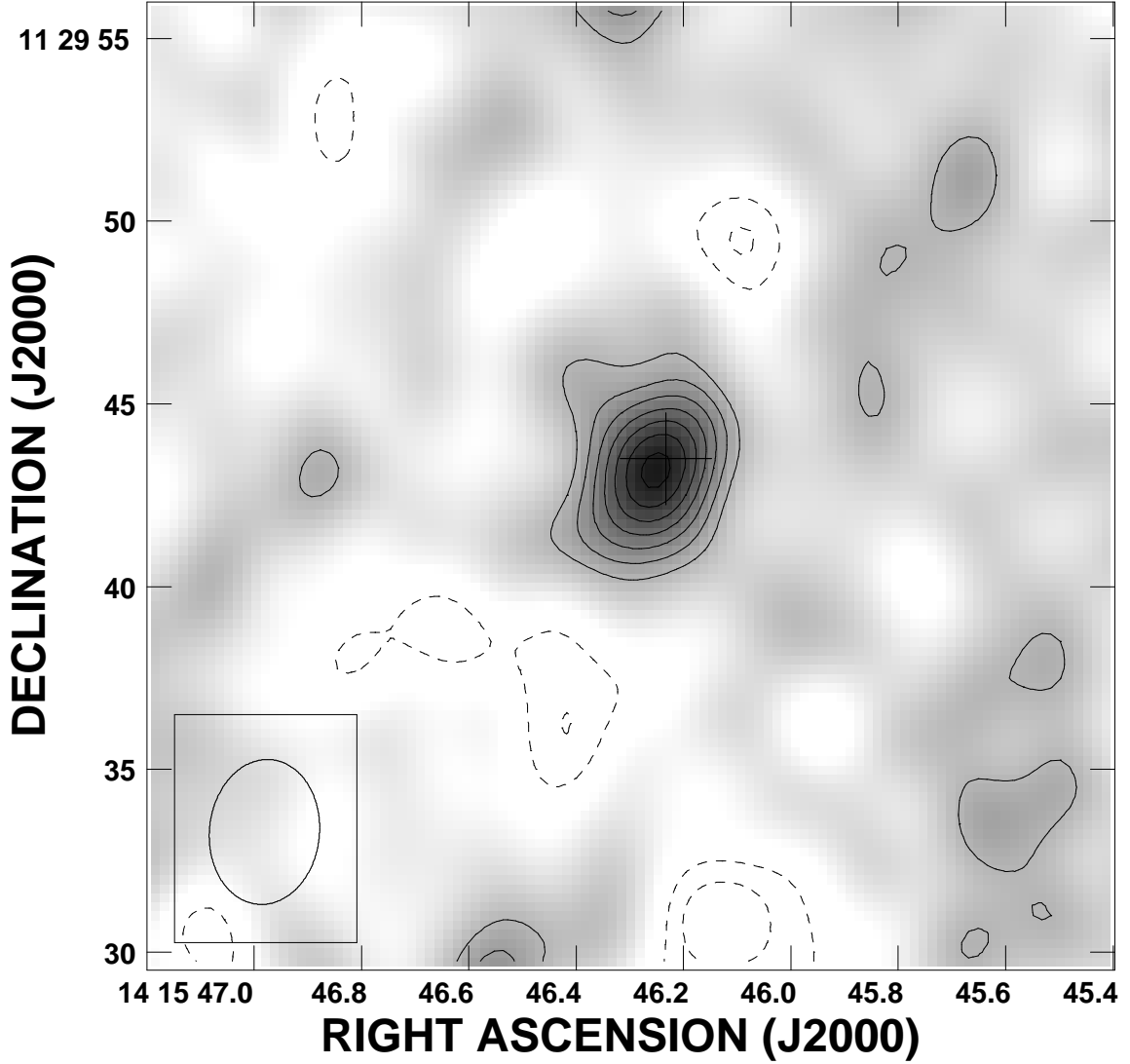


Figure 5.1: VLA detection of $\text{HCO}^+(J=1\rightarrow 0)$ towards the Cloverleaf quasar at a resolution of $4.0'' \times 3.0''$ (as indicated at lower left). Continuum emission was subtracted. The source is marginally resolved. The cross indicates the geometrical center of the CO emission in the Cloverleaf (Alloin et al. 1997, see text). This continuum-subtracted map is integrated over the central 411 km s^{-1} (34.375 MHz). Contours are shown at $(-3, -2, 2, 3, 4, 5, 6, 7, 8) \times \sigma$ ($1 \sigma = 16 \mu\text{Jy beam}^{-1}$).

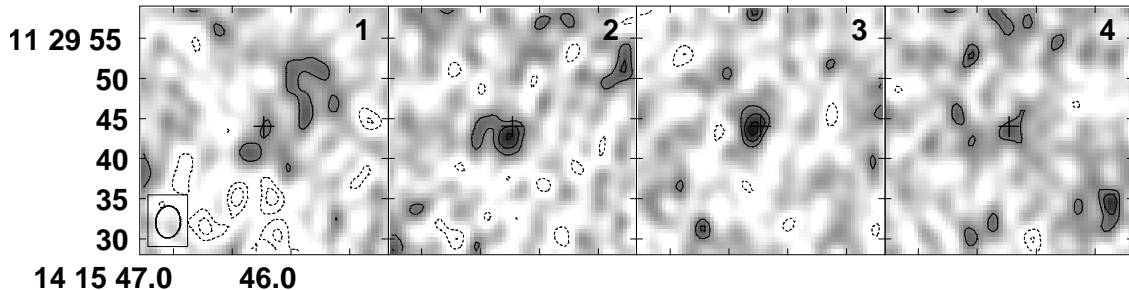


Figure 5.2: Channel maps of the $\text{HCO}^+(J=1\rightarrow 0)$ emission (same region as shown in Fig. 1). One channel width is 6.25 MHz, or 75 km s^{-1} (frequencies increase with channel number and are shown at 25057.228, 25063.478, 25069.728 and 25075.978 MHz). Contours are shown at $(-3, -2, 2, 3, 4)\times\sigma$ ($1\sigma = 50 \mu\text{Jy beam}^{-1}$). The beam size ($4.0''\times 3.0''$) is shown at lower left; the crosses indicate the same position as in Fig. 1.

$\text{HCO}^+(J=1\rightarrow 0)$ line frequency, leading to an effective bandwidth of 43.75 MHz (corresponding to 523 km s^{-1} at 25.1 GHz). In addition, two 50 MHz (corresponding to 598 km s^{-1} at 25.1 GHz) IFs were observed in the so-called quasi-continuum mode at 24.7351 and 24.7851 GHz to monitor the continuum at 12 mm. We chose a setting with both continuum channels below the $\text{HCO}^+(J=1\rightarrow 0)$ line frequency to avoid the significantly worse system temperatures and locking problems of the local oscillator above 25 GHz. The continuum was observed for one-third of the total time to attain the same rms as in the combined line channels.

For data reduction and analysis, the AIPS package was used. The two continuum channels were concatenated in the u - v /visibility plane. The $\text{HCO}^+(J=1\rightarrow 0)$ line data cube was generated by subtracting a CLEAN component model of the continuum emission from the visibility data. All data were mapped using the CLEAN algorithm and “natural” weighting without applying a further taper; this results in a synthesized beam of $4.0''\times 3.0''$ ($\sim 28 \text{ kpc}$ at $z = 2.56$). The final rms in the combined map is $16 \mu\text{Jy beam}^{-1}$ for a 34.375 MHz (corresponding to 411 km s^{-1}) channel and $50 \mu\text{Jy beam}^{-1}$ for a 6.25 MHz (75 km s^{-1}) channel.

5.5 Results

We have detected emission from the $\text{HCO}^+(J=1\rightarrow 0)$ transition line toward the Cloverleaf quasar ($z = 2.56$). The source appears to be marginally resolved in both the continuum and the HCO^+ line maps. Two-dimensional Gaussian fitting yields a continuum peak flux density of $343 \pm 12 \mu\text{Jy beam}^{-1}$. The continuum-subtracted $\text{HCO}^+(J=1\rightarrow 0)$ line map is shown in Figure 5.1. The cross indicates the geometrical center position of the resolved $\text{CO}(J=7\rightarrow 6)$ map at $\alpha = 14^{\text{h}}15^{\text{m}}46^{\text{s}}.233$, $\delta = +11^{\circ}29'43''.50$ (Alloin et al. 1997). The small offset is likely due to the fact that the lens images are not equally bright; that is,

Table 5.1: CO, HCN, and HCO⁺ Line Luminosities in the Cloverleaf

Line	S_ν (μJy)	L' ($10^9 \text{ K km s}^{-1} \text{ pc}^2$)	Ref.
HCO ⁺ ($J=1\rightarrow 0$)	193 ± 28	3.5 ± 0.3	1
HCN($J=1\rightarrow 0$)	240 ± 40	4.3 ± 0.5	2
CO($J=3\rightarrow 2$)	30000 ± 1700	42 ± 7	3

Notes—Luminosities are derived as described by Solomon et al. (1992b): $L'(\text{K km s}^{-1} \text{ pc}^2) = 3.25 \times 10^7 I \nu_{\text{obs}}^{-2} D_L^2 (1+z)^{-3}$, where I is the velocity-integrated line flux in Jy km s^{-1} , D_L is the luminosity distance in Mpc ($z = 2.55784$; Weiß et al. 2003), and ν_{obs} is the observed frequency in GHz. All given luminosities are corrected for this lensing magnification. The HCN and HCO⁺ luminosities are corrected for the finite source size relative to the synthesized VLA beam (see text).

References—(1) This work; (2) Solomon et al. 2003; (3) Weiß et al. 2003.

the center of intensity is offset from the geometric center position. The deconvolved source size from the Gaussian fit is in good agreement with the size of the resolved structure seen in CO($J=7\rightarrow 6$). The line is clearly detected at 8σ over a range of 34.375 MHz (411 km s^{-1}). We derive a line peak flux density of $193 \pm 28 \mu\text{Jy beam}^{-1}$. In Figure 5.2, four channel maps (6.25 MHz, or 75 km s^{-1} each) of the central 25 MHz (300 km s^{-1}) of the HCO⁺($J=1\rightarrow 0$) line are shown. At an rms of $50 \mu\text{Jy beam}^{-1}$, the line is detected at 4σ in the central two channels, and the decline of the line intensity towards the line wings is clearly visible in the outer channels, as expected. We attribute the small offset between the peak positions of channels 2 and 3 to observational uncertainties rather than to a real velocity gradient. We thus derive an HCO⁺($J=1\rightarrow 0$) line luminosity of $L'_{\text{HCO}^+} = 3.5 \times 10^9 \text{ K km s}^{-1} \text{ pc}^2$ (corrected for gravitational magnification, $\mu_L = 11$, and the finite source size relative to the synthesized beam, which leads to a 30% correction based on the source extension seen in CO; see Table 5.1 for details).

We summarize our results in Table 5.1 together with the line fluxes and luminosities for HCN (Solomon et al. 2003) and CO (Weiß et al. 2003). Our HCO⁺($J=1\rightarrow 0$) peak flux density corresponds to $\sim 80\%$ of the HCN($J=1\rightarrow 0$) peak flux of $0.24 \pm 0.04 \text{ mJy}$ derived by Solomon et al. (2003). This corresponds to an $L'_{\text{HCO}^+}/L'_{\text{HCN}}$ luminosity ratio of 0.8, which is consistent with unity within the statistical and systematic uncertainties. They use an extrapolated continuum peak flux at 24.9 GHz of $S_{\text{cont}}(24 \text{ GHz}) = 0.26 \pm 0.03 \text{ mJy}$. The difference from our value may be due to problems with their extrapolation or calibration errors. However, it is also possible that the continuum of the Cloverleaf is variable at 25 GHz.

5.6 Discussion

In the following, we discuss relationships between the emission observed in HCO⁺ and other molecules and the FIR continuum for a sample of low- z spiral and starburst galaxies (Nguyen-Q-Rieu et al. 1992; Imanishi et al. 2004; Gao & Solomon 2004b), low- z (U)LIRGs (Graciá-Carpio et al. 2006; Imanishi et al. 2006), and the Cloverleaf (this work; Solomon et al. 2003; Weiß et al. 2003), as shown in Figure 5.3. As only an upper limit exists for

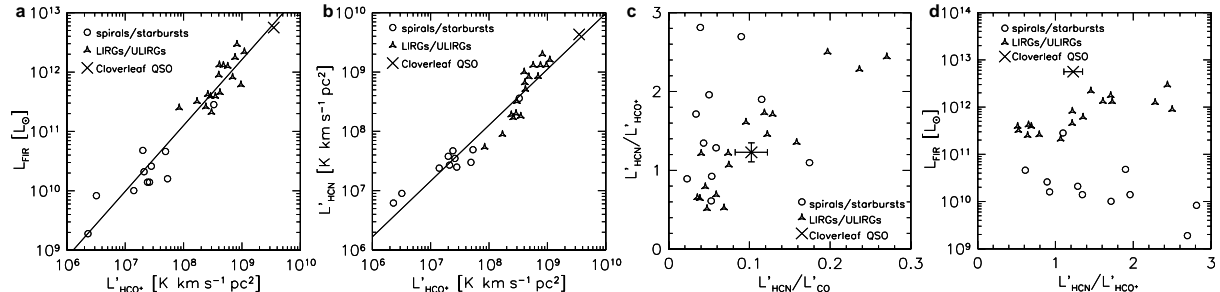


Figure 5.3: HCO^+ luminosity relations for a sample of low- z spiral and starburst galaxies (Nguyen-Q-Rieu et al. 1992; Imanishi et al. 2004; Gao & Solomon 2004b), low- z (U)LIRGs (Graciá-Carpio et al. 2006; Imanishi et al. 2006), and the Cloverleaf (this work; Solomon et al. 2003; Weiß et al. 2003). The Cloverleaf luminosities are corrected for gravitational lensing ($\mu_L = 11$). The solid lines are least-squares fits to all data except the Cloverleaf. The error bars shown for the Cloverleaf indicate the statistical errors of the line luminosity measurements. (See text for more details.)

the $\text{CO}(J=1\rightarrow 0)$ line emission in the Cloverleaf (Tsuboi et al. 1999), we here assume that CO is fully thermalized up to the $3\rightarrow 2$ transition (i.e., $L'_{\text{CO}(1-0)} = L'_{\text{CO}(3-2)}$). We do not discuss effects of differential lensing, which could distort the intrinsic luminosity ratios, as models indicate similar sizes for molecular and dust emission in the Cloverleaf (Solomon et al. 2003).

Figure 5.3a.— L'_{HCO^+} correlates closely with L_{FIR} ; a linear least-squares fit (excluding the Cloverleaf) yields $\log L_{\text{FIR}} = (1.11 \pm 0.06) \log L'_{\text{HCO}^+} + 2.2$. For HCN, Gao & Solomon (2004b) find $\log L_{\text{FIR}} = 0.97 \log L'_{\text{HCN}} + 3.1$ based on a larger sample of local starburst and spiral galaxies. Both slopes are consistent with unity.

Figure 5.3b.— L'_{HCO^+} also correlates closely with L'_{HCN} ; a linear least-squares fit (again excluding the Cloverleaf) yields $\log L'_{\text{HCN}} = (0.94 \pm 0.06) \times \log L'_{\text{HCO}^+} + 0.6$. Figures 5.3a and 5.3b thus exemplify that HCO^+ traces dense molecular gas as well as HCN, and its close correlation with the FIR continuum emission suggests that HCO^+ may also be used as a star formation indicator. It is remarkable how well the Cloverleaf agrees with the correlations found for local galaxies ranging over more than 3 orders of magnitude in FIR luminosity.

Figure 5.3c.—Based on data from Kohno et al. (2001) and Kohno (2005), Imanishi et al. (2006) argue that AGN-dominated galaxies have higher HCN/ HCO^+ and HCN/CO ratios than starburst-dominated galaxies. In this diagram, AGN-dominated galaxies thus fall on the upper right side, and starburst-dominated galaxies fall on the lower left side. For the local starburst/spiral sample, we have taken the $L'_{\text{HCN}}/L'_{\text{HCO}^+}$ ratios from Nguyen-Q-Rieu et al. (1992) and the $L'_{\text{HCN}}/L'_{\text{CO}}$ ratios from Gao & Solomon (2004b). The Cloverleaf clearly falls on the lower left side of the diagram, putting it in the region of “starburst-dominated” galaxies. Indeed, by decomposition of the dust spectrum into a warm (115 K) and a cooler (50 K) component, Weiß et al. (2003) find that about 60% of the dust emission

emerges from the cooler component, which may well be dominated by heating from star formation. However, based on an Arp 220 template, Solomon et al. (2003) have shown that only about 20% of the total FIR luminosity is powered by the starburst. It is therefore unclear whether or not this diagram should indeed be used to constrain the properties of high- z quasars.

Figure 5.3d.—Based on their recent study of local (U)LIRGs, Graciá-Carpio et al. (2006) suggest that the $L'_{\text{HCN}}/L'_{\text{HCO}^+}$ ratio correlates with L_{FIR} ; their results indicate that HCN may not be an unbiased tracer of star formation. We show this relation including their sample together with the spiral/starburst sample described above and the Cloverleaf. We find no evidence for any correlation between $L'_{\text{HCN}}/L'_{\text{HCO}^+}$ and L_{FIR} over the increased luminosity and redshift range. We note that if the relation suggested by Graciá-Carpio et al. (2006) were to hold, we would not have been able to detect the HCO⁺($J=1\rightarrow 0$) line in the Cloverleaf, as $L'_{\text{HCN}}/L'_{\text{HCO}^+}$ would be ~ 3 .

As discussed above, the $L'_{\text{HCN}}/L'_{\text{HCO}^+}$ ratio is consistent with unity over a large range in FIR luminosities. Together with multitransition studies of both molecules available for some of the local galaxies (e.g., Seaquist & Frayer 2000), this result suggests that HCO⁺ does not require special conditions to be excited. Also, it indicates that HCO⁺ and HCN trace physically similar regions. Although consistent with unity within the error bars, the ratio of HCN and HCO⁺ luminosities may be larger than 1 in the Cloverleaf, and several mechanisms to explain such a difference have been discussed in the literature. It has been argued that HCN emission in molecular clouds can be enhanced by mid-IR pumping of a 14 μm vibrational band (Aalto et al. 1995), but HCO⁺ can be mid-IR-pumped under very similar conditions via a 12 μm vibrational band (Graciá-Carpio et al. 2006). Also, Gao & Solomon (2004b) have found that this mechanism does not appear to play a major role (their Fig. 5). It has also been suggested that the chemical abundance of HCN can be enhanced relative to CO and HCO⁺ in the ambient X-ray radiation field of a strong AGN (Lepp & Dalgarno 1996). It is also possible that the HCO⁺ abundance is decreased as a result of the ionizing field produced by cosmic rays (Seaquist & Frayer 2000): Cosmic rays ionize H₂, leading to the production of H₃⁺, which reacts with CO to form HCO⁺. The abundance of HCO⁺ is thus affected by the ratio of cosmic-ray ionization rate and gas density. While a higher ionizing flux favors the production of HCO⁺, it also increases the number of free electrons, which leads to a higher probability for recombination: At a gas density of $3 \times 10^4 \text{ cm}^{-3}$, an ionizing field comparable to that of the Galaxy may already be strong enough to significantly decrease the abundance of HCO⁺ through dissociative recombination of H₃⁺ (see, e.g., Phillips & Lazio 1995), and the ionizing field in the Cloverleaf is probably much stronger than the Galactic one.

Our finding that the HCN-to-HCO⁺ luminosity ratio in the Cloverleaf is close to unity implies that the processes discussed here likely do not play a dominant role. All these chemical arguments, assume that the HCN and HCO⁺ $J = 1 \rightarrow 0$ opacities are low and that the observed line intensities scale with the underlying molecular abundances. Observations of the ¹³C-bearing isotopomers of HCO⁺ and HCN in nearby starburst galaxies have shown that the HCO⁺/H¹³CO⁺ and HCN/H¹³CN ratios are similar to those seen in CO/¹³CO (Nguyen-Q-Rieu et al. 1992; Wang et al. 2004). From this it has been concluded that the

HCO⁺ and HCN opacities are similar to those in CO, with $\tau \simeq 3\text{--}4$ (see also Henkel et al. 1993), that is, the emission is optically thick. This would imply that $L'_{\text{HCN}}/L'_{\text{HCO}^+}$ is solely determined by the relative area filling factors and excitation temperatures of both molecules. As the HCO⁺($J=1\rightarrow 0$) and HCN($J=1\rightarrow 0$) excitation is likely to be close to thermalized for densities of $n(\text{H}_2) \gtrsim 10^5 \text{ cm}^{-3}$, this would naturally explain $L'_{\text{HCN}}/L'_{\text{HCO}^+} \simeq 1$, assuming that both molecules trace regions of similar density (i.e., similar volume). We conclude that HCO⁺ compares favorably with HCN in terms of being a good tracer for dense molecular gas even in FIR-bright objects at high redshift.

It is a pleasure to thank my collaborators on this project:

Fabian Walter (MPIA), Chris Carilli (NRAO), Axel Weiß (MPIfR), Frank Bertoldi (AIfA), Karl Menten (MPIfR), Kirsten K. Knudsen (MPIA), and Pierre Cox (IRAM).

CHAPTER PUBLISHED AS:

Riechers, D. A., Walter, F., Carilli, C. L., Weiß, A., Bertoldi, F., Menten, K. M., Knudsen, K. K., & Cox, P., *'First Detection of HCO⁺ Emission at High Redshift'*, 2006, ApJ, 645, L13

Chapter 6

Dense Molecular Gas III: CN in a $z=2.56$ Quasar Host Galaxy

6.1 Context

Encouraged by the detection of HCO^+ in the Cloverleaf, the search for additional tracers of dense gas in this source was continued. The second molecule that was firmly detected in this search is CN, as shown here. The analysis of the CN line properties is followed by an examination of the Schmidt-Kennicutt relation of CN, based on nearby galaxies and the Cloverleaf. This enables comparison to CO, HCN, and HCO^+ . As mentioned previously, CN is, in a sense, a ‘biased’ tracer relative to HCN, as it is prominent in those dense regions where HCN typically is not (note that CN is a dissociation product of HCN). It thus is an important question whether or not a difference can be seen in the standard diagnostics, such as the Schmidt-Kennicutt relations, when different types of galactic environments are studied [such as starbursts, (U)LIRGs, and distant quasars with a bright AGN].

6.2 Abstract

We report the detection of $\text{CN}(N=3\rightarrow 2)$ emission towards the Cloverleaf quasar ($z = 2.56$) based on observations with the IRAM Plateau de Bure Interferometer. This is the first clear detection of emission from this radical at high redshift. CN emission is a tracer of dense molecular hydrogen gas [$n(\text{H}_2) > 10^4 \text{ cm}^{-3}$] within star-forming molecular clouds, in particular, in regions where the clouds are affected by UV radiation. The HCN/CN intensity ratio can be used as a diagnostic for the relative importance of photodissociation regions (PDRs) in a source, and as a sensitive probe of optical depth, the radiation field, and photochemical processes. We derive a lensing-corrected $\text{CN}(N=3\rightarrow 2)$ line luminosity of $L'_{\text{CN}(3\rightarrow 2)} = (4.5 \pm 0.5) \times 10^9 \text{ K km s}^{-1} \text{ pc}^2$. The ratio between CN luminosity and far-infrared luminosity falls within the scatter of the same relationship found for low- z (ultra-) luminous infrared galaxies. Combining our new results with $\text{CO}(J=3\rightarrow 2)$ and $\text{HCN}(J=1\rightarrow 0)$ measurements from the literature and assuming thermal excitation for all

transitions, we find a CO/CN luminosity ratio of 9.3 ± 1.9 and a HCN/CN luminosity ratio of 0.95 ± 0.15 . However, we find that the CN($N=3 \rightarrow 2$) line is likely only subthermally excited, implying that those ratios may only provide upper limits for the intrinsic $1 \rightarrow 0$ line luminosity ratios. We conclude that, in combination with other molecular gas tracers like CO, HCN, and HCO^+ , CN is an important probe of the physical conditions and chemical composition of dense molecular environments at high redshift.

6.3 Introduction

Investigations of the dense molecular interstellar medium (ISM) in high-redshift galaxies are of fundamental importance to further our understanding of the early phases of galaxy formation and evolution, as it harbors the environments in which the actual star formation is believed to occur. Recent studies of the molecular gas phase in high- z galaxies using CO emission lines have revealed large molecular gas reservoirs with masses in excess of $10^{10} M_{\odot}$ (see review by Solomon & Vanden Bout 2005 and references therein).

However, while the relative brightness of CO emission lines renders this molecule the most common tracer of the requisite material for star formation, the low densities of only $n_{\text{H}_2} \sim 10^2 - 10^3 \text{ cm}^{-3}$ required to excite its lower J transitions (due to its low dipole moment of only $\mu_{\text{D}}^{\text{CO}} = 0.11$) imply that CO is not a specific tracer of dense molecular cloud cores, i.e., the regions where stars are actively formed.

In contrast, recent studies of nearby actively star-forming galaxies have shown that the high dipole molecule HCN ($\mu_{\text{D}}^{\text{HCN}} = 2.98$) is a far better tracer of such dense molecular cores (e.g. Gao & Solomon 2004a, 2004b). The critical density of $n_{\text{H}_2} \sim 10^5 - 10^6 \text{ cm}^{-3}$ to collisionally thermalize its lower J transitions is much higher than that of CO and of the same order as the densities found in bright star-forming regions in the Galaxy (e.g. the Orion Bar; Hogerheijde et al. 1995). A main result in this context is the finding that the HCN luminosity correlates well with the far-infrared (FIR) luminosities (which is commonly used to estimate star formation rates at high redshift) over 7–8 orders of magnitude, from Galactic dense cores to the highest redshift quasars (Wu et al. 2005).

However, in nearby luminous and ultraluminous infrared galaxies (LIRGs/ULIRGs), it has been found that systems with similar HCN/CO and HCN/FIR luminosity ratios may have quite different dense-gas properties regarding their chemical composition, and their gas excitation (e.g., Aalto et al. 2002). To better understand the physical and chemical state of the dense molecular gas phase which directly relates to star formation, it has proven essential to study additional bright tracers of dense gas with properties different from HCN, such as the cyanide radical (CN). Because of its lower dipole moment relative to HCN ($\mu_{\text{D}}^{\text{CN}} = 1.45$), its critical density is lower by about a factor of 5. Observations of CN emission toward the Orion A molecular cloud complex have shown that CN filaments trace the dense interfaces between the molecular cloud and the major ionization fronts (Rodríguez-Franco et al. 1998). It has also been found that the $[\text{CN}]/[\text{HCN}]$ abundance ratio is greatly enhanced in the central region of the starburst galaxy M82, being as high as ~ 5 across the entire nucleus (Fuente et al. 2005). These observations indicate that CN

is a good tracer of gas layers which are affected by photochemistry, since this molecule appears to be predominantly found in regions exposed to ionizing stellar UV radiation. It has also been found that, due to the rapid destruction of other dense gas tracers like HCN, the abundance of CN tends to be enhanced in areas where the UV radiation field is only partly attenuated, such as in zones close to the surface of photodissociation regions (PDRs; Fuente et al. 1993; Sternberg & Dalgarno 1995; Jansen et al. 1995). The CN/HCN intensity ratio can thus be used as a diagnostic for the relative importance of PDRs in a source and a sensitive probe of optical depth, the radiation field, and photochemical processes (e.g., Boger & Sternberg 2005). CN emission may thus in a sense be a more specific tracer for star formation than, e.g., HCN, which only traces regions of dense gas in general. In addition, theoretical studies of the chemical composition of molecular gas for different ionization parameters suggest that the relative abundance of CN may also be enhanced in X-ray-dominated regions (XDRs), such as active galactic nucleus (AGN) environments (Lepp & Dalgarno 1996). This shows why it is desirable to search for CN emission, which is part of our current effort to study molecular tracers other than CO out to high redshifts. Such an investigation is imperative in obtaining more meaningful constraints on the physical properties and chemical composition of the dense molecular ISM in distant galaxies.

In this chapter, we report the first high- z detection of CN($N=3\rightarrow 2$) emission, which was observed towards the Cloverleaf quasar ($z = 2.56$) with the IRAM Plateau de Bure Interferometer (PdBI).¹ Because of its strong gravitational magnification (magnification factor $\mu_L = 11$; Venturini & Solomon 2003), the Cloverleaf is the brightest CO source at high redshift (e.g., Barvainis et al. 1994) and one of the most prolific sources of molecular lines beyond $z=2$. It was the first $z > 2$ source to be detected in HCN (Solomon et al. 2003) and HCO⁺ (Riechers et al. 2006b) emission. It was also detected in both C I fine-structure lines (Barvainis et al. 1997; Weiß et al. 2003, 2005b). We use a standard concordance cosmology throughout, with $H_0 = 71 \text{ km s}^{-1} \text{ Mpc}^{-1}$, $\Omega_m = 0.27$, and $\Omega_\Lambda = 0.73$ (Spergel et al. 2003, 2007).

6.4 Observations

We observed the CN($N=3\rightarrow 2$) transition line ($\nu_{\text{rest}} = 339.4467770 - 340.2791661 \text{ GHz}$ for the different fine-structure [FS] and hyperfine-structure [HFS] transitions of the $v=0$ vibrational state) towards H1413+117 (the Cloverleaf quasar) using the PdBI in D configuration between 2006 July 26 and September 3. At the target redshift of $z=2.55784$ (Weiß et al. 2003), the line is shifted to $\sim 95.6 \text{ GHz}$ (3.14 mm). The total integration time amounts to 17.5 hr using five antennas, resulting in 5.8 hr equivalent on-source time with six antennas after discarding unusable visibility data. The nearby sources 1354+195 and 1502+106 (distance to the Cloverleaf: 9.0° and 12.0°) were observed every 20 minutes for pointing, secondary amplitude, and phase calibrations. For primary flux calibration, several nearby

¹IRAM is supported by INSU/CNRS (France), MPG (Germany), and IGN (Spain).

calibrators (MWC 349, CRL 618, 3C 273, 3C 345, and NRAO 150) were observed during all runs.

The correlator was tuned to a frequency of 95.603 GHz, which corresponds to the central position between the brightest HFS transitions² of the CN($N=3\rightarrow 2$) line at 95.6332 and 95.5736 GHz. The total bandwidth of 580 MHz (~ 1800 km s⁻¹) used for the observations is large enough to cover all FS and HFS transitions of the CN($N=3\rightarrow 2$) line. It also covers enough channels that are free of line emission to constrain the 3 mm continuum emission of the Cloverleaf.

For data reduction and analysis, the IRAM GILDAS package was used. All data were mapped using the CLEAN algorithm and “natural” weighting without applying a further taper; this results in a synthesized beam of $5.3'' \times 4.9''$ (~ 42 kpc at $z = 2.56$). The final rms in the combined map is 0.25 mJy beam⁻¹ for a 190 MHz (corresponding to 596 km s⁻¹) channel, 0.4 mJy beam⁻¹ for a 80 MHz (252 km s⁻¹) channel, and 0.8 mJy beam⁻¹ for a 20 MHz (63 km s⁻¹) channel.

6.5 Theoretical Considerations

Because of its fine structure and hyperfine structure splitting, the CN($N=3\rightarrow 2$) emission line is distributed over 19 lines³ in three main components separated by more than 200 MHz from each other in the rest frame. This separation is of the same order as the kinematical broadening of the CO lines in the Cloverleaf (Weiß et al. 2003), causing the HFS components to be blended. To analyze the intrinsic line shape of the CN($N=3\rightarrow 2$) transition in the Cloverleaf, we calculated a synthetic line profile, assuming optically thin emission in local thermodynamic equilibrium (LTE) to derive the relative intensities of the HFS components. The relative intensities of the components were computed using the laboratory data from Skatrud et al. (1983), and approximation (4) of equation (1) in Pickett et al. (1998). Assuming that the three main CN($N=3\rightarrow 2$) components are kinematically broadened in the same way as the CO lines (416 ± 6 km s⁻¹ FWHM; see Weiß et al. 2003), we obtain the synthetic line profile displayed in Figure 6.1 (*solid line*). Under the given assumptions, the contribution from all HFS lines of component 1 to the total intensity are negligible, and not detectable at the given signal-to-noise ratio (see below). A single Gaussian fit (Fig. 6.1, *dotted line*; 484 km s⁻¹ FWHM, or 116% of the CO lines) agrees with the more detailed model profile (Fig. 6.1, *solid line*) within a few percent in its peak position and integral, i.e., well within the observational errors. Note however that the width and peak position of this Gaussian depends on the relative intensities of the HFS components,

²These components are actually blends of the [$N=3\rightarrow 2$, $J=5/2\rightarrow 3/2$, ($F=7/2\rightarrow 5/2$, $5/2\rightarrow 3/2$, and $3/2\rightarrow 1/2$)] HFS components at $\nu_{\text{rest}} = 340.0315440\text{--}340.0354080$ GHz and [$N=3\rightarrow 2$, $J=7/2\rightarrow 5/2$, ($F=9/2\rightarrow 7/2$, $7/2\rightarrow 5/2$, and $5/2\rightarrow 3/2$)] HFS components at $\nu_{\text{rest}} = 340.2477700\text{--}340.2485764$ GHz (components 2 and 3 in Fig. 6.1).

³We assume that CN is in its ground electronic state ($^2\Sigma$), and that the spins couple according to Hund’s case (b) coupling scheme: $\vec{N} + \vec{S} = \vec{J}$, (FS coupling) and $\vec{J} + \vec{I}_C + \vec{I}_N = \vec{F}$ (HFS coupling). Here, \vec{N} is the rotational angular momentum vector, \vec{S} is the electronic spin, and \vec{I} is a nuclear spin.

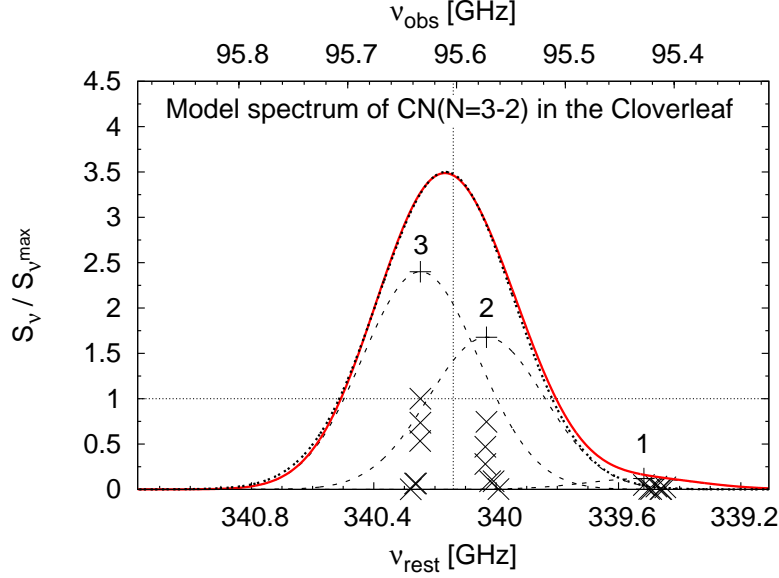


Figure 6.1: Model spectrum of the $\text{CN}(N=3\rightarrow 2)$ emission in the Cloverleaf. The horizontal axes indicate the rest and observed frequencies. The full range of the PdBI bandpass is shown. The vertical axis indicates the predicted intensity, normalized to the $(N=3\rightarrow 2, J=7/2\rightarrow 5/2, F=9/2\rightarrow 7/2)$ component. The relative intensities are computed for the LTE case. The crosses indicate the hyperfine structure components. The plus signs indicate the summed intensities of the components in three different frequency bins. The dashed lines are Gaussian fits to the summed intensities, assuming the width of the $\text{CO}(J=3\rightarrow 2)$ line (Weiß et al. 2003) for the subcomponents (labeled '1'-'3'). The solid line is a sum of all three components, and indicates the model-predicted $\text{CN}(N=3\rightarrow 2)$ line shape. The thick dotted line is a single Gaussian (used to fit the observations), fitted to the model line. The dotted vertical line indicates the tuning frequency, corresponding to zero velocity in Fig. 6.4.

which in turn depend on the above assumptions, in particular, the optical depth. In the optically thin LTE case, components 2 and 3 have a peak strength ratio of 1:1.4. As an example, if they had a ratio of unity, the fitted Gaussian to the line profile would have a FWHM of 603 km s^{-1} , or 145% of the CO lines. We thus conclude that fitting a Gaussian to the observed line profile contains all relevant information, while minimizing the number of free fit parameters, and, thus, is preferred over a more complex fitting procedure to describe and analyze the $\text{CN}(N=3\rightarrow 2)$ profile at the given signal-to-noise ratio.

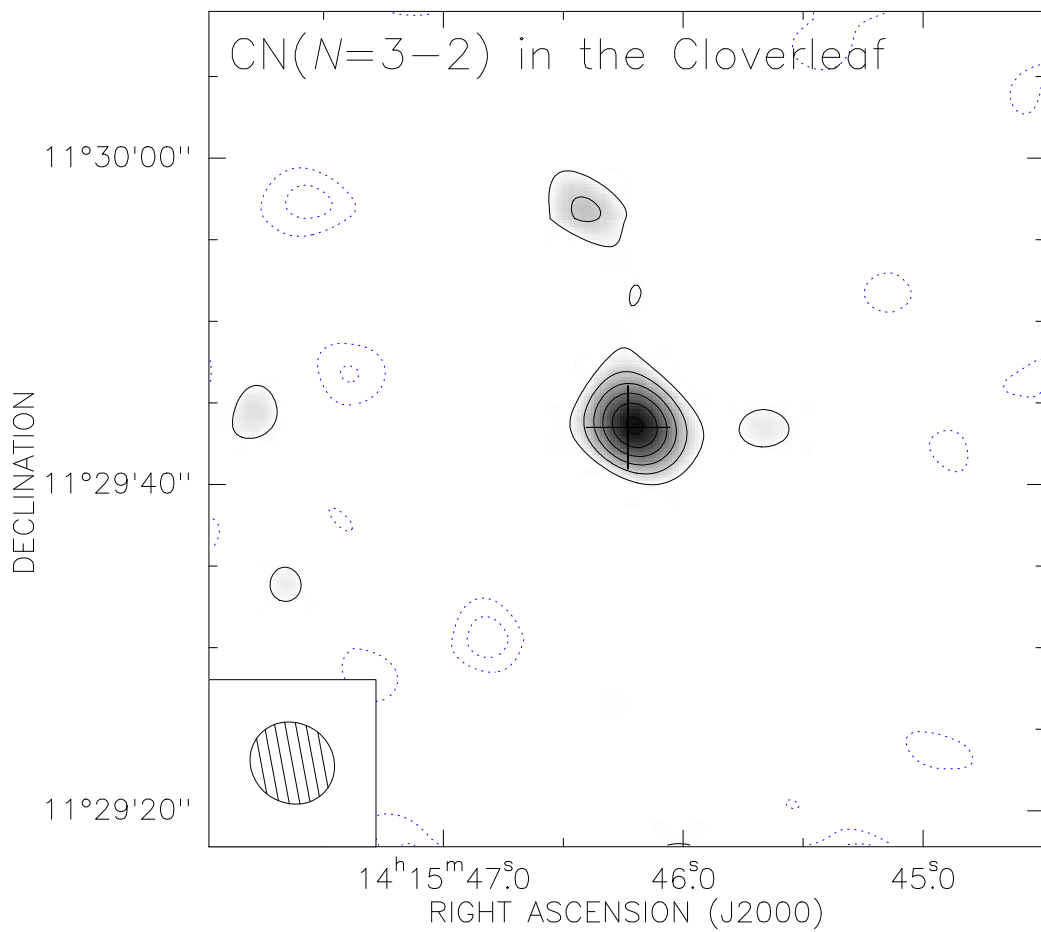


Figure 6.2: Velocity-integrated PdBI map of CN($N=3 \rightarrow 2$) emission towards the Cloverleaf quasar. At a resolution of $5.3'' \times 4.9''$ (as indicated in the bottom left corner), the source is unresolved. The cross indicates the geometrical center of the CO emission in the Cloverleaf (Alloin et al. 1997, see text). Contours are shown at $(-3, -2, 2, 3, 4, 5, 6, 7)\sigma$ ($1\sigma = 0.25 \text{ mJy beam}^{-1}$).

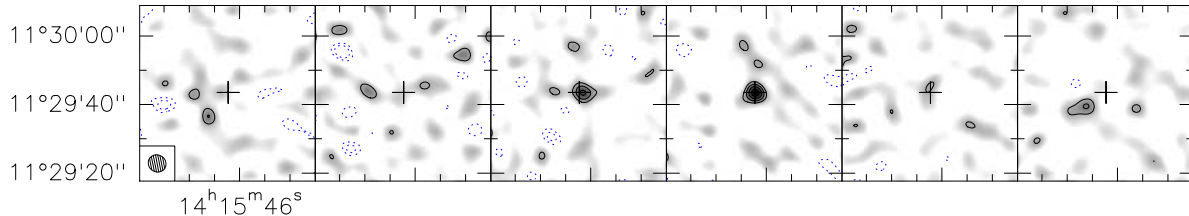


Figure 6.3: Channel maps of the CN($N=3\rightarrow 2$) emission (same region as shown in Fig. 6.2). One channel width is 80 MHz, or 252 km s^{-1} (at 95.4355, 95.5155, 95.5955, 95.6755, 95.7555, and 95.8355 GHz; frequencies increase with channel number). Contours are shown at $(-3, -2, 2, 3, 4, 5) \sigma$ ($1 \sigma = 0.4 \text{ mJy beam}^{-1}$). The beam size ($5.3'' \times 4.9''$) is shown in the bottom left corner; the cross indicates the same position as in Fig. 6.2.

6.6 Results

6.6.1 CN Maps and Spectrum

We have detected emission from the CN($N=3\rightarrow 2$) transition line towards the Cloverleaf quasar ($z = 2.56$). The velocity-integrated CN($N=3\rightarrow 2$) line map is shown in Figure 6.2. The cross indicates the geometrical center position of the resolved CO($J=7\rightarrow 6$) map at $\alpha = 14^{\text{h}}15^{\text{m}}46^{\text{s}}.233$, $\delta = +11^{\circ}29'43''.50$ (Alloin et al. 1997). The line emission is clearly detected at 7σ over a range of 596 km s^{-1} (190 MHz); the source appears unresolved. In Figure 6.3, six channel maps (252 km s^{-1} , or 80 MHz each) of the CN($N=3\rightarrow 2$) line emission are shown. At an rms of $0.4 \text{ mJy beam}^{-1}$, the line is detected at 4 and 5σ in the central channels, and the decline of the line intensity towards the line wings is clearly visible toward the outer channels, as expected.

Figure 6.4 shows the spectrum of the CN($N=3\rightarrow 2$) emission at a resolution of 63 km s^{-1} (20 MHz). Zero velocity corresponds to the tuning frequency of 95.603 GHz. The solid line shows a Gaussian fit to the spectrum. From the fit, we derive a line peak flux density of $1.94 \pm 0.24 \text{ mJy beam}^{-1}$, and a line FWHM of $666 \pm 97 \text{ km s}^{-1}$. The fit provides an upper limit for the continuum emission at the line frequency of $<0.25 \text{ mJy}$. From the channels assumed to be free of line emission, we derive a formal 3σ upper limit to the continuum peak flux density of $0.7 \text{ mJy beam}^{-1}$. Note that the model fit to the dust SED of the Cloverleaf by Weiß et al. (2003) would suggest a continuum flux of $\sim 0.3 \text{ mJy}$ at the CN($N=3\rightarrow 2$) line frequency, which agrees within the errors with the above estimates. However, as the continuum is not detected, we do not subtract a continuum component from the observed spectrum. This leads to an integrated CN($N=3\rightarrow 2$) line flux of $1.37 \pm 0.17 \text{ Jy km s}^{-1}$. The velocity offset of the Gaussian peak relative to the tuning frequency is $-105 \pm 38 \text{ km s}^{-1}$.

The FWHM of the Gaussian fit to the CN($N=3\rightarrow 2$) emission line suggests that its components 2 and 3 have similar peak strengths (different from 1:1.4 as predicted for the optically thin LTE case; Fig. 6.1), which may indicate that the emission is optically thick.

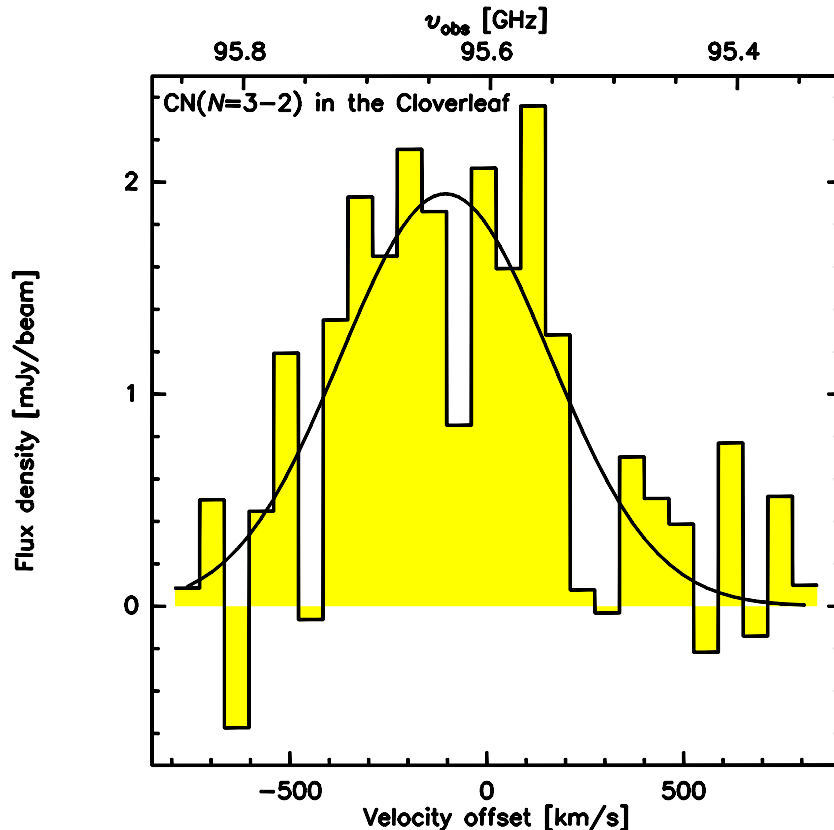


Figure 6.4: Spectrum of the CN($N=3\rightarrow 2$) emission at a resolution of 63 km s^{-1} (20 MHz). The velocity scale is relative to the tuning frequency of 95.603 GHz. The rms per velocity bin is 0.8 mJy. The solid line shows a Gaussian fit to the data.

Within the limited signal-to-noise ratio of the spectrum, the shape of the emission line remains compatible with a two-component structure. It may thus be possible that the two brightest HFS complexes (components 2 and 3) are detected individually, but observations at higher signal-to-noise ratio are needed to confirm this result. In any case, a double Gaussian fit to the line profile gives the same integrated line flux as the single Gaussian fit within the errors.

6.6.2 Line Luminosities

From our observations, we derive a CN($N=3\rightarrow 2$) line luminosity of $L'_{\text{CN}(3-2)} = (4.5 \pm 0.5) \times 10^9 \text{ K km s}^{-1} \text{ pc}^2$ (corrected for gravitational magnification, $\mu_L = 11$; see Table 6.1 for details). This corresponds to 11% of $L'_{\text{CO}(3-2)}$ (Weiß et al. 2003), 105% of $L'_{\text{HCN}(1-0)}$ (Solomon et al. 2003), and 129% of $L'_{\text{HCO}^+(1-0)}$ (Riechers et al. 2006b). Assuming that CN is thermally excited up to the $N=3\rightarrow 2$ transition (i.e., $L'_{\text{CN}(3-2)} = L'_{\text{CN}(1-0)}$) and that optical depth effects can be neglected, this would mean that CN emission in the Cloverleaf

Table 6.1: Molecular Line Luminosities in the Cloverleaf

Line	S_ν (mJy)	L' ($10^9 \text{ K km s}^{-1} \text{ pc}^2$)	Ref.
CN($N=3 \rightarrow 2$)	1.94 ± 0.24	4.5 ± 0.5	1
HCN($J=1 \rightarrow 0$)	0.24 ± 0.04	4.3 ± 0.5	2
HCO ⁺ ($J=1 \rightarrow 0$)	0.19 ± 0.03	3.5 ± 0.3	3
CO($J=3 \rightarrow 2$)	30 ± 1.7	42 ± 7	4

Notes—Luminosities are corrected for gravitational magnification.

References—(1) This work; (2) Solomon et al. 2003; (3) Riechers et al. 2006b; (4) Weiß et al. 2003.

is slightly brighter than that from the other high-density probes HCN and HCO⁺. This is remarkable, as HCN and HCO⁺ have higher critical densities than CN in the ground-state transition, but the critical density of CN($N=3 \rightarrow 2$) is higher than that of HCN($J=1 \rightarrow 0$) and HCO⁺($J=1 \rightarrow 0$). This may indicate a higher relative filling factor of CN relative to HCN and HCO⁺ or even a relatively high chemical abundance of CN. However, with the observations existing at present, it is not possible to disentangle excitation effects from chemical effects.

In addition, observations of HCN($J=4 \rightarrow 3$) towards the Cloverleaf quasar have shown that $L'_{\text{HCN}(4 \rightarrow 3)} / L'_{\text{HCN}(1 \rightarrow 0)} \leq 0.34$ (Solomon et al. 2003, their Table 1 caption; M. Guélin 2007, private communication). This ratio is significantly lower than 1, which implies that the $4 \rightarrow 3$ transition of HCN is subthermally excited. As the CN($N=3 \rightarrow 2$) transition has a somewhat lower but comparable critical density relative to HCN($J=4 \rightarrow 3$), it is likely that the CN($N=3 \rightarrow 2$) transition is also subthermally excited (i.e., $L'_{\text{CN}(3 \rightarrow 2)} < L'_{\text{CN}(1 \rightarrow 0)}$). This would be consistent the finding that CN is clearly subthermally excited in nearby LIRGs and ULIRGs (Aalto et al. 2002). This would also imply that CN is a *brighter* tracer of dense gas than HCN and HCO⁺ in this high-redshift quasar.

6.7 Discussion

In the following, we discuss various relationships between the emission observed in CN and other molecules (CO and HCN) and the far-IR continuum for a sample of local spiral/starburst galaxies (Henkel et al. 1988, 1998, 2007, private communication; Wang et al. 2004; additional CO/HCN/FIR data from Eckart et al. 1990; Nguyen-Q-Rieu et al. 1992; Mauersberger et al. 1996; Mao et al. 2000; Sanders et al. 2003), low- z (U)LIRGs (Aalto et al. 2002), and the Cloverleaf (this work; Solomon et al. 2003; Weiß et al. 2003) as shown in Figure 6.5. Note that due to the weak signal-to-noise ratio of 1σ , we do not include the CN($N=4 \rightarrow 3$) observations of APM 08279+5255 (Guélin et al. 2007, their Table 1) in this discussion.

As CO($J=1 \rightarrow 0$) is not yet detected toward the Cloverleaf, we assume in the following that CO is thermalized up to the $3 \rightarrow 2$ transition, i.e., $L'_{\text{CO}(1 \rightarrow 0)} = L'_{\text{CO}(3 \rightarrow 2)}$ (see Riechers et al. 2006a for justification). Both effects of thermal and subthermal excitation of the CN($N=3 \rightarrow 2$) emission line in the Cloverleaf are discussed; CO, CN, and HCN line intensi-

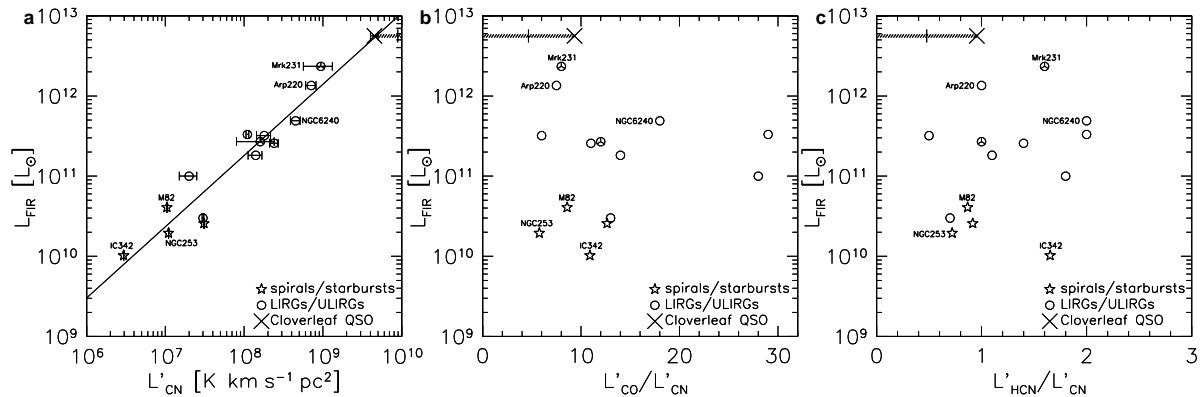


Figure 6.5: CN luminosity relations for a sample of local spiral/starburst galaxies, low- z IR-luminous galaxies, and the Cloverleaf. The Cloverleaf luminosities are corrected for gravitational lensing ($\mu_L = 11$). The two symbols with star insets denote tentative CN detections. The solid line is a least-squares fit to all data except the Cloverleaf. The error bars indicate the statistical errors of the line luminosity measurements. The excitation of the $\text{CN}(N=3 \rightarrow 2)$ transition in the Cloverleaf may be subthermal, which would affect the (extrapolated) $\text{CN}(N=1 \rightarrow 0)$ line luminosity as indicated by the horizontal, shaded regions. As an example, the vertical bars on the shaded regions show a case in which $L'_{\text{CN}(3-2)} = 0.5 L'_{\text{CN}(1-0)}$ in the Cloverleaf. See text for more details.

ties for all low- z galaxies were measured directly in the ground-state transitions; all quoted luminosities are thus $1 \rightarrow 0$ luminosities. We do not discuss effects of differential lensing⁴, as models indicate similar sizes for molecular and dust emission in the Cloverleaf (Solomon et al. 2003).

Wu et al. (2005) find a linear correlation between L'_{HCN} and L_{FIR} over 7–8 orders of magnitude in luminosity, which is believed to indicate that the dense gas tracer HCN is also a good estimator for star formation rates out to high z . If CN were to be a good tracer of dense, actively star-forming gas, a similar trend may be expected between L'_{CN} and L_{FIR} . Figure 6.5a shows that L'_{CN} correlates closely with L_{FIR} ; a linear least squares fit to all galaxies (excluding the Cloverleaf) yields $\log(L_{\text{FIR}}) = (0.89 \pm 0.09) \log(L'_{\text{CN}}) + (4.2 \pm 0.7)$. This slope may suggest a trend of decreasing CN/FIR luminosity ratio towards higher luminosities (see also Aalto et al. 2002). However, it also is consistent with unity within the statistical uncertainties (which are quite large due to the limited sample size) and systematic errors (e.g., different beam sizes for CN line and IR continuum observations) and thus with CN being a valuable tracer of star formation. The Cloverleaf agrees remarkably well with the relation defined by the low- z galaxies [even if the $\text{CN}(N=3 \rightarrow 2)$ transition is subthermally excited, as indicated by the horizontal bar on the shaded region], extending

⁴Note that Chartas et al. (2007) recently reported a likely microlensing event toward the Cloverleaf; however, this event took place close to 2000 April, so 3–7 yr before all of the molecular gas observations of this source discussed in this chapter (obtained between 2003 March and 2006 September).

the observed trend to higher luminosities and out to high redshift.

Gao & Solomon (2004a) observe a rise in dense gas fraction with L_{FIR} . The $L'_{\text{CO}}/L'_{\text{CN}}$ ratio may be considered (the inverse of) a tracer of the dense gas fraction. A significant spread in the $L'_{\text{CO}}/L'_{\text{CN}}$ ratio is found for the sample shown in Figure 6.5*b*, ranging from a few to almost a factor of 30. There is no obvious trend of $L'_{\text{CO}}/L'_{\text{CN}}$ with L_{FIR} ; however, the sample size is too small and heterogeneous to come to a definite conclusion. Note that due to the likely subthermal excitation of the $\text{CN}(N=3\rightarrow 2)$ transition (as indicated by the shaded region), the $L'_{\text{CO}}/L'_{\text{CN}}$ ratio may be considered an upper limit of the “intrinsic,” thermalization-corrected ratio of the $1\rightarrow 0$ transitions for the Cloverleaf.

Assuming that CN traces the UV field (which falls off rapidly with growing distance from star-forming regions, or an AGN), while HCN traces dense gas in general, it would be expected that the HCN/CN ratio stays constant or decreases with increasing L_{FIR} . In this scenario, a decrease in the HCN/CN ratio would correspond to an increase in the filling factor of UV-illuminated clouds with L_{FIR} . This would however also cause a rise in $L'_{\text{CN}}/L_{\text{FIR}}$, which is not observed (Fig. 6.5*a*). If differences in the relative chemical abundances of CN and HCN and optical depth/thermalization effects do not play a major role, one may thus expect $L'_{\text{HCN}}/L'_{\text{CN}}$ to stay fairly constant with L_{FIR} . Based on the observations of their subsample, Aalto et al. (2002) suggest that the HCN/CN intensity ratio may increase slightly with L_{FIR} . Such a trend however is not seen in the larger sample displayed in Figure 6.5*c* (note that $L'_{\text{HCN}}/L'_{\text{CN}}$ for the Cloverleaf may again be considered an upper limit due to possible subthermal excitation of $\text{CN}(N=3\rightarrow 2)$, as indicated by the shaded region). Clearly, improved statistics and better models are required to address this issue in more detail.

Chemical models suggest that CN is produced quite efficiently in the presence of a strong UV field, which also leads to an enhanced ionization rate (Boger & Sternberg 2005). The large observed $[\text{CN}]/[\text{HCN}]$ abundance ratio of ~ 5 toward the molecular disk of M82 may be indicative of a large dense PDR bathed in the intense radiation field of the starburst environment (Fuente et al. 2005), lending observational support to these models. Other models suggest that the relative abundance of CN may also be enhanced in regions with elevated X-ray ionization rates, such as AGN environments (Lepp & Dalgarno 1996; Meijerink & Spaans 2005). Especially in the Cloverleaf, where the central quasar is known to contribute a significant fraction to the heating of the gas and dust (Weiß et al. 2003; Solomon et al. 2003), such a scenario would appear reasonable and may explain the relatively high brightness of CN compared to other dense gas tracers in the Cloverleaf. However, note that in Figure 6.5*c*, the pure starburst galaxies show the brightest CN emission relative to HCN, and galaxies with a relatively strong AGN like Mrk 231 and NGC 6240 have some of the highest $L'_{\text{HCN}}/L'_{\text{CN}}$ ratios. This may indicate that the strength of the UV field in a starburst environment has a significantly greater impact on the global gas-phase production rate of CN in a galaxy than the strength of the X-ray field, lending further support to the supposition that CN is a good star formation tracer. We thus conclude that the XDR scenario alone does not explain the observed dense gas properties of the (U)LIRGs shown in Figure 6.5 without any further assumptions.

Overall, the Cloverleaf follows the $L'_{\text{CN}}-L_{\text{FIR}}$ relation as defined by nearby galaxies

of different types remarkably well and extends this relation to higher luminosities. This relation now appears to hold over almost 3 orders of magnitude. If these findings were to hold for other distant quasars, CN would be an excellent probe of dense molecular environments out to high redshifts. The higher order transitions of CN also appear to be brighter than those of other dense gas tracers like HCN. This may prove to be of particular importance for future high- z studies with the Atacama Large Millimeter/submillimeter Array (ALMA), which will offer the opportunity to probe to fainter galaxy populations in general, but will also be restricted to the higher order transitions of the most common dense molecular gas tracers (typically $3\rightarrow 2$ and higher at $z > 2$).

It is a pleasure to thank my collaborators on this project:

Fabian Walter (MPIA), Pierre Cox (IRAM), Chris Carilli (NRAO), Axel Weiß (MPIfR), Frank Bertoldi (AIfA), and Roberto Neri (IRAM).

CHAPTER PUBLISHED AS:

Riechers, D. A., Walter, F., Cox, P., Carilli, C. L., Weiß, A., Bertoldi, F., & Neri, R., ‘*Detection of Emission from the CN Radical in the Cloverleaf Quasar at $z=2.56$* ’, 2007, ApJ, 666, 778

Chapter 7

Dense Molecular Gas IV: CS in a $z=2.56$ Quasar Host Galaxy

7.1 Context

The most common probe of molecular gas after CO, HCN, and HCO⁺ is CS. Carbon monosulfide is an important part in studies of molecular gas, as it traces regions with different (intermediate) densities and temperatures than CO, HCN, and HCO⁺. In this chapter, its first detection at high redshift is reported. As for HCO⁺ and CN, this initial high redshift detection was achieved by studying the Cloverleaf. The detected CS emission line is even by a factor of ~ 3 less luminous than the detected lines of the other dense gas tracers (HCN, HCO⁺, and CN). To study a possible excitation bias, the Schmidt-Kennicutt relation for CS is not only studied in the ground transition, but also in a higher J transition. This reveals a clear excitation bias for galaxies fainter (in the FIR) than ULIRGs, but no significant bias for the brightest galaxies. The most basic explanation for this difference could be that the ISM in the more luminous systems is denser, causing the higher excitation. This has to be verified by studying the excitation of CS in the Cloverleaf directly in a future investigation. The (poorly constrained) $L'_{\text{CS}}-L_{\text{FIR}}$ relation for the ground-state transition, however, shows the same linear dependence as for other high density molecular gas tracers.

7.2 Abstract

We report the detection of CS($J=3\rightarrow 2$) emission towards the Cloverleaf quasar ($z = 2.56$) based on observations with the Very Large Array. This is the first detection of emission from carbon monosulfide at high redshift. CS emission is a tracer of dense molecular hydrogen gas [$n(\text{H}_2) \gtrsim 5 \times 10^4 \text{ cm}^{-3}$] within star-forming molecular clouds. In nearby galaxies, CS is the strongest nonmaser species after CO, HCN, and HCO⁺. We derive a lensing-corrected CS($J=3\rightarrow 2$) line luminosity of $L'_{\text{CS}(3-2)} = (1.5 \pm 0.3) \times 10^9 \text{ K km s}^{-1} \text{ pc}^2$. Assuming that CS($J=3\rightarrow 2$) is thermally excited, the ratio between CS($J=1\rightarrow 0$) luminosity

and far-infrared luminosity falls within the scatter of the tentative relationship found for low- z normal, starburst, and ultraluminous infrared galaxies [ULIRGs]. Due to the low excitation of CS in nearby normal and starburst galaxies, this does not hold for a directly determined relationship between the CS($J=3\rightarrow 2$) and FIR luminosities. We find a CO/CS luminosity ratio of 27 ± 7 , and that CS($J=3\rightarrow 2$) is about three times less luminous than other dense gas tracers in this source (HCN, HCO⁺, and CN). These ratios agree within a factor of 2 with those in Arp 220, the only nearby ULIRG for which all ratios can currently be determined. If our results were to hold for other galaxies the high redshift detection of CS thus appears to confirm the trend seen for CO, HCN, HCO⁺, and CN that ULIRGs are, within certain limitations, good templates for the molecular composition and excitation of the extreme gas-rich systems at $z > 2$. This implies that these molecules are good probes of environments of different temperatures and densities, and that future studies of their excitation will help to understand the physical conditions in the dense molecular environments of distant starburst systems.

7.3 Introduction

One of the prime goals in studies of galaxy formation and evolution at early cosmic times is to better understand how star formation relates to these processes. A particularly useful diagnostic to study star formation is its close connection to the molecular interstellar medium (ISM) that harbors and feeds it. The molecular phase of the ISM is most commonly probed through its cooling lines, primarily the rotational transitions of CO. CO line emission has been studied in 43 galaxies at $z > 1$ to date, and has revealed large gas masses of $> 10^{10} M_{\odot}$ in practically all these distant systems. (see Solomon & Vanden Bout 2005 for a review).

Due to the fact that the critical densities of only a few times 10^2 to 10^3 cm^{-3} and temperatures of $< 20 \text{ K}$ necessary to excite the lower J rotational transitions of CO are low relative to the median properties of the molecular reservoirs in most galaxies, CO is a good (and, due to its high abundance, bright) indicator of the total amount of molecular gas in a galaxy. However, this implies that CO is not particularly well suited to select the dense cores within the molecular reservoirs, where the actual sites of star formation reside.

In the local universe, the most common tracers of dense molecular environments are HCN, HCO⁺, and CS (see Omont 2007 for a recent review). HCN and HCO⁺ have large dipole moments ($\mu_{\text{D}}^{\text{HCN}} = 2.98$ Debye, $\mu_{\text{D}}^{\text{HCO}^+} = 3.30$ Debye), leading to high critical densities to collisionally excite their lower J transitions. CS has a somewhat smaller dipole moment ($\mu_{\text{D}}^{\text{CS}} = 1.96$ Debye). In general, all three molecules are good tracers of environments of densities of $n_{\text{H}_2} \sim 10^5 - 10^6 \text{ cm}^{-3}$ and higher, where CS traces somewhat warmer, less dense environments. Together with CO, they are sensitive probes of temperature, density, and abundance (and their gradients) within molecular clouds, and thus can constrain the properties of star formation within these regions.

Due to the fact that emission lines from high density molecular tracers are typically by an order of magnitude fainter than those of CO, studies in the distant universe are

challenging. HCN and HCO⁺ have been detected toward some of the brightest $z > 2$ sources. A main result in this context is the finding that the HCN and HCO⁺ luminosities correlate linearly with the far-infrared (FIR) luminosity (which is commonly used to estimate star formation rates in dust and gas rich galaxies) over many orders of magnitude, from Galactic dense cores to high redshift quasars (Wu et al. 2005; Riechers et al. 2006b). However, note that there is an indication that the high redshift sources may deviate from the HCN-FIR luminosity relation toward somewhat higher FIR luminosity (Gao et al. 2007), possibly due to a higher median gas density in those sources (Krumholz & Thompson 2007). CS, the third of the standard dense gas tracers, has not been detected at high redshift to date.

In this chapter, we report the first high- z detection of CS emission, which was observed in the $J=3 \rightarrow 2$ transition toward the Cloverleaf quasar ($z = 2.56$) with the NRAO Very Large Array (VLA).¹ Because of its strong gravitational magnification (magnification factor $\mu_L = 11$; Venturini & Solomon 2003), the Cloverleaf is the brightest CO source at high redshift (e.g., Barvainis et al. 1994) and one of the most prolific sources of molecular lines beyond $z=2$. It was the first $z > 2$ source to be detected in HCN (Solomon et al. 2003), HCO⁺ (Riechers et al. 2006b), and CN (Riechers et al. 2007a) emission. It was also detected in both C I fine-structure lines (Barvainis et al. 1997; Weiß et al. 2003, 2005b). We use a standard concordance cosmology throughout, with $H_0 = 71 \text{ km s}^{-1} \text{ Mpc}^{-1}$, $\Omega_m = 0.27$, and $\Omega_\Lambda = 0.73$ (Spergel et al. 2003, 2007).

7.4 Observations

We observed the CN($N=3 \rightarrow 2$) transition line ($\nu_{\text{rest}} = 146.9690330 \text{ GHz}$) toward H1413+117 (the Cloverleaf quasar) using the VLA in D configuration on 2006 January 9. At the target redshift of $z=2.55784$ (Weiß et al. 2003), the line is shifted to 41.3085 GHz (7.26 mm). The total integration time amounts to 8 hr. Observations were performed in fast-switching mode with 23 antennas, using the nearby source 14160+13204 (distance to the Cloverleaf: 1.8°) was for pointing, secondary amplitude, and phase calibrations. The fast-switching cycles were set to a total length of 250 s, with 200 s on source and 50 on the calibrator. For primary flux calibration, several 3C 286 was observed.

Two intermediate frequency bands (IFs) of 50 MHz (corresponding to 363 km s^{-1} at the redshifted CS($J=3 \rightarrow 2$) line frequency) each were observed simultaneously. The first IF was tuned to the redshifted CS($J=3 \rightarrow 2$) emission line at 41.3149 GHz, the closest possible tuning frequency of the VLA correlator, relative to the redshifted line center. The FWHM of the CO($J=3 \rightarrow 2$) line is $416 \pm 6 \text{ km s}^{-1}$ (Weiß et al. 2003). The offset from the line center thus corresponds to only 11% of the FWHM linewidth. Assuming that the CS($J=3 \rightarrow 2$) line has a width of 70%–100% of the width of the CO($J=3 \rightarrow 2$) line, we estimate that our setup misses 20%–30% of the total line flux due to the missing coverage of the line wings. The second IF was tuned to 41.4649 GHz to measure the source’s continuum close to the line frequency.

¹The National Radio Astronomy Observatory is a facility of the National Science Foundation, operated under cooperative agreement by Associated Universities, Inc.

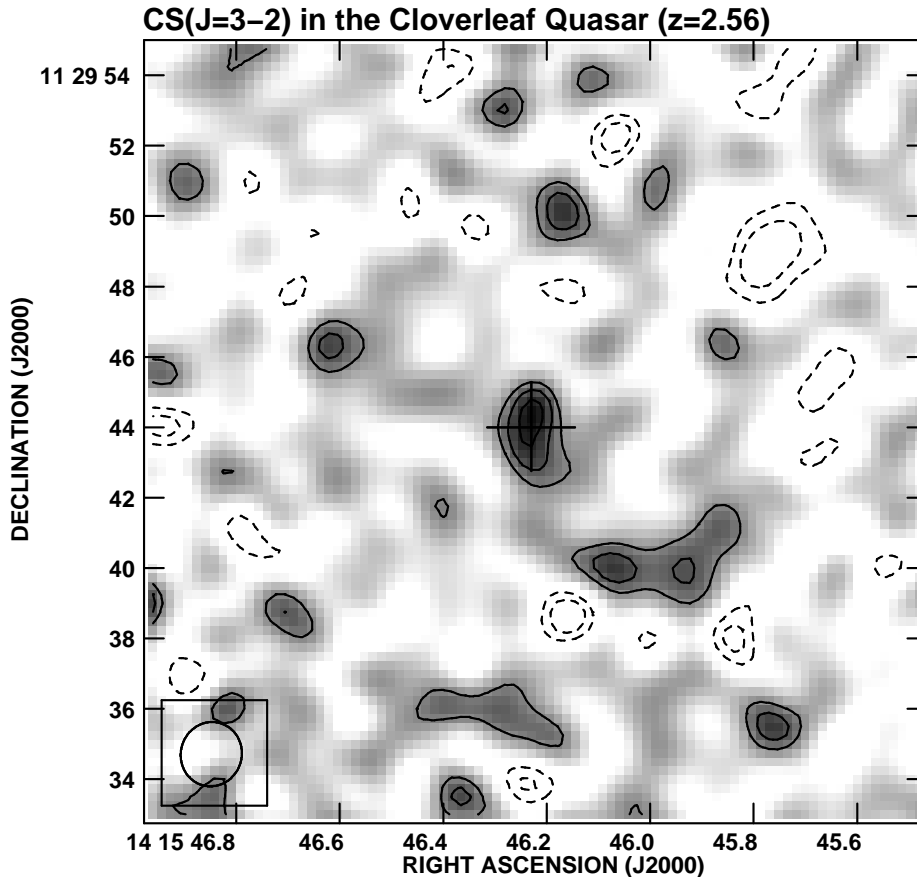


Figure 7.1: VLA map of CS($J=3\rightarrow 2$) emission towards the Cloverleaf quasar. At a resolution of $1.8''\times 1.7''$ (as indicated in the lower left), the source is marginally resolved. The cross indicates the geometrical center of the CO emission in the Cloverleaf. Contours are shown at $(-3, -2, 2, 3, 4)\sigma$ ($1\sigma = 52 \mu\text{Jy beam}^{-1}$).

For data reduction and analysis, the AIPS package was used. The CO($J=3\rightarrow 2$) line dataset was generated by subtracting a CLEAN component model of the continuum emission from the visibility data. All data were mapped using the CLEAN algorithm and “natural” weighting; this results in a synthesized beam of $1.8''\times 1.7''$ (14 kpc at $z = 2.56$). The final rms in the line map is $52 \mu\text{Jy beam}^{-1}$.

7.5 Results

We have detected emission from the CS($J=3\rightarrow 2$) transition line toward the Cloverleaf quasar ($z = 2.56$). The source appears to be marginally resolved in both the continuum and the CS line maps. Two-dimensional Gaussian fitting yields a continuum flux density of $204 \pm 55 \mu\text{Jy}$. This rest-frame 147.5 GHz continuum flux is in agreement with the radio spectral

Table 7.1: Molecular Line Luminosities in the Cloverleaf

Line	L' ($10^9 \text{ K km s}^{-1} \text{ pc}^2$)	L'/L'_{CS}	Ref.
CS($J=3 \rightarrow 2$)	1.5 ± 0.3	1	1
CO($J=3 \rightarrow 2$)	42 ± 7	27 ± 7	2
CN($N=3 \rightarrow 2$)	4.5 ± 0.5	2.9 ± 0.7	3
HCN($J=1 \rightarrow 0$)	4.3 ± 0.5	2.8 ± 0.7	4
HCO ⁺ ($J=1 \rightarrow 0$)	3.5 ± 0.3	2.3 ± 0.5	5

Notes—Luminosities are corrected for gravitational magnification.

References—(1) This work; (2) Weiß et al. 2003; (3) Riechers et al. 2007a (4) Solomon et al. 2003; (5) Riechers et al. 2006b.

energy distribution of the source determined based on continuum fluxes at lower frequencies (Beelen et al. 2006; Riechers et al. 2006b). The continuum-subtracted CS($J=3 \rightarrow 2$) line map is shown in Figure 7.1. The cross indicates the geometrical center position of the resolved CO($J=7 \rightarrow 6$) map at $\alpha = 14^{\text{h}}15^{\text{m}}46^{\text{s}}.233$, $\delta = +11^{\circ}29'43''.50$ (Alloin et al. 1997). The deconvolved source size from the Gaussian fit is in good agreement with the size of the resolved structure seen in CO($J=7 \rightarrow 6$). The line is detected at $\sim 5\sigma$ over a range of 363 km s^{-1} . We find a line flux density of $245 \pm 52 \mu\text{Jy}$ over the 363 km s^{-1} bandpass, corresponding to $0.09 \pm 0.02 \text{ Jy km s}^{-1}$. We thus derive a lensing-corrected CS($J=3 \rightarrow 2$) line luminosity of $L'_{\text{CS}} = (1.5 \pm 0.3) \times 10^9 \text{ K km s}^{-1} \text{ pc}^2$. Note that this corresponds to more than ten times the CS($J=3 \rightarrow 2$) luminosity of Arp 220 (Solomon et al. 1990).

We summarize our results in Table 7.1 together with the line fluxes and luminosities for CO, HCN, HCO⁺, and CN (see Table caption for references). We find a CO($J=3 \rightarrow 2$)/CS($J=3 \rightarrow 2$) line luminosity ratio of 27 ± 7 . If both transitions are thermalized, L'_{CS} thus is less than 4% of L'_{CO} . We also find that L'_{CS} is on average only 38% as bright as the other tracers of dense gas detected in this source (HCN, HCO⁺, and CN). Note that the critical density to excite the CS($J=3 \rightarrow 2$) transition is comparable to that of the HCN($J=1 \rightarrow 0$) and HCO⁺($J=1 \rightarrow 0$) transitions, and that its minimum excitation temperature ($T_{\text{ex,min}} = 14.1 \text{ K}$) is only a few Kelvin above the cosmic microwave background temperature at the Cloverleaf’s redshift ($T_{\text{CMB}} = 9.7 \text{ K}$). As HCO⁺($J=1 \rightarrow 0$) in this source is likely close to thermalized in the Cloverleaf (Riechers et al. 2007, in prep.), this means that CS($J=3 \rightarrow 2$) is likely to be also close to thermalized. The fact that the CS($J=3 \rightarrow 2$) luminosity is significantly lower than the HCO⁺($J=1 \rightarrow 0$) luminosity thus may indicate either a difference in optical depth or chemical abundance, or a different projected distribution of both molecules within the quasar host galaxy.

7.6 Discussion

Relationships between molecular line luminosities (L') as tracers of molecular gas mass and the far-infrared (FIR) luminosity (L_{FIR}) as a tracer of star formation rate (SFR) are believed to be good diagnostics for star-forming environments, and the overall efficiency of mass to be transformed into stars (Schmidt 1959; Kennicutt 1998a, 1998b; Solomon et al. 1997; Gao & Solomon 2004a, 2004b). These relationships and their slopes can be

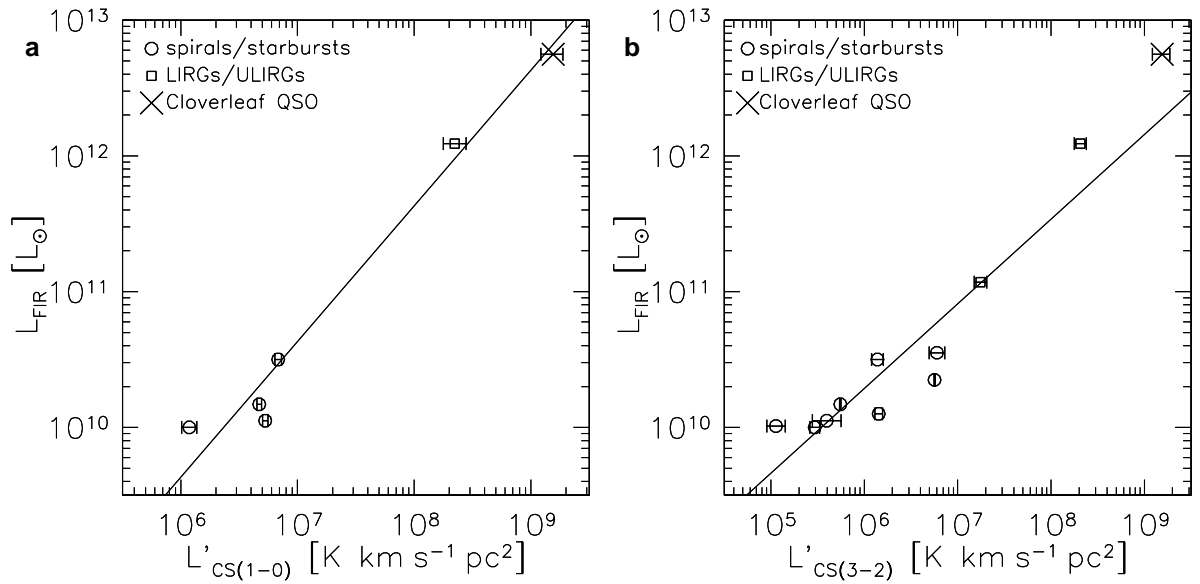


Figure 7.2: Relations between the CS and FIR luminosities for a sample of local spiral/starburst galaxies, low- z IR-luminous galaxies, and the Cloverleaf. The Cloverleaf luminosities are corrected for gravitational lensing ($\mu_L = 11$). The solid lines are least-squares fits to all data except the Cloverleaf. The error bars indicate the statistical errors of the line luminosity measurements. *Left*: Relation between CS($J=1\rightarrow 0$) and FIR luminosities. *Right*: Relation between CS($J=3\rightarrow 2$) and FIR luminosities.

understood based on the relation between the median gas density in a galaxy and the critical density of the molecule under examination, and the dependence of the SFR on the dynamical time scale of molecular cloud collapse (which also depends on the gas density; see Krumholz & Thompson 2007 for a model, and discussion by Riechers et al. 2007b).

In general, such relationships have a linear slope for molecular line transitions that have high critical densities relative to the median density in a galaxy (and thus pick out the densest regions where star formation is believed to occur), and have a nonlinear slope for transitions with low critical densities that trace the bulk of the emission (assuming thermal equilibrium). Relations with a linear slope are thus considered good tracers of star-forming cores, and thus an indirect measure for the star formation rate (e.g., Gao & Solomon 2004a, 2004b; Wu et al. 2005).

We here study the relation between L'_{CS} and L_{FIR} for a sample of local spiral/starburst galaxies and (U)LIRGs (Mauersberger & Henkel 1989; Mauersberger et al. 1989; Solomon et al. 1990; Paglione et al. 1995; Curran et al. 2001; Wang et al. 2004; Martín et al. 2006; Greve et al. 2006), and the Cloverleaf (Figure 7.2).

In Figure 7.2a, the relationship between $L'_{\text{CS}(1-0)}$ and L_{FIR} is shown. For Arp 220, the only nearby ULIRG in the sample (*square symbol*), the CS($J=1\rightarrow 0$) luminosity is extrapolated from the CS($J=2\rightarrow 1$) and CS($J=3\rightarrow 2$) transitions (Greve et al. 2006). Note that the CS($J=3\rightarrow 2$) transition is almost thermalized, as the difference between the CS($J=2\rightarrow 1$) and CS($J=3\rightarrow 2$) brightness temperatures is only 8% for this source, i.e., well within the observational uncertainties. For the Cloverleaf, we assume that the CS($J=3\rightarrow 2$) transition is thermalized, in agreement with the CO and HCO⁺ excitation in this source (Barvainis et al. 1997; Riechers et al. 2007, in prep.). Unfortunately, only four nearby galaxies were measured directly in the CS($J=1\rightarrow 0$) transition. A linear least squares fit to all galaxies (excluding the Cloverleaf) yields $\log(L_{\text{FIR}}) = (1.00 \pm 0.16) \log(L'_{\text{CS}(1-0)}) + (3.6 \pm 1.1)$. Even though the fit is poorly defined due to the small sample size, this suggests a strong, linear relation between $L'_{\text{CS}(1-0)}$ and L_{FIR} , and that CS($J=1\rightarrow 0$) is a good tracer of dense, star-forming cores in these galaxies. This is expected for the normal galaxies in the sample, as the typical median molecular gas density in such galaxies is significantly lower than the critical density of CS($J=1\rightarrow 0$) ($n_{\text{crit}}^{\text{CS}(1-0)} \simeq 5 \times 10^4 \text{ cm}^{-3}$). The Cloverleaf also follows this relation remarkably well, in spite of the fact that it lies above the local $L'_{\text{HCN}(1-0)}-L_{\text{FIR}}$ relation (as do all other high- z HCN detections, Gao et al. 2007), even though HCN($J=1\rightarrow 0$) and CS($J=3\rightarrow 2$) have comparable critical densities. However, note that the uncertainties in the CS-FIR relation are too large to pick up such a trend if present. A nearby sample of statistically significant size is required to further investigate this issue.

In Figure 7.2b, the relationship between $L'_{\text{CS}(3-2)}$ and L_{FIR} is shown. All values are directly measured CS($J=3\rightarrow 2$) luminosities. The statistics are better than for the $L'_{\text{CS}(1-0)}-L_{\text{FIR}}$ relation. A linear least squares fit to all galaxies (excluding the Cloverleaf) yields $\log(L_{\text{FIR}}) = (0.62 \pm 0.09) \log(L'_{\text{CS}(3-2)}) + (6.5 \pm 0.6)$. This fit is clearly non-linear. While all galaxies with $L_{\text{FIR}} < 10^{12} L_{\odot}$ appear to follow a trend, Arp 220 (the nearby ULIRG in the sample) and the Cloverleaf clearly lie above this trend. This simply reflects the excitation bias within the sample: the median densities in normal nearby galaxies are too

low to significantly excite CS($J=3\rightarrow 2$). The CS spectral line energy distribution in the nearby starburst galaxy NGC 253 already peaks at CS($J=3\rightarrow 2$), which, in contrast to Arp 220 and the Cloverleaf, thus is clearly subthermally excited in this galaxy (Martín et al. 2005). This naturally explains the apparent increase in the $L_{\text{FIR}}/L'_{\text{CS}}$ ratio as traced by CS($J=3\rightarrow 2$). Although the statistics are significantly better, the $L'_{\text{CS}(3-2)}-L_{\text{FIR}}$ thus is not a good diagnostic for star formation properties without being able to correct for the excitation properties of every single galaxy in the sample.

We thus conclude that the $L'_{\text{CS}(1-0)}-L_{\text{FIR}}$ relation appears to be a useful diagnostic for star formation properties that however lacks statistical significance at present, even in the nearby universe. The Cloverleaf follows this relation and extends it toward higher luminosity. After HCN, HCO⁺ and CN, CS now is the fourth dense gas tracer that appears to follow a linear relation with the FIR luminosity. Only HCN currently has the statistics to detect small deviations (as found towards high luminosity; Gao et al. 2007; Riechers et al. 2007b). This may suggest that the properties of nearby ULIRGs can indeed be used as templates to further study the properties of the extreme high redshift systems. Future excitation studies of above dense gas tracers thus may reveal whether or not the trend in the HCN-FIR relation at high luminosity is indeed due to a higher density of the starbursts, or just a bias of HCN as a tracer of dense gas.

It is a pleasure to thank my collaborators on this project:

Fabian Walter (MPIA), Chris Carilli (NRAO), Axel Weiß (MPIfR), and Frank Bertoldi (AIfA).

CHAPTER IS A MANUSCRIPT IN PREPARATION:

Riechers, D. A., Walter, F., Carilli, C. L., et al., ‘*Carbon Monosulfide in the Host Galaxy of the Cloverleaf Quasar at $z=2.56$* ’, in preparation

Chapter 8

Dense Molecular Gas V: Search for H₂O at $z=3.2$

8.1 Context

In this chapter, a search for redshifted H₂O is presented. Even though water is the third most abundant molecule in the universe, it is not one of the standard dense gas tracers (the focus of this study thus differs from the previous chapters). This is mostly due to the fact that the strong atmospheric water lines prohibit observation of all but the brightest extraterrestrial sources. This, however, is only true at $z=0$. For significantly redshifted sources, some water lines get redshifted into standard observing windows. Due to the lack of nearby studies (and the relatively complicated rotational level splitting), observations of H₂O are not a particular focus of high redshift studies. In a sensitivity-limited field of study such as high- z molecular line observations (rotational transitions of molecules different from CO are by at least an order of magnitude fainter than CO), it still has the potential to become an important dense gas tracer. This is due to the fact that star-forming cores, such as Orion, show maser-amplified emission in some millimeter and centimeter transitions of water, which can be significantly brighter than those of primarily thermally excited dense gas tracers. It thus may be possible that the extreme starbursting systems at high redshift also host conditions that allow maser amplification. One of these masing transitions is the 183 GHz H₂O($3_{13} \rightarrow 2_{20}$) transition, which was studied here in a CO-bright quasar at $z=3.2$.

8.2 Abstract

We present a search for 183 GHz H₂O($3_{13} \rightarrow 2_{20}$) emission in the infrared-luminous quasar MG 0751+2716 with the NRAO Very Large Array (VLA). At $z = 3.200 \pm 0.001$, this water emission feature is redshifted to 43.6 GHz. Unlike the faint rotational transitions of HCN (the standard high-density tracer at high z), H₂O($3_{13} \rightarrow 2_{20}$) is observed with high maser amplification factors in Galactic star forming regions. It therefore holds the potential to trace high-density star-forming regions in the distant universe. If indeed all star-forming

regions in massively star-forming galaxies at $z > 3$ have physical properties similar to those of, e.g., the Orion or W49N molecular cloud cores, the flux ratio between the maser-amplified H₂O(3₁₃→2₂₀) and the thermally excited CO($J=1$ →0) transitions may be as high as factor of 20 (but has to be corrected by their relative filling factor). MG 0751+2716 is a strong CO($J=4$ →3) emitter, and therefore one of the most suitable targets to search for H₂O(3₁₃→2₂₀) at cosmological redshifts. Our search resulted in an upper limit in line luminosity of $L'_{\text{H}_2\text{O}} < 0.6 \times 10^9 \text{ K km s}^{-1} \text{ pc}^2$. Assuming a brightness temperature of $T_b(\text{H}_2\text{O}) \simeq 500 \text{ K}$ for the maser emission and CO properties from the literature, this translates to a H₂O(3₁₃→2₂₀)/CO($J=4$ →3) area filling factor of less than 1%. However, this limit is not valid if the H₂O(3₁₃→2₂₀) maser emission is quenched, i.e., if the line is only thermally excited. We conclude that, if our results were to hold for other high- z sources, H₂O does not appear to be a more luminous alternative to HCN to detect high-density gas in star-forming environments at high redshift.

8.3 Introduction

Over the past several years, massive amounts of dust and gas have been detected in distant quasars, allowing us to study the properties of molecular gas in the early epoch of galaxy formation. Molecular gas in high-redshift galaxies is commonly traced by CO emission and to date has been found in more than 30 galaxies at $z > 2$, out to the highest redshift quasar, SDSS J1148+5251 at $z = 6.42$ (Walter et al. 2003, 2004; Bertoldi et al. 2003b). The observed molecular gas masses in excess of $10^{10} M_\odot$ provide the requisite material for star formation (SF; e.g., Solomon & Vanden Bout 2005).

The presence of abundant molecular gas, the fuel for SF, has led to the hypothesis that the tremendous far-infrared (FIR) luminosities ($> 10^{12} L_\odot$) of these high-redshift objects are powered not only by active galactic nuclei (AGNs) but also by major starbursts, suggesting that this population represents the formation of large spheroidal galaxies beyond redshift 2 (Blain et al. 2002). However, the relative contribution to the FIR luminosity from dust heated by SF and AGN activity in high- z sources remains subject to discussion (e.g., Andreani et al. 2003).

While the lower J transitions of CO are a good indicator for the total molecular gas content of a system (e.g., Carilli et al. 1999, 2002b; Riechers et al. 2006a), they can be excited at relatively low densities; the critical density lies at only $n_{\text{H}_2} \simeq 10^3 \text{ cm}^{-3}$. Hence, it is a relatively poor tracer of the denser gas directly involved in massive SF. The standard tracer of the dense molecular gas phase is HCN, and the critical density required to excite its lower J transitions is $n_{\text{H}_2} \simeq 10^5 \text{ cm}^{-3}$ (due to a higher dipole moment in comparison to CO). In this context, recent studies of the dense molecular gas phase in local ($z < 0.3$) luminous and ultraluminous infrared galaxies (LIRGs/ULIRGs) have shown a correlation between the HCN luminosity and the star-formation rate (SFR) as traced by the FIR luminosity. This correlation is much tighter than that between the CO and FIR luminosities (Solomon et al. 1992c; Gao & Solomon 2004a, 2004b). Thus, observations of HCN toward high- z sources hold the potential to pin down the contribution of SF to the total FIR luminosity.

Unfortunately, emission lines from HCN in LIRGs/ULIRGs are typically fainter than those of CO by a factor of 4–10 (or even a factor of 25–40 in ordinary spiral galaxies; Gao & Solomon 2004a), which hinders systematic HCN surveys at cosmological distances using current telescopes. Up to now, deep observations of HCN at $z > 2$ have resulted in four detections and four upper limits (Solomon et al. 2003; Vanden Bout et al. 2004; Carilli et al. 2005; Wagg et al. 2005).

Due to the faintness of emission connected with thermally excited rotational transitions of HCN, it is important to investigate whether another physical process can be found that produces emission lines with significantly higher luminosities. The 183 GHz ($3_{13} \rightarrow 2_{20}$) emission line of para-H₂O holds the potential to be such a tracer: in warm, dense, star-forming regions ($n_{\text{H}_2} > 10^5 \text{ cm}^{-3}$), this line is collisionally pumped at relatively low kinetic temperatures ($T_{\text{kin}} = 50 - 100 \text{ K}$; e.g., Cernicharo et al. 1994). In contrast to compact H₂O maser sources at 22 GHz, the 183 GHz maser emission is spatially extended in high-mass (Orion, Cernicharo et al. 1994; W49N, González-Alfonso et al. 1995; Sgr B2, Cernicharo et al. 2006) and even low-mass (HH7–11; Cernicharo et al. 1996) star-forming regions. Due to maser amplification, the observed 183 GHz H₂O($3_{13} \rightarrow 2_{20}$) line brightness temperatures in these regions exceed those observed in CO($J=1 \rightarrow 0$) by up to a factor of 20 (e.g., for Orion, Cernicharo et al. 1994; Schulz et al. 1995).

However, the H₂O($3_{13} \rightarrow 2_{20}$) line is strongly absorbed by the terrestrial atmosphere, rendering detection in nearby galaxies very difficult. The first successful extragalactic detection of H₂O($3_{13} \rightarrow 2_{20}$) has been reported in NGC 3079 (Humphreys et al. 2005). Previous searches in low- z LIRGs/ULIRGs have only resulted in upper limits (Combes et al. 1997). Recently, the H₂O($3_{13} \rightarrow 2_{20}$) transition has also been detected towards Arp 220 (Cernicharo et al. 2006; see Table 8.1). At high redshift, only the ($2_{11} \rightarrow 2_{02}$) transition of para-H₂O at 752.033 GHz (rest frame) has tentatively been detected in the $z \simeq 2.3$ QSO IRAS F10214+4724 (Encrenaz et al. 1993; Casoli et al. 1994).

In this chapter, we report on a search for maser emission from the 183 GHz water line in the strongly lensed, radio-loud $z = 3.2$ QSO MG 0751+2716 using the VLA.¹ Due to its strong magnification, MG 0751+2716 is the brightest CO source at high redshift that can be observed in the H₂O($3_{13} \rightarrow 2_{20}$) transition with the VLA. Its L'_{CO} and L_{FIR} (see Table 8.1) are comparable to local starburst galaxies like Arp 220. This suggests that this source is undergoing massive star-formation, which contributes significantly to its FIR luminosity (e.g., Fig. 8 in Solomon & Vanden Bout 2005). We use a standard concordance cosmology throughout, with $H_0 = 71 \text{ km s}^{-1} \text{ Mpc}^{-1}$, $\Omega_m = 0.27$, and $\Omega_\Lambda = 0.73$ (Spergel et al. 2003).

8.4 Observations

We observed the H₂O($3_{13} \rightarrow 2_{20}$) transition ($\nu_{\text{rest}} = 183.3101 \text{ GHz}$) towards MG 0751+2716 using the VLA in D configuration on 2004 June 19 and 27. At the target z of 3.200, this transition is redshifted to 43.6453 GHz (6.87 mm). The total on-sky integration time

¹The Very Large Array is a facility of the National Radio Astronomy Observatory, operated by Associated Universities, Inc., under a cooperative agreement with the National Science Foundation.

amounts to 16 hr. The observations were performed in fast-switching mode using the nearby source 0745+241 for secondary amplitude and phase calibration. The observations were carried out under good weather conditions with 26 antennas. The phase stability in all runs was good (typically $<15^\circ$ rms for the longest baselines). For primary flux calibration, 3C 286 was observed during each run.

Two 50 MHz (corresponding to 344 km s^{-1} at 43.6 GHz) intermediate frequencies (IFs) were observed simultaneously in the so-called quasi-continuum mode. One IF was centered on the line frequency at 43.6351 GHz (closest possible tuning frequency, offset by $\sim 70 \text{ km s}^{-1}$ from the CO($J=4\rightarrow 3$) line center of Barvainis et al. 2002), and the second IF was centered at two frequencies symmetrically offset by 150 MHz (1030 km s^{-1} , i.e., at 43.4851 and 43.7851 GHz) from the line frequency to monitor the 7 mm continuum of MG 0751+2716 simultaneously. Despite the small offset from the line center, the frequency/velocity coverage is well matched to a line with a FWHM similar to the CO($J=4\rightarrow 3$) line reported by Barvainis et al. (2002).

For data reduction and analysis, the AIPS² package was used. The two continuum channels were concatenated in the u - v /visibility plane. The data were mapped using the CLEAN algorithm and “natural” weighting; this results in a synthesized beam of $1.8'' \times 1.7''$ ($\sim 13 \text{ kpc}$ at $z = 3.2$) at a major axis position angle of 78° . The final rms in both the line channel and the combined continuum channel is $60 \mu\text{Jy beam}^{-1}$.

8.5 Results

In the top panel of Figure 8.1, the final map of the ON channel (line+continuum emission) is shown, while the middle panel shows the map of the two OFF (combined continuum) channels, representing the continuum-only flux. The source is clearly detected in both maps. To derive the total flux density of the source, a two-dimensional Gaussian was fitted to the detected source structure. Our best fit for MG 0751+2716 gives a Gaussian diameter of $2.3'' \times 2.3''$ (source convolved with the synthesized beam); i.e., the emission appears only marginally resolved in our observations, as our beam is too large to recover the lens image substructure seen at higher resolution (Carilli et al. 2005). The integrated flux density in the ON channel is $10.3 \pm 0.2 \text{ mJy}$ (peak: $6.12 \pm 0.06 \text{ mJy beam}^{-1}$), and the continuum flux in the combined OFF channels is $10.3 \pm 0.2 \text{ mJy}$ (peak: $5.88 \pm 0.06 \text{ mJy beam}^{-1}$). Using the VLA 42.2 GHz measurement of 13.2 mJy (Carilli et al. 2005) and a spectral index of $\beta = -1.2$ (Lehár et al. 1997), an extrapolated flux density of 12.7 mJy can be calculated, which is higher than what was derived from our observations. Therefore, continuum variability cannot be excluded.

In the bottom panel of Figure 8.1, the continuum-subtracted line map is shown. This map was generated by subtracting a CLEAN component model of the continuum emission (combined OFF channel) from the visibility data of the ON channel, which was then imaged by applying the CLEAN algorithm with the same parameters used to create the continuum model. No clear evidence for the H₂O($3_{13}\rightarrow 2_{20}$) line emission is found. Thus,

²See <http://www.aoc.nrao.edu/aips/>.

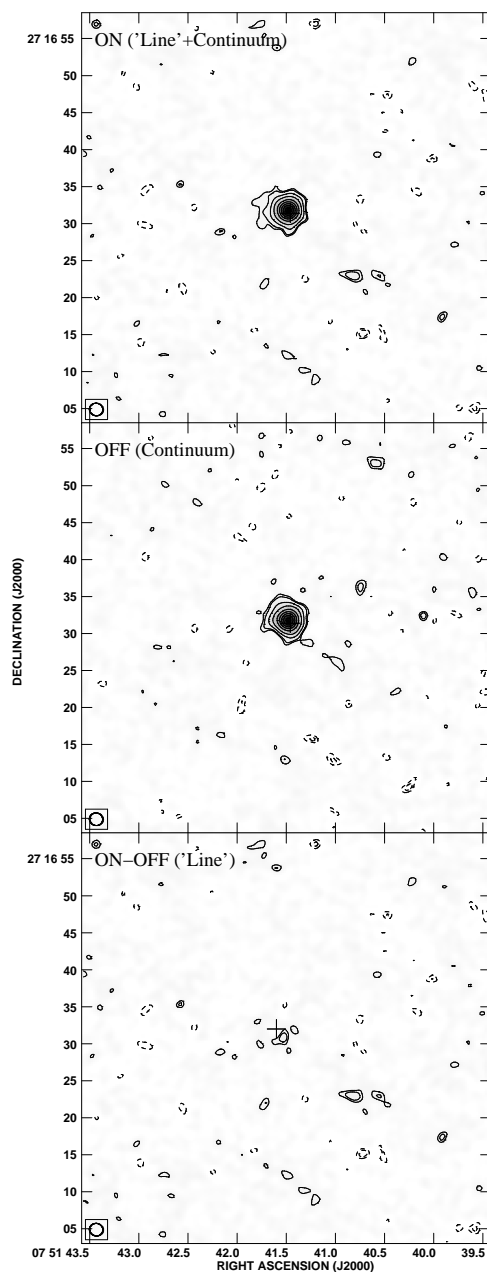


Figure 8.1: VLA observations of MG 0751+2716 at a resolution of $1.8'' \times 1.7''$ at a major axis position angle of 78° . The circle in the bottom left corner of each map represents the FWHM of the restoring CLEAN beam. *Top*: Map of the central 50 MHz (344 km s^{-1}) “ON” channel at 43.6 GHz (183.3 GHz rest frame), the frequency for which the H_2O line is expected. *Middle*: Combined map of the two 50 MHz “OFF” (continuum only) channels symmetrically offset by 150 MHz (1030 km s^{-1}) each from the H_2O line frequency. The source is marginally resolved in both maps. *Bottom*: Continuum-subtracted (“ON-OFF”) map. No clear evidence for $\text{H}_2\text{O}(3_{13} \rightarrow 2_{20})$ line emission is found within the uncertainties of the observations. All three maps are shown with $(-4, -3, 3, 4, 8, 16, 32, 48, 64, 80, 96) \times 60 \mu\text{Jy beam}^{-1}$ contours.

Table 8.1: Extragalactic para-H₂O(3₁₃→2₂₀) Emission: Fluxes, Luminosities, and Area Filling Factors

Object	z	D_L (Mpc)	ν_{obs} (GHz)	$S_{\text{H}_2\text{O}}$ (mJy)	$L'_{\text{CO}}{}^a$ ($10^9 L_I$)	$L'_{\text{H}_2\text{O}}{}^a$ ($10^9 L_I$)	L_{FIR} ($10^{12} L_{\odot}$)	FF	References
MG 0751+2716 ^b	3.200	27940	43.6453	<0.18	10.0	< 0.6	1.2	<1%	1,2,3
Mrk 1014	0.1631	774	157.6048	<26	7.8	< 2.9	2.2	<5%	4,5
VII Zw 244	0.1324	616	161.8775	<26	3.9	< 0.7	0.14	<2%	4,5
NGC 3079	0.003723	16	182.6302	550	1.1	0.0041	0.021	0.05%	6,7
Arp 220	0.018126	78	180.0680	170	5.9	0.29	1.3	0.4%	8,9,10

Notes—Line luminosity unit is $L_I = \text{K km s}^{-1} \text{ pc}^2$.

For MG 0751+2716, the CO($J=4\rightarrow3$) FWHM line width (corrected for the VLA bandpass; Barvainis et al. 2002) of 350 km s^{-1} is utilized to derive $L'_{\text{H}_2\text{O}}$, whereas the CO($J=1\rightarrow0$) FWHM line widths of 210 km s^{-1} and 80 km s^{-1} (Combes et al. 1997) are assumed for Mrk 1014 and VII Zw 244.

^aDerived as described by Solomon et al. (1992b): $L'_X [\text{K km s}^{-1} \text{ pc}^2] = 3.25 \times 10^7 I \nu_{\text{obs}}^{-2} D_L^2 (1+z)^{-3}$, where X is the molecule, I is the velocity-integrated line flux in Jy km s^{-1} , D_L is the luminosity distance in Mpc, and ν_{obs} is the observed frequency in GHz.

^bThis QSO is lensed by a factor of $\mu_L = 17$ (Barvainis et al. 2002). All given luminosities are corrected for lensing.

References—(1) This work, (2) Barvainis et al. 2002; (3) Carilli et al. 2005; (4) Combes et al. 1997; (5) Alloin et al. 1992; (6) Koda et al. 2002; (7) Humphreys et al. 2005; (8) Cernicharo et al. 2006; (9) Solomon et al. 1992c; (10) Solomon et al. 1997.

we set a 3σ upper limit of $S_{\text{H}_2\text{O}} < 180 \mu\text{Jy}$ on the peak flux of H₂O(3₁₃→2₂₀) emission. For MG 0751+2716, we thus derive an upper limit for the H₂O(3₁₃→2₂₀) line luminosity of $L'_{\text{H}_2\text{O}} < 0.6 \times 10^9 \text{ K km s}^{-1} \text{ pc}^2$ (3σ limit, corrected for gravitational magnification, $\mu_L = 17$, Barvainis et al. 2002; see Table 8.1).

8.6 Discussion

8.6.1 Intrinsic Line Brightness Temperatures

Given that the 183 GHz water maser line most likely arises from extended regions associated with star formation (Cernicharo et al. 1994), we can use our upper limit together with the CO($J=4\rightarrow3$) line luminosity (Barvainis et al. 2002) to estimate how much of the molecular gas in MG 0751+2716 may be associated with massive star-forming regions. Radiative transfer models based on the H₂O(3₁₃→2₂₀) emission line show that it is inverted in warm and dense environments ($T_{\text{kin}} > 40 \text{ K}$, $n_{\text{H}_2} > 5 \times 10^4 \text{ cm}^{-3}$), which are typically found in star-forming regions, and that the resulting line brightness temperature critically depends on the underlying physical conditions. It is known to range from thermalized emission up to line temperatures of $\sim 10,000 \text{ K}$ (Cernicharo et al. 1994; Combes et al. 1997). As an example, observations of the 183 GHz water maser towards Orion IRc2 show that emission arises from narrow (few km s^{-1}) line features with up to $\simeq 2000 \text{ K}$ peak temperatures as well as from a broad ($\simeq 200 \text{ km s}^{-1}$) emission plateau with $\simeq 500 \text{ K}$ peak line brightness temperature (Cernicharo et al. 1994, 1999). As an order-of-magnitude estimate, we assume in the following that the H₂O(3₁₃→2₂₀) line in MG 0751+2716 arises from an environment

similar to Orion's, with an intrinsic brightness temperature of $T_b(\text{H}_2\text{O}) \simeq 500$ K. Only the CO($J=4\rightarrow 3$) line has been observed so far in MG 0751+2716, therefore the brightness temperature of the CO emission is not well constrained. However, the dust continuum temperature of $T_{\text{dust}} \simeq 40$ K in MG 0751+2716 (Barvainis & Ivison 2002) is consistent with those observed in most other high- z QSOs (e.g., Beelen et al. 2006). In addition, the CO brightness temperature in well-studied high- z objects such as IRAS F10214+4724 agrees within a factor of ~ 2 with the dust temperature (e.g., Downes et al. 1995). By analogy, we here assume $T_b(\text{CO}) \simeq 40$ K.

8.6.2 Area Filling Factor

The combined ratios of the brightness temperatures and line luminosities of H₂O and CO ($T_b(\text{H}_2\text{O}) \simeq 500$ K, $T_b(\text{CO}) \simeq 40$ K, $L'_{\text{H}_2\text{O}} < 0.6 \times 10^9$ K km s⁻¹ pc², $L'_{\text{CO}} = 10.0 \times 10^9$ K km s⁻¹ pc²) can be used to estimate the relative area filling factor (FF) of both molecules. By this means, our observed upper limit on the 183 GHz H₂O line luminosity together with the CO($J=4\rightarrow 3$) line luminosity translates into an upper limit on the H₂O/CO area FF of $< 1\%$.

To better understand the relevance of this FF limit derived from our observations, we now give an independent estimate for the FF based on the FIR luminosity and geometrical arguments. For this purpose, we assume in the following that all 183 GHz H₂O emission in MG 0751+2716 is created in hot, star-forming cores like the one found in the central region of Orion. Assuming $L_{\text{FIR}} = 1.2 \times 10^5 L_{\odot}$ for the central 1 arcmin² of the Orion Nebula (corresponding to an area of 0.013 pc² at a distance of 450 pc; Werner et al. 1976), we find that 10^7 of these cores are needed to account for the FIR luminosity in MG 0751+2716 (Table 8.1). Assuming a size of 0.013 pc² each, 10^7 of such cores would fill a disk with an equivalent radius of 200 pc. Taking the observed CO($J=4\rightarrow 3$) line FWHM and luminosity into account, and assuming $T_b(\text{CO}) \simeq 40$ K, for MG 0751+2716, we can calculate that the dust and CO are distributed over a region with an equivalent radius of 450 pc. Comparing the derived disk sizes, we thus find an expected H₂O/CO area FF of $\sim 20\%$. This estimate is much higher than what is actually observed.

8.6.3 Comparison with Other Extragalactic Studies

Our results for MG 0751+2716 are in line with observations of the radio-quiet QSOs Mrk 1014 (PG 0157+001, $z = 0.16$) and VII Zw 244 (PG 0838+770, $z = 0.13$; see Table 8.1), the only two other infrared-luminous galaxies for which upper limits on the 183 GHz H₂O line have been reported (Combes et al. 1997) to date. Using the same assumptions of the intrinsic line brightness temperatures as for MG 0751+2716, the nondetections in these galaxies imply FFs of the water line relative to CO($J=1\rightarrow 0$) of $< 5\%$ and $< 2\%$ for Mrk 1014 and VII Zw 244, respectively. As CO emission appears to be close to thermalized up to the CO($J=4\rightarrow 3$) transition in high- z QSOs (Weiss et al. 2005a), these limits are directly comparable to MG 0751+2716.

In Arp 220 ($z = 0.018$), the H₂O(3₁₃→2₂₀) line was detected with a line luminosity of $L'_{\text{H}_2\text{O}} = 2.9 \times 10^8 \text{ K km s}^{-1} \text{ pc}^2$ (Cernicharo et al. 2006). With the CO luminosity given in Solomon et al. (1992c), this translates to a H₂O/CO FF of 0.4%. Arp 220 has a FIR luminosity similar to that of MG 0751+2716, which might suggest a similar H₂O/CO FF. This suggests that the H₂O(3₁₃→2₂₀) line might be detectable in MG 0751+2716 if the sensitivity was increased only by a factor of a few.

For the recent first extragalactic H₂O(3₁₃→2₂₀) detection in the LINER NGC 3079 (Humphreys et al. 2005), the H₂O/CO luminosity ratio (using same brightness temperatures as before) translates into a H₂O/CO area FF of only 0.05%. However, it is difficult to assess the relevance of the NGC 3079 results for MG 0751+2716, as the former is not a ULIRG. For lower luminosity galaxies, it has been found that the HCN/CO luminosity ratio is significantly lower (2.5%–4% rather than 10%–25%; Gao & Solomon 2004a); by analogy, lower H₂O/CO luminosity ratios may also be expected in galaxies with FIR luminosities that are significantly lower than in a ULIRG.

8.6.4 Possible Interpretations of the Nondetection

Our observations suggest that the H₂O/CO area FF in MG 0751+2716 is significantly lower than the simple estimates based on the distribution and temperature of the dust and CO predict. However, other reasons for the weakness of the water emission should also be considered; as discussed in Combes et al. (1997), the physical conditions required to efficiently pump the 183 GHz line to the assumed 500 K may not be present. There are strong differences in the conditions for H₂O line emission among Galactic star-forming regions. For example, the H₂O(3₁₃→2₂₀) maser emission in Sgr B2(N/M) is much weaker than that in Orion IRc2. The extent of the maser-emitting regions in both sources is of order 1 pc, but the observed brightness temperature in Sgr B2 is 1–2 orders of magnitude lower, reaching only few tens of Kelvin (Cernicharo et al. 1994, 2006). This is much lower than the 500 K we assumed for a typical H₂O emitting region. The 183 GHz H₂O lines are thus amplified only by a factor of 3 relative to CO in this source. For high densities and/or column densities, which are known to be present in the compact molecular distributions of LIRGs, the maser emission of the 183 GHz line may even be quenched. This would lead to thermalized emission without maser amplification (Cernicharo et al. 1994; Combes et al. 1997). For thermalized emission in an optically thick environment, the H₂O(3₁₃→2₂₀) line is not expected to be stronger than those of other high-density gas tracers such as HCN. In Arp 220, the HCN luminosity is $L'_{\text{HCN}} = 9.4 \times 10^8 \text{ K km s}^{-1} \text{ pc}^2$, i.e., it is brighter than H₂O(3₁₃→2₂₀) by a factor of 3 (Cernicharo et al. 2006; Graciá-Carpio et al. 2006). The H₂O and HCN luminosities in Arp 220 would thus even be consistent with $T_b(\text{H}_2\text{O}) = T_b(\text{HCN})$ and an area FF that is smaller for H₂O than for HCN. This suggests that only a small fraction of the dense gas is giving rise to H₂O emission. Carilli et al. (2005) set a 3σ limit of $L'_{\text{HCN}} < 1.0 \times 10^9 \text{ K km s}^{-1} \text{ pc}^2$ on the HCN($J=2\rightarrow 1$) line luminosity in MG 0751+2716, which is twice as high as our limit for $L'_{\text{H}_2\text{O}}$.

It also remains a possibility that the reason for our nondetection is due to limitations in our observing mode. Due to the small fraction of gas giving rise to the H₂O(3₁₃→2₂₀) emis-

sion compared to CO, its line width could be much smaller than that of the CO($J=4\rightarrow 3$) transition. This has recently been found in NGC 3079 (Humphreys et al. 2005), where the difference in line width is more than a factor of 10. As our observations had to be done using 50 MHz (344 km s^{-1}) channels, the emission from a narrow line would be diluted over the full velocity range covered by that channel, rendering detection unlikely even at the achieved sensitivity. However, in Arp 220, which is likely more similar to MG 0751+2716, the H₂O($3_{13}\rightarrow 2_{20}$) line has a width of 350 km s^{-1} . Such a line width would match our observing mode very well. Finally, differential lensing may have an impact on the measured luminosity ratios ($\mu_L = 17$), particularly if the CO and H₂O emissions do not emerge from the same regions.

Given the aforementioned results, we find that water maser activity does not outshine emission from rotational transitions of CO or HCN in the $z = 3.2$ QSO MG 0751+2716. If our results can be generalized, we conclude that H₂O (despite the fact that it potentially traces hot, star-forming cores) does not appear to be a more luminous alternative to HCN to detect high-density gas in star-forming environments at high redshift.

It is a pleasure to thank my collaborators on this project:

Axel Weiß (MPIfR), Fabian Walter (MPIA), Chris Carilli (NRAO), and Kirsten K. Knudsen (MPIA).

CHAPTER PUBLISHED AS:

Riechers, D. A., Weiss, A., Walter, F., Carilli, C. L., & Knudsen, K. K., ‘A Search for H₂O in the Strongly Lensed QSO MG 0751+2716 at $z = 3.2$ ’, 2006, ApJ, 649, 635

Chapter 9

Molecular Line Mapping I: A Compact Quasar Host Galaxy at $z=3.91$

9.1 Context

Perhaps the most exciting issue in the context of high redshift QSO studies is the prospect to actually resolve the host galaxies. One important aspect of such observations is to also obtain spectral information which allows us to dynamically resolve these systems, and therefore to derive dynamical masses. Currently, the only means by which to do so is to study the molecular gas and dust content, since it can be observed at frequencies where the central AGN does not overshadow the whole galaxy. It is therefore one of the key science drivers of the Atacama Large Millimeter Array (ALMA) to obtain such high resolution observations out to the highest redshifts (see ALMA Design Reference Science Plan [DRSP]¹). However, with the Very Large Array (VLA), it is possible to conduct such observations already today for the few known bright CO sources at the highest redshifts (and even more so with the upcoming EVLA). To explore this difficult but unique area of high- z observations, a large project with the VLA was started to study the CO emission of three of the CO-brightest quasars at $z>3.5$ (i.e., half of all CO-detected quasars at $z>3.5$ in 2005/2006².) at the maximum possible spatial resolution, i.e., $0.15''$ - $0.3''$, which corresponds to a maximum resolution of 1.0 kpc at $z=4$ for unlensed sources. In this chapter, the first source is presented: APM08279+5255 (two more sources are presented in the subsequent chapters). This is a strongly gravitationally lensed quasar. A previous study reported a massive, widely extended molecular gas reservoir around this source (Papadopoulos et al. 2001). However, as described in Chapter 3, this finding could not be confirmed. In fact, it will here be shown that the molecular reservoir is very compact, and

¹<http://www.strw.leidenuniv.nl/~alma/drsp.shtml>

²Two of the other sources were done as science demonstration; see Carilli et al. (2002b), and Figure 2.7; Walter et al. (2004), and Figure 1.6

difficult to resolve even with the aid of gravitational magnification.

9.2 Abstract

We have mapped the molecular gas content in the host galaxy of the strongly lensed high redshift quasar APM08279+5255 ($z = 3.911$) with the Very Large Array (VLA) at $0.3''$ resolution. The CO($J=1\rightarrow 0$) emission is clearly resolved in our maps. The CO($J=1\rightarrow 0$) line luminosity derived from these maps is in very good agreement with a previous single-dish measurement. In contrast to previous interferometer-based studies, we find that the full molecular gas reservoir is situated in two compact peaks separated by $\lesssim 0.4''$. Our observations reveal, for the first time, that the emission from cold molecular gas is virtually cospatial with the optical/near-infrared continuum emission of the central AGN in this source. This striking similarity in morphology indicates that the molecular gas is situated in a compact region close to the AGN. Based on the high resolution CO maps, we present a revised model for the gravitational lensing in this system, which indicates that the molecular gas is lensed by only a factor of 4, and that there are no strong differential lensing effects between the central AGN and the circumnuclear molecular disk. This model suggests that the CO is situated in a disk of ~ 550 pc radius that is possibly seen at an inclination of $\lesssim 25^\circ$, i.e., relatively close to face-on. From the CO luminosity, we derive a molecular gas mass of $M_{\text{gas}} = 5.3 \times 10^{11} \mu_L^{-1} M_\odot$ for this galaxy. From the CO structure and linewidth, we derive a dynamical mass of $M_{\text{dyn}} \sin^2 i = 4.0 \times 10^{10} M_\odot$. Based on a revised mass estimate for the central black hole of $M_{\text{BH}} = 9.0 \times 10^{10} \mu_L^{-1} M_\odot$ and the results of our molecular line study, we find that the mass of the stellar bulge of APM08279+5255 falls short of the $M_{\text{BH}}-\sigma_{\text{bulge}}$ relationship of nearby galaxies by more than an order of magnitude, lending support to recent suggestions that this relation may break down at high redshift.

9.3 Introduction

Several different populations of distant galaxies have been detected to date, out to a (spectroscopically confirmed) redshift of $z=7.0$ (see Ellis 2007 for a review). It is of fundamental importance to study such young galaxies in great detail in order to constrain their nuclear, stellar, and gaseous constituents and their physical properties and chemical abundances. Understanding these different characteristics of high redshift galaxy populations and their progression through cosmic times is vital to develop a unified picture of galaxy formation and evolution. One key aspect in these high- z galaxy studies are sensitive, high-resolution radio observations of the molecular gas phase, i.e., the raw material that fuels star formation.

Since its initial discovery at $z>2$ more than a decade ago (Brown & Vanden Bout 1991; Solomon et al. 1992b), observations of spectral line emission from interstellar molecular gas in distant galaxies have revolutionized our understanding of some of the most luminous objects that populate the early universe. This is due to the fact that the physical state of the

molecular interstellar medium (ISM) plays a critical role in the evolution of a galaxy. The total amount of molecular gas in a galaxy determines for how long starburst activity can be maintained, while its temperature and density are a direct measure for the conditions under which star formation can occur (see Solomon & Vanden Bout 2005 for a review). Also, there is growing evidence that the observed relationships between black hole mass and galaxy bulge velocity dispersion ($M_{\text{BH}}-\sigma_*$; Ferrarese & Merritt 2000; Gebhardt et al. 2000), black hole mass and host bulge concentration (i.e., Sersic index; Graham et al. 2001; Graham & Driver 2007), and, ultimately, black hole mass and bulge mass ($M_{\text{BH}}-M_{\text{bulge}}$; Magorrian et al. 1998; Häring & Rix 2004), may be a consequence of an active galactic nucleus (AGN) feedback mechanism acting on its surrounding material, at least in the most luminous systems (Silk & Rees 1998; Di Matteo et al. 2005). Such an AGN-driven wind will also interact with the molecular gas, the material which will eventually form the stellar bulges in galaxies at high redshift, but also feed the active nucleus itself. Observations of the dynamical structure and distribution of molecular gas in distant galaxies may even reveal the initial cause of event (e.g., mergers) for both star formation and AGN activity, an important test for recent cosmological models (e.g., Springel et al. 2005; Narayanan et al. 2006).

High angular resolution observations of molecular gas in high- z galaxies are, to date, exclusively being obtained in the rotational transitions of carbon monoxide (CO). In the past few years, a number of submillimeter galaxies (SMGs; Genzel et al. 2003; Downes & Solomon 2003; Tacconi et al. 2006) and quasars (Alloin et al. 1997) at $z > 2$ have been studied at a linear resolution of up to 5 kpc at the target redshifts (1 kpc = 0.12'' at $z=2$), primarily using the IRAM Interferometer on Plateau de Bure (PdBI). In some cases, gravitational lensing aids in zooming in further on these systems. However, the only telescope that currently allows us to attain resolutions of sub-kpc to 1 kpc scale at even higher redshifts ($z \gtrsim 4$, where 1 kpc $\gtrsim 0.14''$) is the NRAO's Very Large Array (VLA)³. First sub-arcsecond resolution CO imaging with the VLA has been obtained toward the distant quasars BR 1202-0725 ($z=4.69$; Carilli et al. 2002b), APM 08279+5255 ($z=3.91$; Lewis et al. 2002a), PSS J2322+1944 ($z=4.12$; Carilli et al. 2003; Riechers et al., in prep.), and SDSS J1148+5251 ($z=6.42$; Walter et al. 2004).

We here report on new, more sensitive high-resolution observations of CO($J=1 \rightarrow 0$) emission towards the strongly lensed quasar APM 08279+5255 ($z = 3.911$).

APM 08279+5255 was already⁴ imaged during the Palomar Sky Survey (PSS) in 1953, a decade before the discovery of the first quasar was reported in the literature (Schmidt 1963). About 45 years later, it was 'officially' discovered in an automatic plate measuring facility (APM) survey for distant cool carbon stars, and identified as a 15th magnitude, radio-quiet broad absorption line (BAL) quasar with an IRAS Faint Source Catalog (FSC) counterpart at a redshift of $z_{\text{opt}}=3.87$ (Irwin et al. 1998). APM 08279+5255 was found to have an unprecedented apparent bolometric luminosity of $L_{\text{bol}}=7 \times 10^{15} L_{\odot}$, about 20% of which is

³The Very Large Array is a facility of the National Radio Astronomy Observatory, operated by Associated Universities, Inc., under a cooperative agreement with the National Science Foundation.

⁴Due to the source's enormous optical brightness, much older images may exist.

emitted in the (far-)infrared (Lewis et al. 1998). This extreme value was early on found to be due to strong gravitational lensing (Irwin et al. 1998), producing three close (maximum separation $<0.4''$), almost collinear images in the optical/near-infrared (Ibata et al. 1999; Egami et al. 2000). Due to the lack of a detection of the lensing galaxy, and an indication for significant microlensing effects, the true nature of the gravitational lens configuration (and thus the magnification factor μ_L) in this system remains subject to debate (e.g., Egami et al. 2000; Lewis et al. 2002a) despite the fact that APM08279+5255 is one of the best-studied sources in the distant universe. In addition to its enormous continuum brightness at basically every astronomically relevant wavelength, APM08279+5255 is also one of the brightest CO sources at high redshift (Downes et al. 1999). It also exhibits unusually bright HCN (Wagg et al. 2005) and HCO⁺ (Garcia-Burillo et al. 2006) emission, and was recently also detected in C I (Wagg et al. 2006) emission. The properties of its molecular gas content have recently been modeled based on observations of the CO($J=1\rightarrow 0$) up to CO($J=11\rightarrow 10$) rotational ladder (‘CO spectral line energy distribution’, or SLED) with the NRAO Green Bank Telescope (GBT)⁵ and the IRAM 30 m telescope (Riechers et al. 2006a; Weiß et al. 2007). We use a standard concordance cosmology throughout, with $H_0 = 71 \text{ km s}^{-1} \text{ Mpc}^{-1}$, $\Omega_M = 0.27$, and $\Omega_\Lambda = 0.73$ (Spergel et al. 2003, 2007).

9.4 Observations

We here report new, sensitive high-resolution observations of the CO($J=1\rightarrow 0$) emission line in APM08279+5255. To better constrain the molecular gas properties in this source, we also re-derive the strength of the CO($J=2\rightarrow 1$) emission line, based on more sensitive (archival) observations than reported previously (Papadopoulos et al. 2001). In this context, we also present a search for the CN($N=1\rightarrow 0$) emission line in this galaxy, a tracer of the dense fraction of the molecular gas phase (see Riechers et al. 2006a for more details on this data). To further investigate the AGN and starburst environments in this source, we augment our analysis of the molecular gas properties with a study of the radio continuum properties, based in part on archival observations. A fraction of the archival continuum data was used in previous studies of this source (Ibata et al. 1999; Ivison 2006; see Tab. 9.1 for details).

9.4.1 VLA Data

CO($J=1\rightarrow 0$) and 23.5 GHz continuum [new]

We observed the CO($J=1\rightarrow 0$) transition line ($\nu_{\text{rest}} = 115.2712018 \text{ GHz}$) towards APM08279+5255 using the VLA in B, C, and D configuration between 2005 April 07 and 2005 December 02. At the target redshift of 3.911, the line is redshifted to 23.472 GHz (12.77 mm, K band). The total on-sky integration time amounts to 51.25 hr (see Tab. 9.1 for

⁵The Green Bank Telescope is a facility of the National Radio Astronomy Observatory, operated by Associated Universities, Inc., under a cooperative agreement with the National Science Foundation.

Table 9.1: New (2005) and Archival (1998–2001) VLA Observations Summary

Date	Configuration	Duration	Band	Type	Reference
2005 Apr 07	B	6.75 h	K	CO($J=1\rightarrow 0$)	1
2005 Apr 08	B	6.0 h	K	CO($J=1\rightarrow 0$)	1
2005 Apr 09	B	5.25 h	K	CO($J=1\rightarrow 0$)	1
2005 Apr 10	B	6.0 h	K	CO($J=1\rightarrow 0$)	1
2005 Apr 18	B	7.5 h	K	CO($J=1\rightarrow 0$)	1
2005 May 01	B	4.0 h	C	Continuum	1
2005 Sep 12	C	8.25 h	K	CO($J=1\rightarrow 0$)	1
2005 Sep 20	C	7.5 h	K	CO($J=1\rightarrow 0$)	1
2005 Dec 02	D	4.0 h	K	CO($J=1\rightarrow 0$)	1
1998 Jun 18	BnA	3.0 h	X	Continuum	2
1998 Jul 28	B	2.5 h	X	Continuum	1
		2.0 h	U	Continuum	1
1998 Aug 11	B	3.0 h	X	Continuum	1
		3.5 h	U	Continuum	1
2000 Apr 24	C	13.0 h	Q	CO($J=2\rightarrow 1$)	3
2000 Sep 16	D	4.0 h	Q	CO($J=2\rightarrow 1$)	1
2001 Jan 21	A	2.25 h	L	Continuum	4
2001 Oct 20	D	9.0 h	Q	CO($J=2\rightarrow 1$)	1

Notes—Maximum baselines of VLA configurations are: A - 36.4 km, B - 11.4 km, C - 3.4 km, D - 1.03 km. BnA is a hybrid configuration where the antennas on the east and west arms of the array are in the shorter of the two denoted configurations, and the north arm is in the more extended configuration.

References—(1) this work; (2) Ibata et al. 1999; (3) Papadopoulos et al. 2001; (4) Ivison 2006.

details). Observations were performed in fast-switching mode (see, e.g., Carilli & Holdaway 1999) using the nearby source 08248+55527 for secondary amplitude and phase calibration. Observations were carried out under excellent weather conditions with 25 antennas. The phase stability in all runs was excellent (typically $<15^\circ$ for the longest baselines). The phase coherence was checked and approved by imaging the calibrator source 08087+49506 with the same calibration cycle as that used for the target source. For primary flux calibration, 3C 286 was observed during each run.

Two 25 MHz intermediate frequencies (IFs) with seven 3.125 MHz channels each were observed in ‘spectral line’ mode centered at the CO($J=1\rightarrow 0$) line frequency, leading to an effective bandwidth of 43.75 MHz (corresponding to 558 km s^{-1} at 23.5 GHz; ‘ON’ channels). Two 50 MHz (corresponding to 638 km s^{-1} at 23.5 GHz) IFs were observed in continuum mode at 23.3649 GHz and 23.5649 GHz (± 100 MHz offset from the line frequency) to measure the source’s continuum at 13 mm (‘OFF’ channels). The continuum was observed for one third of the total time to attain the same rms as in the combined line channels.

For data reduction and analysis, the *AIPS*⁶ package was used. The two continuum channels were concatenated in the uv/visibility plane. The CO($J=1\rightarrow 0$) line image was generated by subtracting a CLEAN component model of the continuum emission from the visibility data. All data were mapped using the CLEAN algorithm. The velocity-integrated maps shown in Fig. 9.1 are imaged using robust 1 weighting and combining B and C array data, leading to a synthesized clean beam size of $0.30'' \times 0.29''$ in the CO($J=1\rightarrow 0$) line map and $0.32'' \times 0.29''$ in the continuum map (note that D array data were omitted in

⁶<http://www.aoc.nrao.edu/aips/>

these maps to improve the shape and size of the synthesized beam). The final rms over the full bandwidth of 43.75 MHz (558 km s^{-1}) in the CO($J=1\rightarrow 0$) map is $16 \mu\text{Jy beam}^{-1}$, and the rms over the 100 MHz continuum bandpass is $13 \mu\text{Jy beam}^{-1}$. In Fig. 9.2, four velocity channel maps (9.375 MHz, or 120 km s^{-1} each) of the central 37.5 MHz (480 km s^{-1}) of the CO($J=1\rightarrow 0$) line are shown. To maximize the sensitivity in individual channels the data were imaged using natural weighting and combining B and C array data, achieving a resolution of $0.34'' \times 0.33''$. Hanning smoothing was applied to the image cube, resulting in an rms of $27 \mu\text{Jy beam}^{-1}$ per channel. The velocity-integrated CO($J=1\rightarrow 0$) and 23.5 GHz continuum maps of the combined B, C *and* D array data shown in Fig. 9.3 and Fig. 9.6, top right, are imaged using natural weighting and a gaussian taper, leading to synthesized beams of $1.19'' \times 1.14''$ and $1.19'' \times 1.10''$, and an rms of $19 \mu\text{Jy beam}^{-1}$ for both maps.

CO($J=2\rightarrow 1$) [archival]

Spectral line observations of the CO($J=2\rightarrow 1$) transition line ($\nu_{\text{rest}} = 230.53799 \text{ GHz}$) towards APM08279+5255 were carried out between 2000 Apr 24 and 2001 Oct 20 using the VLA in C and D configuration. The C array data was published by Papadopoulos et al. (2001). We here re-analyze this data, and add in shorter (unpublished) D array spacings to improve the sensitivity of the data. At the target redshift of 3.911, the CO($J=2\rightarrow 1$) line is redshifted to 46.943 GHz (6.39 mm, Q band). The total on-sky integration time amounts to 26 hr (see Tab. 9.1 for details). Observations were performed in fast-switching mode using the nearby source 08248+55527 for secondary amplitude and phase calibration. Observations were carried out under excellent weather conditions with up to 27 antennas. For primary flux calibration, 3C 48 and 3C 286 were observed. Observations were set up in quasi-continuum mode; two 50 MHz IFs were observed simultaneously at 46.9149 GHz and 46.9649 GHz to cover the central $\sim 640 \text{ km s}^{-1}$ of the spectral line.

Data were mapped using the CLEAN algorithm at natural weighting; this results in a synthesized beam of $1.11'' \times 0.93''$ and an rms of $65 \mu\text{Jy beam}^{-1}$ (no map shown here).

1.4 GHz continuum [archival]

Continuum observations at 1.400 GHz (L band) towards APM08279+5255 were carried out on 2001 Jan 21 using the VLA in A configuration. This data was recently published by Ivison (2006; no map shown). The total on-sky integration time amounts to 2.25 hr (see Tab. 9.1 for details). Observations were performed in spectral line mode using the nearby source 0824+558 for secondary amplitude and phase calibration. Observations were set (no map shown here) up using two IFs and seven 3.125 MHz channels per IF, leading to an effective bandwidth of 43.75 MHz (corresponding to $\sim 9400 \text{ km s}^{-1}$ at 1.4 GHz). Observations were carried out under good weather conditions with 27 antennas. For primary flux calibration, 3C 48 was observed.

Data were mapped using the CLEAN algorithm at robust 0 weighting; this results in a synthesized beam of $1.42'' \times 1.15''$ and an rms of $33 \mu\text{Jy beam}^{-1}$ (see Fig. 9.6, top left).

4.5 GHz continuum [new]

Continuum observations at 4.5276 GHz (C band) towards APM08279+5255 were carried out on 2005 May 01 using the VLA in B configuration. The total on-sky integration time amounts to 4 hr (see Tab. 9.1 for details). Observations were performed in spectral line mode using the nearby source 08248+55527 for secondary amplitude and phase calibration. Observations at 4.5276 GHz were set up using thirty-one 390.625 kHz channels, leading to an effective bandwidth of 12.109375 MHz (corresponding to 802 km s^{-1} at 4.5276 GHz). Observations were carried out under excellent weather conditions with 25 antennas. The phase stability in this run was excellent. For primary flux calibration, 3C 286 was observed during each run.

Data were mapped using the CLEAN algorithm at natural weighting; this results in a synthesized beam of $1.55'' \times 1.42''$ and an rms of $40 \mu\text{Jy beam}^{-1}$ (see Fig. 9.6, bottom left).

8.4 GHz continuum [archival]

Continuum observations at 8.4 GHz (X band) towards APM08279+5255 were carried out between 1998 Jun 18 and Aug 11 using the VLA in BnA and B configuration. The BnA array data was published by Iyata et al. (1999). We here re-analyze this data, and add in shorter B array spacings to improve the sensitivity and image quality of the data. The total on-sky integration time amounts to 8.5 hr (see Tab. 9.1 for details). Observations were performed in quasi-continuum mode (two 50 MHz IFs were observed simultaneously at 8.4351 GHz and 8.4851 GHz) using the nearby sources 0749+540 and 0820+560 for secondary amplitude and phase calibration. Observations were carried out under good weather conditions with 27 antennas. For primary flux calibration, 3C 48 and 3C 147 were observed.

Data were mapped using the CLEAN algorithm. Imaging the data with natural weighting results in a synthesized beam of $0.73'' \times 0.42''$ and an rms of $10 \mu\text{Jy beam}^{-1}$ (see Fig. 9.6, bottom right). Imaging the data with uniform weighting results in a synthesized beam of $0.63'' \times 0.22''$ and an rms of $20 \mu\text{Jy beam}^{-1}$ (see Fig. 9.7).

14.9 GHz continuum [archival]

Continuum observations at 14.9 GHz (U band) towards APM08279+5255 were carried out on 1998 Jul 28 and Aug 11 using the VLA in B configuration. The total on-sky integration time amounts to 5.5 hr (see Tab. 9.1 for details). Observations were performed in quasi-continuum mode (two 50 MHz IFs were observed simultaneously at 14.9149 GHz and 14.9649 GHz) using the nearby source 0749+540 for secondary amplitude and phase calibration. Observations were carried out under good weather conditions with 27 antennas. For primary flux calibration, 3C 48 was observed.

Data were mapped using the CLEAN algorithm at natural weighting; this results in a synthesized beam of $0.51'' \times 0.44''$ and an rms of $44 \mu\text{Jy beam}^{-1}$ (no map shown here).

9.4.2 GBT Data

CN($N=1\rightarrow 0$)

As part of our wide-band high- z molecular line study (Riechers et al. 2006a), we observed the $F=3/2\rightarrow 1/2$, $F=5/2\rightarrow 3/2$, $F=1/2\rightarrow 1/2$, and $F=3/2\rightarrow 3/2$ hyper-fine structure transitions of the CN($N=1\rightarrow 0$, $v=0$, $J=3/2\rightarrow 1/2$) line ($\nu_{\text{rest}} = 113.4881420 - 113.5089340$ GHz) towards APM08279+5255 with the GBT between 2004 December 15 and 19 for a total of 22.5 hr (15 hr on source). At the target redshift of 3.911, these lines are redshifted to 23.109-23.113 GHz (12.97 mm, K band), and can be observed simultaneously (in-band) with CO($J=1\rightarrow 0$) at the GBT (see Riechers et al. 2006a for a more detailed description and results on the CO observations). Observations were performed in ON-OFF position switching mode using the nearby source J0753+538 for secondary amplitude and pointing calibration, correcting for the atmospheric opacity. The pointing accuracy was typically 3". Observations were carried out under excellent weather conditions. For primary flux calibration, 3C147 and 3C286 were observed during each run. The dual-beam, dual-polarization 18-26 GHz receiver was used for all observations. The beam size at our observing frequency is 32" (~ 230 kpc at the source's redshift), i.e. much larger than our target.

Two 800 MHz IFs with 2048 390.625 kHz (5 km s^{-1}) channels and two orthogonal polarizations each were observed simultaneously. The first IF was centered on the redshifted CO($J=1\rightarrow 0$) frequency at 23.4663 GHz, and the second IF was tuned 700 MHz bluewards. Therefore, the observed CN($N=1\rightarrow 0$) fine structure transition lines are located at the lower end of the first IF.

For data reduction and analysis, the AIPS⁺⁺⁷ and GBT IDL⁸ packages were used. Final combination, binning, and baseline subtraction were done with GILDAS/CLASS⁹. An rms of $65 \mu\text{Jy}$ was attained in these observations.

9.5 Results

9.5.1 CO($1\rightarrow 0$) Line and 23.5 GHz Continuum Emission

We have resolved the emission from the CO($J=1\rightarrow 0$) transition line towards APM08279+5255 ($z = 3.91$), as well as the continuum emission at the same frequency (Fig. 9.1). The left panel of Fig. 9.1 shows the CO($J=1\rightarrow 0$) and continuum emission, the middle panel the continuum-subtracted CO($J=1\rightarrow 0$) emission, and the right panel the 23.5 GHz continuum emission. The continuum-subtracted CO($J=1\rightarrow 0$) line emission (Fig. 9.1, middle) is clearly resolved into two peaks (north-east and south-west). From 2-dimensional Gaussian fitting we find a line peak flux density of $131 \pm 16 \mu\text{Jy beam}^{-1}$ for the north-eastern CO peak at $\alpha=08^{\text{h}}31^{\text{m}}41^{\text{s}}.708\pm 0^{\text{s}}.001$, $\delta=+52^{\circ}45'17''.58\pm 0''.02$ and a line peak flux density of $87 \pm 16 \mu\text{Jy beam}^{-1}$ for the south-western CO peak at

⁷<http://www.aips2.nrao.edu>.

⁸<http://gbtidl.sourceforge.net>.

⁹<http://www.iram.fr/IRAMFR/GILDAS/>.

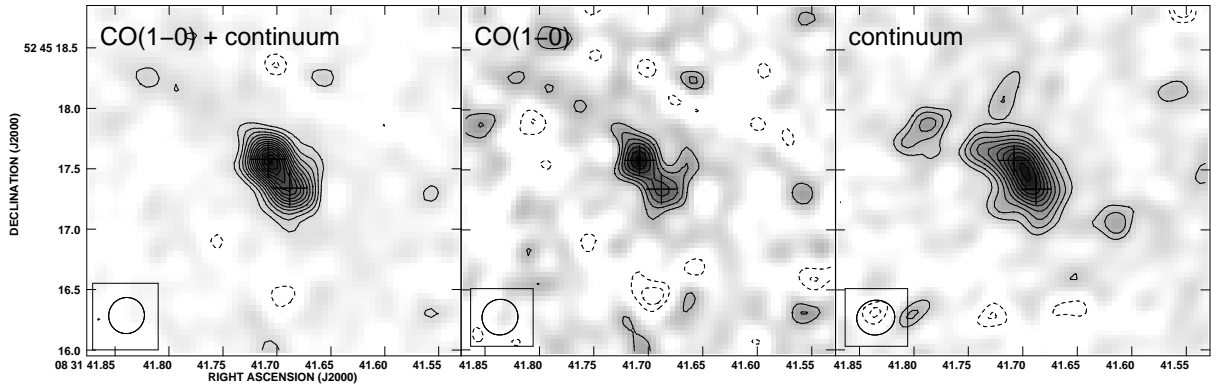


Figure 9.1: High-resolution VLA maps of CO($J=1\rightarrow 0$) + continuum (*left*), CO($J=1\rightarrow 0$) only (*middle*), and 23.5 GHz continuum (*right*) emission towards APM08279+5255 at a resolution of $0.30/0.30/0.32''\times 0.29''$ (robust 1 weighting; left to right; beam size indicated in the bottom left corner of each panel). Contours are shown in steps of the rms noise, starting at $\pm 2\sigma$ ($1\sigma = 16/16/13\ \mu\text{Jy beam}^{-1}$). *Left*: Image of the CO($J=1\rightarrow 0$) and continuum emission. The source is clearly resolved, and detected at a peak strength of 15σ . This map is integrated over the central $558\ \text{km s}^{-1}$ ($43.75\ \text{MHz}$) of the CO($J=1\rightarrow 0$) emission. *Middle*: Image of the CO($J=1\rightarrow 0$) emission. Continuum emission was subtracted. The source is clearly resolved into two CO peaks (8σ and 5σ signal-to-noise), as indicated by the plus signs. This continuum-subtracted map is integrated over the same range as in *left* the panel. *Right*: Image of the 23.5 GHz continuum emission (peak: 11σ). The emission appears resolved and peaks centrally between the CO($J=1\rightarrow 0$) peaks (as indicated by the plus signs). This continuum map is integrated over a bandwidth of 100 MHz.

Table 9.2: CO/CN Line Peak and Continuum Fluxes

Transition/Frequency	S_ν (μJy)	Configuration
CO($J=1\rightarrow 0$)	285 ± 27^a	BCD
CO($J=2\rightarrow 1$)	1637 ± 65^b	CD
CN($N=1\rightarrow 0$)	<195	[GBT]
1.4 GHz	1160 ± 33	A
4.5 GHz	551 ± 40	B
8.4 GHz	446 ± 20	BnA/B
14.9 GHz	303 ± 93^c	B
23.5 GHz	376 ± 19	BCD
46.9 GHz (estimated) ^d	405^{+310}_{-330}	—

Notes—Fluxes are derived from convolved maps for all datasets with linear resolutions higher than $1.2''$, and agree with those derived from Gaussian fitting to the unconvolved data within 10%.

^aPeak flux from Gaussian fitting to the unsmoothed 14 channel spectrum.

^bNot corrected for the estimated 46.9 GHz continuum contribution.

^cTentative detection.

^dEstimated based on the FIR-to-radio SED. The lower limit is given by the model of the FIR-only part of the continuum, and the upper limit is estimated by linear interpolation (in the log-log plane) of the 23 GHz and 94 GHz continuum measurements.

$\alpha=08^{\text{h}}31^{\text{m}}41^{\text{s}}.688\pm 0^{\text{s}}.004$, $\delta=+52^{\circ}45'17''.34\pm 0''.05$ (astrometric errors are derived from the fit). This corresponds to a peak flux ratio of $b(\text{SW,NE})=0.66 \pm 0.15$. The separation between both peaks is $d(\text{SW,NE})=0.31'' \pm 0.05''$.

The continuum emission (Fig. 9.1, right) is also clearly resolved and has about the same extent as the CO($J=1\rightarrow 0$) line emission, but is not resolved into two individual peaks. The emission rather peaks centrally between the two CO peaks indicated by the plus signs. For the continuum emission at this resolution, we derive a peak flux density of $147 \pm 12 \mu\text{Jy beam}^{-1}$ by fitting a single two-dimensional Gaussian.

In Fig. 9.2, four (continuum-subtracted) channel maps (9.375 MHz, or 120 km s^{-1} each) of the central 37.5 MHz (480 km s^{-1}) of the CO($J=1\rightarrow 0$) line are shown. The line is resolved into the two CO($J=1\rightarrow 0$) peaks defined above in the central two channels, and the decline of the line intensity towards the line wings is clearly visible in the outer channels, as expected. Due to the slight asymmetry of the CO($J=1\rightarrow 0$) line with respect to our central tuning frequency, only little emission is detected in the blueward outer channel, the lack of extended emission in this channel is therefore ascribed to low signal-to-noise rather than different structure relative to the other channels. From the central line channels, we derive a line peak flux density of $185 \pm 27 \mu\text{Jy beam}^{-1}$ for the north-eastern CO peak and a line peak flux density of $101 \pm 27 \mu\text{Jy beam}^{-1}$ for the south-western CO peak.

To derive the full CO($J=1\rightarrow 0$) and 23.5 GHz continuum flux of APM 08279+5255, we have imaged the whole B, C, and D array dataset with natural weighting, but tapered to a linear resolution of $\sim 1.2''$ (Fig. 9.3 and Fig. 9.6, top right). At this resolution, the source appears at best marginally resolved, and we derive that we outresolve at most 10% of the integrated flux. From the integrated maps, we derive an CO($J=1\rightarrow 0$) peak flux density of $210 \pm 19 \mu\text{Jy beam}^{-1}$, and a continuum peak flux density of $372 \pm 19 \mu\text{Jy beam}^{-1}$. The

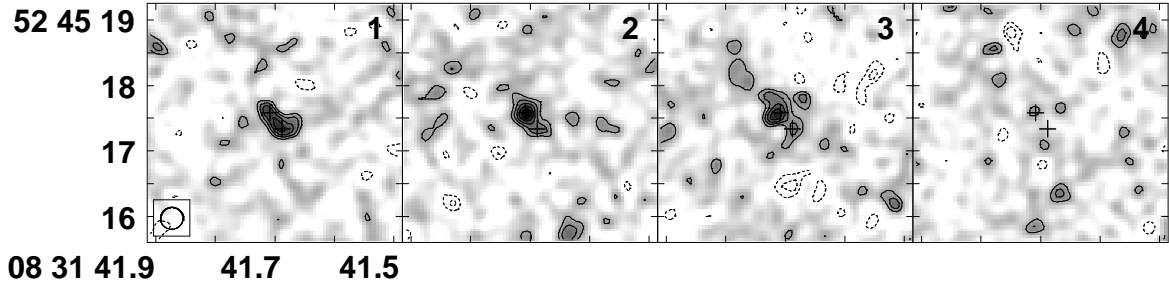


Figure 9.2: Channel maps of the CO($J=1\rightarrow 0$) emission (same region is shown as in Fig. 9.1). The beam size ($0.34''\times 0.33''$; natural weighting) is shown in the bottom left corner. The plus signs indicate the same positions as in Fig. 9.1. Contours are shown in steps of the rms noise, starting at $\pm 2\sigma$ ($1\sigma = 27\ \mu\text{Jy beam}^{-1}$). One channel width is 9.375 MHz, or $120\ \text{km s}^{-1}$ (frequencies increase with channel number and are shown at 23451.539, 23460.914, 23470.289, and 23479.664 MHz).

complete beam-corrected source fluxes (derived from 2-dimensional Gaussian fitting to the source) in both maps agree with the peak fluxes within the errors. It also agrees well with the beam-corrected fluxes in the full resolution dataset within the error bars. From the central line channels, we derive a CO($J=1\rightarrow 0$) line peak flux density of $285 \pm 27\ \mu\text{Jy beam}^{-1}$.

This peak flux agrees well with that derived from single-dish observations. Figure 9.4 shows the central part of the CO($J=1\rightarrow 0$) spectrum we have obtained with the GBT (Riechers et al. 2006a). This spectrum has a resolution of $75\ \text{km s}^{-1}$ at an rms of $65\ \mu\text{Jy}$ per channel. The solid black line is a Gaussian fit to that data. Overplotted on this spectrum, we show the flux of the four $120\ \text{km s}^{-1}$ channels of Fig. 9.2 (but for the tapered BCD array dataset). The error bars indicate the rms per channel ($40\ \mu\text{Jy}$). This clearly demonstrates that, within the error bars, our interferometric observations recover the same amount of CO emission as the single-dish observations obtained with a $\sim 32''$ observing beam.

9.5.2 CO($2\rightarrow 1$) Line Emission

The CO($J=2\rightarrow 1$) transition line towards APM08279+5255 ($z = 3.91$) is also detected (see also discovery paper by Papadopoulos et al. 2001). To extract the full CO($J=2\rightarrow 1$) line flux, we convolved the map with a circular beam of $1.2''$ diameter. From 2-dimensional Gaussian fitting, we then derive a line peak flux density of $1637 \pm 65\ \mu\text{Jy beam}^{-1}$.

We note that during none of the (archival) CO($J=2\rightarrow 1$) observations, the continuum at 46.9 GHz was measured. However, Papadopoulos et al. (2001) report a limit of $3\sigma = 0.9\ \text{mJy}$ on the continuum emission at 43.3 GHz. This means that up to half of the CO($J=2\rightarrow 1$) emission reported above may be attributed to 7 mm continuum emission rather than CO($J=2\rightarrow 1$) emission (see Sect. 4.3 for further discussion).

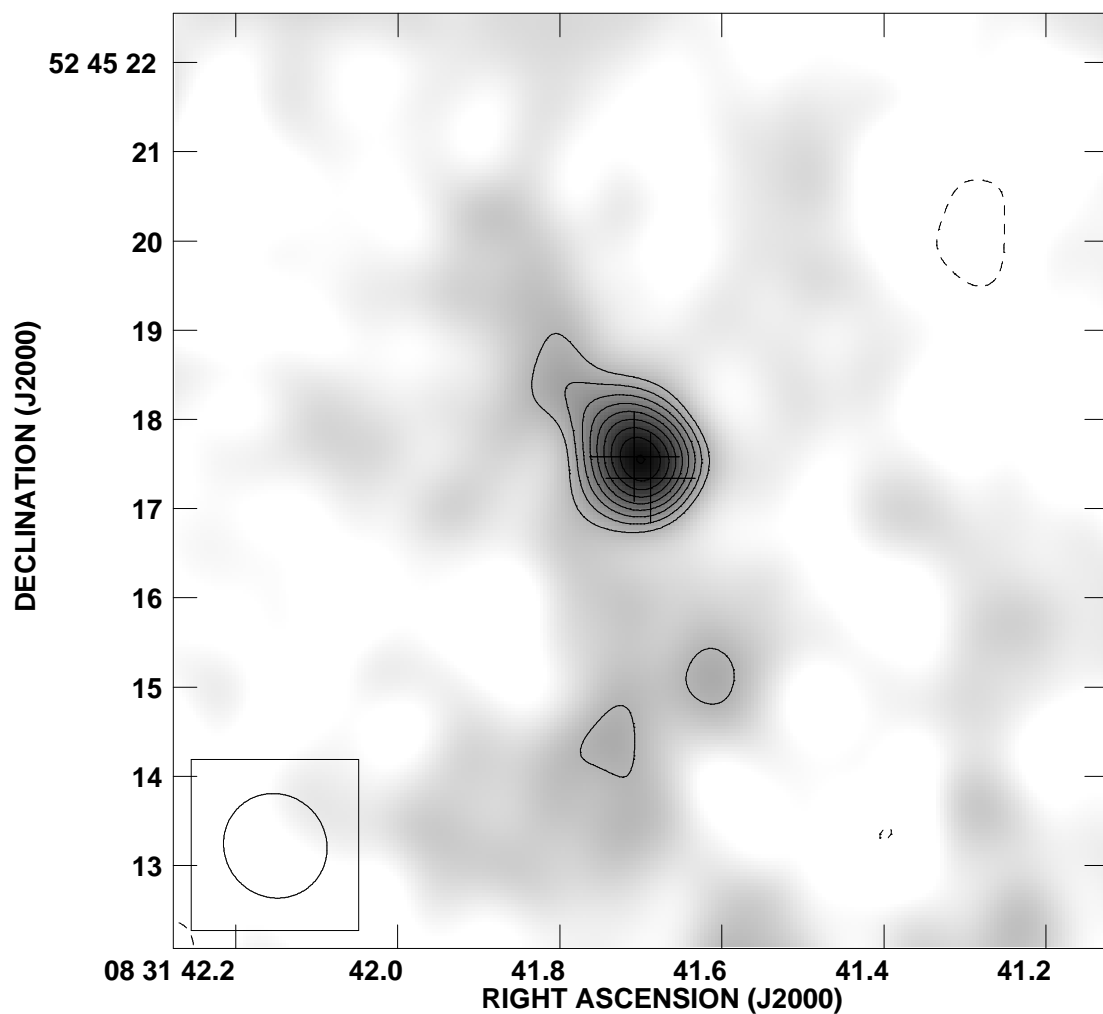


Figure 9.3: Map of the CO($J=1\rightarrow 0$) emission as shown in Fig. 9.1 (*middle*), but including D array short spacings, and tapered to a resolution of $1.19''\times 1.14''$ (natural weighting; beam size indicated in the bottom left corner). Contours are shown in steps of the rms noise, starting at $\pm 3\sigma$ ($1\sigma = 19\mu\text{Jy beam}^{-1}$; 11σ peak). The plus signs indicate the same positions as in Fig. 9.1. The emission appears practically unresolved, and there is no indication of any extended emission.

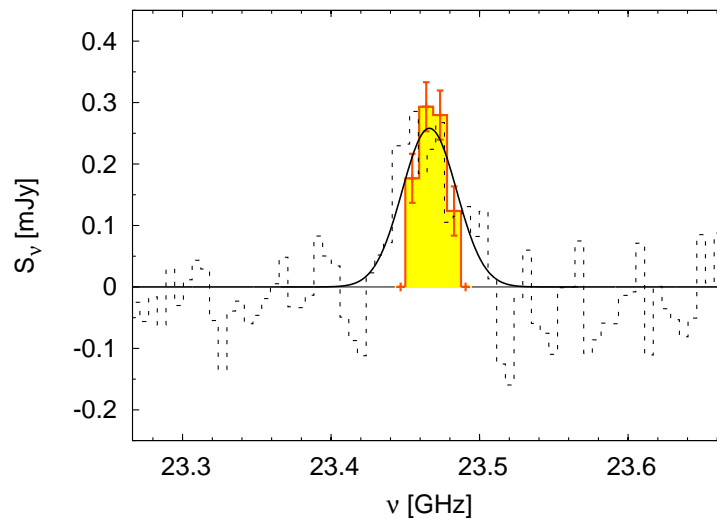


Figure 9.4: GBT spectrum of CO($J=1\rightarrow 0$) emission from APM 08279+5255 (Riechers et al. 2006a) at a resolution of 5.86 MHz (75 km s^{-1} , dashed line). The rms per channel is $65 \mu\text{Jy}$. The thin black line shows a Gaussian fit to the data. Overplotted is the peak flux densities of our new VLA CO($J=1\rightarrow 0$) data in the four 120 km s^{-1} channels shown in Fig. 9.2, but tapered to the resolution shown in Fig. 9.3. The error bars indicate the rms per channel of $40 \mu\text{Jy}$. This overlay shows that the GBT (single-dish) and the VLA (interferometer) detect the same amount of flux within the errors.

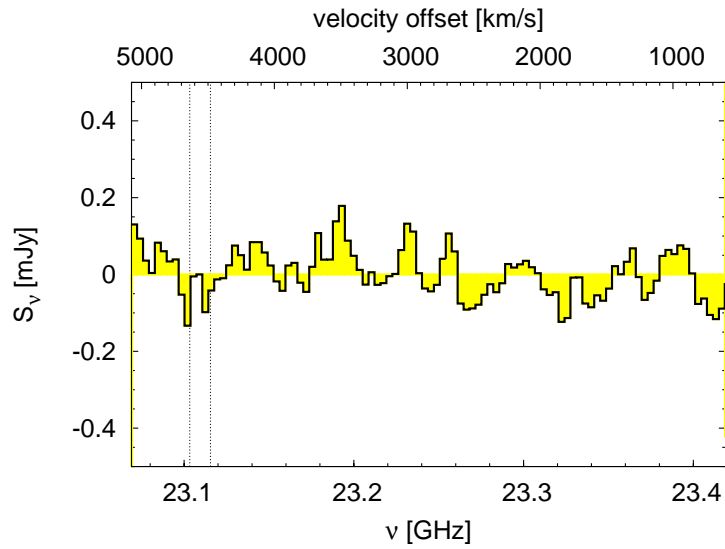


Figure 9.5: Redshifted CN($N=1\rightarrow 0$) spectrum of APM08279+5255 at a resolution of 3.5 MHz (45 km s^{-1}), obtained with the GBT. The velocity scale is relative to the CO($J=1\rightarrow 0$) peak. The global rms is $65 \mu\text{Jy}$. No emission is detected. The dashed lines indicate the range where the strongest fine structure components of the CN($N=1\rightarrow 0$, $v=0$, $J=3/2\rightarrow 1/2$) multiplet, i.e. the $F=3/2\rightarrow 1/2$, $F=5/2\rightarrow 3/2$, $F=1/2\rightarrow 1/2$, and $F=3/2\rightarrow 3/2$ transitions, are expected to peak. If the CN emission comes from a similar region than the CO emission, these components are expected to be blended.

9.5.3 The Search for CN(1–0) Line Emission

To measure the total CO luminosity, we have obtained wide-band CO($J=1\rightarrow 0$) observations toward APM08279+5255 with the GBT (see Riechers et al. 2006a for details). The bandwidth of these observations was high enough to also search for redshifted CN($N=1\rightarrow 0$) emission within the same setup (see Fig. 9.5). The strongest hyper-fine structure components of the CN($N=1\rightarrow 0$, $v=0$, $J=3/2\rightarrow 1/2$) multiplet, i.e. the $F=3/2\rightarrow 1/2$, $F=5/2\rightarrow 3/2$, $F=1/2\rightarrow 1/2$, and $F=3/2\rightarrow 3/2$ transitions, have rest frequencies of 113.4881420, 113.4909850, 113.4996430, and 113.5089340 GHz. At $z = 3.911$, this corresponds to 23.109, 23.110, 23.111, and 23.113 GHz. Accounting for the uncertainty in redshift (Riechers et al. 2006a), the dashed lines in Fig. 9.5 indicate the region where these transitions are expected to peak. We note that, if the CN emission comes from a similar region than the CO emission, these components are expected to be blended due to their large linewidth ($\gtrsim 500$ km s $^{-1}$, or 39 MHz FWHM, Riechers et al. 2006a; Weiß et al. 2007). At an rms of $65 \mu\text{Jy}$, we do not detect any emission. We thus set a 3σ limit of $195 \mu\text{Jy}$ on the peak strength of the CN($N=1\rightarrow 0$) emission in APM08279+5255.

9.5.4 Continuum Emission at 1.4 GHz

Using the VLA in A array, 1.4 GHz continuum emission from APM08279+5255 was detected by Ivison (2006). From this analysis, Ivison (2006) derived a continuum flux density of 3.05 ± 0.07 mJy. APM08279+5255 was previously detected at 1.4 GHz in the VLA-FIRST survey (White et al. 1997), but at significantly lower resolution and signal-to-noise. However, the 1.4 GHz continuum flux of $897 \pm 148 \mu\text{Jy beam}^{-1}$ derived from the VLA-FIRST data is significantly lower than that of Ivison (2006). To obtain a coherent dataset, we thus re-analyzed the A-array data by Ivison (2006). We derive a continuum peak flux density of $1160 \pm 33 \mu\text{Jy beam}^{-1}$ (see Fig. 9.6, top left). This value is consistent with that found from the VLA-FIRST survey data, but significantly lower than that derived by Ivison (2006). Our result was independently confirmed by Ivison (2007, priv. comm.). We thus use our revised 1.4 GHz continuum flux in the following.

9.5.5 Continuum Emission at 4.5 GHz

We have detected continuum emission at 4.5 GHz towards APM08279+5255 using the VLA in B array. APM08279+5255 remains unresolved in our observations (see Fig. 9.6, bottom left). We derive a continuum peak flux density of $551 \pm 40 \mu\text{Jy beam}^{-1}$. We also detect another continuum source about $3''$ south of APM08279+5255, which is detected at a peak flux density of $180 \pm 40 \mu\text{Jy beam}^{-1}$ (this source was first detected at 8.4 GHz by Ibata et al. 1999, see peak position derived below). At the given signal-to-noise, it is unclear whether this source is extended or not. APM08279+5255 has been detected at 4.5 GHz previously (Ivison 2006), but at a factor of 4 worse linear resolution (VLA C array, $\sim 5.5''$). Thus, APM08279+5255 and the source detected $3''$ south are blended at this resolution in Ivison's data, and the continuum flux of APM08279+5255 at 4.5 GHz is

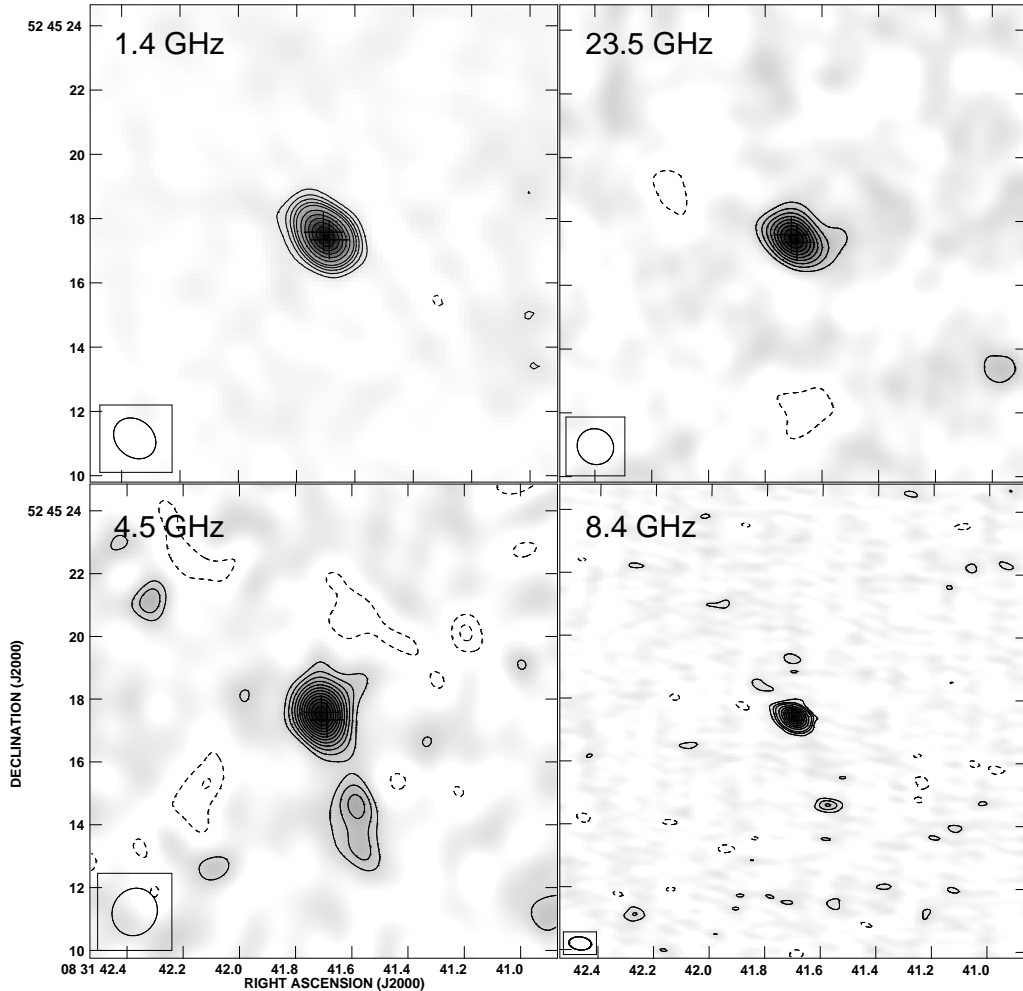


Figure 9.6: VLA maps of 1.4, 4.5, 8.4, and 23.5 GHz continuum emission towards APM08279+5255 (1.4 GHz: robust 0, rest: natural weighting). The plus signs indicate the same positions as in Fig. 9.1. *Top left*: Image of the 1.4 GHz continuum emission at a resolution of $1.42'' \times 1.15''$ (as indicated in the bottom left corner). Contours are shown at $(-3, 3, 5, 7, 9, 11, 15, 19, 23, 27, 31, 35) \times \sigma$ ($1\sigma = 33 \mu\text{Jy beam}^{-1}$). This continuum map is integrated over a bandwidth of 43.75 MHz. *Top right*: Image of the 23.5 GHz continuum emission tapered to a resolution of $1.19'' \times 1.10''$. Contours are shown in steps of twice the rms noise, starting at $\pm 3\sigma$ ($1\sigma = 19 \mu\text{Jy beam}^{-1}$; 19σ peak). This continuum map is integrated over a bandwidth of 100 MHz. *Bottom left*: Image of the 4.5 GHz continuum emission at a resolution of $1.55'' \times 1.42''$. Contours are shown in steps of the rms noise, starting at $\pm 2\sigma$ ($1\sigma = 40 \mu\text{Jy beam}^{-1}$; 13σ peak). This continuum map is integrated over a bandwidth of 12.11 MHz. *Bottom right*: Image of the 8.4 GHz continuum emission at a resolution of $0.73'' \times 0.42''$. Contours are shown at $(-3, 3, 5, 7, 11, 15, 19, 23, 27, 31) \times \sigma$ ($1\sigma = 10 \mu\text{Jy beam}^{-1}$). This continuum map is integrated over a bandwidth of 100 MHz. In the 4.5 and 8.4 GHz maps, a radio source is detected about $3''$ south of APM08279+5255 (at $\alpha = 08^{\text{h}}31^{\text{m}}41^{\text{s}}.576$, $\delta = +52^{\circ}45'14''.66$; 4σ and 7σ peak strength). This source remains undetected at 1.4 and 23.5 GHz (also undetected at 14.9 and 46.9 GHz).

Table 9.3: Continuum Fluxes of VLA J083141+524514

Frequency	S_ν (μJy)	Configuration
1.4 GHz	<100	A
4.5 GHz	180 ± 40	B
8.4 GHz	83 ± 10	BnA/B
14.9 GHz	<130	B
23.5 GHz	<40	BCD
46.9 GHz	<200	CD

Notes—Source is detected at position $\alpha = 08^{\text{h}}31^{\text{m}}41^{\text{s}}.576$, $\delta = +52^{\circ}45'14''.66$.

overestimated. The 4.5 GHz continuum flux derived from Ivison’s data (his Fig. 2, bottom panel) is in good agreement with the sum of the 4.5 GHz continuum fluxes of both sources in our analysis. We thus use our revised 4.5 GHz continuum flux of APM08279+5255 in the following.

9.5.6 Continuum Emission at 8.4 GHz

Continuum emission from APM08279+5255 was first detected at 8.4 GHz by Ibata et al. (1999) using the VLA in BnA array. We here combine this data with shorter B array spacings to improve the sensitivity of the data (see Fig. 9.6, bottom right). For APM08279+5255, we derive a 8.4 GHz peak flux density of $446 \pm 20 \mu\text{Jy beam}^{-1}$ (map convolved with a circular beam of $1.2''$ diameter for flux extraction), consistent with the value given by Ibata et al. (1999) of $0.45 \pm 0.03 \text{ mJy}$. We also detect the ‘southern’ source described in the previous subsection. It is detected at higher signal-to-noise and resolution in the unconvolved map than at 4.5 GHz. We thus use the 8.4 GHz data to derive the peak position of the source. The position of $\alpha=08^{\text{h}}31^{\text{m}}41^{\text{s}}.576 \pm 0^{\text{s}}.006$, $\delta=+52^{\circ}45'14''.66 \pm 0''.03$ is in good agreement with the peak of the 4.5 GHz continuum (source designation from now on: VLA J083141+524514). From the unconvolved, naturally weighted emission line map, we derive a peak flux density of $83 \pm 10 \mu\text{Jy beam}^{-1}$. Note that VLA J083141+524514 is detected in none of the other bands, 3σ upper limits are given in Tab. 9.3.

We also imaged APM08279+5255 with uniform weighting (Fig. 9.7). The emission is clearly resolved into two peaks at this higher resolution, which coincide with the $\text{CO}(J=1 \rightarrow 0)$ peaks as indicated by the plus signs. Interestingly, both peaks appear to have the same brightness at 8.4 GHz ($205 \pm 20 \mu\text{Jy beam}^{-1}$ for the north-eastern peak, and $(204 \pm 20 \mu\text{Jy beam}^{-1}$ for the south-western peak). This is consistent with the naturally weighted image, where the emission peaks centrally between the $\text{CO}(J=1 \rightarrow 0)$ peak positions, and possibly caused by a combination of two differentially lensed components of the source with different spectral index. VLA J083141+524514 remains unresolved at this higher resolution.

9.5.7 Continuum Emission at 14.9 GHz

Continuum emission at 14.9 GHz was searched for towards APM08279+5255. We tentatively detect emission at the center of the $\text{CO}(J=1 \rightarrow 0)$ peak positions. This emission

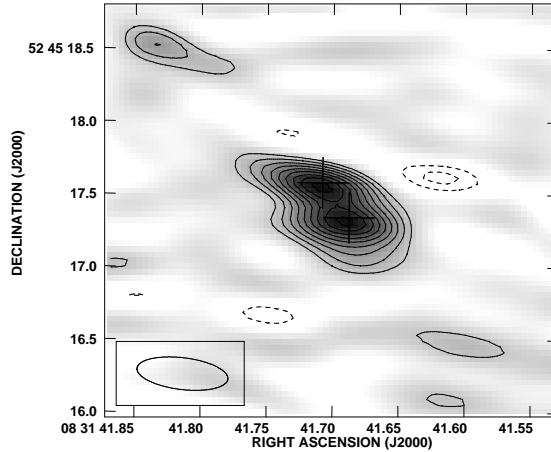


Figure 9.7: Uniformly weighted 8.4 GHz continuum map. The beam size ($0.63'' \times 0.22''$) is shown in the bottom left corner. Contours are shown in steps of the rms noise, starting at $\pm 2\sigma$ ($1\sigma = 20 \mu\text{Jy beam}^{-1}$). The source is clearly resolved into two peaks at this resolution (10σ each), which coincide with the CO($J=1 \rightarrow 0$) peaks (as indicated by the plus signs, see Fig. 9.1).

appears to be resolved and elongated along the same axis as the CO($J=1 \rightarrow 0$) emission. The peak flux density measured at this position is $161 \pm 44 \mu\text{Jy beam}^{-1}$. However, since the detected flux density is $< 4\sigma$, this measurement has to be treated with caution, and more sensitive data is required to confirm this result. Convolution of this image with a circular beam of $1.2''$ diameter as above, we derive a flux density of $303 \pm 93 \mu\text{Jy beam}^{-1}$, which we will treat as a tentative detection in the following. We summarize all our results in Tab. 9.2.

9.6 Analysis

9.6.1 Spectral Energy Distribution

Detailed continuum observations are now available for APM 08279+5255. Figure 9.8 shows the near-infrared-to-radio ($\sim 1 \mu\text{m} - 1 \text{ m}$, or 300 THz–300 MHz) spectral energy distribution (SED). The mid-IR-to-far-IR part of the spectrum has been modeled previously (Rowan-Robinson 2000; Beelen et al. 2006), indicating that a two component fit to the dust emission may be necessary to reproduce the data (a ‘warm’ AGN dust torus component plus a ‘cold’ starburst component; see also the multiple-component models by Blain et al. 2003). Recently, Weiß et al. (2007) have presented a model for the dust continuum which also assumes two components, but which is additionally constrained by model parameters which

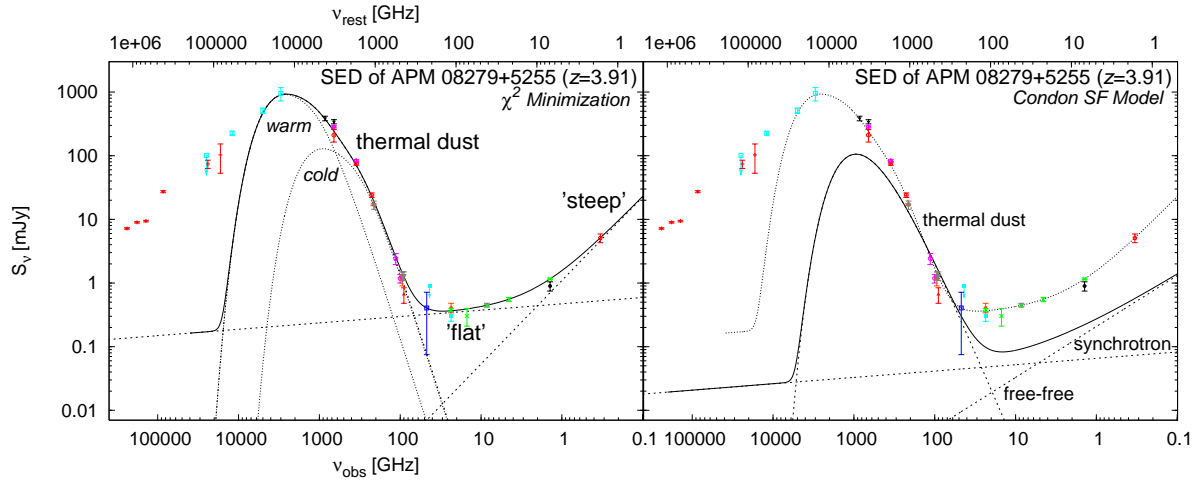


Figure 9.8: Near-infrared-to-radio spectral energy distribution (SED) of APM 08279+5255. The crosses indicate the measurements described in this chapter, and the open square gives an estimate for the 46.9 GHz continuum flux. All other signs indicate detections and upper limits from the literature (White et al. 1997; Irwin et al. 1998; Lewis et al. 1998; Ibata et al. 1999; Downes et al. 1999; Egami et al. 2000; Papadopoulos et al. 2001; Barvainis & Ivison 2002; Lewis et al. 2002a; Wagg et al. 2005, 2006; Beelen et al. 2006; Ivison 2006; and Weiß et al. 2007). *Left*: The solid line represents a model fit to the thermal dust continuum, and a two-component power-law fit to the radio continuum emission. The components are indicated by the dashed lines. The parameters for the model for the dust part of the continuum are adopted from Weiß et al. (2007); the dotted lines indicate the ‘cold’ and ‘warm’ subcomponents of their model. The parameters of the ‘flat’ and ‘steep’ spectrum components are determined by least-squares power law fitting. *Right*: The solid line represents a model of the thermal dust, free-free, and synchrotron emission SED components of a star-forming galaxy, as described by Condon (1992). The thick dashed lines indicate those components. Only the ‘cold’ dust subcomponent which is dominated by heating from star formation is considered for the model. The thin dashed line shows the model in the left panel for comparison (see text for more details).

result from a study of multiple rotational transitions of CO and HCN.

However, no detailed analysis of the radio continuum properties of APM08279+5255 has been conducted so far. We here present two modeling approaches. The first model aims at finding an overall good fit to the data while minimizing the number of free parameters. The second model aims at constraining which fraction of the total radio continuum emission is due to star formation (i.e., not AGN-related¹⁰).

Best Fit SED Model

As our focus lies on fitting the radio data, we restrict our analysis to the mid-IR-to-radio part of the spectral data (60 μm to 90 cm). Thermal dust emission is mainly caused by ionizing and non-ionizing ultra-violet (UV) radiation from massive stars and (in quasars) possibly the central AGN. This radiation is processed by the dust and then re-radiated in the far-infrared wavelength regime. To minimize the number of free parameters, we adopt the results of Weiß et al. (2007) to describe the dust continuum part of the SED. As discussed by Weiß et al., this implies dust masses of $M_{\text{d,cold}} = 2.6 \times 10^9 \mu_L^{-1} M_\odot$ and $M_{\text{d,warm}} = 7.0 \times 10^7 \mu_L^{-1} M_\odot$ and dust temperatures of $T_{\text{d,cold}} = 75 \text{ K}$ and $T_{\text{d,warm}} = 220 \text{ K}$ for the ‘cold’ and ‘warm’ dust components, a dust disk with a magnified equivalent radius of $r_0 = 1300 \text{ pc}$, relative area filling factors of 78% and 22%, and a dust absorption coefficient exponent of $\beta=2$ to describe its frequency dependence (μ_L denotes the lensing magnification, the index d denotes thermal dust emission). Using these parameters and equations 3, 4, 5, and 6 of Weiß et al. (2007) fully describes the model used here for the dust emission. The observed flux density of the dust emission will be denoted as $S_{\nu,\text{d}}$ in the following. To extend this model to the radio continuum, we added a double power-law component, which we fit by the χ^2 minimization technique. The full expression for the model flux density takes the form:

$$S_\nu(\nu) = S_{\nu,\text{d}}(\nu) + \sum_{i=\text{flat,steep}} c_i \times \nu^{\alpha_i}, \quad (9.1)$$

where ν indicates the frequency in GHz, c indicates a constant coefficient, α denotes a spectral index, and i indicates the index denoting the ‘flat’ and ‘steep’ power-law components.

To solve equation (1), we attempted to fit the observed SED with three degrees of complexity. In the first step, we fixed the dust term to the model parameters by Weiß et al. (2007, see above), and fitted the ‘flat’ and ‘steep’ components with a four-parameter double power law least-squares fit. The best fits to the ‘flat’ component result in α_{flat} values close to -0.1. However, the fitting uncertainty of this component is quite large due to the relatively small region where this component actually dominates the emission. In the second step, we thus fixed α_{flat} to -0.1. The remaining three free parameters are fairly well constrained. Our best-fitting model to the composite spectrum then gives a ‘steep’ power

¹⁰Note that our models do not account for possible AGN variability in this source (for which no evidence has been found to date).

law index of $\alpha_{\text{steep}} = -1.31 \pm 0.27$, and ‘steep’ and ‘flat’ coefficients of $c_{\text{steep}} = 1.09 \pm 0.13$ and $c_{\text{flat}} = 0.47 \pm 0.06$. The ‘steep’ power law index suggests that APM 08279+5255 may be an ultra-steep spectrum source ($\alpha_{\text{steep}} < -1.2$; e.g., Bondi et al. 2007), which may indicate that it evolves in a dense environment (Klamer et al. 2006). In the third step, we left single or pairs of parameters of the Weiß et al. (2007) dust model as free parameters to test the stability of the solution. This however did not further improve our best solution. Our final SED model is shown in the left panel of Fig. 9.8.

Model SED of a Star-forming Galaxy

Due to the fact that APM 08279+5255 is a composite AGN-starburst system, it is likely that both components contribute to the continuum emission at radio wavelengths. Note that the ‘warm’ dust component in the Weiß et al. model of APM 08279+5255, which is likely dominated by AGN heating, contributes $\sim 90\%$ to the far-infrared (FIR) luminosity. This finding implies that a clear separation of AGN and starburst contributions to the radio luminosity should be possible.

We here investigate what fraction of the radio emission can be produced by the starburst component in APM 08279+5255. Based on the SED of the Milky Way and first principles, Condon (1992) has developed a model for the radio-through-FIR emission from ‘normal’ galaxies, which is solely attributed to a stellar origin. This model contains three components: one for thermal dust emission, one for thermal (mostly free-free) radio emission, and one for non-thermal (mostly synchrotron) radio emission. The two radio components are described by power laws. This model also fits the starburst galaxy M82 very well.

Free-free emission is either associated with the ionized gas in HII regions surrounding hot young stars, or the environment of the active galactic nucleus, and therefore an indicator for the total photoionization rate. If the thermal, optically thin free-free (or thermal bremsstrahlung) radiation emerges from a 10^4 K photoionized gas, a spectral index of $\alpha_{\text{ff}} = -0.1$ (notation analogue to above) is expected, and thus assumed in the Condon model. The free-free power-law coefficient c_{ff} then parameterizes the emission measure, the source size and the electron temperature. However, note that free-free emission can only be described by a simple power law if the emission is optically thin.

The (at typical radio wavelengths) optically thin (non-thermal) synchrotron emission is produced in supernova explosions and remnants (SNRs) through acceleration of cosmic ray electrons, spiraling in a galaxy’s magnetic field. Detection of strong synchrotron emission from relativistic electrons thus indicates the presence of a large-scale magnetic field (Turner et al. 1998). In starburst galaxies, it may indicate a concentration of SNRs associated with localized and intense star formation. Synchrotron emission usually shows a spectral index of $-1.2 \leq \alpha_{\text{sync}} \leq -0.4$, with a typical value of -0.8 , which is assumed in the Condon model. Here, the synchrotron power-law coefficient c_{sync} parameterizes the type II supernova rate (assuming that supernova remnants dominate the non-thermal synchrotron emission).

In the Condon (1992) model, all three components (dust heating, free-free, and synchrotron) are directly proportional to the star-formation rate (SFR) in a galaxy. The dust emissivity β , the dust temperature T_d , and the SFR are the only model parameters. We

here adopt $\beta=1.5$ from Condon’s model. Due to the fact that the ‘warm’ dust component in APM08279+5255 is likely heated by the AGN, we here only consider the ‘cold’ component, which likely traces the dominant fraction of the dust heated by star formation. We thus adopt $T_d=75$ K. The only remaining free parameter thus is the SFR. Assuming a SFR of $4000 \mu_L^{-1} M_\odot \text{ yr}^{-1}$ provides a reasonable fit to the spectrum of the cold dust of APM08279+5255 (see Fig. 9.8, right). However, this model only recovers $\sim 20\%$ of the radio emission. Yun & Carilli (2002) suggested some changes to the Condon model¹¹, which would result in about a factor of 2 less radio flux compared to the original Condon model. Although it is difficult to assess the validity of a simple Condon model for a warm, starbursting quasar like APM08279+5255, this result leads us to conclude that the radio continuum emission in this source is dominantly AGN-related. This is in agreement with our best-fit model, as it implies an ultra-steep radio spectrum component, which is usually associated with a source where AGN-related emission dominates the energy output at radio frequencies (e.g., high redshift radio galaxies and quasars; Athreya et al. 1997; Pentericci et al. 2000). The ultra-steep spectrum component in AGN-driven radio sources is often associated with extended radio emission. Interestingly, the best-fit model also requires a relatively bright ‘flat’-spectrum component to originate from the radio AGN. The core of the archetypical radio galaxy Cygnus A has a flat spectrum at radio wavelengths, which dominates over the steep-spectrum emission from the hotspots at higher frequencies (e.g., Eales et al. 1989). A similar ‘composite’ effect (extended steep-spectrum component, flat core component) may cause the apparent flattening of the radio spectrum of APM08279+5255.

9.6.2 Comparison to Previous CO(1–0) Imaging

The CO($J=1\rightarrow 0$) transition line in APM08279+5255 was targeted twice before with the VLA, first at C array resolution ($1.5'' \times 1.4''$, Papadopoulos et al. 2001), and then followed up at higher B array resolution ($0.39'' \times 0.28''$, Lewis et al. 2002a). Both observations were setup in quasi-continuum mode, i.e. lacking any spectral information of the CO($J=1\rightarrow 0$) line. In both observations, CO($J=1\rightarrow 0$) line and 23.3649 GHz continuum emission were detected towards the source. Papadopoulos et al. (2001) detect unresolved continuum emission at a flux density level of 0.30 ± 0.05 mJy. Lewis et al. (2002a) detect continuum emission at a flux density of 0.41 ± 0.07 mJy, and the resolved structure coincides with our continuum map in structure and position. Both flux densities are in agreement with our result within the errors, although some intrinsic variability cannot be excluded.

Papadopoulos et al. (2001) report the detection of resolved CO($J=1\rightarrow 0$) emission towards APM08279+5255, which extends over scales of $\gtrsim 7'' \times 2.25''$ (their 3σ contour) at a resolution convolved to $2.25'' \times 2.25''$ ($7''$ correspond to ~ 30 kpc at the target redshift of 3.911). They quote an integrated flux for the ‘nuclear CO($J=1\rightarrow 0$) emission’ (the inner $\sim 1''$) of 0.150 ± 0.045 Jy km s^{-1} .

¹¹They suggest a different initial mass function, an update to the H α normalization, and a small correction factor for the supernova rate.

From our new VLA observations, we derive an integrated CO($J=1\rightarrow 0$) flux of $0.168 \pm 0.015 \text{ Jy km s}^{-1}$ assuming a line FWHM of $556 \pm 55 \text{ km s}^{-1}$ (Riechers et al. 2006a; width of our bandpass: 558 km s^{-1}). This corresponds to a CO($J=1\rightarrow 0$) line luminosity of $L'_{\text{CO}(1\rightarrow 0)} = (10.6 \pm 0.9) \times 10^{10} \mu_L^{-1} \text{ K km s}^{-1} \text{ pc}^2$ (see Tab. 9.4). From the CO($J=1\rightarrow 0$) spectrum obtained with the GBT, Riechers et al. (2006a) find $0.152 \pm 0.020 \text{ Jy km s}^{-1}$. The 3σ contour of the extended CO($J=1\rightarrow 0$) reservoir of Papadopoulos et al. (2001, their Fig. 1) corresponds to a flux density of $120 \mu\text{Jy beam}^{-1}$. In our CO($J=1\rightarrow 0$) map which was tapered to a linear resolution of $\sim 1.2''$ (Fig. 9.3, similar to the resolution of their observations), this would correspond to 6.3σ . Even at less than half this flux level ($3\sigma = 57 \mu\text{Jy beam}^{-1}$), we find no evidence for any extended flux. We note that our observations even include shorter (D array) baselines than Papadopoulos et al. (2001) and are therefore more sensitive to extended structure. We thus exclude the possibility that our observations out-resolve the extended emission, and conclude that there is no bright, extended CO($J=1\rightarrow 0$) reservoir in APM08279+5255.

Lewis et al. (2002a) find resolved CO($J=1\rightarrow 0$) emission on sub-arcsec scale at moderate signal-to-noise. The peak of the emission reported in their paper roughly coincides with our north-eastern CO($J=1\rightarrow 0$) peak. However, our new, by a factor of 2 more sensitive (in terms of rms noise) high-resolution data does not show the extended structure that is present in their CO($J=1\rightarrow 0$) map, which we thus conclude to be a noise artifact. Lewis et al. (2002a) derive an integrated CO($J=1\rightarrow 0$) flux of $0.22 \pm 0.05 \text{ Jy km s}^{-1}$ from their observations, in agreement with the three independent results given above within the errors (adopting only the ‘nuclear CO($J=1\rightarrow 0$) emission’ from the report of Papadopoulos et al.).

9.6.3 On the 46.9 GHz Continuum Emission

As mentioned previously, the continuum emission at the line frequency (46.9 GHz) was not monitored in parallel during the (archival) CO($J=2\rightarrow 1$) observations. Papadopoulos et al. (2001) report a limit of $3\sigma = 0.9 \text{ mJy}$ on the continuum emission at 43.3 GHz. This corresponds to $\sim 55\%$ of the CO($J=2\rightarrow 1$) peak flux. Therefore, the ‘real’ CO($J=2\rightarrow 1$) flux towards APM08279+5255 may be lower by up to a factor of 2. Based on our SED modeling, we now attempt to set additional limits to the continuum contribution to the emission detected at the CO($J=2\rightarrow 1$) frequency to attain some tighter constraints.

A first-order estimate for the 46.9 GHz continuum flux is provided by examining the overall spectral energy distribution of APM08279+5255. The SED model presented in Fig. 9.8 predicts a continuum flux at 46.9 GHz of $405 \mu\text{Jy}$. This estimate is plotted as the square symbol in Fig. 9.8. A lower constraint is provided by the fit to the thermal part of the SED ($75 \mu\text{Jy}$), and an upper constraint is given by linear interpolation of the 23 GHz and 94 GHz continuum flux measurements ($715 \mu\text{Jy}$). For illustration, these constraints are plotted as error bars to this model-predicted data point. We however note that the 23 GHz and 94 GHz measurements were obtained at different epochs, therefore this estimate does not account for possible variability of the millimeter continuum.

As another estimate, we assume that both the emission from CO($J=1\rightarrow 0$) and CO($J=2\rightarrow 1$) are fully thermalized and optically thick. The CO($J=2\rightarrow 1$) peak flux should

Table 9.4: Line Intensities, Luminosities, and Ratios

Line	I (Jy km s ⁻¹)	L' (10 ¹⁰ μ_L^{-1} K km s ⁻¹ pc ²)	$L'/L'_{\text{CO}(1-0)}$	data reference
CO($J=1\rightarrow 0$)	0.168 ± 0.015	10.6 ± 0.9	1	1,2
CO($J=2\rightarrow 1$)	0.81 ± 0.18	12.8 ± 2.9	1.21 ± 0.30	1,3
CO($J=4\rightarrow 3$)	3.7 ± 0.2	14.7 ± 0.9	1.39 ± 0.16	4
CO($J=6\rightarrow 5$)	6.7 ± 1.2	11.8 ± 2.1	1.12 ± 0.23	4
CO($J=9\rightarrow 8$)	11.8 ± 0.6	9.2 ± 0.4	0.89 ± 0.10	4
CO($J=10\rightarrow 9$)	11.9 ± 2.0	7.5 ± 1.2	0.71 ± 0.14	4
CO($J=11\rightarrow 10$)	11.3 ± 1.9	5.9 ± 1.0	0.56 ± 0.11	4
CN($N=1\rightarrow 0$)	<0.06	<3.9	<0.37	1

Notes—Luminosities are apparent values uncorrected for gravitational magnification. They are derived as described by Solomon et al. (1992b): $L'[\text{K km s}^{-1} \text{pc}^2] = 3.25 \times 10^7 I \nu_{\text{obs}}^{-2} D_L^2 (1+z)^{-3} \mu_L^{-1}$, where I is the velocity-integrated line flux in Jy km s⁻¹, D_L is the luminosity distance in Mpc, ν_{obs} is the observed frequency in GHz, and μ_L is the lensing magnification factor.

References—(1) this work; (2) Riechers et al. 2006a; (3) Papadopoulos et al. 2001; (4) Weiß et al. 2007.

then be four times higher than the CO($J=1\rightarrow 0$) peak flux. For the CO($J=1\rightarrow 0$) peak flux, an average over the whole 558 km s⁻¹ bandpass ($210 \pm 19 \mu\text{Jy}$) is assumed to match the velocity resolution of the CO($J=2\rightarrow 1$) observations as closely as possible. In comparison to the measured flux at the CO($J=2\rightarrow 1$) frequency ($1637 \pm 65 \mu\text{Jy}$), this predicts a contribution of the continuum flux of $\sim 800 \mu\text{Jy}$, which is twice as high as the SED-based estimate. This discrepancy may be explained by different optical depths of the emission from different rotational CO transitions. If the opacity of the CO($J=1\rightarrow 0$) emission is much lower than that of the higher J transitions, it may actually have a lower luminosity than the emission from these transitions [contrary to the effects of (sub-)thermal excitation]. This would allow the CO($J=2\rightarrow 1$) line peak flux to be more than four times higher than the CO($J=1\rightarrow 0$) peak flux. Note that such an effect may actually be observed towards APM08279+5255 in the $J \geq 4$ transitions (Weiß et al. 2007; see also Tab. 9.4).

We conclude that APM08279+5255 likely exhibits a 46.9 GHz continuum flux of at least 0.4 mJy, i.e. 25% of the measured CO($J=2\rightarrow 1$) flux. We thus estimate the ‘real’ CO($J=2\rightarrow 1$) line peak flux to be ~ 1.2 mJy. From this, we derive a CO($J=2\rightarrow 1$) line luminosity of $L'_{\text{CO}(2-1)} = (12.8 \pm 2.9) \times 10^{10} \mu_L^{-1} \text{K km s}^{-1} \text{pc}^2$.

9.6.4 A Limit for the CN Luminosity

Due to its fine structure (fs) and hyperfine structure (hfs) splitting, the CN($N=1\rightarrow 0$) emission line is distributed over 9 lines¹² in its $v=0$ vibrational state. These lines are distributed in 2 main components separated by about 350 MHz in the rest frame. While the hfs transitions within these main components are blended if their kinematical broadening is similar to that of the CO/HCN lines in APM08279+5255, the components themselves are still

¹²We assume that CN is in its ground electronic state ($^2\Sigma$), and that the spins couple according to Hund’s case (b) coupling scheme: $\vec{N} + \vec{S} = \vec{J}$, (fs coupling) and $\vec{J} + \vec{I}_C + \vec{I}_N = \vec{F}$ (hfs coupling). Here, \vec{N} is the rotational angular momentum vector, \vec{S} is the electronic spin, and \vec{I} is a nuclear spin.

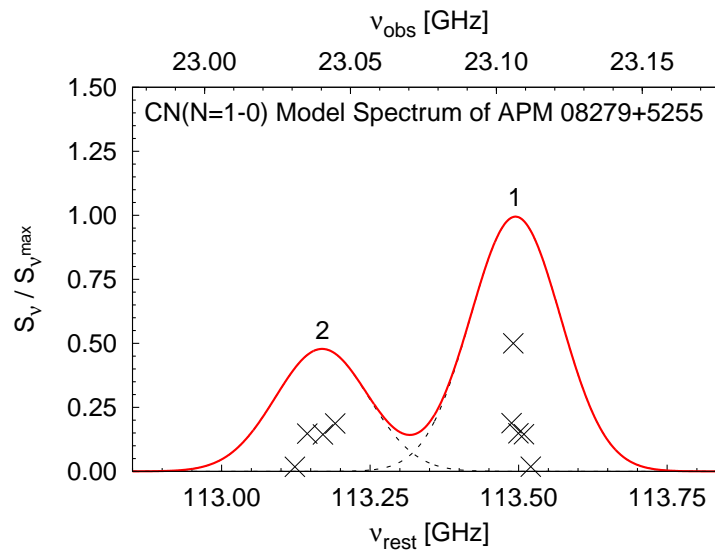


Figure 9.9: Model spectrum of the CN($N=1 \rightarrow 0$) emission in APM08279+5255. The horizontal axes indicate the rest and observed frequencies. The vertical axis indicates the predicted intensity, normalized to the peak of the emission. The relative intensities of the fs and hfs components are computed for the LTE case. The crosses indicate the hfs components. The dashed lines are Gaussian fits to the summed intensities in the two main frequency bins, assuming the average width of the higher J CO lines (Weiß et al. 2007) for the subcomponents (labeled '1' and '2'). The solid line is a sum of all components, and indicates the model-predicted CN($N=1 \rightarrow 0$) line shape.

clearly separated. To obtain a proper limit on the integrated CN($N=1\rightarrow 0$) line flux (and thus on the total CN luminosity), we calculated a synthetic line profile, assuming optically thin emission in the Local Thermodynamic Equilibrium (LTE) case to derive the relative intensities of the hfs components. The relative intensities of the components were computed using the laboratory data from Skatrud et al. (1983), and approximation (4) of equation (1) of Pickett et al. (1998). Assuming that all CN($N=1\rightarrow 0$) hfs components are kinematically broadened in the same way as the higher J CO lines (~ 500 km s $^{-1}$ FWHM; see Weiß et al. 2007), we obtain the synthetic line profile displayed in Fig. 9.9 (solid line). The two main components (dashed lines) have a peak strength ratio of 2:1. The brightest main component is fully covered by our bandpass, the second component, however, was close to the edge, and thus only covered in part by the part of the spectrum that was properly calibratable. For the derivation of the limit on the integrated CN($N=1\rightarrow 0$) line flux, we thus consider the peak flux limit for the brightest component to derive the relative intensity limits for all subcomponents in the LTE case. Under these assumptions, we derive a limit of $I_{\text{CN}} < 0.06$ Jy km s $^{-1}$ for the integrated line flux, and thus a limit of $L'_{\text{CN}} < 3.9 \times 10^{10} \mu_L^{-1}$ K km s $^{-1}$ pc 2 for the line luminosity. This corresponds to a luminosity ratio limit of $L'_{\text{CN}}/L'_{\text{CO}} \leq 0.37$. Note that Guélin et al. (2007) recently observed the CN($N=4\rightarrow 3$) transition towards APM 08279+5255; however, due to strong blending with the HNC($J=5\rightarrow 4$) line, it remains unclear whether or not the line is detected.

9.6.5 Radio Luminosity

In general, the monochromatic rest-frame 1.4 GHz radio luminosity is defined as:

$$L_{1.4\text{GHz}} = \frac{4\pi D_L^2}{(1+z)^{1+\alpha_{1.4}}} S_{1.4\text{GHz}}. \quad (9.2)$$

However, we here calculate $L_{1.4\text{GHz}}$ based on the 1.4 GHz flux predicted by our best-fit SED model. In the above equation, this would correspond to using a spectral index of $\alpha_{1.4} = -1.05$. We thus obtain $L_{1.4\text{GHz}} = (1.90 \pm 0.05) \times 10^{26} \mu_L^{-1}$ W Hz $^{-1}$ (not lensing corrected), about 10 times the radio luminosity of M87 ($L_{1.4\text{GHz}} = (1.76 \pm 0.07) \times 10^{25}$ W Hz $^{-1}$; Laing & Peacock 1980). In an analogous manner, we derive a 5 GHz radio luminosity of $L_{5\text{GHz}} = (4.75 \pm 0.34) \times 10^{25} \mu_L^{-1}$ W Hz $^{-1}$. Here, the model prediction would correspond to a spectral index of only $\alpha_5 = -0.67$.

Studies of the radio luminosity function of quasars and its evolution have identified a bimodality in the source distribution, separating them into radio-quiet and radio-loud quasars. However, two generally different definitions of radio loudness have been put forward, one based on the optical-to-radio flux ratio (e.g., Schmidt 1970; Kellerman et al. 1989), and one only based on the monochromatic radio luminosity (e.g., Peacock et al. 1986; Schneider et al. 1992). However, Ivezić et al. (2002) argue that for optically selected quasars, both definitions are similar within the flux-limited samples that were examined. We thus restrict our analysis to the radio luminosity-based estimate here. Due to different assumptions and definitions, a range of threshold values for the radio loudness definition is found in the literature. For the radio-based definition, we here adopt the range

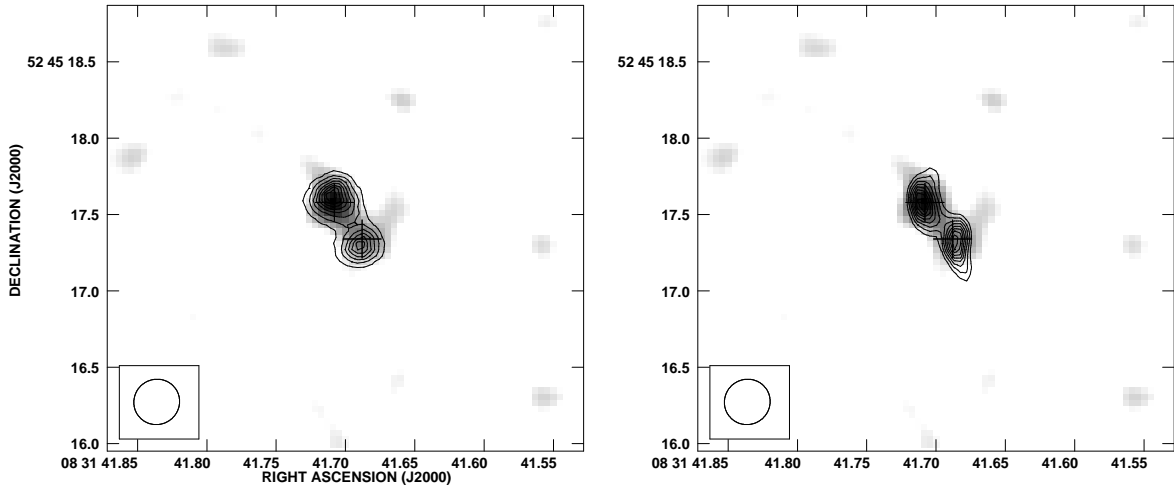


Figure 9.10: Morphology of APM08279+5255 at different wavelengths. *Left*: Contours of $2.2\ \mu\text{m}$ continuum emission (Egami et al. 2000) overlaid on the $\text{CO}(J=1\rightarrow 0)$ emission. *Right*: Contours of hard X-ray emission (Chartas et al. 2002) overlaid on the $\text{CO}(J=1\rightarrow 0)$ emission. Contours in both panels are 20%, 30%, ..., 90% of the peak flux of the emission. The CO greyscale scales between 2σ and the peak flux of the emission (see Fig. 9.1). The crosses indicate the CO peak positions. The size of the synthesized beam of the CO observations is indicated in the bottom left corner.

of $L_{5\text{ GHz}} = (1.0\text{--}5.6) \times 10^{25}\ \text{W Hz}^{-1}$ given by Schneider et al. (1992). Changing the cutoff within this range does not change the relations they find dramatically. Even without correcting for gravitational lensing, APM08279+5255 clearly falls within the transition region between radio-quiet and radio-loud sources. As this source is known to be substantially gravitationally magnified (see also discussion below), we conclude that it is a radio-quiet quasar by this definition.

9.6.6 Morphology at X-Ray to Radio Wavelengths

Optical imaging of APM08279+5255 with HST NICMOS has revealed three pointlike, almost collinear images with very similar colors (Ibata et al. 1999). A spectroscopic follow-up study with the STIS spectrograph on board HST has shown that these three images have essentially identical spectral shapes, and thus are, indeed, all images caused by gravitational lensing (Lewis et al. 2002). These three optical images A, B, and C¹³ are separated by $d(A,B) = 0.377'' \pm 0.002''$ and $d(A,C) = 0.150'' \pm 0.006''$, and have brightness ratios of

¹³By convention, A is the brightest image, and C is the faintest image.

$b(A,B)=0.773 \pm 0.007$ and $b(A,C)=0.175 \pm 0.008$, i.e., $b(A+C,B)\simeq 0.66$. The north-eastern CO peak corresponds to a blend of optical images A+C, and the south-western CO peak to optical image B. The CO image peak brightness ratio of $b(SW,NE)=0.66 \pm 0.15$ thus agrees very well with the optical observations. The separation of the CO images is by $\sim 20\%$ lower than that of optical images A and B, which agrees with the assumption that the north-eastern CO component is actually a blend of optical images A+C, which we will assume in the following.

Ibata et al. (1999) find an offset of $0.6''$ between the positions of HST image A and the 8.4 GHz continuum source, which is not thought to be real. We here confirm this offset for six different radio frequency bands, which all are consistent in position among each other to high precision. In the following, we thus assume that this offset is due to HST astrometric errors, and shift all images at other wavelengths to the radio coordinates.

The three images of APM08279+5255 were also resolved in the (observed frame) near-infrared (NIR) continuum at $2.2\mu\text{m}$ in ground-based adaptive optics observations with the Keck telescopes (Egami et al. 2000) at a resolution where images A and C are still significantly blended, similar to our CO($J=1\rightarrow 0$) observations. The left panel of Fig. 9.10 shows an overlay of the $2.2\mu\text{m}$ continuum emission and the CO($J=1\rightarrow 0$) emission. The $2.2\mu\text{m}$ has been de-rotated (see caption of Fig. 1 of Egami et al. 2000 for the rotation angle) and aligned to the radio coordinates. The resolution of the NIR observations is by about a factor of 2 higher than that of the CO observations, and thus peaks close to the position of image A rather than between A and C. The image separation of the two peaks thus is $d(A,B)=0.38''$, in agreement with the optical images. Taking this into account, it is striking how similar the morphologies of the NIR and CO emission are, even though they are expected to emerge from largely different scales (hot dust around the central AGN vs. cold molecular gas in an extended star-forming ring), and thus to be differentially lensed. This similarity of morphologies even holds for hard X-ray emission from the central engine (Chartas et al. 2002, see Fig. 9.10, right), which is expected to be by many orders of magnitude more compact than the CO emission. Even the image separation $d(A,B)=0.38''\pm 0.01''$ of the two main peaks (image A and C are again significantly blended) is the same as in the optical/NIR, and thus in agreement with the CO observations under the above assumptions.

In addition, the rest-frame 2.7 mm continuum underlying the CO($J=1\rightarrow 0$) line shows a different, more extended structure than the CO emission¹⁴ (see Fig. 9.1). This may be due to a foreground source that emits in the continuum, but does not contribute to the line emission due to its different redshift. Another, probably more likely explanation is that the different structure is due to differential lensing. If the 2.7 mm continuum emission were to be due to star formation, it would be possible that it is dominated by a free-free component that is not co-spatial with the CO emission, but extended out to kpc scales. However, the SED of APM08279+5255 rather indicates that a major fraction of emission at this wavelength is AGN-related. This may suggest that the differentially lensed emission is

¹⁴A possible caveat is that the bandwidth of our observations is too narrow to image the CO($J=1\rightarrow 0$) line wings. It however is highly unlikely that this significantly alters this conclusion.

due to 100 pc to kpc-scale outflow from the nucleus. Higher resolution observations using a very long baseline radio interferometer are required to further investigate the nature of this phenomenon. In the following, we will refer to this emission as ‘the extended component’. This differentially lensed, extended component may also contribute significantly to the continuum emission at 7.3 mm (8.4 GHz observed frame), which also shows a different structure compared to other wavelengths.

The morphological similarity of the strongly lensed quasar APM 08279+5255 on largely different scales (<0.1 pc to few 100 pc) as well as the different structure of the extended continuum component (probably few 100 pc to kpc) severely constrains the lens configuration, and any valid lens model will have to be able to reproduce this scaling effect.

9.7 Gravitational Lensing

9.7.1 Direct Constraints on the Lensing Properties from the CO Observations

The brightness temperature T_b of a lensed source is a conserved quantity under gravitational lensing, as the latter is a purely geometrical effect. Due to the fact that APM 08279+5255 is resolved in our CO($J=1\rightarrow 0$) observations, we can derive the observed brightness temperatures $T_b^{\text{obs},z}$ at redshift z for images A+C and B directly from the observed peak fluxes using

$$T_b^{\text{obs},z} = \frac{c^2}{2k_B\nu_{\text{obs}}^2\Omega_{\text{beam}}} S_\nu, \quad (9.3)$$

where Ω_{beam} is the beam solid angle. These brightness temperatures can be converted to rest-frame observed brightness temperatures T_b^{obs} via

$$T_b^{\text{obs}} = (1+z)T_b^{\text{obs},z}. \quad (9.4)$$

While CO($J=1\rightarrow 0$) images A+C and B are individually detected in our observations, their true size is smaller than our observing beam. The observed brightness temperatures T_b^{obs} are thus diluted by the beam (radius: r_{beam}) and smaller than the true T_b . The size of the lensed images can be expressed by an equivalent radius r_0 , which assumes that each image is a filled, circular lensed disk. Energy conservation then gives:

$$T_b^{\text{obs}}/T_b = (r_0/r_{\text{beam}})^2. \quad (9.5)$$

This relation is implied in the plot shown in Fig. 9.11a. The observed, beam-diluted (Rayleigh-Jeans) brightness temperatures of images A+C ($T_b^{\text{obs},A+C}=33.4$ K) and B ($T_b^{\text{obs},B}=18.3$ K) are indicated by vertical lines. The three curves indicate the beam-corrected brightness temperatures for different equivalent radii (which, by definition, cross with the observed rest-frame brightness temperatures at r_0/r_{beam} , as indicated by the long horizontal line) for images A+C, B, and all images together. From Large Velocity Gradient (LVG)

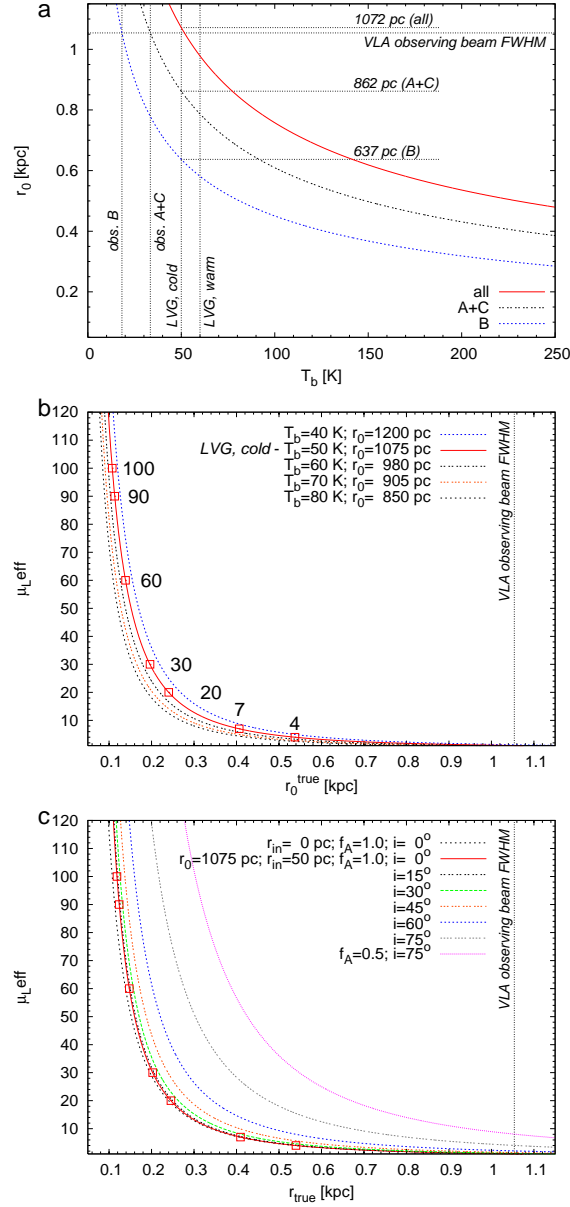


Figure 9.11: Observational constraints on the intrinsic brightness temperature T_b and the lensing properties of APM08279+5255. **a:** Relation between T_b and the lensed equivalent disk radius r_0 . The vertical lines indicate the observed CO($J=1 \rightarrow 0$) brightness temperatures for the blended images A and C and image B, and the LVG predicted brightness temperatures for the ‘cold, dense’ (50 K) and ‘warm’ (60 K) CO($J=1 \rightarrow 0$) components from the model by Weiß et al. (2007). The horizontal lines indicate the lensed equivalent disk radii for the different images for a true T_b of 50 K, and the total r_0 for all images. The fourth horizontal line indicates the VLA beam radius, and also appears in panels **b** and **c**. **b:** Relation between the true, unlensed equivalent disk radius r_0^{true} and the effective lensing magnification factor μ_L^{eff} for different T_b . For $T_b=50$ K, different μ_L^{eff} are highlighted. **c:** Relation between the true, unlensed radius r_{true} of the CO ring and μ_L^{eff} for the $T_b=50$ K solution assuming an inner ring radius r_{in} of 50 pc for different inclinations i and area filling factors f_A . For comparison, a solution without an inner boundary is shown (see text for details).

modeling of the CO($J=1\rightarrow 0$) to CO($J=11\rightarrow 10$) SLED, Weiß et al. (2007) have derived that the molecular gas in APM08279+5255 can be modeled with two gas components, a ‘cold, dense’ component with a H₂ density of $n(\text{H}_2)=10^5 \text{ cm}^{-3}$ and a kinetic gas temperature of $T_{\text{kin}}=65 \text{ K}$ which contributes about 70% to the total CO($J=1\rightarrow 0$) luminosity, and a ‘warm’ component with a H₂ density of $n(\text{H}_2)=10^4 \text{ cm}^{-3}$ and a kinetic gas temperature of $T_{\text{kin}}=220 \text{ K}$ which contributes about 30% to the total CO($J=1\rightarrow 0$) luminosity. For the ‘cold, dense’ component, their model predicts a true CO($J=1\rightarrow 0$) brightness temperature of $T_{\text{b}}^{\text{cold}}=50 \text{ K}$, and for the ‘warm’ component, it predicts $T_{\text{b}}^{\text{warm}}=60 \text{ K}$. Both T_{b} are indicated in Fig. 9.11a by vertical lines. Assuming $T_{\text{b}}=50 \text{ K}$, as predicted by the LVG models for the dominant gas component, images A+C and B fill equivalent disks with radii of $r_0^{\text{A+C}}=862 \text{ pc}$ and $r_0^{\text{B}}=637 \text{ pc}$. This corresponds to a total lensed equivalent disk with a radius of $r_0=1072 \text{ pc}$, consistent with the results of Weiß et al. (2007) within the uncertainties. This also implies beam area filling factors of 67% and 37% for images A+C and B. These are significant fractions of the beam size, and may indicate that increasing the resolution by only a factor of 2–3 would be sufficient to detect substructure within the individual images. Assuming a 30% contribution of a warmer component with $T_{\text{b}}=60 \text{ K}$ does not significantly alter any of these predictions. Even assuming much higher T_{b}^{CO} than typically observed in nearby warm, ultra-luminous infrared galaxies (ULIRGs, e.g., Downes & Solomon 1998) of a few hundred Kelvins does not change the predicted r_0 by more than about a factor of 2. Also, the directly observed (beam-diluted) brightness temperatures limit the true T_{b} to be at least $\sim 30 \text{ K}$ considering that the contribution of image C to A+C is likely minor.

The effective lensing magnification μ_L^{eff} is defined as the ratio between the observed apparent luminosity and the true luminosity. It thus is a direct measure for the ratio of the observed equivalent disk size r_0 and the true equivalent disk size r_0^{true} via

$$\mu_L^{\text{eff}} = (r_0/r_0^{\text{true}})^2. \quad (9.6)$$

This relation is displayed in Fig. 9.11b for a range of T_{b} . The $T_{\text{b}}=50 \text{ K}$ model discussed above is indicated by the solid line and the boxes (highlighting selected magnification factors). Using only the given constraints without modeling the system in more detail, a large range of magnification factors would be in agreement with the CO data. However, the impact of changing the intrinsic T_{b} is relatively minor, as all curves occupy a narrow range in this plot.

The case of a completely filled, circular CO disk as discussed so far is a very particular solution, even appreciating the fact that the CO is likely situated in a relatively compact, rotating circumnuclear ring. In a more realistic approach, the CO disk has an inner boundary r_{in} at a certain distance from the central hot nucleus, due to the simple fact that molecular gas cannot survive at distances where the ionizing radiation field is strong enough to dissociate the diatomic CO (and H₂) molecules. It thus is a ring rather than a disk. Also, it is likely that we do not see this ring face-on, but at a certain inclination i towards the line of sight (LOS). Also, the molecular material may be distributed in clouds and/or clumps rather than smoothly, and thus may have an area filling factor f_{A} smaller

than 1. This can be expressed as (see also Weiß et al. 2007):

$$r_{\text{true}} = \left[\frac{(r_0^{\text{true}})^2 + r_{\text{in}}^2}{f_A \cos i} \right]^{1/2}. \quad (9.7)$$

Note that $i=0^\circ$ corresponds to face-on. Also, we use a thin disk approximation, neglecting the geometrical thickness of the CO ring. This simplification leads to an overprediction of r_{true} for high inclinations. This approximation is justified, as the high observed optical brightness of the source in combination with the detection of large amounts of dust in its circumnuclear torus suggests that we have a relatively unobscured view on the AGN, and thus that we likely see the galaxy at a relatively small inclination ($i < 35^\circ$).

In Fig. 9.11c, a range of inclinations is shown for the $T_b=50$ K model in the $\mu_L^{\text{eff}}-r_{\text{true}}$ plane. An inner ring boundary of $r_{\text{in}}=50$ pc is assumed unless stated otherwise. For comparison, a solution without an inner ring boundary is shown for $i=0^\circ$. The change of the predicted r_{true} is only minor, in particular for the solutions with low magnifications. In general, the figure shows that the range of solutions for high inclinations is significantly different from that for low inclinations. However, in the preferred range of $0^\circ < i < 35^\circ$, the solutions are fairly similar. While r_{in} and i can be constrained relatively well by existing observations, this is not at all true for f_A . As an example, a solution with $i=75^\circ$ and $f_A=0.5$ is shown. The difference in area filling factor has a large impact on the predicted solutions. As another example, solutions for $i=0^\circ$, $f_A=0.5$ and $i=60^\circ$, $f_A=1.0$ are indistinguishable. The *structure* of the molecular ISM thus is an unknown in this discussion that has significant impact. There are two more interesting results to note: First, the resolution of our observations and A+C/B brightness ratio alone set a meaningful lower limit on the magnification of models with $f_A \cos i$ significantly smaller than 1. Second, the models with $f_A \cos i$ close to 1 predict very compact CO rings for high magnifications ($r_{\text{true}}=100\text{--}150$ pc).

Although the results presented in this subsection significantly constrain the allowed parameter space for potential lensing models, they do not allow to strongly constrain the actual magnification. In the following, we thus discuss existing lensing models in more detail, show their limitations, and suggest a new model which overcomes part of the problems of previous models.

9.7.2 Lens Modeling: Previous Models

In most classical lensing models, the surface density of the lensing galaxy is expressed by an ellipsoidal with a core of finite radius. However, high-resolution observations of the central regions of galaxies indicate that the luminosity profiles of some of the most massive galaxies appear to have central cusps rather than cores with finite radii (e.g., Faber et al. 1997). Such distributions are reminiscent of the cusp power-law density profiles with a break radius used for dark matter halos in cosmological simulations (e.g., Navarro, Frenk & White 1997, ‘NFW’), but, in these observations, seen for the stellar component of the galaxies. The (baryonic) density profile of the lensing galaxy of APM 08279+5255 has been

modeled with both core (Ibata et al. 1999; Egami et al. 2000) and cusp (Munoz et al. 2001; Lewis et al. 2002a) configurations previously.

Cored Singular Isothermal Ellipsoid Models

The model of Egami et al. (2000) is a modified singular isothermal ellipsoid (SIE) model with a finite core. Such models have six parameters: the Einstein radius, the core radius, the ellipticity of the lensing potential and its position angle, and the (2-dimensional) center position of the source. For a three image source like APM 08279+5255, observations offer six relevant constraints for the model: two relative image brightnesses, and two relative (2-dimensional) image positions. In addition, the fact that the three images are almost collinear requires the ellipticity to be close to zero, and thus predicts an almost circular lensing potential. The geometry of lensing systems requires that any non-singular mass distribution produces an odd number of lens images (Burke 1981). However, if the core is very small, one of the images is de-magnified, and thus unlikely to be observable (note that an even number of images is observed toward most lens systems). The fact that the third image of APM 08279+5255 is not strongly de-magnified thus also restricts the core to be non-singular, and thus to have a rather large radius within this model. Egami et al. (2000) find a core radius of $0.2''$, corresponding to 1.2–1.7 kpc at $0.5 < z < 3.5$, the likely redshift range of the lensing galaxy, which appears extreme even for the most massive elliptical galaxies. In particular, quasar image C is located only $0.03''$ (180–250 pc) from the center of the lensing potential. As the authors already state themselves, one thus might expect differential reddening of image C in this configuration, which is not observed. However, the most problematic point of the Egami et al. (2000) model is that it predicts a rapid change of morphology with source size (their Fig. 7). For the X-ray to near-infrared observations, where most of the emission likely comes from the central < 0.1 –1 pc region, their model correctly predicts a three image configuration. This even holds true for a source size of 20 pc, where the images are elongated, but still clearly separated, and thus would be picked up as three pointlike images by observations at a resolution of, e.g., $0.3''$. However, for source sizes of 50 pc and larger, the images start to form arcs and rings, and ultimately at 220 pc, a filled sphere. However, in our CO($J=1 \rightarrow 0$) observations, we probe scales of 100–500 pc (see above), depending on the lensing magnification, but still see the 3-image structure as observed in the X-ray-to-NIR wavelength regime. Moreover, the extended components seen in radio continuum emission, which likely probes few 100 pc to kpc scales, gets lensed into an arc-like structure rather than a filled sphere (see Fig. 9.1, right). While this model predicts high effective lensing magnifications of $\mu_L^{\text{eff}} \sim 100$ (and thus a plausible explanation for the extreme observed properties of APM 08279+5255), it is ruled out by the structure detected in our CO and radio continuum maps.

Cusp Models

As mentioned above, there is mounting evidence that galaxy cores are mostly very small, and that their mass distribution possesses a significant cusp (Rusin & Ma 2001; Winn et

al. 2004). Munoz et al. (2001) thus suggested a complementary model to the one by Egami et al. (2000), assuming a cusp configuration for the lens in APM08279+5255. Instead of a core radius, such models are parameterized by a cusp power-law index and a break radius, i.e., 7 parameters in total, and thus underconstrained by a three-image lens without further assumptions. For APM08279+5255, cusps with a small break radius are favoured, and lead to high magnification factors of $\mu_L^{\text{eff}} \sim 100$, similar to the Egami et al. (2000) model. However, the source can only be modeled with relatively shallow cusps with a small power-law index (0.2–0.4 rather than 1–2 as observed toward most galaxies). Such shallow cusps are, indeed, relatively similar to cores with finite radii (corresponding to a power-law index of 0). The authors conclude that the lens may be a spiral galaxy, since some spiral galaxies appear to have finite central densities rather than steep cusps.

Keeton & Kochanek (1998) and Bartelmann & Loeb (1998) have shown that highly flattened, highly inclined potentials, as found, e.g., for disks of edge-on spiral galaxies, can form a ‘naked cusp’ caustic. In such a configuration, the inner diamond caustic extends outside the elliptical caustic, producing three roughly collinear images with similar brightness. The central third image is not strongly de-magnified, which is different from typical core and cusp models. However, a generic feature of such models with a naked cusp in an inclined spiral is that the overall magnification is significantly smaller than in large core lenses. Such a peculiar lens configuration, however, is expected to be rare.

Lewis et al. (2002a) have developed a lensing model of the APM08279+5255 system based on such a highly elliptical lens, where the quasar core of the lensed galaxy is situated in the direct vicinity of a naked cusp. In their model, the inclined disk of the lens has a projected axis ratio of 0.25, and a rotational velocity of 200 km s^{-1} . It has a core radius of $0.065 h^{-1} \text{ kpc}$, and is truncated at an outer radius of $8 h^{-1} \text{ kpc}$. This truncated, flattened disk is assumed to sit in a spherical halo. Due to the possible detection of microlensing (Lewis et al. 2002; Chartas et al. 2002), the observed optical and X-ray brightnesses of the individual images may not reflect the true relative macrolensing magnifications. Their brightness ratios thus are not considered a hard constraint for the lens mass model. Apart from the optical image positions, Lewis et al. (2002a) also considered the structure seen in their CO($J=1 \rightarrow 0$) map a constraint for the lensing model. While the continuum emission underlying the CO($J=1 \rightarrow 0$) emission in their maps is lensed into an arc and aligned with the optical emission, the CO($J=1 \rightarrow 0$) emission appears significantly more extended. They thus assumed that the CO disk in APM08279+5255 has to be large enough to reach out beyond the naked cusp and into the 5-image central caustic structure. The resulting lensing magnification of the optical emission is $\mu_L^{\text{opt}}=7$, and image brightness ratios of $b(A,B)=0.75$ and $b(A,C)=0.75$. The model reproduces the brightness ratio between images A and B (which is not subject to extreme changes) relatively well, while image C is significantly brighter than observed. The lensing magnification of the CO emission in their model is only $\mu_L^{\text{CO}}=2.5\text{--}3$. The true size of the CO disk thus is $400\text{--}1000 \text{ pc}$, and the CO becomes the dominant contributor to the total mass within the central kpc of the QSO. Due to the significantly lower lensing magnification factor compared to previous studies, this model predicts that APM08279+5255 is intrinsically an extremely bright source at X-ray-to-FIR wavelengths, rather than being modestly bright.

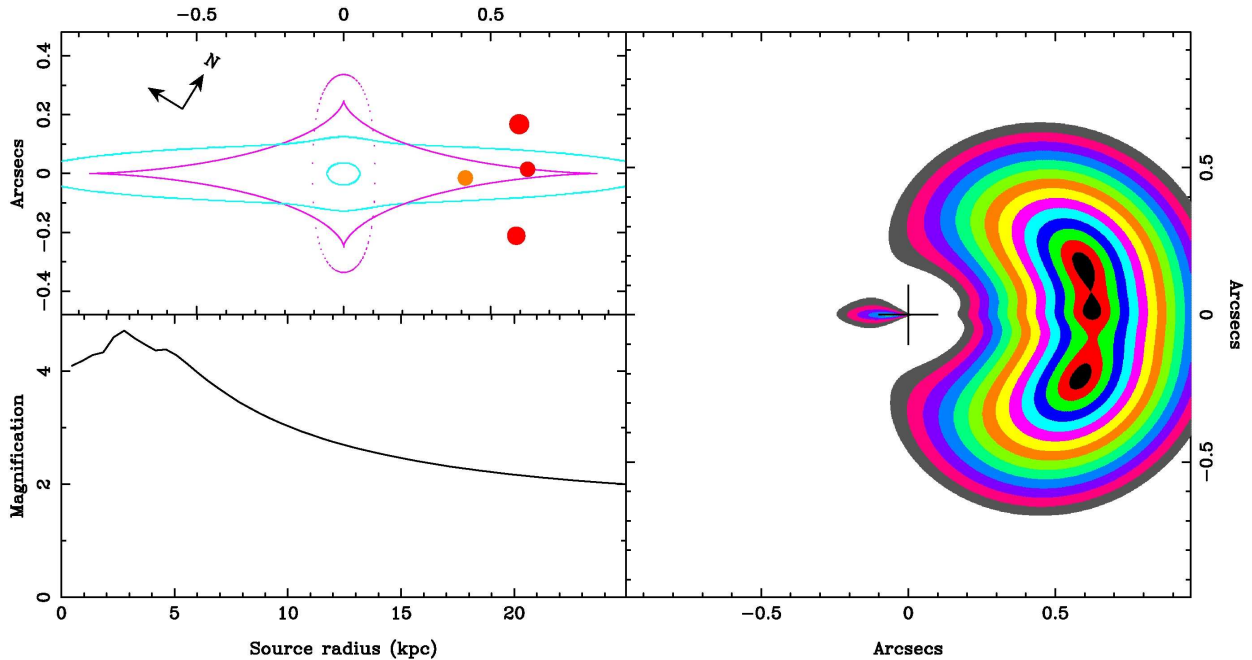


Figure 9.12: New lensing model for APM08279+5255, assuming a highly inclined spiral lens. The top left panel shows the caustic and critical line structure. The orange circle indicates the source position, and the red circles represent the corresponding image locations. The right panel shows the image configuration for a range of source sizes. The color contours depict an increase in radius in 0.25 kpc steps. The bottom left panel shows the corresponding overall magnification as a function of radius. In this model, the CO($J=1\rightarrow 0$) emitting region has a true radius of ~ 0.5 kpc or less.

Our new, improved high-resolution CO($J=1\rightarrow 0$) maps have revealed that the extended CO arc found by Lewis et al. (2002a) is a noise artifact, and that the lensed CO emission is coincident with the optical images. In contrast to the underlying, slightly more extended continuum emission, it even shows the image structure seen in the optical. Assuming that the CO emission is more compact than assumed by Lewis et al. (2002a) and lies within the region of the naked cusp, their model describes these new observations quite well. Their model then suggests that the CO-emitting region has a true radius of 350 pc or less, and has a larger magnification factor close to that of the optical emission. However, this model was derived taking the extended CO structure found by Lewis et al. (2002a) as a constraint. To find the best-fitting model to existing observations, it thus is desirable to perform a new parameter study.

9.7.3 Lens Modeling: New Model

In light of our new observations of APM08279+5255, we have conducted an extensive, systematic parameter study of the lensing configurations allowed within the constraints of its observed properties. All considered models assume lensing by an inclined spiral galaxy.

As described above, multiwavelength observations of APM08279+5255 at different epochs appear to indicate that the image ratios change, possibly due to microlensing. Thus, they cannot be considered hard constraints for the primary lens. Leaving the relative image brightnesses as free parameters, however, would sacrifice two observational constraints, and, in fact, under-constrain most lens models. Models considered good thus are required to reproduce $b(A,B)$ relatively well (due to the relatively minor observed fluctuations), and to reproduce C as the faintest image.

In Fig. 9.12, we show the model that gives the overall best fit to the observed properties at different wavelengths within our study. The highly inclined disk of the lens in this model has a projected axis ratio of only 0.09. It is truncated at an outer radius of $15 h^{-1}$ kpc, and has a rotational velocity of 140 km s^{-1} . The top left panel of Fig. 9.12 shows the caustic and critical line structure, as well as the position of APM08279+5255 in the source and image planes. The model predicts $b(A,B)=0.84$, and $b(A,C)=0.57$, respectively. The brightness ratio of images A and B is close to the observed value. The total magnification of a point-like source in this model is only 4.15, and thus relatively modest. The bottom left panel shows the differential total magnification as a function of the source radius. The total magnification scales down by only a factor of 2 from source radii of few pc out to 20 kpc, showing that differential lensing effects do not strongly influence the observed flux ratios. Out to 5 kpc, it varies by less than 20%. The SED shown in Fig. 9.8 thus is predicted to not be strongly distorted by differential lensing effects over the whole spectral range. The right panel of Fig. 9.12 shows the observed image configuration and overall morphology for a range of source sizes. The morphology of the CO($J=1\rightarrow 0$) observations is consistent with having a true source radius of 500 pc or less in this model. This is consistent with a lensing factor of 4 in Fig. 9.11, assuming an inclination of $<30^\circ$ and a high CO area filling factor. In the following, we will assume $r_{\text{true}}=550 \text{ pc}$ and $\mu_L=4$ for the CO($J=1\rightarrow 0$)-emitting region, consistent with both observations and the lensing model. The model also correctly reproduces the 2.7 mm continuum emission underlying the CO line emission, assuming that the extended continuum emission component comes from a region of about 1 kpc size. A more detailed description and analysis of the uncertainties within this model of the gravitational lensing in APM08279+5255 will be described by G. Lewis et al. (2007, in prep.).

9.8 Black Hole, Gas and Dynamical Masses

9.8.1 Black Hole Mass

The enormous energy output that powers the huge bolometric luminosity L_{bol} of APM08279+5255 is produced by a central super-massive black hole (SMBH) that is fed

Table 9.5: Mass Budget in the Central Region of APM 08279+5255

Component	Mass	Mass Fraction
	$[10^{10} (\mu_L^{-1}) M_\odot]$	(%)
Molecular Gas	53/13	57.4
Dust	0.35/0.09	0.4
Black Hole	9.0/2.3	9.7
Stellar Bulge ^a	30/7.5	32.5

Notes—Here, we assume $i=25^\circ$, $r_{\text{true}}=550$ pc, and $\mu_L=4$. Masses are uncorrected/corrected for lensing, assuming $\mu_L=4$.

^aFraction within the radius of the CO disk.

through an accretion disk. There are several ways to constrain the SMBH mass from observation. The most basic approach is to assume that the gradient of the radiation pressure driving gas out of the central region is exactly counterbalanced by the gravitational force attracting infall of the same material. This equality of forces provides a limiting mass for the SMBH. Assuming that dominant mechanism contributing to the opacity is Thomson scattering off free electrons (Eddington 1921) leads to:

$$\left(\frac{M_{\text{BH}}}{M_\odot}\right) = 7.7 \times 10^{-39} \left(\frac{L_{\text{Edd}}}{\text{erg s}^{-1}}\right). \quad (9.8)$$

Assuming $L_{\text{bol}}=L_{\text{Edd}}$ gives $M_{\text{BH}}^{\text{Edd}}=2.1 \times 10^{11} \mu_L^{-1} M_\odot$.

Another, perhaps better constrained estimate is provided by observations of the $2s^2S_{1/2}-2p^2P_{1/2,3/2}$ resonance transitions of the C^{3+} ion ($\text{C IV } \lambda\lambda 1548, 1550$). From reverberation mapping of nearby active galactic nuclei, Vestergaard & Peterson (2006) have found an empirical relation between the $\text{C IV } \lambda\lambda 1548, 1550$ FWHM linewidth $\Delta v_{\text{FWHM}}^{\text{C IV}}$, the rest-frame UV continuum luminosity at 1350 \AA , and the mass of the central black hole:

$$\left(\frac{M_{\text{BH}}}{M_\odot}\right) = 4.6 \times \left(\frac{\Delta v_{\text{FWHM}}^{\text{C IV}}}{\text{km s}^{-1}}\right)^2 \left(\frac{\lambda L_\lambda(1350 \text{ \AA})}{10^{44} \text{ erg s}^{-1}}\right)^{0.53}. \quad (9.9)$$

From the spectrum by Irwin et al. (1998), we thus derive $M_{\text{BH}}^{\text{C IV}}=9.0 \times 10^{10} \mu_L^{-1} M_\odot$, or about half of the Eddington limit. However, note that the reverberation-based masses underlying this equation are uncertain by a factor of about 3 (Vestergaard & Peterson 2006). Also, part of the wings of the C IV line in APM 08279+5255 are subject to strong absorption, making the derivation of the linewidth somewhat uncertain. However, the estimated width of the C IV line is similar to that of the $\text{Pa}\alpha$ and $\text{Pa}\beta$ lines of hydrogen (Soifer et al. 2004). Finally, the accretion disk may be inclined toward the line of sight, which would also influence this result.

9.8.2 Molecular Gas Mass

To derive molecular gas masses M_{gas} from CO luminosities in high redshift quasars, it currently is the most common approach to adopt a well-established conversion factor α_{CO} for nearby ULIRGs ($\alpha_{\text{CO}}=0.8 M_\odot (\text{K km s}^{-1} \text{ pc}^2)^{-1}$; Downes & Solomon 1998). This is

justified by the fact that the observed brightness temperatures in distant quasars appear to be similar to those of local ULIRGs. However, α_{CO} also depends on the gas density, which appears to be much higher in APM08279+5255. Weiß et al. (2007) thus re-derive a much higher conversion factor of $\alpha_{\text{CO}} \simeq 5 \text{ M}_{\odot} (\text{K km s}^{-1} \text{ pc}^2)^{-1}$ for this source. From our CO($J=1 \rightarrow 0$) luminosity, we thus derive $M_{\text{gas}} = 5.3 \times 10^{11} \mu_L^{-1} \text{ M}_{\odot}$. This corresponds to about six times M_{BH} (based on the CIV estimate), assuming no significant differential lensing effects act between the scales of the SMBH and of the molecular gas reservoir. This is somewhat lower than the factor of roughly ten found by Shields et al. (2006) for a larger sample of distant gas-rich quasars, but in agreement within the large spread of observed values.

9.8.3 Dynamical Mass

From Newtonian mechanics, a dynamical mass can be derived for the rotating molecular disk in APM08279+5255 (e.g., Solomon & Vanden Bout 2005):

$$\left(\frac{M_{\text{dyn}}}{\text{M}_{\odot}} \right) = 2.34 \times 10^5 \left(\frac{r_{\text{true}}}{\text{kpc}} \right) \left(\frac{\Delta v_{\text{FWHM}}^{\text{CO}}}{\text{km s}^{-1}} \right)^2 \sin^{-2} i, \quad (9.10)$$

where $\Delta v_{\text{FWHM}}^{\text{CO}}$ is the observed CO linewidth, and r_{true} is the derived true radius of the CO disk. Using the observed CO($J=1 \rightarrow 0$) linewidth of $556 \pm 55 \text{ km s}^{-1}$ (Riechers et al. 2006a), and using $r_{\text{true}} = 550 \text{ pc}$, we derive $M_{\text{dyn}} \sin^2 i = 4.0 \times 10^{10} \text{ M}_{\odot}$. This dynamical mass of the central region of APM08279+5255 corresponds to the sum of black hole mass, gas mass, dust mass and stellar mass (plus dark matter). Assuming a gas-to-dust ratio of 150 (Weiß et al. 2007), the contribution of dust to the total mass budget is negligible. For the moment, we will also assume that the mass fraction of the stellar bulge in the central 550 pc is small, i.e., that $M_{\text{dyn}} \sin^2 i \simeq (M_{\text{gas}} + M_{\text{BH}})$. Assuming a face-on, unlensed disk, $M_{\text{gas}} + M_{\text{BH}}$ would exceed the dynamical mass by a factor of 15.5, and thus is ruled out by the observations. Assuming $\mu_L = 4$, we thus find that the CO disk in APM08279+5255 can be inclined by at most $i = 30^\circ$ to not exceed the dynamical mass. With $\Delta v_{\text{rot}} = \Delta v_{\text{FWHM}}^{\text{CO}} \sin^{-1} i$, this implies a rotational velocity of 1095 km s^{-1} .

9.8.4 Stellar Bulge Mass Limit

As mentioned in the previous section, there is a third important constituent to the dynamical mass, i.e., the mass of the stellar bulge. This is a quantity that currently cannot be observed in the highest redshift galaxies. However, from our observations and theoretical considerations, we can derive a limit for the mass fraction of the stellar bulge within r_{true} . Carilli & Wang (2006) find that high-redshift gas-rich QSOs have a median $\Delta v_{\text{FWHM}}^{\text{CO}}$ of 300 km s^{-1} , at a mean inclination of $\langle i \rangle = 13^\circ$ (see their erratum). This corresponds to a mean rotational velocity of $\langle \Delta v_{\text{rot}} \rangle = 1335 \text{ km s}^{-1}$. Assuming that this value applies to APM08279+5255, we derive an inclination of $i = 25^\circ$. Assuming $M_{\text{dyn}} \sin^2 i = (M_{\text{gas}} + M_{\text{dust}} + M_{\text{BH}} + M_{\text{bulge}})$, and a gas-to-dust ratio of 150, this corresponds to a bulge mass of

$M_{\text{bulge}}=3.0 \times 10^{11} \mu_L^{-1} M_{\odot}$, or $M_{\text{bulge}}=3.4 M_{\text{BH}}$ ($0.57 M_{\text{gas}}$; see also Tab. 9.5) for $\mu_L=4$. For comparison, if a model with $\mu_L=100$ (and thus $r_{\text{true}}=125 \text{ pc}$) that fits the data were to exist, it would give $M_{\text{bulge}}=4.4 \times 10^{12} \mu_L^{-1} M_{\odot}$, or $M_{\text{bulge}}=50 M_{\text{BH}}$ ($8.4 M_{\text{gas}}$). This means that for low- μ_L models, the gas component dominates the total baryonic mass budget in the central region of APM 08279+5255, while for high- μ_L models, the stellar bulge is the dominant contributor.

9.8.5 Limitations of this Analysis

The maximum CO velocity widths predicted by the Carilli & Wang (2006) unified model exceed the rotational velocities of the most rapidly rotating nearby giant ellipticals by about a factor of 2. This may suggest that the observed linewidths in the systems with broader but not multiply peaked CO lines are not due to rotationally supported disks, but possibly in a later stage of a major merger where the disk is not self-gravitating yet. In that case, the mean inclination of quasar host galaxies derived by Carilli & Wang may overpredict the rotational velocities for gravitationally bound molecular disks. This is of particular concern for APM 08279+5255, as its CO velocity width is already the highest observed among the distant quasars. If the measured CO linewidth was that of a gravitationally bound disk and representative for the rotational velocity inside a present day giant elliptical, the inclination could not be much lower than $i=60^\circ$. This leaves a factor of 2–3 discrepancy in the M_{dyn} estimate relative to the $i=30^\circ$ solution.

The uncertainties in the luminosity-based mass estimates are a factor of a few. Together with the uncertainties in disk size and lensing factor, and the contribution of dark matter to the mass budget, the real inclination of the molecular disk remains uncertain (as only a factor of 3–4 difference exists between high and low inclination solutions). Due to the degeneracy of area filling factor f_A and inclination, our results thus are still in agreement with those of Weiß et al. (2007) within conservative error estimates, even with the new morphological constraints.

9.9 On the Radio–Far-Infrared Correlation

In the local universe, star-forming galaxies follow a tight correlation between the monochromatic radio continuum luminosity at 1.4 GHz and the far-infrared luminosity (L_{FIR}), which holds over more than 4 orders of magnitude (e.g., Condon et al. 1991; Condon 1992; Yun et al. 2001; Bell 2003). This correlation is probably due to coupling between infrared thermal dust emission due to heating by young stars and non-thermal radio synchrotron emission from supernova explosions and SNRs (e.g., Helou et al. 1985), and constitutes the basis for the Condon model described above. The radio–FIR correlation can be expressed via the so-called q -parameter (Helou et al. 1985):

$$q = \log \left(\frac{L_{\text{FIR}}}{9.8 \times 10^{-15} L_{\odot}} \right) - \log \left(\frac{L_{1.4\text{GHz}}}{\text{W Hz}^{-1}} \right). \quad (9.11)$$

The apparent FIR luminosity of APM08279+5255 is $L_{\text{FIR}}=(2.0 \pm 0.5) \times 10^{14} \mu_L^{-1} L_{\odot}$ (Beelen et al. 2006; Weiß et al. 2007). We thus obtain $q=2.03$, a value which falls well within the range of values found for IRAS galaxies (Yun et al. 2001), and consistent with the values found for other dust and gas-rich high- z quasars (Carilli et al. 2004; Beelen et al. 2006; Wang et al. 2007). A common interpretation of a q value close to the radio-FIR correlation is that star formation is the dominant process to power both the radio and FIR emission. However, using the dust model of Weiß et al. (2007), our analysis of APM08279+5255 has shown that the AGN likely powers the dominant fraction of both the FIR and the radio emission. We obtain this conclusion based on the fact that the SED of APM08279+5255 cannot be fitted with a simple Condon model (which motivates the star formation interpretation of the radio-FIR correlation). We thus conclude that caution has to be used when interpreting the properties of dust and gas-rich high- z quasars based on the radio-FIR correlation alone.

9.10 Discussion

The observed properties of APM08279+5255 are undoubtedly peculiar. It thus is important to understand whether this peculiarity is due to a rare lens configuration, possibly leading to very high lensing magnification factors and significant differential lensing effects, or whether APM08279+5255 is a source that is just moderately magnified by gravitational lensing and thus intrinsically extreme.

APM08279+5255 shows broad absorption lines in the optical/UV, and emission from high excitation lines like C IV and N V close to the central nucleus (Irwin et al. 1998), kinematically blueshifted relative to the molecular gas and C I emission by about 2500 km s^{-1} (Downes et al. 1999; Wagg et al. 2006). The quasar also shows relativistic X-ray broad absorption lines from even higher emission lines of iron from gas situated within the UV BAL region (Chartas et al. 2002; Hasinger et al. 2002). The BALs come from an outflow of highly ionized gas from the accretion disk, mostly driven by radiation pressure. This outflow distributes the accretion disk material over the central region of the quasar, and out into the host galaxy. The X-ray BAL region is likely a dust-free, high column density absorber responsible for shielding, as indicated by the detection of an iron K-shell absorption edge (Hasinger et al. 2002). This shielding is responsible for the typical X-ray faintness of BAL QSOs. The X-ray luminosity alone thus is not a good measure for the energy output of APM08279+5255. The detection of strong iron lines also indicates that the X-ray BAL emission comes from significantly metal-enriched gas with possibly super-solar metallicities. While this strongly indicates that the gas has already been processed in a starburst cycle, it however is biased toward the very central region (possibly $<0.1 \text{ pc}$). It thus cannot be assumed ad hoc that the metallicity is super-solar over the whole scale of the galaxy. The continuum X-ray emission in APM08279+5255 has a photon index that is in qualitative agreement with a radio-quiet quasar (RQQ). The optical/IR shape of the SED is also consistent with APM08279+5255 being a RQQ. Even more so, it follows the radio-quiet locus of the radio-FIR correlation, which indicates that the copious

amounts of dust in this source may be heated to a significant fraction by newly formed young stars, while the radio synchrotron emission may originate from supernova remnants (Irwin et al. 1998; Beelen et al. 2006). However, our analysis of the radio and dust properties indicates that most of the radio/FIR emission is AGN-related. Within the unified theory of AGN galaxies, the smoothness of the IR spectrum, in particular the lack of a pronounced IR peak, indicates that the accretion disk in this radio-quiet quasar is seen close to face-on (Soifer et al. 2004). This agrees well with the enormous optical brightness and the flatness of the optical spectrum (Irwin et al. 1998; Egami et al. 2000), indicating a lack of obscuration and thus an angle of view which clearly lies within the ionization cone. The hot dust in the parsec-scale accretion disk is heated by the central AGN, and extends outwards into a warm dusty torus, extending out to 100 pc scales. The luminous AGN in APM08279+5255 is the dominant power source out to large scales, generating a large (far-)infrared luminosity by heating the dust. The apparent FIR luminosity of APM08279+5255 is $L_{\text{FIR}} = (2.0 \pm 0.5) \times 10^{14} \mu_L^{-1} L_{\odot}$ (Beelen et al. 2006; Weiß et al. 2007). Weiß et al. (2007) have found that about 90% of the FIR luminosity are powered by the AGN, while only 10% are due to star formation. This explains why a significant fraction of the dust in APM08279+5255 on extended (100s pc) scales is warmer than in typical ULIRGs, or even other high- z , dust-rich QSOs. It also explains why APM08279+5255 is an outlier on the $L'_{\text{CO}}-L_{\text{FIR}}$ relation (e.g., Riechers et al. 2006a), which is set by galaxies where the FIR luminosity is dominated by heating from star formation. Subtracting the 90% of L_{FIR} powered by the AGN, APM08279+5255 follows the $L'_{\text{CO}}-L_{\text{FIR}}$ relation quite well. However, note that even though the apparent FIR luminosity of APM08279+5255 is extreme, this indicates that only 3% of the total quasar power (as measured by L_{bol}) are re-emitted in the FIR wavelength regime (assuming no differential lensing effects play into the ratio). We find that 80–90% of the radio luminosity in APM08279+5255 are powered by the AGN, and only 10–20% by the starburst. Due to the fact that these ratios are similar to those found for the FIR luminosity, APM08279+5255 still follows the radio–FIR correlation for star-forming galaxies.

APM08279+5255 thus is a radio-quiet, optically luminous dust-rich quasar in which the central accretion disk and dust torus are seen close to face-on (note however the above concern about the inclination). Its high FIR luminosity can be explained by dust heating of the AGN, as can be the high temperature of the dust. It even explains the high CO excitation if the molecular gas is situated in a rather compact (and thus dense) circumnuclear ring seen at a low inclination toward the line of sight, just like the central region. The high dust and gas temperatures and relatively high densities also explain the exceptional HCN (and HCO^+) excitation in this system, as IR-pumping via the $\nu_2=1$ vibrational bending mode becomes efficient at such high temperatures (Weiß et al. 2007). Without shielding and self-shielding, the gas and dust would be even warmer than observed. Assuming that only the fraction of L_{bol} reradiated in the FIR reaches out to the molecular regions, the temperature at a radius of 125 pc would still be 200 K. Even at 550 pc, the temperature would not drop significantly below 100 K. The LVG-predicted temperatures for the cool, dense gas component ($T_{\text{kin}} = 65$ K) thus require self-screening if the gas is indeed located in

164 9. Molecular Line Mapping I: A Compact Quasar Host Galaxy at $z=3.91$

a 550 pc region around the AGN.¹⁵ Note that all the above may be considered extreme (i.e., rarely observed). However, all of these effects can be explained physically without assuming extreme and/or differential lensing effects. The CO luminosity in APM 08279+5255 is relatively modest (compared to other high- z sources) even without correcting for lensing. If L_{FIR} is corrected assuming a lensing magnification factor of only 4, as suggested by our new model, it is not the highest observed value even without correcting for AGN heating. Both L'_{CO} and L_{FIR} are higher for the $z=4.7$ quasar BR 1202-0725, which is thought to be unlensed, but undergoing a massive, gas-rich merger event¹⁶ (Carilli et al. 2002b; Riechers et al. 2006a).

Correcting for $\mu_L=4$ predicts $M_{\text{BH}}=2.3 \times 10^{10} M_{\odot}$ for APM 08279+5255. This appears to be extreme compared to more typical SMBH masses of a few times $10^9 M_{\odot}$ of high- z quasars. However, comparable or even higher black hole masses are found for BRI 1335-0417 ($z=4.41$) and BR 1202-0725 (however based on strongly absorbed C IV emission lines; Storrie-Lombardi et al. 1996; Shields et al. 2006). Moreover, Vestergaard (2004) has found that for the range of black hole masses, an upper envelope of $M_{\text{BH}} \sim 10^{10} M_{\odot}$ is observed over a large range in redshift ($4 \lesssim z \lesssim 6$ for her sample). So, again, while APM 08279+5255 appears relatively extreme, even its AGN properties are far from being unique in a scenario assuming only $\mu_L=4$. The extreme optical luminosity may then be explained by a luminous AGN episode of such a few times $10^{10} M_{\odot}$ SMBH, which accretes at (super-)Eddington rates (within the uncertainties of the BH mass estimators). Also, the formation of such a SMBH at the high mass end of the BH mass function by a redshift of 4 is consistent with ‘downsizing’, which predicts that such high mass black holes form at the high density peaks at high redshift, and are built up rapidly by vigorous accretion (e.g., Di Matteo et al. 2007). Due to the fact that the SMBH in APM 08279+5255 is among the most massive black holes that are observed, it is likely to end up as a central cD galaxy of a massive cluster. For such galaxies, recent cosmological simulations suggest that a large fraction of the mass of the black hole grows from mergers with other black holes rather than being accreted by a single progenitor black hole (Sijacki et al. 2007).

In addition to M_{BH} , we were also able to derive a limit on the mass of the stellar bulge (M_{bulge}) for APM 08279+5255. However, our dynamical mass estimate, which is used as the predictor for M_{bulge} , is only valid for the inner region of the galaxy where the bulk of the molecular gas is found. For the $\mu_L=4$ model, this describes a region with a radius of 550 pc. For galaxies with $M_{\text{BH}} > 10^9 M_{\odot}$ used in local studies of the $M_{\text{BH}}-\sigma_{\text{bulge}}$ relation, it has been found that the host galaxies are typically giant elliptical galaxies with effective radii of 1.5–8 kpc (Tremaine et al. 2002; Faber et al. 1997). Assuming that the volume density of stellar luminosity (and thus mass) flattens with radius from r^{-2} to r^{-1} in the inner region of the elliptical host galaxy (Gebhardt et al. 1996), or even that it flattens into a ‘core’, a significant fraction of the bulge mass is expected to be found inside the inner 550 pc. From

¹⁵Due to the fact that $T \propto \mu_L^{-1/4}$ and $\mu_L \propto r_{\text{true}}^2$, the $\mu_L=4$ model requires more screening than the previous $\mu_L=100$ models.

¹⁶Both the CO and FIR emission in BR 1202-0725 are however distributed over at least two distinct components, which then each have comparable but lower luminosities than APM 08279+5255.

the local $M_{\text{BH}}-M_{\text{bulge}}$ relationship, it is expected that $M_{\text{bulge}} \sim 700 M_{\text{BH}}$. For the inner region of APM08279+5255, we have found $M_{\text{bulge}} = 3.4 M_{\text{BH}}$. This value falls short by more than two orders of magnitude compared to the local estimate. Even if corrected for a 10 kpc radius host galaxy, a clear offset from the local $M_{\text{BH}}-M_{\text{bulge}}$ relationship remains¹⁷. This is consistent with the findings of Shields et al. (2006) for a larger number of high- z quasars (but based on less certain dynamical mass estimates), and may indicate a breakdown of the local $M_{\text{BH}}-M_{\text{bulge}}$ relationship toward high redshift, as also suggested by Walter et al. (2004). This is also consistent with observations of a sample of $z \sim 0.36$ Seyfert 1 galaxies (Woo et al. 2006), which also shows a clear offset from the local $M_{\text{BH}}-\sigma_{\text{bulge}}$ relation. These observations together appear to indicate that the mass correlation between SMBHs and their stellar bulges is not a universal property, but rather an endpoint of a long-lasting evolutionary process throughout cosmic times. We thus conclude that the SMBH in APM08279+5255 appears to already be largely in place, while the buildup of the stellar bulge is still in progress.

If the assumptions made to derive the properties of APM08279+5255 are correct, this result has several interesting implications. It appears as if SMBH growth and formation through gas dissipation and accretion (and possibly mergers) was the main characteristic during the early formation of this source (even relative to star formation). Since the SMBH in APM08279+5255 is already found at the high mass end of the black hole mass function, it is expected that most of the molecular gas present at $z=3.9$ is either blown out or formed into stars by $z=0$, while only a minor fraction is accreted onto the black hole. Moreover, if APM08279+5255 is to evolve into a galaxy that fulfills the $M_{\text{BH}}-\sigma_{\text{bulge}}$ relation by $z=0$, a significant fraction of the molecular gas is has to actually end up in stars. In fact, even if the whole amount of molecular gas that is currently present in the host galaxy of APM08279+5255 were to be converted into stars (i.e., at an efficiency of 100%) by $z=0$, it would not be sufficient to reach the local $M_{\text{BH}}-\sigma_{\text{bulge}}$ relation. If our picture of this galaxy is correct, this result implies that the buildup of the stellar bulge cannot be accomplished by only converting the observed molecular gas reservoir into stars, but relies to a significant part on the accumulation of stellar matter via other mechanisms. Although further details are difficult to quantify at present, it thus is likely that a significant fraction of the spheroid will be produced via mergers. It has been suggested that a common, growth-limiting feedback mechanism acting on both star formation and black hole assembly is the physical explanation for the local $M_{\text{BH}}-\sigma_{\text{bulge}}$ relation. Assuming that such a mechanism exists, quasar winds as a form of AGN feedback would be an obvious candidate for a system like APM08279+5255 (Silk & Rees 1998). One difficulty with this assumption would then be that the SMBH in this source already accretes radiatively highly efficiently at (super-)Eddington rates (see above), where such feedback effects are expected to be very strong to regulate the further growth of the SMBH. If this effect were to also regulate star formation in the host galaxy, it would be expected to shut off both on a relatively

¹⁷Note that the local $M_{\text{BH}}-\sigma_{\text{bulge}}$ relationship is difficult to reconcile even with a $\mu_L=100$ model, which leaves more room for M_{bulge} within M_{dyn} (i.e., $M_{\text{bulge}}=50 M_{\text{BH}}$), but also has to assume host galaxy size relations for less massive black holes.

short timescale by pushing the remaining gas outwards. The build-up of the stellar bulge then can only proceed further through hierarchical merging, which is expected to again feed both the SMBH and star formation. To end up anywhere near the local $M_{\text{BH}}-\sigma_{\text{bulge}}$ relation through a self-regulated mechanism, APM08279+5255 thus is required to form and/or accumulate stars more efficiently (relative to the black hole feeding/merger rate) than in the past.

There are two main points that support the $\mu_L=4$ model. First, the observed CO($J=1\rightarrow 0$) properties give rather tight constraints on the allowed combinations of intrinsic CO disk size and magnification strength for the favoured range of low disk inclinations, assuming a relatively high CO area filling factor. The $\mu_L=4$ model lies well within the range of these constraints. Second, the spatially resolved multiwavelength observations of APM08279+5255 show similar morphologies of the lensed source from the X-ray to radio wavelength regime, probing sub-pc to hundreds of pc scales, while showing a different morphology out to kpc scales. The $\mu_L=4$ model produces this quite naturally, predicting modest effects of differential lensing. The high lensing magnification models suggested so far do not reproduce the second characteristic. Also, for low inclinations, they predict a very compact CO disk of only about 100 pc diameter. This is by a factor of a few less than in typical ULIRGs (Downes & Solomon 1998). The $\mu_L=4$ model, on the other hand, produces a CO disk of 550 pc diameter, which is in a more typical regime.

While some properties of APM08279+5255, like the optical luminosity and expected strong tidal forces from the black hole, may still favour a scenario in which the source is highly magnified by gravitational lensing, there thus are several arguments that favour models with low μ_L . It thus is important to note that, if a high- μ_L was to be found that fits the observed morphological properties of APM08279+5255, further studies would be necessary to exclude one scenario or the other. Based on the existing observations, no definitive conclusion can be drawn – the final decision can only be made by detecting the lens itself. The lensing model presented in this chapter aids in developing a quite consistent picture of APM08279+5255 based on the existing observations, describing the source as a dust and gas-rich galaxy with a very massive, active black hole. The deep gravitational potential of the central region of this source causes the molecular gas to be rather dense, while the strong, penetrating AGN radiation causes it (and the dust) to be rather warm. The whole system may be seen relatively close to face-on (the inclination is however difficult to constrain). It has a co-eval starburst which only contributes about 10% to the FIR dust heating, but still produces more than $500 M_{\odot} \text{ yr}^{-1}$ (Weiß et al. 2007, correcting for $\mu_L=4$). The star formation in this galaxy takes place far off the black hole mass–bulge mass scaling relation of nearby galaxies, suggesting that the latter is subject to significant evolution throughout cosmic times.

9.11 Summary

In this chapter, we present improved, high resolution CO($J=1\rightarrow 0$) observations toward the $z=3.9$ BAL quasar APM08279+5255 with the VLA. We also present multiwavelength radio

continuum observations, and a search for $\text{CN}(N=1\rightarrow 0)$ emission. The source's properties are investigated based on a revised model of the gravitational lensing in this system.

From our comprehensive analysis, we obtain the following main results:

1. The $\text{CO}(J=1\rightarrow 0)$ emission is resolved and has a (lensed) source size of $\sim 0.3''$. The structure shows a morphology that is very similar to the X-ray/optical/NIR morphology, indicative of three images of a compact, gravitationally lensed source (of which two are blended in the CO maps). In particular, we do not find any evidence for extended $\text{CO}(J=1\rightarrow 0)$ emission over a scale of several arcseconds, in contrast to previous reports (cf. Papadopoulos et al. 2001). The whole single-dish $\text{CO}(J=1\rightarrow 0)$ flux found by Riechers et al. (2006a) is recovered from the compact structure detected in our VLA maps. The rest-frame 2.7 mm continuum emission underlying the $\text{CO}(J=1\rightarrow 0)$ line is slightly more extended than the CO source, and may correspond to differentially lensed emission either due to free-free radiation from the starburst or extended AGN-related emission (in agreement with the overall steep spectral index). A radio source is detected $3''$ south of APM 08279+5255 in two out of six radio continuum bands (see also Ibata et al. 1999), but not related to the high redshift quasar.

2. We derive an apparent $\text{CO}(J=1\rightarrow 0)$ luminosity of $L'_{\text{CO}(1-0)} = (10.6 \pm 0.9) \times 10^{10} \mu_L^{-1} \text{ K km s}^{-1} \text{ pc}^2$. This is by about 20% lower than the re-derived $\text{CO}(J=2\rightarrow 1)$ luminosity, and even by 40% lower than the $\text{CO}(J=4\rightarrow 3)$ luminosity. This may indicate that the optical depth in the lower J CO transitions is only modest, as already indicated by previous studies (Riechers et al. 2006a; Weiß et al. 2007). Due to the high gas density, the $\text{CO}(J=1\rightarrow 0)$ luminosity corresponds to a total apparent H_2 molecular gas mass of $M_{\text{gas}} = 5.3 \times 10^{11} \mu_L^{-1} M_{\odot}$.

3. We set a limit on the $\text{CN}(N=1\rightarrow 0)$ luminosity in this source, which we derive to be $< 37\%$ of the $\text{CO}(J=1\rightarrow 0)$ luminosity.

4. The radio continuum SED of APM 08279+5255 is likely dominated by AGN emission. Based on a starburst galaxy model (Condon 1992), we conclude that free-free and synchrotron emission from the host galaxy contribute $\lesssim 20\%$ to the radio continuum emission (note that this fraction is clearly model-dependent). We also find that the AGN lies in the transition region between radio-quiet and radio-loud quasars, and is in overall agreement with being radio-quiet. The low frequency part of the radio SED is (ultra-)steep, which is commonly found in high- z quasars with extended radio emission. The overall spectral slope of the radio SED is in agreement with synchrotron emission that may originate from both the starburst and the AGN.

5. In spite of the fact that both the FIR (Weiß et al. 2007) and radio continuum emission in APM 08279+5255 appear to be dominantly powered by the AGN, it follows the radio-FIR correlation for star-forming galaxies without correcting for the AGN contribution to the radio/FIR luminosities ($\sim 80\text{--}90\%$ in both cases).

6. From our CO maps, we derive observed brightness temperatures of $T_{\text{b}}^{\text{obs}, \text{A+C}} \simeq 33 \text{ K}$ for the blend of optical quasar images A+C and $T_{\text{b}}^{\text{obs}, \text{B}} \simeq 18 \text{ K}$ for quasar image B. Assuming a true brightness temperature of 50 K as predicted by LVG models of the CO excitation (Weiß et al. 2007), this corresponds to a lensed CO equivalent disk with a radius of $\sim 1075 \text{ pc}$.

7. Our revised lensing model of APM08279+5255 predicts that the luminosity is only enhanced by a lensing magnification factor of about $\mu_L=4$ over the whole observed wavelength range. Assuming that the CO disk is seen relatively close to face-on ($i<30^\circ$) and has a large area filling factor, this model is consistent with a CO ring that has an unlensed radius of about 550 pc.

8. From C IV observations of APM08279+5255 and a scaling relation of nearby galaxies from the literature, we derive an apparent black hole mass of $M_{\text{BH}}=9.0 \times 10^{10} \mu_L^{-1} M_\odot$, which corresponds to about half of the Eddington limit. This also corresponds to about 17% of the molecular gas mass.

9. From our CO maps and model, we derive a dynamical mass of $M_{\text{dyn}} \sin^2 i = 4.0 \times 10^{10} M_\odot$ for APM08279+5255. Assuming $\mu_L=4$, this indicates an inclination of $i<30^\circ$, consistent with observations at all wavelength within an unified scheme. Assuming an average rotational velocity for high- z quasars, this even sets a limit on the mass of the stellar bulge within the central 550 pc of $M_{\text{bulge}}=3.4 M_{\text{BH}}$, which falls by almost two orders of magnitude short of the $M_{\text{BH}}-M_{\text{bulge}}$ relation observed for nearby galaxies (see also discussion by Weiß et al. 2007). We thus conclude that the SMBH in this distant quasar is already in place, while the buildup of the stellar bulge is still in progress. A similar indication was found for the $z=6.4$ quasar SDSS J1148+5251 (Walter et al. 2004), and thus suggests a breakdown of this relation at early cosmic times.

The observations presented herein highlight the importance of spatially and dynamically resolved studies of molecular gas in galaxies at $z \gtrsim 4$ for our general picture of galaxy formation and evolution. In the next decade, the Expanded Very Large Array (EVLA) will enable us to commence such studies at improved sensitivities and spectral resolution. The low J transition studies of molecular gas with the EVLA will be complemented by observations of the higher J transitions with the Atacama Large (Sub-)Millimeter Array (ALMA) at even higher spatial resolution. Both instruments will allow us to probe significantly deeper down the luminosity function(s) of the different populations of high redshift galaxies using molecular gas studies, and thus largely improve our picture of galaxies in the early universe.

It is a pleasure to thank my collaborators on this project:

Fabian Walter (MPIA), Chris Carilli (NRAO), and Geraint Lewis (University of Sydney).

CHAPTER TO BE PUBLISHED AS:

Riechers, D. A., Walter, F., Carilli, C. L., & Lewis, G. F., ‘*Imaging the Molecular Gas in a $z=3.9$ Quasar Host Galaxy at 0.3" Resolution: A Central, sub-kiloparsec Scale Star Formation Reservoir in APM08279+5255*’, 2007, ApJ, to be submitted

Chapter 10

Molecular Line Mapping II: Zoom-In Through a $z=4.12$ Einstein Ring

10.1 Context

As shown in the previous chapter, gravitational lensing does not always help much to resolve distant sources. However, sometimes it does help tremendously. One of these cases is shown here. The molecular gas in the distant quasar host galaxy of PSS J2322+1944 ($z=4.1$) is not only lensed into a full Einstein ring (magnifying scales in the plane of the background galaxy by more than a factor of three), but also dynamically resolved, showing how different kinematic components of the galaxy are lensed differentially by the foreground galaxy. This is the first time that such an effect has been observed, and aided by a model of the lens system, allows us to study the host galaxy of PSS J2322+1944 to unprecedented detail, more than five years before such studies will become possible with ALMA.

10.2 Abstract

We present high-resolution ($0.3''$) Very Large Array (VLA) imaging of the molecular gas in the host galaxy of the high redshift quasar PSS J2322+1944 ($z = 4.12$). These observations confirm that the molecular gas in the host galaxy of this quasar is lensed into a full Einstein ring, and reveal the internal dynamics of the molecular gas in this system. The ring has a diameter of $\sim 1.5''$, and thus is sampled over ~ 20 resolution elements by our observations. Through a model-based lens inversion, we recover the velocity gradient of the molecular reservoir in the quasar host galaxy of PSS J2322+1944. The Einstein ring lens configuration enables us to zoom in on the emission and to resolve scales down to 650 pc. From the model-reconstructed source, we find that the molecular gas is distributed on a scale of 3 kpc, and has a total mass of $M(\text{H}_2) = 1.7 \times 10^{10} M_\odot$. The lens configuration also allows us to tie the optical emission to the molecular gas emission, and suggests that the active galactic nucleus (AGN) does not reside in the center of the molecular reservoir. Together with the (at least partially) disturbed structure of the CO, this suggests that the

170 10. Molecular Line Mapping II: Zoom-In Through a $z=4.12$ Einstein Ring

system is interacting. Such an interaction, possibly caused by a major ‘wet’ merger, may be responsible for both feeding the quasar and fueling the massive starburst of $760 M_{\odot} \text{yr}^{-1}$ in this system, in agreement with recently suggested scenarios of quasar activity and galaxy assembly in the early universe.

10.3 Introduction

A fundamental aspect in studies of galaxy formation and evolution is to understand the connection between AGN and starburst activity. The existence of a physical connection between both processes is suggested by the finding that present day galaxies show a strong relationship between the mass of their central supermassive black holes (SMBHs) and the mass and concentration of their stellar spheroids (Magorrian et al. 1998; Ferrarese & Merritt 2000; Gebhardt et al. 2000; Graham et al. 2001). If these relations were due to a coevolution of both components during the early assembly of a galaxy, high-redshift quasars and their associated host galaxies would be ideal laboratories to study these processes.

The cosmological distances of high redshift quasars make it difficult to resolve emission from their host galaxies at longer wavelengths (where the AGN does not outshine all other emission), even if they are bright enough to be detected. The resolution of such observations can be boosted by the use of gravitational lenses as natural telescopes, in particular those in Einstein ring configurations. Due to the compactness of the AGN, optical quasars in Einstein ring lens configurations are rare. Due to their greater extent, the host galaxies of quasars are much more likely to cross the inner Einstein ring caustic of a gravitational lens.

Studies of molecular gas, the prerequisite material that fuels star formation, have become an important tool to probe distant quasar host galaxies (see Solomon & Vanden Bout 2005 for a general review), and revealed large molecular gas reservoirs of $>10^{10} M_{\odot}$ in a number of these sources. These galaxies typically show huge far-infrared (FIR) luminosities in excess of $10^{13} L_{\odot}$, which are thought to be powered by starbursts (and possibly AGN). Observations of molecular gas trace the regions that can host massive starbursts. In addition, the velocity structure of molecular line emission has the potential to constrain the dynamical state of such distant galaxies.

In this chapter, we report on high ($0.3''$) angular resolution Very Large Array (VLA)¹ observations of CO in the host galaxy of the $z=4.12$ quasar PSS J2322+1944, one out of only two known $z>4$ galaxies that are both gravitationally lensed and detected in molecular gas emission (the other being BRI 0952–0115 at $z=4.43$; Guilloteau et al. 1999). In spite of the fact that this source shows only two unresolved quasar images in the optical, previous CO observations have shown that the molecular gas reservoir in its host galaxy is lensed into an Einstein ring (Carilli et al. 2003). These observations were also used to derive a first lensing model for this source. Based on the dynamical structure revealed by our new, higher resolution observations of PSS J2322+1944, we have developed a new lensing model to

¹The Very Large Array is a facility of the National Radio Astronomy Observatory, operated by Associated Universities, Inc., under a cooperative agreement with the National Science Foundation.

reconstruct the spatially resolved velocity gradient of the gas in the unlensed galaxy. We use a concordance, flat Λ CDM cosmology throughout, with $H_0=71 \text{ km s}^{-1} \text{ Mpc}^{-1}$, $\Omega_M=0.27$, and $\Omega_\Lambda=0.73$ (Spergel et al. 2003, 2007).

10.4 Observations

We observed the CO($J=2\rightarrow 1$) transition ($\nu_{\text{rest}} = 230.53799 \text{ GHz}$) towards PSS J2322+1944 using the VLA in B configuration between 2006 June 19 and July 3, and in C configuration between 2002 October 21 and November 15 (these short spacings data were published in the original study by Carilli et al. 2003). The total on-sky integration time in the 11 observing runs amounts to 70.5 hr. At $z = 4.119$, the line is redshifted to 45.0351 GHz (6.66 mm). Observations were performed in fast-switching mode (see, e.g., Carilli & Holdaway 1999) using the nearby source 23307+11003 for secondary amplitude and phase calibration. Observations were carried out under excellent weather conditions with 26 or 27 antennas. The phase stability in all runs was excellent (typically $<15^\circ$ for the longest baselines). The phase coherence was checked by imaging the calibrator source 23207+05138 with the same calibration cycle as that used for the target source. For primary flux calibration, 3C48 was observed during each run. Due to the restrictions of the VLA correlator, one 50 MHz intermediate frequency (IF) with seven 6.25 MHz channels was observed centered at the CO($J=2\rightarrow 1$) line frequency, leading to an effective bandwidth of 43.75 MHz (corresponding to 291 km s^{-1} at 45.0 GHz). This encompasses most of the CO line width as measured in the CO($J=5\rightarrow 4$) transition ($273\pm 50 \text{ km s}^{-1}$ FWHM, Cox et al. 2002), but does not cover the outer line wings and the continuum. Earlier observations set a 2σ limit of $150 \mu\text{Jy}$ on the continuum emission (Carilli et al. 2002a).

For data reduction and analysis, the AIPS package was used. All data were mapped using the CLEAN algorithm and natural weighting. A velocity-integrated CO($J=2\rightarrow 1$) map of this dataset is shown in Figure 10.1. The synthesized clean beam has a size of $0.33''\times 0.30''$.² The final rms over the bandwidth of 37.5 MHz (250 km s^{-1} , the noisy edge channel is omitted) is $48 \mu\text{Jy beam}^{-1}$. In Fig. 10.3, seven velocity channel maps (6.25 MHz, or 42 km s^{-1} each) of the CO($J=2\rightarrow 1$) are shown after Hanning smoothing (rms: $77 \mu\text{Jy beam}^{-1}$).

10.5 Results

In Figures 10.1 and 10.2, the integrated CO($J=2\rightarrow 1$) emission over the central 250 km s^{-1} is shown at a linear resolution of $0.3''$, and convolved to $0.5''$ (to improve the signal-to-noise ratio). The emission is clearly resolved over multiple beams, and extended on a scale of $\sim 1.5''$. The distribution of the gas is reminiscent of a full, almost spherical molecular Einstein ring, consistent with previous indications of such a structure in lower resolution

²Imaging B array data only gives a resolution of $0.17''\times 0.15''$ (natural weighting), or $0.12''\times 0.11''$ (uniform weighting).

172 10. Molecular Line Mapping II: Zoom-In Through a $z=4.12$ Einstein Ring

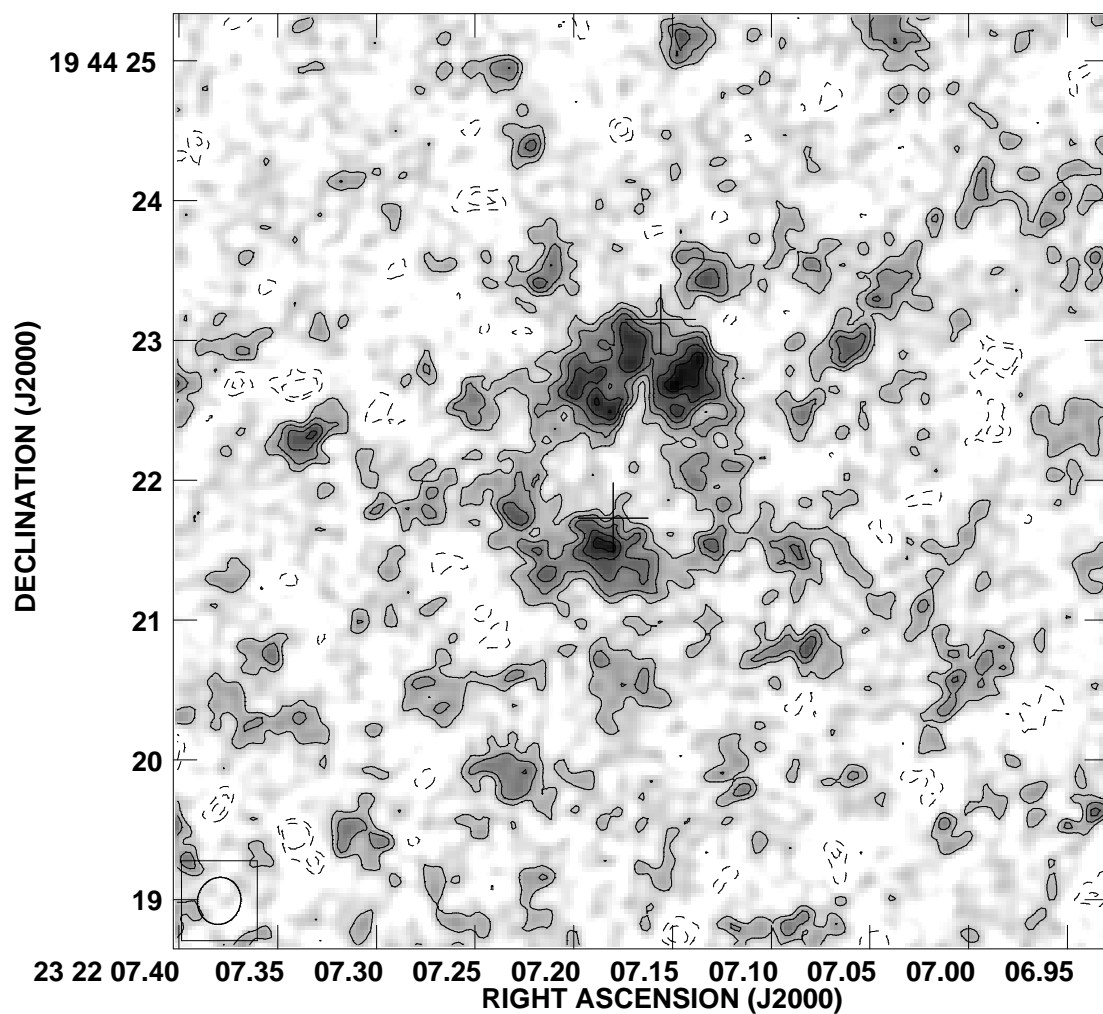


Figure 10.1: VLA map of the $\text{CO}(J=2\rightarrow 1)$ emission toward PSS J2322+1944 (integrated over the central 37.5 MHz, or 250 km s^{-1}). Contours are shown at $(-3, -2, 1, 2, 3, 4, 5)\times\sigma$ ($1\sigma = 48 \mu\text{Jy beam}^{-1}$). The beam size ($0.33''\times 0.30''$) is shown in the bottom left corner. The crosses show the positions of the optical quasar images, and the cross sizes represent the relative astrometric error.

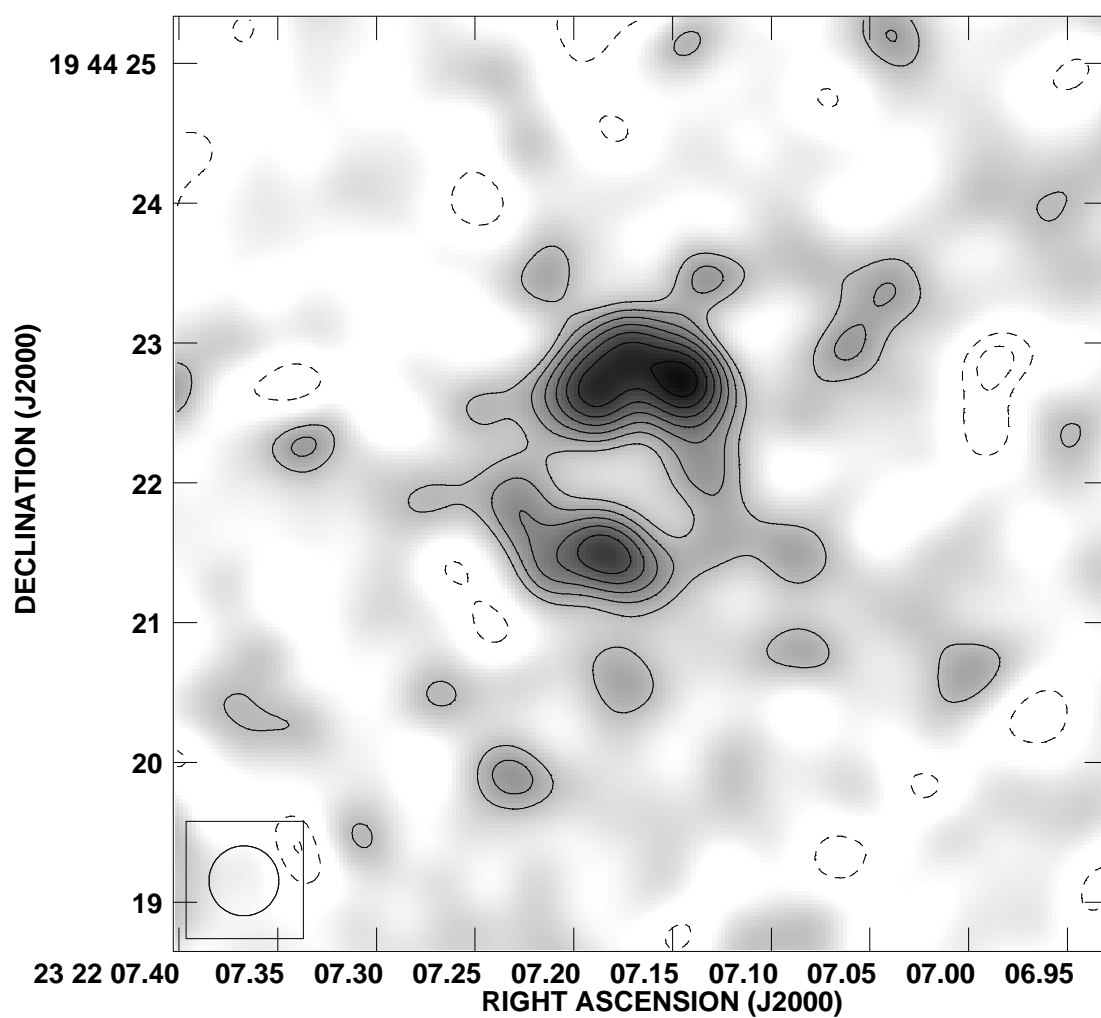


Figure 10.2: VLA map of the CO($J=2\rightarrow 1$) emission toward PSS J2322+1944 as shown in Figure 10.1, but convolved to a linear resolution of $0.5''$ (as shown in the lower left). Contours are shown at $(-3, -2, 2, 3, 4, 5, 6, 7, 8)\times\sigma$ ($1\sigma = 50\ \mu\text{Jy beam}^{-1}$).

174 10. Molecular Line Mapping II: Zoom-In Through a $z=4.12$ Einstein Ring

observations (Carilli et al. 2003). The emission varies in intensity along the ring, showing clear substructure. The two brightest peaks of the emission are consistent within the two images of the optical quasar (indicated as crosses in Figure 10.1) within the relative astrometric errors ($\sim 0.5''$), although there is an offset.

The apparent surface brightness variations along the ring set strong constraints on the geometry of the lens configuration. The brightest CO peak on the ring can be used to set a lower limit on the intrinsic brightness temperature of the molecular gas. The peak strength of $280 \pm 48 \mu\text{Jy beam}^{-1}$ corresponds to a beam-averaged, rest-frame brightness temperature of $T_b = 12.6 \text{ K}$.

We derive a total CO($J=2 \rightarrow 1$) flux density of $2.50 \pm 0.32 \text{ mJy}$, which is consistent with that found by Carilli et al. (2002a). This corresponds to a total molecular gas mass³ of $M(\text{H}_2) = 9.0 \times 10^{10} \mu_L^{-1} M_\odot$ (where μ_L is the lensing magnification factor, see below). This is in agreement with the value found by Riechers et al. (2006a) based on the CO($J=1 \rightarrow 0$) luminosity within the errors.

In Figures 10.3 and 10.4, seven 42 km s^{-1} wide velocity channels are shown at the full resolution of $0.3''$, and convolved to $0.5''$ to improve the signal-to-noise ratio (channel 7 was omitted from the data shown in Figures 10.1 and 10.2 due to higher noise). Although the maps are noisy, emission along the Einstein ring is detected in all channels. Clearly, the emission is moving systematically along the ring from the red part of the CO($J=2 \rightarrow 1$) line to the blue. Note that there are many peaks of similar surface brightness (peak fluxes of $350\text{--}400 \mu\text{Jy beam}^{-1}$, or $T_b = 16\text{--}18 \text{ K}$) that are found at different positions at different velocities. This indicates, to first order, a dynamical structure of uniform surface brightness, where the components at different velocities get projected to different positions in the lens plane. This puts us in the unique situation to model this gravitational lens system in detail, including the dynamics of the background galaxy.

10.6 Gravitational Lens Inversion

10.6.1 Method: Bayesian Inference

Due to the fact that the characteristics of the lensing galaxy towards PSS J2322+1944 are currently not known, and due to the limited signal-to-noise and resolution of the data, it is not possible to derive a unique solution for the inversion of the gravitational lens. We thus explored the parameter space permitted by the data to find the best possible solution by following a Bayesian approach, using the Markov Chain Monte Carlo code by Brewer & Lewis (2006). This approach does not simply aim at minimizing χ^2 to find the best model (which may “overfit” the data by fitting part of the noise), but finds the most probable solution by comparing models within the range of plausible fits (i.e., a broad region in parameter space with higher χ^2 can outweigh a solution that minimizes χ^2 , but only in a small region of parameter space that may be coincidentally selected by adding up noise).

³Assuming constant T_b between CO($J=2 \rightarrow 1$) and CO($J=1 \rightarrow 0$), and a ULIRG CO luminosity to H_2 mass conversion factor of $\alpha = 0.8 M_\odot (\text{K km s}^{-1} \text{ pc}^2)^{-1}$ (Downes & Solomon 1998).

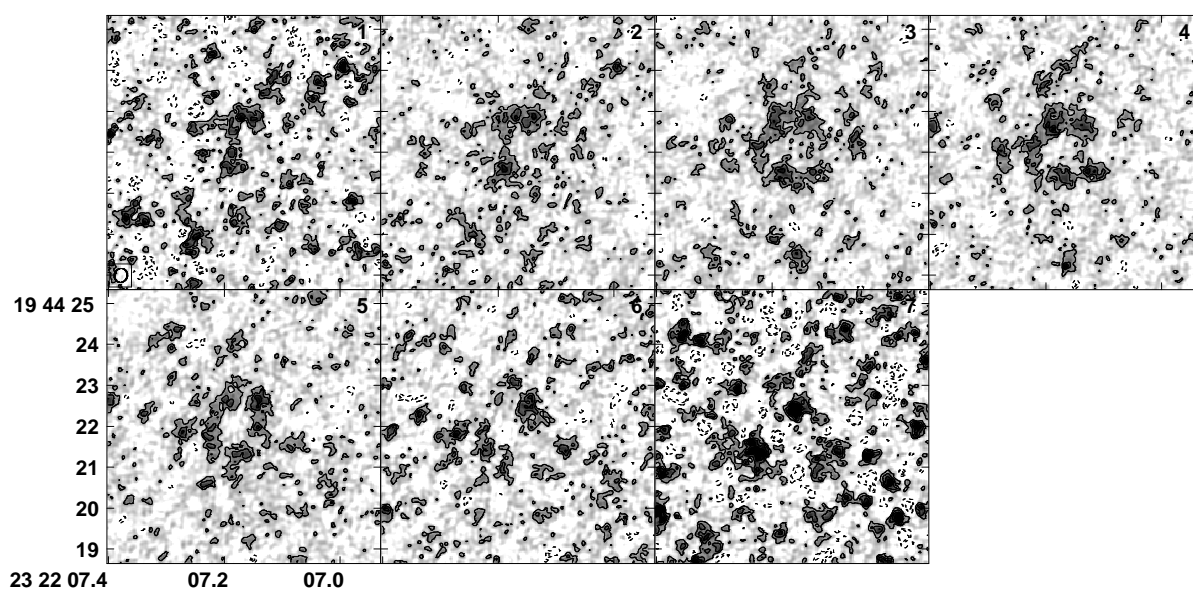


Figure 10.3: Channel maps of the CO($J=2\rightarrow 1$) emission. The same region is shown as in Fig. 10.1. One channel width is 6.25 MHz, or 42 km s^{-1} (frequencies increase with channel number and are shown at 45016.35, 45022.60, 45028.85, 45035.10, 45041.35, 45047.60, and 45053.85 MHz). Contours are shown at $(-3, -2, 1, 2, 3, 4) \times \sqrt{2}\sigma$ ($1\sigma = 77 \mu\text{Jy beam}^{-1}$). Note that the noise in channel 7 is by a factor of $\sqrt{2}$ higher relative to the other channels. The beam size is shown in the bottom left corner of the first panel.

176 10. Molecular Line Mapping II: Zoom-In Through a $z=4.12$ Einstein Ring

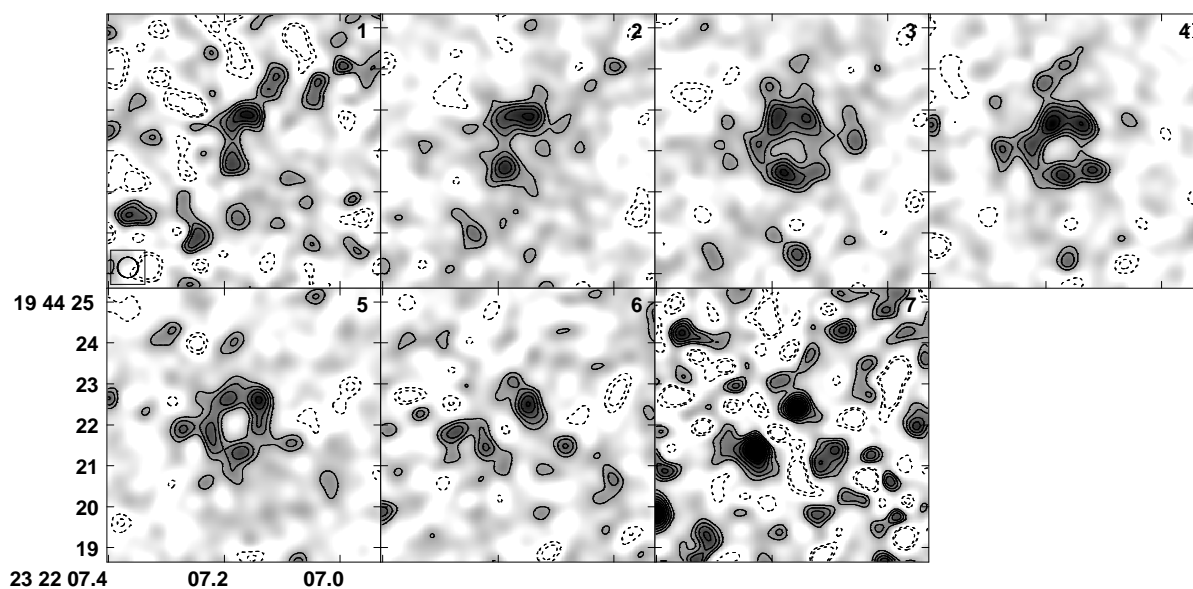


Figure 10.4: Channel maps of the CO($J=2 \rightarrow 1$) emission as shown in Figure 10.3, but convolved to a linear resolution of $0.5''$ (as shown in the lower left corner of the first panel). Contours are shown at $(-3, -2, 2, 3, 4, 5, 6) \times \sigma$ ($1\sigma = 80 \mu\text{Jy beam}^{-1}$).

The lensed image of the source was reconstructed based on the integrated emission line map and the structure detected in the velocity channels, and then used to derive a common model of the lensing galaxy’s projected density profile that reproduces the emission in all channels simultaneously. Due to the differential structure among the velocity channels, this implies that the reconstructed source components after lens inversion will be different for each velocity channel, and reproduce the velocity gradient across the source. In our study, the lens was parameterised as a singular isothermal elliptical potential with five free parameters, which are the strength b of the lens, the ellipticity q of the potential, the central position (x_c, y_c) of the lensing source, and the angle of orientation θ of the projected density profile.

10.6.2 Application to Interferometric Data

Interferometer maps are reconstructed from visibility data using a scale that samples one synthesized interferometer beam (i.e., resolution element) with multiple pixels. This means that the per pixel noise is not independent for all pixels. To determine the typical scale of noise correlations, it has to be taken into account that, due to the natural weighting of the baselines, not all pixels in one resolution element are strictly correlated [only those that fall within the resolution element defined by the longest baselines ($\sim 1.7\text{M}\lambda$)]. We find that at the scale of the images ($0.03'' \text{ pixel}^{-1}$), $1/62$ of the pixels is effectively independent (corresponding to 106 pixels on the scale of the Einstein ring). To not “overfit” the image due to noise, only this fraction of information can be used to computationally determine the lens properties. In practice, this was confirmed by requiring that the residuals of the model images have the same statistical properties as the background in the observed maps.

10.6.3 Modeling Results

For the “best” model of the lens, we find $b = 1.227'' \pm 0.023''$, $q = 0.969 \pm 0.014$, $x_c = 0.121'' \pm 0.039''$, and $y_c = 0.179'' \pm 0.047''$ for the strength, ellipticity, and position (coordinates are relative to the center of the model images). With a probability of 62% (38%), the angle of orientation of the potential is $\theta = 109.2^\circ \pm 7.1^\circ$ ($-27.5^\circ \pm 7.3^\circ$). This “best” solution was obtained by averaging over the range of plausible reconstructions of the model sources and their corresponding images in the lens plane. Due to the fact that $q \simeq 1$, the lens potential is close to circular, as is the projected lens density profile. The overall lensing magnification is $\mu_L = 5.34 \pm 0.34$.

In Figure 10.5, the model-reconstructed sources are shown in the lens plane (*middle row*), and after lens inversion (*top row*), together with the observations (*bottom row*). The columns give the results for the seven different velocity channels shown in Figure 10.3. The lens models are identical for all velocity channels, i.e., the different distribution of molecular gas between the velocity channels is due to the intrinsic velocity structure of the model source. Note the difference in scale between the lensed and unlensed source. The linear resolution of $0.30''$ of the CO($J=2\rightarrow 1$) observations corresponds to only $0.09''$ (or 650 pc) in the source plane. The gravitational lens thus does not only boost the apparent

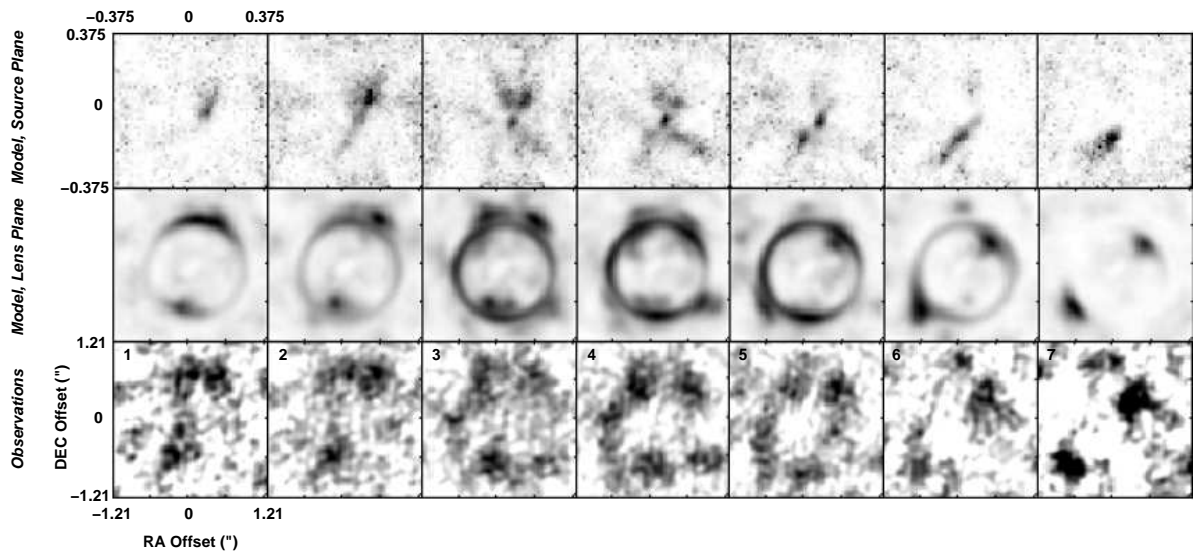


Figure 10.5: Reconstructed model images of the 42 km s^{-1} $\text{CO}(J=2 \rightarrow 1)$ velocity channels, and source morphologies after lens inversion. The *bottom* row shows the observed $\text{CO}(J=2 \rightarrow 1)$ emission in the velocity channels as shown in Figure 10.3. The *middle* row shows the model-reconstructed images of the channel maps in the lens plane (same scale as bottom). The *top* row shows the reconstructed images in the source plane after lens inversion. The linear resolution of $0.30''$ in the lens plane corresponds to $0.09''$ (or 650 pc) in the source plane (scale given on top).

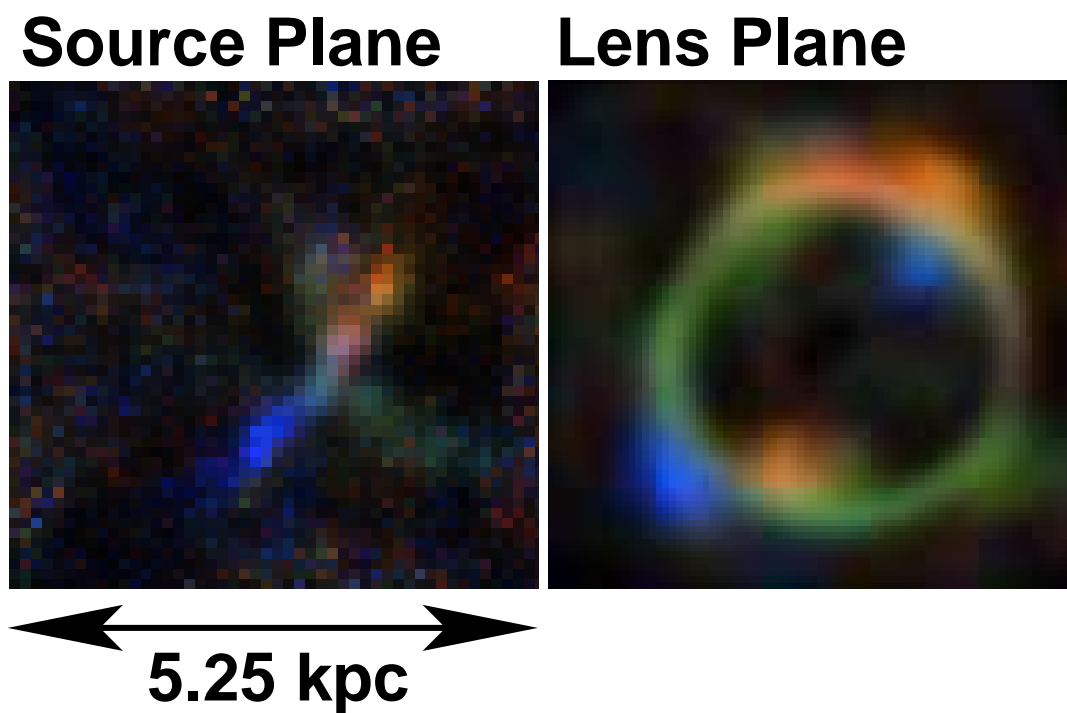


Figure 10.6: RGB composite color map of the model-reconstructed CO($J=2\rightarrow 1$) velocity channels shown in Figure 10.5, with three colors encoding the velocity range of the emission [red: redshifted (channels 1-2), green: central (channels 3-5), blue: blueshifted (channels 6-7)]. The bar at the bottom indicates the scale in the source plane. *Right:* Image of the Einstein ring in the lens plane. *Left:* Image of the model-reconstructed quasar host galaxy in the source plane.

180 10. Molecular Line Mapping II: Zoom-In Through a $z=4.12$ Einstein Ring

brightness of the source, but also acts as a natural telescope, and helps to zoom in on the emission. In Figure 10.6, a color composite map of the modeled distribution of the CO in the velocity channels is shown. Orange corresponds to the redshifted part of the emission line, green corresponds to the central part, and blue corresponds to the blueshifted part. In the *right* panel, the image in the lens plane is displayed, and in the *left* panel, the image in the source plane is shown after lens inversion. A clear velocity gradient is seen in both images. The brightest part of the emission shows a systemic velocity structure that would be in agreement with an inclined, almost edge-on, rotating disk of ~ 1.5 kpc radius within the uncertainties of the data and modeling. If gravitationally bound, this structure encloses a dynamical mass of $M_{\text{dyn}} = 2.6 \times 10^{10} \sin^{-2} i M_{\odot}$ (assuming a linewidth of 273 km s^{-1} as given above). However, there is also indication for a second, possibly tidal component (blue/green). This structure is slightly bent, but also has an extent of almost 3 kpc, similar to the brighter component. Each component extends over at least 4-5 resolution elements in the source plane, and thus is clearly resolved. Unfortunately, the relative astrometry of the optical and radio data is not good enough to determine where exactly the quasar is situated in the reconstructed image. However, note that in the red line wing, the northern peak of the Einstein ring is brighter (as in the optical), while in the blue line wing, the southern peak is brighter. If our model is correct, the fact that the optical emission shows two images rather than a full or at least partial Einstein ring then suggests that the optical quasar is associated with the red part of the emission. If the AGN is indeed located in the upper part of the disklike structure rather than in the center, one may speculate that the spatial and velocity structure of the reconstructed source is more likely to be due to interaction than due to a rotating disk.

10.7 Discussion

We have imaged and modeled a molecular Einstein ring at $z=4.12$. Our high resolution CO($J=2 \rightarrow 1$) maps of the lensed quasar host galaxy of PSS J2322+1944 (a double image optical quasar) reveal spatially resolved structure that shows a clear velocity gradient in the CO emission line. By performing a (non-unique) model-based lens inversion of the Einstein ring, we are able to reconstruct the velocity structure of this distant quasar host galaxy. The gravitational lensing effect acts as a natural telescope, and allows us to zoom in on the molecular gas reservoir down to a linear scale of only 650 pc, sufficient to reveal velocity structure over almost 10 resolution elements in the source plane. Our novel modeling of this system reveals how the molecular gas crosses the central caustic (causing the appearance of the Einstein ring) moving from the redshifted to the blueshifted molecular emission, and shows that the optical quasar is most likely associated with the redshifted part of the molecular reservoir. The full reservoir has a mass of $M(\text{H}_2) = 1.7 \times 10^{10} M_{\odot}$ (corrected for lensing magnification). If the gas in the “disk-like” molecular component was gravitationally bound, the molecular gas mass alone could fully account for the dynamical mass in this system if the system were to be seen close to edge-on. Due to the fact that the AGN is probably largely offset from the center (close to the

redshifted part) of the CO emission, we conclude that the molecular gas and dust are likely dominantly heated by star formation. From the apparent FIR luminosity of the source ($L_{\text{FIR}} = 2.7 \times 10^{13} \mu_L L_{\odot}$; Cox et al. 2002), we derive a star formation rate of $760 M_{\odot} \text{yr}^{-1}$ (assuming standard conversions and not accounting for a possible AGN contribution to L_{FIR} ; Kennicutt 1998a, 1998b). At least part of the CO emission of the reconstructed source does not follow a systemic trend in velocity. In this picture, this structure may be due to interaction, possibly caused by a major merger. Such an event could both feed the AGN and fuel the starburst, and thus be responsible for the coeval assembly of a supermassive black hole and the stellar bulge in this system. Future observations of the FIR continuum at comparable spatial resolution may shed more light on this situation.

The observations and modeling presented herein demonstrate the power of spatially and dynamically resolved molecular gas studies in strongly lensed, distant AGN/starburst systems to provide direct evidence for the scenarios of quasar activity and galaxy assembly in the early universe as suggested by recent cosmological simulations (e.g., Springel et al. 2005). The boost in line intensity and spatial resolution provided by Einstein ring lens configurations are currently the only means by which to probe the dynamical structure of the most distant star-forming galaxies at sub-kiloparsec resolution. Such observations provide an important foundation for future observations of molecular gas and dust in the early universe with the Atacama Large Millimeter/submillimeter Array (ALMA), which will be able to probe more typical galaxy populations at high redshift t comparable and higher physical resolution, even without the aid of gravitational lensing.

It is a pleasure to thank my collaborators on this project:

Fabian Walter (MPIA), Chris Carilli (NRAO), Brendon Brewer and Geraint Lewis (University of Sydney), Pierre Cox (IRAM), and Frank Bertoldi (AIfA).

CHAPTER TO BE PUBLISHED AS:

Riechers, D. A., Walter, F., Carilli, C. L., Brewer, B. J., Lewis, G. F., Cox, P., & Bertoldi, F., ‘*A Molecular Einstein Ring at $z=4.12$: Imaging the Quasar Host Galaxy of PSS J2322+1944 Through a Cosmic Lens*’, 2007, ApJL, to be submitted

182 10. Molecular Line Mapping II: Zoom-In Through a $z=4.12$ Einstein Ring

Chapter 11

Molecular Line Mapping III: Formation of a $z=4.41$ Quasar Host

11.1 Context

As shown in the previous two chapters, studies of distant gravitationally lensed sources can help to probe to smaller scales and fainter galaxy populations, and provide a wealth of information about such systems. The accuracy of the results, however, will always depend on the quality of the lensing model. The ultimate goal thus is to be able to also study the structure of distant galaxies that are not lensed. The third distant galaxy in the sample studied in molecular gas emission at high resolution with the VLA is BRI 1335-0417, a $z=4.4$ quasar without any evidence for gravitational magnification or distortion. Due to the lack of lensing, a linear resolution of $0.15''$ is required to probe scales of 1.0 kpc. This resolution is achieved in the observations presented here, and also provides sufficient velocity resolution to even dynamically resolve the system. This study reveals a $z=4.4$ quasar host galaxy forming in a high-mass major merger, such as predicted by state-of-the-art cosmological simulations. This is the first time that such an event can directly be observed at high redshift, and an important precursor for future studies of molecular gas in the most distant galaxies with ALMA.

11.2 Abstract

We present high-resolution Very Large Array (VLA) imaging of the molecular gas in the host galaxy of the high redshift quasar BRI 1335-0417 ($z = 4.41$). Our VLA observations of the CO($J=2\rightarrow 1$) emission have a linear resolution of $0.15''$ (1.0 kpc) and resolve the molecular gas emission both spatially and in velocity. The molecular gas in BRI 1335-0417 is extended on scales of 5 kpc, and shows a complex structure. At least three distinct components encompassing at least two thirds of the total molecular mass are identified in velocity space, which are embedded in a structure that harbors about one third of the total molecular mass in the system. From the CO luminosity, we find that the molecular

gas reservoir has a total mass of $9.2 \times 10^{10} M_{\odot}$. The CO($J=2 \rightarrow 1$) emission has an average brightness temperature of 10 K above the cosmic microwave background (CMB). Accounting for the CMB, this is comparable to the gas temperatures found in the central regions of nearby ultra-luminous infrared galaxies (ULIRGs). The spatial and velocity structure of the molecular reservoir in BRI 1335–0417 is inconsistent with a simple gravitationally bound disk, but resembles a merging system. Our observations are consistent with a major, gas-rich (wet) merger that both feeds an accreting supermassive black hole (causing the bright quasar activity), and fuels a massive starburst that builds up the stellar bulge in this galaxy. Our study of this $z > 4$ quasar host galaxy may thus be the most direct observational evidence that ‘wet’ mergers at high redshift are related to AGN activity.

11.3 Introduction

Great progress has been made in recent years both observationally and theoretically to further our understanding of galaxy formation and evolution from the early epochs of galaxy formation to the present universe. One basic prediction of cosmological simulations is that during the early epoch of hierarchical galaxy formation, some of the most massive galaxies are already formed in major merger events (e.g., Springel et al. 2005). These mergers are believed to commonly trigger both AGN and starburst activity in such early systems, which is regulated via AGN feedback (e.g., Hopkins et al. 2005). Such feedback may be responsible for the present-day “ $M_{\text{BH}}-\sigma_v$ ” relation between black hole mass and bulge velocity dispersion (Ferrarese & Merritt 2000; Gebhardt et al. 2000).

Studies of molecular gas (the requisite material to fuel star formation) in young galaxies are an essential ingredient to understand their physical properties in more detail (e.g., the nature of the Schmidt-Kennicutt law between total gas mass and star formation rate; Schmidt 1959; Kennicutt 1998a, 1998b). Molecular gas (typically CO) has been detected in 43 galaxies at $z > 1$ to date, revealing large molecular reservoirs of $> 10^{10} M_{\odot}$ in most cases (see Solomon & Vanden Bout 2005 for a review). However, these studies rely almost exclusively on the integrated properties of the line emission, as the molecular reservoirs in these distant galaxies are difficult to resolve. To date, only the $z=4.69$ and $z=6.42$ quasars BR 1202–0725 and SDSS J1148+5251, two of the most distant gas-rich galaxies could be resolved in molecular gas emission without the aid of gravitational magnification (Omont et al. 1996; Carilli et al. 2002b; Walter et al. 2004).

In this chapter, we report on high angular resolution ($0.15''$; 1.0 kpc) Very Large Array (VLA)¹ observations of molecular gas in the host galaxy of a dust-rich, optically identified quasar at a redshift of 4.41, corresponding to only 1.4 Gyr after the Big Bang. We use a concordance, flat Λ CDM cosmology throughout, with $H_0=71 \text{ km s}^{-1} \text{ Mpc}^{-1}$, $\Omega_{\text{M}}=0.27$, and $\Omega_{\Lambda}=0.73$ (Spergel et al. 2003, 2007).

¹The Very Large Array is a facility of the National Radio Astronomy Observatory, operated by Associated Universities, Inc., under a cooperative agreement with the National Science Foundation.

11.4 Observations

We observed the CO($J=2\rightarrow 1$) transition ($\nu_{\text{rest}} = 230.53799$ GHz) towards BRI 1335–0417 using the VLA in B configuration on 2005 April 11, 13, and 22, and in C configuration on 2005 September 16. The total on-sky integration time amounts to 29 hr. At $z = 4.4074$, the line is redshifted to 42.6338 GHz (7.03 mm). Observations were performed in fast-switching mode (see, e.g., Carilli & Holdaway 1999) using the nearby source 13515-01513 for secondary amplitude and phase calibration. Observations were carried out under excellent weather conditions with 25 antennas. The phase stability in all runs was excellent (typically $<15^\circ$ for the longest baselines). The phase coherence was checked by imaging the calibrator source 13569+02144 with the same calibration cycle as that used for the target source. For primary flux calibration, 3C286 was observed during each run. Given the restrictions of the VLA correlator, two 25 MHz intermediate frequencies (IFs) with seven 3.125 MHz channels each were observed simultaneously centered at the CO($J=2\rightarrow 1$) line frequency, leading to an effective bandwidth of 43.75 MHz (corresponding to 308 km s^{-1} at 42.6 GHz). This encompasses a major fraction of the CO line width as measured in the CO($J=5\rightarrow 4$) transition ($420 \pm 60 \text{ km s}^{-1}$ FWHM, Guilloteau et al. 1997), but does not cover the line wings and the continuum. Earlier observations set a 2σ limit of $240 \mu\text{Jy}$ on the continuum emission, in agreement with an expected flux of $\sim 34 \mu\text{Jy}$ as derived from the continuum spectral energy distribution of this source (Carilli et al. 1999).

For data reduction and analysis, the AIPS package was used. All data were mapped using the CLEAN algorithm. Two data sets were created in for the final analysis. The first dataset includes both the B- and C-array data, and are imaged using natural weighting. A velocity-integrated CO($J=2\rightarrow 1$) map of this dataset is shown in Fig. 11.1. The synthesized clean beam has a size of $0.23'' \times 0.18''$ (1.6×1.2 kpc). The final rms over the full bandwidth of 43.75 MHz (308 km s^{-1}) is $50 \mu\text{Jy beam}^{-1}$. To boost the resolution, the second dataset includes B array data only, and are imaged using robust 0 (i.e., intermediate between natural and uniform) weighting (Fig. 11.2), achieving a resolution of $0.16'' \times 0.14''$ (1.1×0.95 kpc). This results in an rms of $58 \mu\text{Jy beam}^{-1}$ per channel. In Fig. 11.3, seven velocity channel maps (6.25 MHz, or 44 km s^{-1} each) of the CO($J=2\rightarrow 1$) line based on the combined BC-array data are shown. A Gaussian taper was applied to the UV data at a baseline length of $800 \text{ k}\lambda$ (longest baseline in the B array data: $\sim 1.6 \text{ M}\lambda$), resulting in a resolution of $0.32'' \times 0.30''$ (2.2×2.0 kpc). This results in an rms of $150 \mu\text{Jy beam}^{-1}$ per channel. These channel maps are combined into a three color overlay in Fig. 11.4.

11.5 Results

11.5.1 Morphology of the Molecular Gas Reservoir

In Figure 11.1, the integrated CO($J=2\rightarrow 1$) emission over the full measured bandpass (308 km s^{-1}) is shown at a linear resolution of 1.4 kpc. The emission is clearly spatially resolved over many beams, and extended out to a scale of 5 kpc ($\sim 0.7''$, deconvolved for the

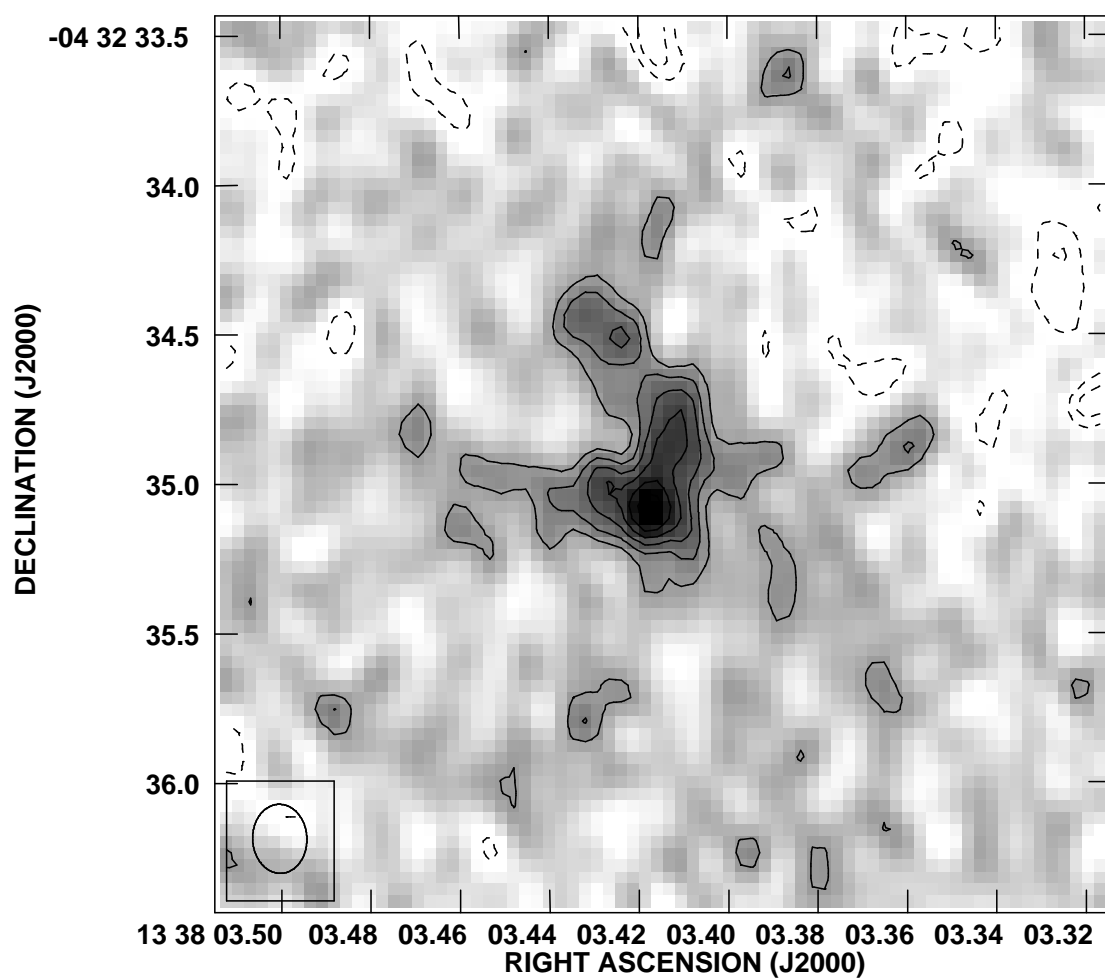


Figure 11.1: VLA map of the CO($J=2\rightarrow 1$) emission toward BRI1335–0417 (integrated over the central 43.75 MHz, or 308 km s^{-1}), imaged using the combined B and C array dataset and natural weighting. Contours are shown at $(-3, -2, 2, 3, 4, 5, 6, 7)\times\sigma$ ($1\sigma = 50\ \mu\text{Jy beam}^{-1}$). The beam size ($0.23''\times 0.18''$) is shown in the bottom left corner.

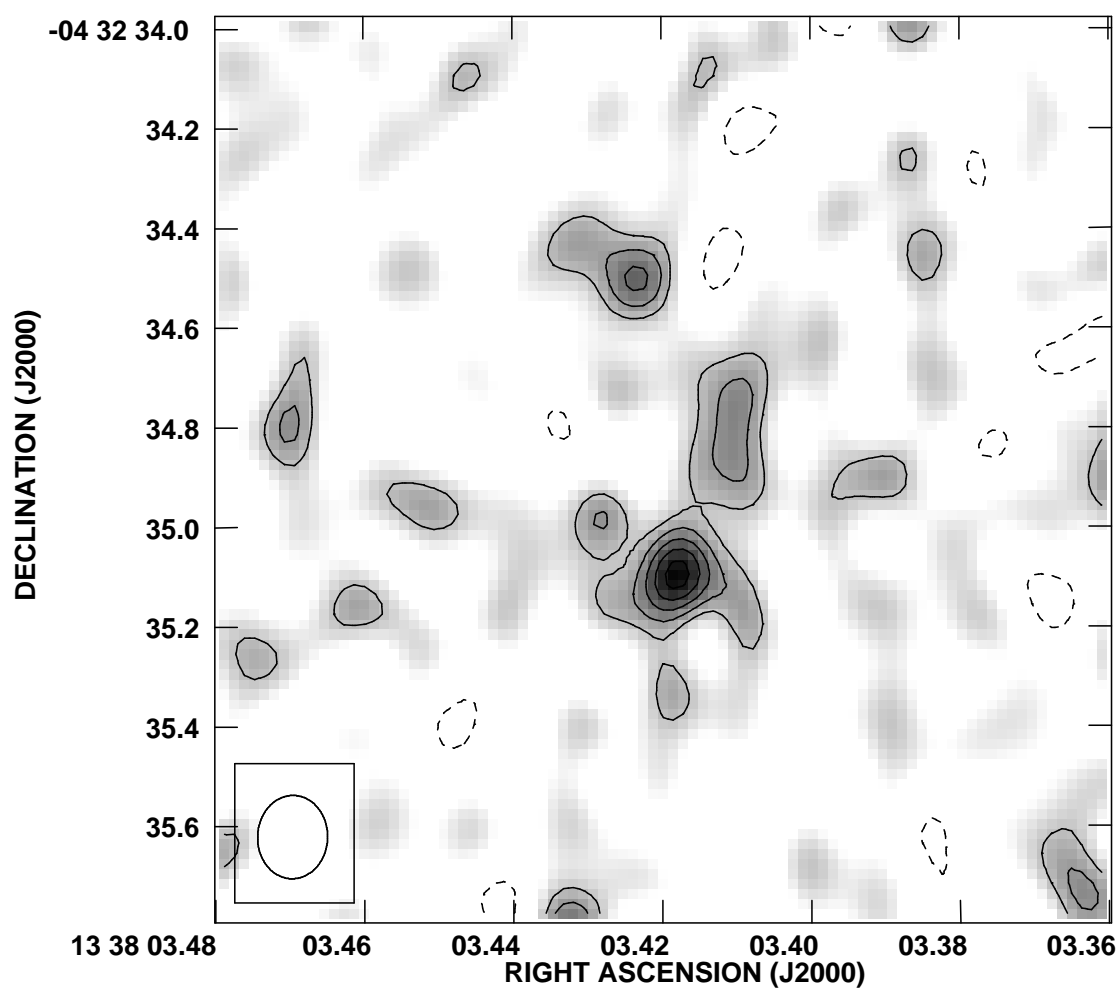


Figure 11.2: CO($J=2\rightarrow 1$) emission line map of BRI 1335–0417 at ~ 1 kpc resolution, imaged using B array data only and robust 0 weighting (zoomed-in version of Figure 11.1). Contours are shown at $(-3, -2, 2, 3, 4, 5, 6)\times\sigma$ ($1\sigma = 58\mu\text{Jy beam}^{-1}$). The beam size ($0.16''\times 0.14''$) is shown in the bottom left corner.

beam size). Two distinct peaks of the emission are identified, both of which are extended, and embedded in a continuous molecular structure. The northern component has a peak flux density of $216 \pm 50 \mu\text{Jy beam}^{-1}$, and the southern component has a peak flux density of $388 \pm 50 \mu\text{Jy beam}^{-1}$. In Figure 11.2, a zoomed-in version of this map at 1.0 kpc ($0.15''$) linear resolution is shown. At this resolution, some of the more diffuse structure is resolved out. Clearly, the southern component breaks up. One of the subcomponents extends toward the northern peak, consistent with the extension of the southern component in Figure 11.1. A third, small peak is found at 3σ significance. In addition, it appears that the different spatial components are distributed in a complex way. Note that the emission is likely not enhanced or distorted by gravitational magnification. In the higher resolution map, the northern component has a peak flux density of $246 \pm 58 \mu\text{Jy beam}^{-1}$, and the southern component has a peak flux density of $375 \pm 58 \mu\text{Jy beam}^{-1}$. The connecting component has a peak flux density of $202 \pm 58 \mu\text{Jy beam}^{-1}$. These three peaks alone encompass a molecular gas mass² of $M(\text{H}_2) = 4.1 \times 10^{10} M_\odot$, corresponding to about two thirds of the mass of $M(\text{H}_2) = 6.6 \times 10^{10} M_\odot$ derived from the integrated emission seen in the naturally weighted dataset ($I_{\text{CO}(2-1)} = 0.43 \pm 0.02 \text{ Jy km s}^{-1}$, in agreement with previous results by Carilli et al. 2002b). Accounting for the flux in the linewings that is not covered by our observations, the full reservoir has an estimated mass of $M_{\text{tot}}(\text{H}_2) = 9.2 \times 10^{10} M_\odot$. At $z=4.4074$, the brightest peak in the highest resolution map corresponds to a beam-averaged, rest-frame brightness temperature of $T_b=60 \text{ K}$. The average for the full $\text{CO}(J=2 \rightarrow 1)$ reservoir is $T_b=10 \text{ K}$, which sets a lower limit to the temperature of the molecular gas. Note that the minimum excitation temperature of $\text{CO}(J=2 \rightarrow 1)$ is $T_{\text{ex}}=16.6 \text{ K}$, which however is only 1.8 K above the cosmic microwave background (CMB) temperature at $z=4.41$.

11.5.2 Dynamical Structure of the CO Distribution

In Figure 11.3, the $\text{CO}(J=2 \rightarrow 1)$ emission is shown in seven 44 km s^{-1} wide velocity channels, smoothed to a linear resolution of $\sim 2 \text{ kpc}$. The emission is clearly dynamically resolved and is moving, to first order, from north to south between the red and blue velocity channels (i.e., with increasing channel number). In addition, the center channel (#4) shows a bright, compact peak, which corresponds to a narrow velocity component. This peak is weighted down in the integrated line maps, and corresponds to the third small peak of the southern component in Figure 11.2. Figure 11.4 shows a composite color map of the velocity channel maps. The left panel includes all velocity channels, while the central channel (covering the range from -22 km s^{-1} to $+22 \text{ km s}^{-1}$) is excluded from the right panel. The emission is clearly moving from redshifted to blueshifted emission in the right panel. However, the emission in the (green) central channels do not mainly follow the north-south extension, but also show an east-west extension, indicating an additional, distinct velocity component in the system. The overall peak of the emission where all components overlap

²Assuming constant T_b between $\text{CO}(J=2 \rightarrow 1)$ and $\text{CO}(J=1 \rightarrow 0)$, and a ULIRG CO luminosity to H_2 mass conversion factor of $\alpha=0.8 M_\odot (\text{K km s}^{-1} \text{ pc}^2)^{-1}$ (Downes & Solomon 1998).

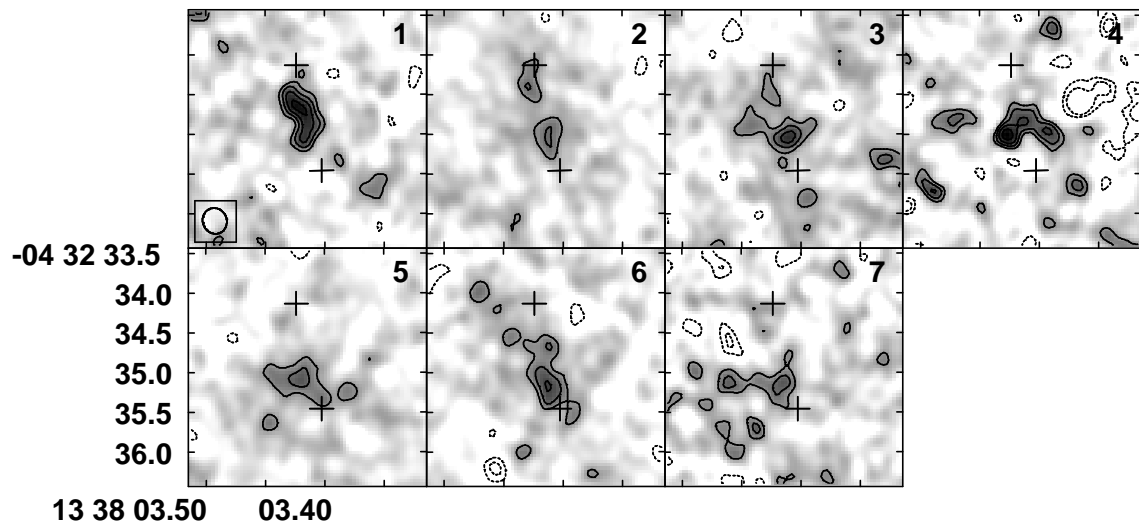


Figure 11.3: Channel maps of the CO($J=2\rightarrow 1$) emission in BRI 1335–0417. The same region is shown as in Figure 11.1. One channel width is 6.25 MHz, or 44 km s^{-1} (frequencies increase with channel number and are shown at 42615.050, 42621.300, 42627.550, 42633.800, 42640.050, 42646.300, and 42652.550 MHz). Contours are shown at $(-3, -2, 2, 3, 4, 5)\times\sigma$ ($1\sigma = 150 \mu\text{Jy beam}^{-1}$). The beam size (tapered to $0.32''\times 0.30''$) is shown in the bottom left corner; the crosses indicate the extent of the emission.

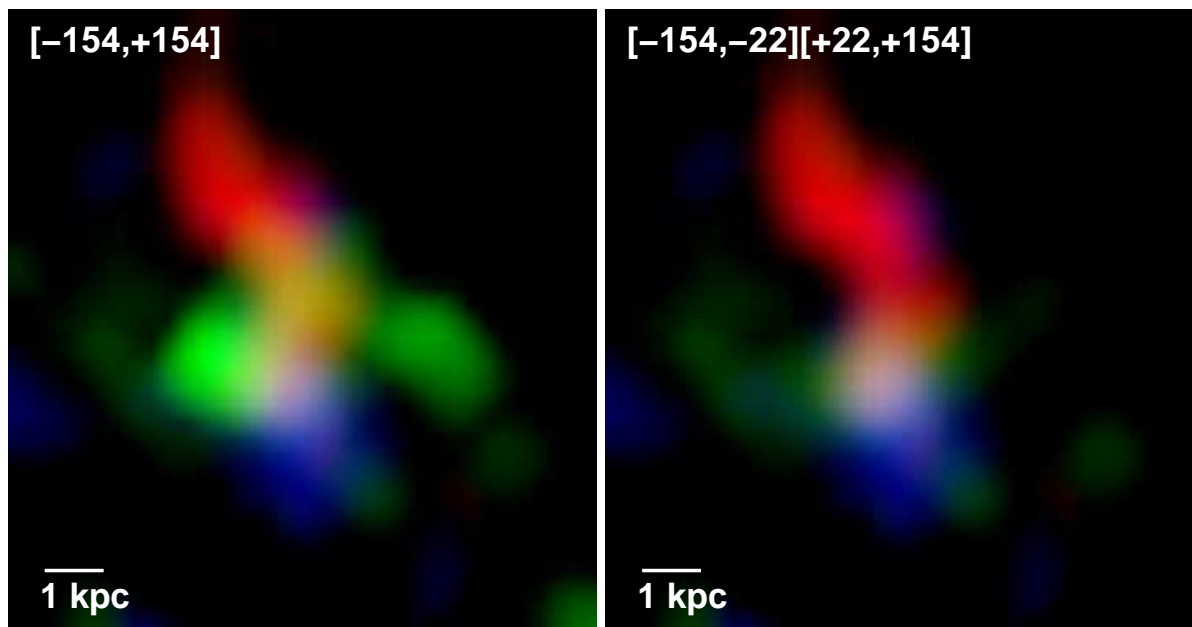


Figure 11.4: RGB composite color map representation of the CO($J=2\rightarrow 1$) velocity channels shown in Fig. 11.3, with three colors encoding the velocity range of the emission [red: redshifted (channels 1-2 in Figure 11.3), green: central (channels 3-5), blue: blueshifted (channels 6-7)]. The velocity range covered (relative to the line center) in km s^{-1} is indicated in the top left corner, and the linear scale is indicated in the bottom left corner of each panel. *Left*: All velocity channels (1-7). *Right*: All except the central channel (channel 4).

(seen as a ‘white spot’ in the figure) corresponds to the southern peak in the integrated line map. The velocity structure is thus more complex than that of a simple, inclined, rotating disk. The central, compact, narrow velocity component has a peak flux density of $853 \pm 150 \mu\text{Jy beam}^{-1}$, corresponding to a beam-averaged, rest-frame peak brightness temperature of $T_b=6\text{ K}$. It is likely that this component is associated with the optical quasar. However, the relative astrometry of the radio and optical observations (Storrie-Lombardi et al. 1996) is unfortunately not accurate enough to verify this assumption.

11.6 Discussion

We present maps of the molecular gas distribution in a quasar host galaxy at $z=4.4$ at 1.0 kpc spatial resolution. The VLA data show that the molecular gas reservoir in this galaxy is not only distributed over a scale of ~ 5 kpc, but also structured in velocity space. This is the first time that the molecular gas in a quasar host galaxy at such a high redshift (or, indeed, at any redshift greater than ~ 0) has ever been resolved both spatially and dynamically over multiple beams. The emission in BRI 1335–0417 is resolved into at least three distinct components harboring at least $1\text{--}2 \times 10^{10} M_\odot$ of molecular gas each, and at least another $2 \times 10^{10} M_\odot$ is found in the more diffuse molecular medium in between these concentrations. Each of the subcomponents hosts a few times the molecular gas mass of nearby ULIRGs such as Arp 220 (Downes & Solomon 1998). The total molecular gas mass and distribution are reminiscent of those in the $z=4.69$ and $z=6.42$ quasars BR 1202–0725 and SDSS J1148+5251 (Omont et al. 1996; Carilli et al. 2002b; Riechers et al. 2006a; Walter et al. 2004), albeit concentrated to much smaller scales than in BR 1202–0725, and showing much more detailed structure than both. Accounting for the temperature of the CMB, the CO($J=2\rightarrow 1$) emission traces a region where the gas has an average temperature of at least 29 K (depending on optical depth and beam dilution), which is comparable to the temperatures in nearby ULIRGs. From the FIR luminosity of the source ($L_{\text{FIR}}=3.1 \times 10^{13} L_\odot$), a star formation rate (SFR) of $4650 M_\odot \text{ yr}^{-1}$ can be derived (assuming standard conversions; Kennicutt 1998a, 1998b). This does not account for possible heating of the dust by the AGN. However, if the dust in this source has an extension and non-uniform distribution similar to that of the molecular gas, local heating (rather than heating of a central source) is likely to be responsible for most of the dust emission. Assuming as an upper limit that all of the gas is converted into stars, the SFR corresponds to a gas depletion timescale of only $2 \times 10^7 \text{ yr}$. This means that the starburst can only be maintained for a relatively short time, unless gas can be resupplied on timescales of $\sim 10^7 \text{ yr}$.

If the molecular gas in this system was gravitationally bound, the CO linewidth and distribution would predict a dynamical mass of $M_{\text{dyn}}=1.0 \times 10^{11} \sin^{-2} i M_\odot$, which could account for both the total molecular gas mass and the mass of the black hole of $M_{\text{BH}}=6 \times 10^9 M_\odot$ (Shields et al. 2006), but not for a substantial fraction of a $\sim 4 \times 10^{12} M_\odot$ stellar bulge as predicted by the local $M_{\text{BH}}\text{--}\sigma_v$ relation (Ferrarese & Merritt 2000; Gebhardt et al. 2000; unless the inclination toward the line-of-sight is very high, which would predict very large CO linewidths).

However, the overall structure of BRI 1335–0417 looks rather disturbed, both spatially and in its velocity structure. While the general north-south extension of the source may be in agreement with rotating structure, this is not true for the central part of the emission, in particular the compact peak seen in the central channel. This, and the structure seen in the high-resolution CO($J=2\rightarrow 1$) map (Figure 11.2), are more reminiscent of the disturbed gas reservoirs in major mergers, such as seen in the nearby Antennae (NGC 4038/39, e.g., Wilson et al. 2000). If BRI 1335–0417 was an interacting system, the northern component may be in the process of merging with the southern component, which likely hosts the luminous quasar. The connecting component then may be the part where the two galaxies overlap and merge. Note that this region alone would be massive enough to host more than 10 of the largest molecular complexes found in the overlap region of the Antennae (Wilson et al. 2000).

Cosmological simulations predict that the merger rates at $z=4.4$ are substantially higher than at $z=0$. Such scenarios imply that during the early epoch of hierarchical galaxy formation, some of the most massive galaxies form in major merger events (e.g., Springel et al. 2005). Such major, ‘wet’ mergers are believed to commonly trigger both AGN and starburst activity, and lead to high excitation of the molecular gas during both the hierarchical buildup of the host galaxy and the quasar phase (e.g., Narayanan et al. 2007). In simulations, such objects often show multiple CO emission peaks, arising from molecular gas concentrations that have not yet fully coalesced.

We conclude that the observed properties of BRI 1335–0417 (AGN and extreme starburst activity, high CO excitation, extended morphology over 5 kpc scales) are connected to the ongoing buildup of the quasar host galaxy. Such a signpost of early galaxy assembly then could be considered direct observational proof of the scenarios proposed by cosmological simulations, and enable us to directly investigate the connection between quasar activity and high-mass merger events at early cosmic times.

It is a pleasure to thank my collaborators on this project:

Fabian Walter (MPIA), Chris Carilli (NRAO), and Frank Bertoldi (AIfA).

CHAPTER TO BE PUBLISHED AS:

Riechers, D. A., Walter, F., Carilli, C. L., & Bertoldi, F, ‘*Formation of a Quasar Host Galaxy 1.4 Billion Years After the Big Bang*’, 2007, ApJL, to be submitted

Chapter 12

Summary and Outlook

12.1 Summary

The main goal of this thesis was to better understand the properties of star formation and galaxy assembly in the early universe, in particular quasars. One of the most important aspects in this field of research is to understand the properties of the molecular gas in the host galaxies of these high redshift systems, since it is the molecular gas that is directly connected with the processes leading to star formation. To achieve significant progress in this field, this research has placed emphasis on three main topics:

- How Massive are the Molecular Gas Reservoirs of Distant Quasars?
- What are the Composition and Excitation of the Molecular ISM in Distant Quasars?
- What is the Structure and Dynamical Mass of the Host Galaxies of Distant Quasars?

These topics were studied in the context of star formation, the connection to which was made by examining the respective connections between molecular gas mass and the star formation rate in galaxies from $z=0$ out to high redshift sources. In the following, the main results are briefly summarized, and it is shown how they contribute to our understanding of galaxies in the early universe in a more general context.

12.1.1 Masses of Molecular Gas Reservoirs in Distant Quasars

Observations of molecular gas are a key tool for studying the formation and evolution of galaxies in the early universe. Over the past decade, great progress has been made in this field, leading to the detection of CO emission towards 43 galaxies between redshifts of 1 and 6.4 (~ 15 of them being quasars), right back into the Epoch of Reionization (see Solomon & Vanden Bout 2005 for a review). Although it appears to be a very basic question, considerable diversity persists on the issue of how to extract molecular gas masses from measured CO fluxes in high- z galaxies. One of the main reasons is that observations of most of the $z > 2$ galaxies detected in CO to date have been done for $J > 3$ transitions (J denotes

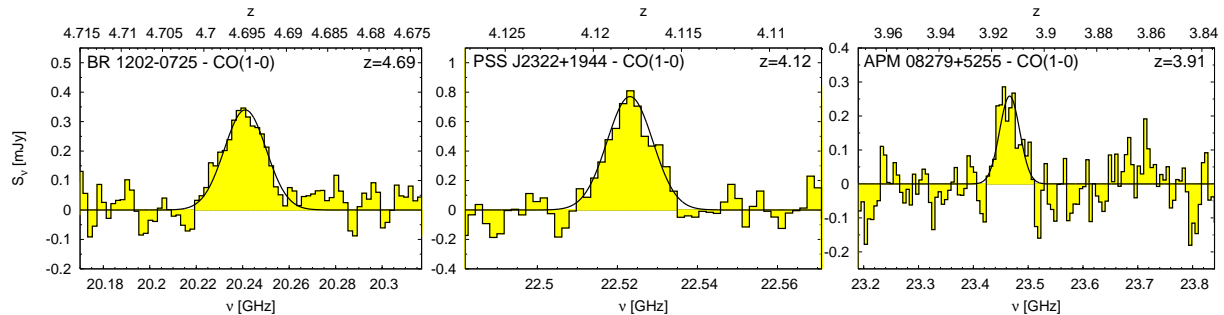


Figure 12.1: **CO($J=1\rightarrow 0$) Measurements — Mass Estimates.** Recent CO($J=1\rightarrow 0$) spectroscopy of three high- z QSOs obtained with the GBT and Effelsberg 100 m telescopes (Riechers et al. 2006a). These are the first high- z molecular gas detections ever obtained with 100 m radio telescopes, and the highest resolution CO($J=1\rightarrow 0$) spectra that have been taken for high- z galaxies. To date, they provide the best estimates for the total molecular gas masses of these quasars.

the upper rotational quantum number of the transition) due to technical limitations. Although these higher- J transitions exhibit higher peak flux densities than the ground-state ($J=1$) transition, it is possible that emission from these higher-order transitions is biased towards the more excited gas close to a central starburst. Therefore, these transitions do not necessarily trace the bulk of the molecular gas reservoir which can be seen in emission from the CO($J=1\rightarrow 0$) transition.

To further investigate this question, a project was started that capitalizes on the improved capabilities of the NRAO Green Bank Telescope (GBT) and the MPIfR Effelsberg telescope, both ~ 100 m in diameter, to search for CO($J=1\rightarrow 0$) emission towards three $z \geq 4$ QSOs ($\sim 20\%$ of all $z > 2$ quasar CO detections). After ~ 130 hours of observations in total, we detected emission from all three high- z quasars, being the first successful $z \geq 4$ molecular gas study with 100 m single dish radio telescopes (see Figure 12.1; Riechers et al. 2006a). In contrast to previous interferometer observations available for a small number of sources, we here obtain full CO line profiles due to significantly larger bandwidth and spectral resolution. These new detections thus pose a promising prelude for future broad-band high- z CO searches with the advent of the first ‘ z -Machines’ in the near future. Based on these full-profile spectra, the CO fluxes can be derived with good accuracy and result in typical molecular gas masses of $4 \times 10^{10} M_{\odot}$. Since the quasars in our sample have estimated star formation rates of several $1000 M_{\odot} \text{ yr}^{-1}$, the depletion timescale of these gas reservoirs is $10^7\text{--}10^8$ yr. Interestingly, the derived molecular gas masses are consistent with those derived from $J=4$ CO transitions, demonstrating that there are no massive extended, low-excitation CO reservoirs as, e.g., claimed previously for one of the sources in our sample (APM 08279+5255, Papadopoulos et al. 2001).

To further interpret our results, we carried out Large Velocity Gradient (LVG) models based on the higher- J CO transitions. These models provide estimates for a range of

physical properties of the molecular gas, such as the gas densities, temperatures, and overall excitation (all results: Riechers et al. 2006a). These more detailed models confirm that, indeed, the CO($J=1\rightarrow 0$) luminosities (and thus, total molecular gas masses) can be predicted very well based on higher J transitions in these distant quasars, due to the fact that the mid J ($J=3$ and $J=4$) transitions trace the same amount of material (in contrast to nearby spiral galaxies like the Milky Way).

Due to the fact that this holds for all sources in the sample, which represent $\sim 20\%$ of all CO-detected high- z quasars, this was taken as a basis to predict the full CO luminosities (and thus, total molecular gas masses), in all high- z quasars detected in CO emission. As most of the other CO-detected distant galaxies also show highly excited CO emission, this study was extended to other galaxy types. This provides, for the first time, a basis to extend the locally observed relation between total molecular gas mass and star formation rate (as derived from the FIR luminosity) to high redshift, which is important to understand if the conditions for star formation are different in the extreme systems at high redshift from local “normal” and star-forming galaxies. Due to the fact that the distant galaxies have higher CO and FIR luminosities, it also significantly extends the range over which this relation can be probed. The main results found based on the $L'_{\text{CO}}-L_{\text{FIR}}$ relation are that 1) the high redshift systems naturally extend the (nonlinear) local relation, indicating that there is no significant evolution in the efficiency at which molecular gas is transformed into stars, at least on a global level, 2) there is no change in the global trend at the highest luminosities, showing that there is no extraordinarily massive reservoir of molecular gas in the brightest systems, and 3) there is no significant difference between galaxies with and without a central AGN, indicating that AGN heating plays a minor role in powering the FIR luminosity on a global level, even for most of the quasars.

12.1.2 Composition of Molecular Gas Reservoirs in Distant Quasars

One important aspect in high- z molecular gas studies is the finding that CO is a good tracer for the total amount of molecular gas in a galaxy, but not a particular indicator for the dense molecular environments hosting the material that is more intimately associated with star formation itself. The most common molecular tracers of such star-forming *cores* in nearby galaxies are HCN, HCO⁺, and CS (see, e.g., Gao & Solomon 2004a, 2004b; Nguyen-Q-Rieu et al. 1992; Solomon et al. 1990), but also CN and HNC (Aalto et al. 2002).¹ These molecules have significantly higher dipole moments than CO, leading to higher critical densities. While the critical densities of the lower J transitions of CO are lower than the median density in most galaxies (causing them to trace the bulk of the molecular gas), those of the high density tracers are significantly higher than the median densities in most galaxies (causing them to trace only the high density tail of the mass distribution). It has been shown that studies of more than one molecular tracer help to significantly reduce

¹Note that this list of common molecular tracers is almost complete (except for rare isotopomers of the same molecules) rather than randomly selected from the list of ~ 50 known extragalactic tracer molecules (which are mostly exotic and/or complex, i.e., difficult to model and thus suboptimal probes of physical conditions).

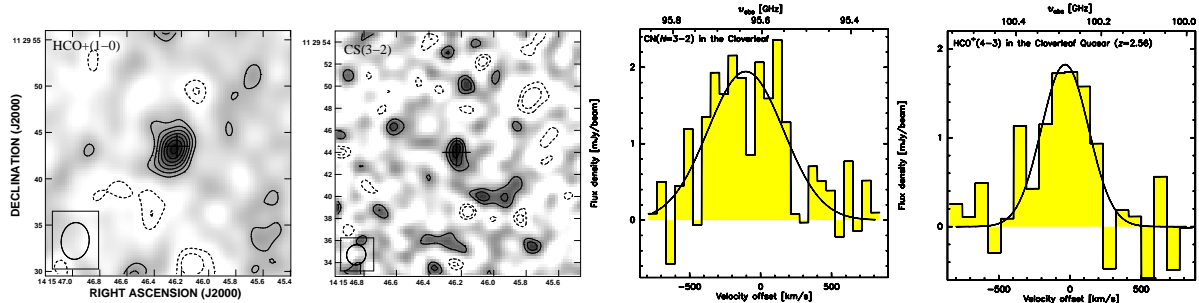


Figure 12.2: **Dense Molecular Gas Tracers at High Redshift.** First detections of $\text{HCO}^+(J=1\rightarrow 0)$ [left, Riechers et al. 2006b], $\text{CS}(J=3\rightarrow 2)$ [middle left, Riechers et al. 2008b, in prep.], $\text{CN}(N=3\rightarrow 2)$ [middle right, Riechers et al. 2007a], and $\text{HCO}^+(J=4\rightarrow 3)$ [right, Riechers et al. 2008a, in prep.] in the Cloverleaf ($z=2.56$), obtained with the VLA and the PdBI. This is the first time that emission from these molecules has been detected at high z , raising the total number of known molecules in the early universe from 2 (CO/HCN) to 5.

the degeneracy of LVG model solutions, which are essential to understand the physical properties (in particular excitation) of the molecular gas (see Weiß et al. 2007). This is mostly due to the fact that different molecules trace regions of different temperatures and densities, but also structure within the molecular ISM. One exception are HCN and HCO^+ , which are excited under similar conditions (due to similar dipole moments and fundamental line frequencies). This means that they are sensitive probes for properties such as abundance variations of N and O, and the relative strength of ionizing fields even with limited knowledge about the excitation conditions.

To better understand the medium and high density components of the molecular ISM in high- z quasar host galaxies, a molecular line survey with the VLA and PdBI was undertaken in the CO-brightest $z > 2$ QSO: the Cloverleaf. So far, this study has led to the detection of emission from three new molecules (compared to only two known at high z so far): HCO^+ (the first detection of a molecule at high z other than CO/HCN; Riechers et al. 2006b, 2008a, in prep.), CN (Riechers et al. 2007a), and CS (Riechers et al. 2008b, in prep., see Figure 12.2), all molecules with unique properties detected in a number of local starburst galaxies and (U)LIRGs (which serve as templates for interpretation). Due to the fact that only integrated emission line properties can be measured, the relations between molecular line luminosity [as a tracer of (in this case dense) molecular gas mass] and FIR luminosity (as a measure for the star formation rate) are used as a prime diagnostic to examine the properties of distant luminous quasars like the Cloverleaf. To first order, it follows all relations set by nearby normal, starburst and infrared (ultra)luminous galaxies, and extends them to high redshift and higher luminosity. This indicates that the molecular gas properties of nearby galaxies, in particular ULIRGs, can serve as good templates to model the extreme systems at high redshift. In contrast to the CO-FIR luminosity relation, the relations for HCN, HCO^+ , CS, and CN are linear (see Figure 12.3). If L_{FIR} is a

good tracer for the star formation rate, this means that the dense gas tracers are also a good indicator of star formation, even out to high redshift (in contrast to CO, which also traces more diffuse molecular gas that does not directly participate in star formation). To turn this argument around, dense gas is known to reside nested deep in molecular clouds, shielded from strong, external radiation. It thus is less likely to be biased by highly energetic radiation from an AGN than the mostly optically thin dust. In particular for distant quasars like the Cloverleaf, the linearity of a dense gas-FIR relation implies that AGN heating does not dominate the FIR emission, and that the FIR luminosity indeed is a good indicator for the SFR. Note that the $z=3.9$ quasar APM08279+5255 is known to be an exception from this, as modeling of the line excitation and continuum SED shows that the AGN radiation heats both the dust and molecular gas to a significant fraction (Weiss et al. 2007; Riechers et al. 2007c). In consequence, it is an outlier on relations between molecular line luminosity and FIR luminosity (Riechers et al. 2006a; Gao et al. 2007). The fact that we now have a range of dense gas tracers that all draw a common picture shows, for the first time, that the HCN-FIR diagnostic is not biased due to the fact that HCN favours certain conditions (contrary to the worries expressed, e.g., by Gracia-Carpio et al. 2006), but that indeed density is the key to understand the relation between molecular gas tracers and star formation [and thus star formation efficiency (SFE), the ratio of molecular gas mass and star formation rate] in a more universal picture. Following the initial results of this investigation, a model for these relations was put forward by Krumholz & Thompson (2007). This model suggests that, indeed, the the median density of the molecular gas in a galaxy is the essential parameter to understand the SFE in that galaxy. Interestingly, this model predicts that the SFE increases towards higher median galaxy densities. There is indeed an indication for such an increase in slope for the HCN-FIR relation toward the highest luminosities (i.e., the high redshift sources), which may indicate that the densities in these galaxies are higher. The statistical uncertainties in the relations for HCO^+ , CS, and CN are currently too high to be able to confirm this trend. However, LVG modeling of the different tracers will be able to address the question if the gas in the distant systems are indeed higher once excitation ladders are observed. First models based on the excitation of HCO^+ in the Cloverleaf, the only high- z galaxy and molecule currently available for such a study, appear to confirm this assumption (Riechers et al. 2008a, in prep.).

A second, in part more technical issue in the context of dense molecular gas studies is that transitions of thermally excited dense gas tracers are by at least an order of magnitude fainter than those of CO, which is already difficult to detect at high redshift. There is one theoretical possibility for line emission from less abundant, higher dipole moment molecules to be brighter than emission from CO: maser amplification. The most abundant molecule that has shown maser and mega-maser activity in the nearby universe is H_2O . Also, water has a transition ladder that can be observed in centimeter/millimeter atmospheric windows at high redshift. To follow up this idea, the redshifted 183 GHz fine structure line of para- H_2O towards the $z = 3.2$ QSO MG 0751+2716 was studied with the VLA (Riechers et al. 2006c). This source is the third brightest CO source detected at high redshift, and the brightest source that allowed observations of potentially high frequency masing water lines at high redshift with the VLA. Unfortunately, this pilot study has yielded no detection.

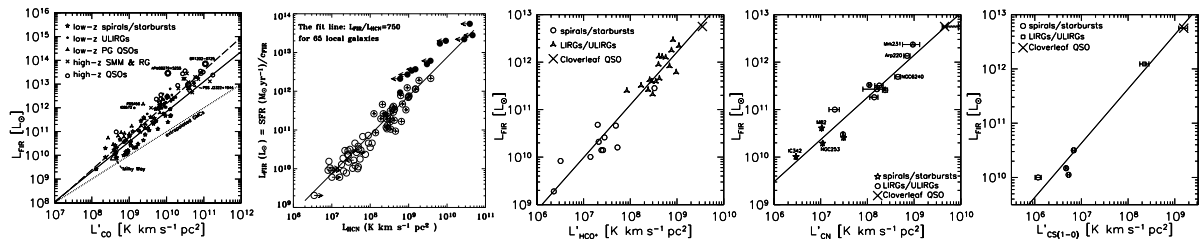


Figure 12.3: **Schmidt-Kennicutt Law for Different Molecular Tracers.** Relations between molecular line luminosity and FIR luminosity at low and high redshift for CO (Riechers et al. 2006a), HCN (Gao et al. 2007), HCO⁺ (Riechers et al. 2006b), CN (Riechers et al. 2007a), and CS (Riechers et al. 2008b, in prep.).

Based on a comparison to the nearby ULIRG Arp 220, the standard high redshift template galaxy for dust and molecular gas observations, it is most likely that there is no significant maser amplification, and that our non-detection means that the 183 GHz water line is only excited thermally.

12.1.3 Mapping the Molecular Gas in Distant Quasars

Perhaps the most exciting issue in the context of high redshift QSO studies is the prospect to resolve the host galaxies. One important aspect of such observations is to also obtain spectral information which allows us to actually dynamically resolve these systems, and therefore derive dynamical masses. Currently, the only means by which to do so is to study the molecular gas and dust content, since it can be observed at frequencies where the central AGN does not overshine the whole galaxy. It is therefore one of the key science drivers of the Atacama Large Millimeter Array (ALMA) to obtain such high resolution observations out to the highest redshifts (see ALMA Design Reference Science Plan [DRSP]). However, with the Very Large Array (VLA), it is possible to conduct such observations already today for the few known bright CO sources at the highest redshifts (and even more so with the upcoming EVLA). To explore this difficult but unique area of high- z observations, a large project with the VLA was initiated to study the CO emission of three of the CO-brightest quasars at $z > 3.5$ (i.e., half of all CO-detected quasars at $z > 3.5$ in 2005/2006²) at the maximum possible spatial resolution, i.e., 0.15''-0.3'', which corresponds to a maximum resolution of 1.0 kpc at $z=4$ for unlensed sources.

The three quasars in the sample are quite different, and demonstrate the richness of results that can be obtained from CO observations at high spatial and velocity resolution. The first source, APM08279+5255 ($z=3.91$), is a triply lensed source with a maximum image separation of 0.38'' (note that the brightest and the faintest image are partly blended, even in HST observations, Ibata et al. 1999). The optical/NIR images of this source are

²Two of the other sources were done as science demonstration; see Carilli et al. (2002b), and Figure 2.7; Walter et al. (2004), and Figure 1.6.

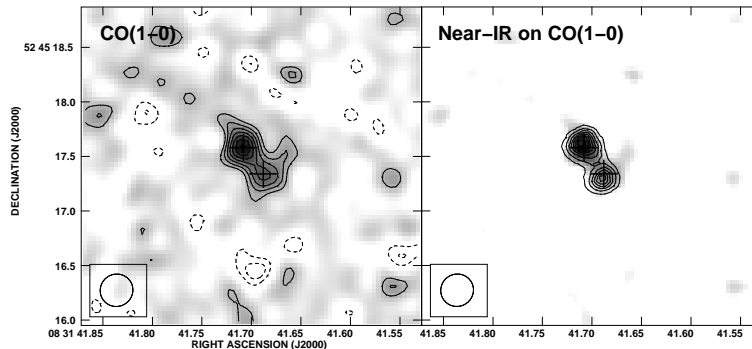


Figure 12.4: **High-resolution CO($J=1\rightarrow 0$) observations of the $z=3.91$ quasar APM 08279+5255.** *Left:* Integrated CO($J=1\rightarrow 0$) emission at a linear resolution of $0.3''$. *Right:* $2.2\ \mu\text{m}$ AGN continuum emission overlaid on the CO($J=1\rightarrow 0$) emission. Even though this source is strongly lensed, the CO emission is very compact (Riechers et al. 2007c).

pointlike, as expected for a quasar. At the source's redshift, $0.38''$ corresponds to only $2.7\ \text{kpc}$, which is a few times the size of typical circumnuclear rings in nearby ULIRGs (Downes & Solomon 1998). The CO($J=1\rightarrow 0$) observations of this source at $0.3''$ resolution presented in this thesis clearly resolve the lens images (Figure 12.4, left). They show that, despite the strong gravitational magnification of the molecular gas reservoir, the emission is very compact, and cospatial with the AGN continuum emission detected in the near-infrared (Figure 12.4, right; Egami et al. 2000). This finding disagrees with the claim of Papadopoulos et al. (2001) that the CO($J=1\rightarrow 0$) emission is extended on $30\ \text{kpc}$ (few arcsecond) scale, but is in explicit agreement with the CO($J=1\rightarrow 0$) flux derived from single-dish CO($J=1\rightarrow 0$) observations integrated over much larger scales (Riechers et al. 2006a, see Chapter 3), and observations of higher J CO transitions (Downes et al. 1999; Weiß et al. 2007). The new lens model based on the high resolution observations of this source confirms that the source is compact, and that all molecular gas resides in a region of $\sim 500\ \text{pc}$ radius. The dynamical mass derived from the width of the CO emission line and the size (and probable inclination) of the emitting region can account for the mass of the black hole and the molecular gas and dust in this system. It however is not large enough to account for a massive stellar bulge as predicted by the local $M_{\text{BH}}-\sigma_v$ relation, indicating that the buildup of the stellar bulge is still in progress, while the supermassive black hole appears to be largely in place. Combining the results of this study with those by Weiß et al. (2007) shows that the dust and gas heating and the radio continuum emission in this source are dominated by the AGN, and that the compact gas reservoir is unusually dense. This causes a high excitation of the molecular gas in this source. However, note that, due to the fact that both L_{FIR} and L_{radio} are boosted by the AGN, this source still follows the radio-FIR correlation of nearby star-forming galaxies.

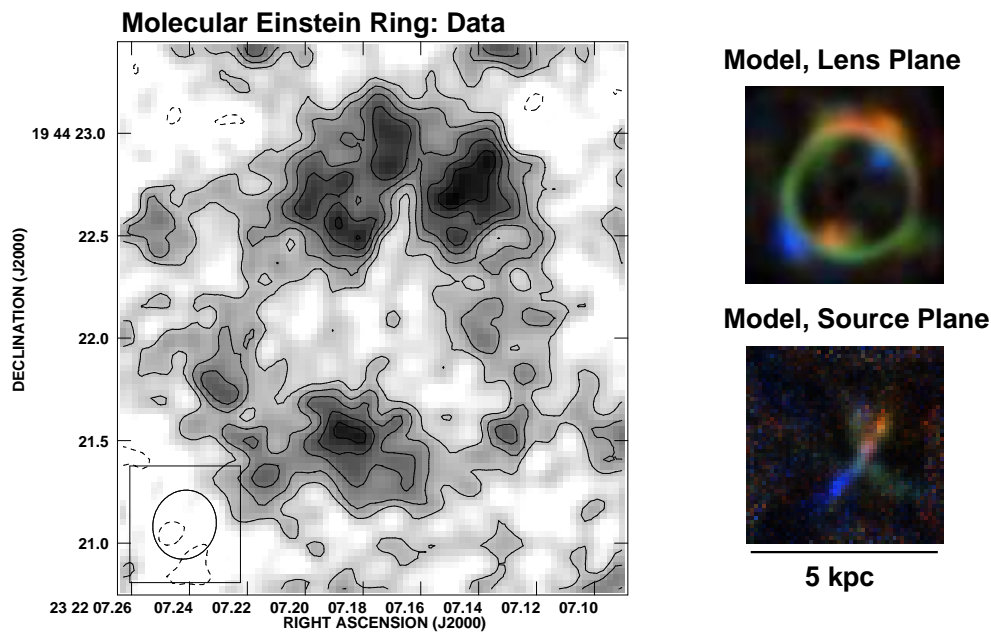


Figure 12.5: **High-resolution CO($J=2\rightarrow 1$) observations of the $z=4.12$ quasar PSS J2322+1944.** *Left:* Integrated CO($J=2\rightarrow 1$) emission at a linear resolution of $0.3''$. The molecular gas is lensed into a full Einstein ring, contrary to the optical emission, which only shows to pointlike images. *Right:* Lens model of the source based on the dynamical structure seen in the velocity channels. Orange corresponds to the red part of the emission line, green to the center, and blue to the blue part. The *top right* panel shows the reconstructed image in the lens plane, and the *bottom right* panel shows the image in the source plane after lens inversion. Apart from boosting the luminosity, lensing helps to zoom in on this source: the linear resolution in the reconstructed image is $0.09''$, or 650 pc at $z=4.12$ (Riechers et al. 2007d).

The second source, PSS J2322+1944 at $z=4.12$, is a double image optical quasar with an image separation of $\sim 1.5''$ (Djorgovski 2007, private communication). The VLA CO($J=2\rightarrow 1$) observations of this source at $0.3''$ resolution show clear evidence for differential lensing, as the molecular gas is lensed into a full, almost perfectly circular Einstein ring (Figure 12.5, left). Due to the fact that the velocity channels show dynamical structure, this system can be modeled dynamically. In Figure 12.5, top right, the model-reconstructed image of the Einstein ring in the lens plane is shown. The velocity structure is encoded in the color scale, showing a clear gradient. In Figure 12.5, bottom right, a reconstructed image of the source after lens inversion is shown. The source shows dynamical structure on 3 kpc scale at a linear resolution of 650 pc ($0.09''$, aided by the magnifying effect of the lens). If this structure is gravitationally bound, it encompasses a dynamical mass of $2.6 \times 10^{10} \sin^{-2} i M_{\odot}$. This is larger than the total molecular gas mass derived from the CO luminosity ($1.7 \times 10^{10} M_{\odot}$). However, if the system were to be seen close to edge-on, the molecular gas alone could account for most of the dynamical mass. This estimate would be different if either a) the structure is not gravitationally bound, b) the system is seen almost face-on, or c) the CO luminosity to H₂ mass conversion factor in this system is largely different from nearby ULIRGs. This may be substantiated by the facts that a) the reconstructed source seen in CO($J=2\rightarrow 1$) shows some tidal structure, possibly a sign of interaction, b) the optical quasar appears to be almost unobscured, and c) the mass conversion factor is largely different in APM 08279+5255 (Weiß et al. 2007), one of the few distant systems where this could be determined with some degree of certainty. However, if indeed most of the mass is in the form of molecular gas (with minor contributions from dust and the central black hole), there is not much room for a massive stellar bulge as predicted by the local $M_{\text{BH}}-\sigma_v$ relation.

The third source, BRI 1335-0417 at $z=4.41$, is a quasar that shows a single point source in the optical. There is no sign of gravitational lensing in this galaxy. Within the context of this study, the CO($J=2\rightarrow 1$) emission line could be imaged at $0.15''$ linear resolution, corresponding to 1.0 kpc at the source's redshift (Figure 12.6). Like PSS J2322+1944, it clearly shows dynamical structure in the velocity channels. Together with the lensed PSS J2322+1944, this is the first time that the molecular gas in a quasar host galaxy at such a high redshift (or, indeed, at any redshift greater than ~ 0) has ever been clearly resolved both spatially and dynamically, enabling us to constrain the physical properties of this system to unprecedented detail (and to sneak peek into the ALMA era). Unlike the other two sources, the structure is not influenced by gravitational lensing, and thus, can be interpreted directly. The CO($J=2\rightarrow 1$) emission in this $z=4.4$ quasar host galaxy is clearly spatially resolved over many beams and shows a complex, disturbed structure. Also, the emission is clearly dynamically resolved and shows that the CO emission is moving (to first order) from north to south between the red and blue velocity channels. It however is obvious that the velocity structure is more complex than for a rotating disk. Also, the overall structure looks rather disturbed, reminiscent of the molecular gas distribution in nearby mergers (e.g., NGC 4038/39, the Antennae). The bright peak in the third channel is clearly offset from the peak of the integrated emission line map and represents a distinct peak, probably associated with the quasar. The observations thus

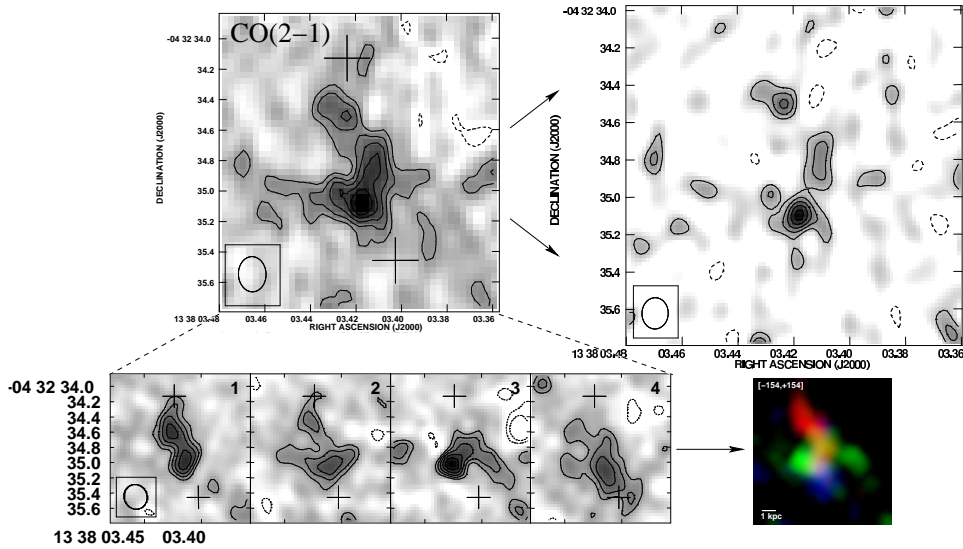


Figure 12.6: **High-resolution CO($J=2\rightarrow 1$) observations of the $z=4.41$ quasar BRI 1335-0417.** *Top:* Integrated CO($J=2\rightarrow 1$) emission at a linear resolution of $0.2''$ (*left*), and $0.15''$ (*right*, corresponding to 1.0 kpc). The emission is not lensed, but clearly resolved, and breaks up into several parts at the highest resolution. *Bottom:* Velocity channels of the emission (*left*), and three colour overlay at higher velocity resolution (*right*). Red/green/blue correspond to the red/central/blue parts of the emission line. The molecular line emission is clearly dynamically resolved and shows a disturbed structure, reminiscent of nearby major mergers (Riechers et al. 2007e).

show massive amounts ($7 \times 10^{10} M_{\odot}$) of molecular gas in the distant quasar host of BRI 1335-0417 ($z=4.41$), which shows a clearly disturbed structure (both spatially and dynamically), and is reminiscent of a major ‘wet’ (gas-rich) merger. It is thus highly likely that we witness the assembly of a $z=4.4$ quasar host galaxy, providing direct evidence for the scenarios predicted by state-of-the-art cosmological simulations. Such scenarios imply that during the early epoch of hierarchical galaxy formation, some of the most massive galaxies form in major merger events. Such major, ‘wet’ mergers are believed to commonly trigger both AGN and starburst activity, in agreement with the huge far-infrared luminosity of $3 \times 10^{13} L_{\odot}$, which is powered by star formation at a rate of $4500 M_{\odot} \text{ yr}^{-1}$, and the detection of an optical quasar in BRI1335-0417.

The study of these three sources has shown that molecular gas observations of some of the highest redshift galaxies at 1 kpc resolution are possible already today, and even allow to resolve the emission in velocity space. Gravitational lensing sometimes helps to zoom-in even further on the emission, however, a good model for the lens configuration is required to derive the intrinsic properties of lensed sources with any reliability. The ultimate goal is to use such observations to determine dynamical masses. It was possible to determine a dynamical mass from the molecular gas observations for the three systems in this study (two of the galaxies show evidence for interaction, i.e., the molecular gas is not fully gravitationally bound). In all cases, the dynamical mass is of the same order as the sum of the molecular gas mass and the black hole mass. This means that no massive stellar bulge or massive dark matter component is required to explain the dynamical mass found in the central regions of these galaxies.

The observations shown here probe the high mass end of the highest redshift galaxies, and enable us to directly investigate the connection between quasar activity and high-mass merger events at early cosmic times. This signpost of early galaxy assembly is important observational proof for the cosmological scenarios that have been suggested over the past few years (e.g., Springel et al. 2005b). These observations have only now become possible with the recent improvement of the VLA, and are a vital foundation for molecular gas observations with ALMA in the coming decade.

12.2 Outlook

12.2.1 Molecular Gas Masses at High Redshift

In a three sentence summary, this study has shown that the CO excitation in high z quasars is high, and that the bulk of the molecular gas in these systems is highly excited (as opposed to “normal” nearby galaxies, where this only applies to the star-forming cores). This can be explained with dust and gas heating by star formation (rather than the AGN), as the distant quasars on average fulfill the same relation between total molecular gas mass (as predicted by the CO luminosity) and star formation rate (as predicted by FIR luminosity) as nearby galaxies with and without AGNs, as do other high redshift sources with extrapolated CO($J=1\rightarrow 0$) luminosities within the uncertainties. This also suggests that the overall properties of star formation do not change with redshift, even if the efficiency with which molecular gas is transformed into stars appears to increase with luminosity (an explanation follows in the next section).

Given the main results of our study, the question occurs what to do as a next step. To first order, it seems as if the CO($J=1\rightarrow 0$) observations presented here provide a valuable test for a number of standard assumptions that have not been confirmed previously, but are confirmed by our study. Clearly, it would be interesting to extend the sample size to more sources (selected out of the existing sample with molecular gas detections). It would be interesting to confirm our results for other types of galaxies, in particular the submillimeter galaxies (SMGs). The $z=2.52$ SMG SMM J16359+6612 is the galaxy with the lowest CO excitation of all galaxies where such studies were done (Weiß et al. 2005a, 2007, 2008, in prep.), i.e., even the mid J CO transitions are subthermally excited. If it turns out that for this and similar sources, the CO($J=1\rightarrow 0$) luminosity is still predicted correctly by the LVG models based on the higher J transitions (meaning that they also do not contain a cold, massive, low excitation molecular gas component such as found in the Milky Way), it will provide the final necessary piece of information to evaluate if the general picture drawn above is correct. If so, this would mean that gas masses can be predicted correctly from higher J CO transitions, and that the $L'_{\text{CO}}-L_{\text{FIR}}$ relation can be applied in a general fashion.

The next greater step then would be to do “blind” CO($J=1\rightarrow 0$) searches, meaning without prior knowledge of the precise CO redshift from higher J transitions (note that redshifts from optical/IR emission lines may be offset from the systemic redshift where the CO is found - this is the main limitation for present day CO searches, as the bandwidth of radio and millimeter telescopes is very narrow). This is a significant step, as all CO-detected high redshift galaxies were initially detected in a mid or high J CO transition. This means that these studies are systematically biased towards sources where the CO is highly excited. They thus would miss galaxies where the whole CO reservoir has a low excitation (such as in normal spiral galaxies). Direct searches for CO($J=1\rightarrow 0$) emission thus have the potential to discover new, previously unknown populations of high redshift galaxies. Also, if such a search can be done without previously known optical redshifts, it will become possible to study other, potentially optically faint populations, such as extremely dusty

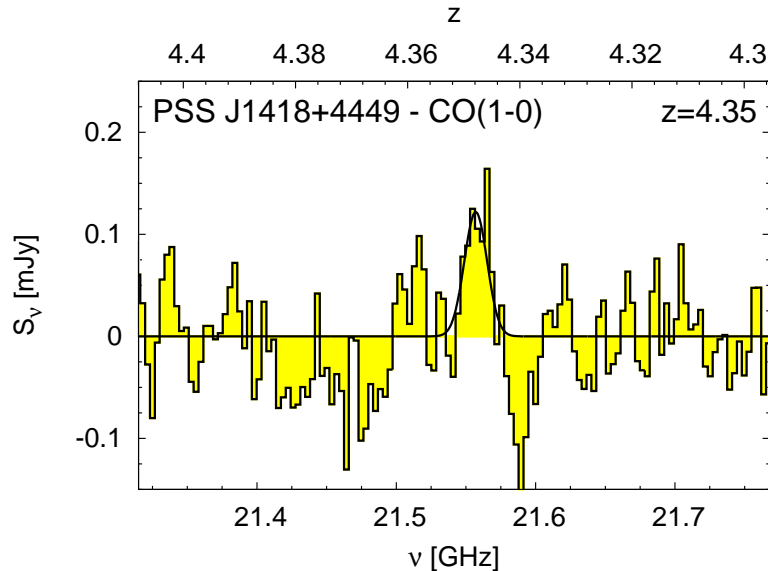


Figure 12.7: A search for CO($J=1\rightarrow 0$) line emission in PSS J1418+4449 ($z=4.35$), a dust-rich quasar. This spectrum corresponds to 30 hr of observations on source with the GBT. Due to the remaining uncertainties (in particular the systemic redshift relative to the optical emission lines), it is unclear whether or not the line is detected at the present signal-to-noise.

starbursting galaxies that are too obscured to produce bright UV emission, but are still bright in the millimeter cooling lines of the molecular ISM.

The main question that occurs now is, are the observations outlined above possible, and, if not, when will they be possible? Although a number of groups have tried to use the GBT for the past five years, our high resolution, high signal-to-noise CO($J=1\rightarrow 0$) spectra are still the only ones reported for quasars in the literature (Hainline et al. 2006 reported a fourth detection in a submillimeter galaxy). This is mainly due to the fact that these sensitive studies are on the edge of what is possible with single-dish telescopes, and thus are very dependent on excellent weather conditions that maximize the performance of the instruments, and on high receiver (i.e., spectral baseline) stability. In addition, until very recently, radio observing windows only covered very few (i.e., five) quasars (and few other galaxies) with known CO redshifts. The new K_a band receiver at the GBT covers a much larger fraction of the redshift range (in particular the valuable $2 < z < 3$ range, covering the peak epoch of star formation and quasar activity), which promises a remedy for the latter issue, but will be limited by the same technical problems as previous studies. Note that we looked at the brightest examples of high- z CO-detected galaxies that were available, but still had to obtain very long integrations per source, taken under optimal weather conditions.

This implicitly addresses the question about “blind” CO($J=1\rightarrow 0$) searches. In complement to the observations of CO-detected quasars, we also have executed such a search

in some of the most dust-rich quasars that were not detected in CO emission so far. Figure 12.7 shows the results for one such source, PSS J1418+4449 at $z=4.35$ (optical redshift: $z=4.32$). This spectrum corresponds to about 30 hr observations on source under good weather conditions, after preselection of the best scans. This is comparable to (and even on the higher end of) the time spent on the sources with known CO redshifts that we detected. Note that the peak of the CO($J=1\rightarrow 0$) line candidate is by a factor of two weaker than the weakest of our detected sources (which already would have been difficult to clearly identify without previously known redshift). Despite the significant integration time that went into the spectrum, the quality of the spectral baseline (defined zero level of the spectral channels) and signal-to-noise are not sufficient to claim a detection. This shows how hard-pushed such searches are - note that most of the sources that are observed today are by an order of magnitude or more fainter than the galaxies that were detected at $z>2$ early on. Future “z-Machines”, i.e., wide-band spectrometers for “blind” CO searches, such as the Zpectrometer for the GBT (see Baker et al. 2005), are being built to circumvent the main problem of today’s high- z CO searches (apart from the emission lines being very faint): the lack of bandwidth to detect CO based on optical redshifts alone (except for the fraction of the sources where the offset is very small) without “stepping” through the redshift space. However, such instruments will suffer from the same limitations as stated above, as they will be connected to the same single-dish telescopes that are in use today. In addition, these instruments will have less spectral resolution than the current receivers, rendering line identification even more difficult. Without additional advancement in radio receiver technology, studies of highly redshifted molecular lines with single-dish radio telescopes thus will remain difficult.

If this is the case, the next question that comes to mind is whether this can be done more efficiently with next generation interferometers. Clearly, the greatly improved sensitivity of ALMA will cause a revolution in this field, as it will enable us to probe much further down the luminosity function, i.e., to not only detect the extreme starbursts at high redshift in molecular gas and FIR dust emission, but also more normal (L_* -ish) galaxies. This will beyond doubt improve our picture of the star formation history of the universe in a more general fashion, not only at its high mass end. It will also enable us to probe further out, and detect extreme starbursts out to $z\geq 10$ (and beyond), both in dust and molecular gas emission. ALMA will be able to obtain source counts of distant galaxies per field of view similar to the deepest optical surveys of today. While the multiple bands of ALMA will then enable to obtain continuum-based “photometric” redshifts, the bandwidth of 8-16 GHz still only provides a few per cent in $\Delta z/z$ for high redshift CO searches in the standard observing bands. Also, due to the fact that ALMA is a millimeter to submillimeter facility, ALMA will only be able to observe high J CO transitions (and atomic lines such as C II, N II, and O I) at high redshift, and thus still be limited by the excitation bias of today’s CO searches (even more so at $z>7$, where only CO lines can be observed that are not highly excited even in the most extreme starbursts).

However, ALMA is not the only new long wavelength interferometer of the next decade. The currently ongoing upgrade of the VLA to the EVLA will be completed by 2013, about the time when the full ALMA becomes operational. The EVLA will not be as sensitive

as ALMA, but, in a sense, still be its lower³ frequency counterpart⁴, long before the SKA will be available at the lower frequency end. The EVLA will also offer a bandwidth of 8 GHz, which not only largely increases the continuum sensitivity of the array relative to the VLA, but also offers a $\Delta z/z$ of 40-50% at $z=4-5$ in the 1.3 cm band, paired with a larger field of view compared to ALMA. Also, if the receivers below the 1.3 cm band will increase in sensitivity as estimated, the EVLA will be able to observe CO($J=1\rightarrow 0$) at any redshift where gas-rich galaxies are believed to exist. In addition, the bandwidth of the EVLA will be sufficient to pick up different isotopomers of a molecule (e.g., ^{12}CO , the main isotopomer, and ^{13}CO), which are usually relatively close in frequency, within one setup (if sufficiently bright). Although isotopomers different from the main species are usually faint due to their low abundance, the fact that they are usually optically thin makes them a good tracer of mass. This is important to reduce the uncertainty in α , the conversion factor between molecular mass and line luminosity, which is currently only estimated well at $z=0$.

While ALMA will clearly revolutionize the field of high redshift molecular gas observations, the particular field of determining molecular gas masses at high redshift, and de-biasing these studies from molecular line excitation, will most likely be revolutionized by the EVLA.

12.2.2 Molecular Tracers of Star Formation at High Redshift

In a three sentence summary, this study of dense molecular gas at high redshift has more than doubled the number of molecules known in the distant universe, which has proven to be a key to understand the relation between molecular gas and star formation rate in high redshift galaxies in much more detail than possible before. In connection with the work by Gao et al. (2007) and a theoretical investigation by Krumholz & Thompson (2007), this has shown that dense molecular gas tracers such as HCN, HCO⁺, CS, and CN are good, (within the framework of these studies) unbiased probes for the star formation rate and the efficiency of transforming molecular gas into stars. This is an important foundation for future investigations of molecular excitation, which depends on the assumption that nearby galaxies, in particular ULIRGs, can serve as templates for extremely luminous high- z quasars, where both AGN and starbursts determine the properties of the molecular ISM.

Clearly, the detailed study of the molecular ISM in the one high redshift galaxy presented here can only be understood as a pilot study. Like all studies within the framework of this thesis, this pilot study was aimed at providing a foundation for selecting and interpreting observations of distant galaxies with future facilities, in particular ALMA. Due to the greatly improved sensitivity and bandwidth that ALMA will offer, many molecular transitions can be observed with one setup, and it is important to create a basis for

³Low frequency here means the regime between 1.3 cm and 7 mm, which is still considered high frequency in traditional radio astronomy.

⁴In addition, upgraded versions of CARMA and the PdBI will cover the part of the sky that is inaccessible to ALMA.

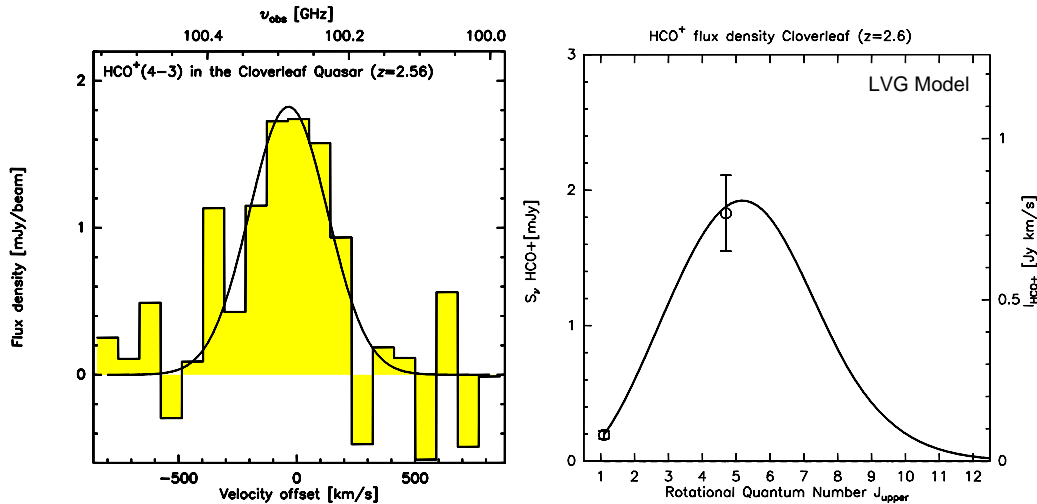


Figure 12.8: **HCO⁺ Excitation in the Cloverleaf.** *Left:* Detection of HCO⁺ ($J=4 \rightarrow 3$) in the Cloverleaf. *Right:* LVG model of the excitation of HCO⁺ in the Cloverleaf, based on the HCO⁺ ($J=1 \rightarrow 0$) and HCO⁺ ($J=4 \rightarrow 3$) transitions. The ground transition is almost thermalized, but all higher transitions are clearly subthermally excited. The model predicts $T_{\text{kin}}=50$ K and $n(\text{H}_2) = 10^{5.2} \text{ cm}^{-3}$. The filling factor of the dense clouds is 7.2% (Riechers et al. 2008a, in prep.).

interpretation of such studies as early as possible. This will give us a head start on designing future molecular line surveys in an efficient way, as we will know which probes are physically the most useful to look for in the distant universe.

Taking one step back, the question occurs what the immediate next steps will be. So far, studies of the different molecular tracers have shown that we can describe distant galaxies with the ISM physics that have been studied in detail in the local universe. There is a hint of changing properties in the HCN-FIR relation toward the distant systems (see Chapter 4, and references therein), which however can be described relatively straightforward by an increase in star formation efficiency due to a stronger concentration of the starbursts in a denser medium. This is particularly important, as it is a great unknown to which extent AGN in the powerful quasars at high redshift may influence the properties of the ISM. So far, the best answer is that it does not seem to be dominating any of the properties we can study, and if it dominates, the galaxy will stand out in basically all properties (Schmidt-Kennicutt relation, molecular line excitation, and thus the underlying fundamental properties) and has to be understood on an individual basis (e.g., APM08279+5255 at $z=3.9$, Weiß et al. 2007; Riechers et al. 2007c). It would be great to improve on the statistics of the relations for the dense gas tracers different from HCN (in particular obtaining more coherent, larger nearby galaxy samples - note that such studies are currently progressing, see, e.g., Gracia-Carpio et al. 2007); as, so far, nearby ULIRGs appear to be proper templates once one dense gas tracer is measured. Note that this is not due to the fact that the distant sources are always similar to ULIRGs. On the contrary,

there are a number of properties that are different in gas-rich galaxies close to and beyond the peak epochs of quasar activity. This is simply owed to the fact that we have only few diagnostics, which are constrained by relatively few galaxies even at $z=0$ (even for HCN, the second most commonly studied molecule in the universe). To better understand these differences, good databases of nearby galaxies are required.

The essential next step in the context of this study is to understand if, and to what extent, ULIRGs are good templates for the high- z systems is to study the excitation of CO, HCN, HCO⁺, CN, and CS, preferentially in the Cloverleaf (started in CO and HCO⁺, Weiß et al. 2008, in prep.; Riechers et al. 2008a, in prep., see Figure 12.8), and a few more sources. If radiative transfer models then still show that the environments are similar to ULIRGs, just denser (as indicated by the HCN-FIR luminosity relation, Gao et al. 2007; Riechers et al. 2007b), it may not be necessary to carry out expensive investigations to study a range of molecules in many distant systems in the near-term future, i.e., before the EVLA and ALMA are available. Even though the observations in the Cloverleaf project provide an important piece to the puzzle, it would then be the most effective to concentrate near-term studies of the excitation of CO and the one or two brightest dense gas tracers, most likely HCN and HCO⁺, in the distant universe.

These studies will then provide the basis to selecting targets for ALMA surveys, which will offer the necessary resolution, sensitivity, and source counts to enable detailed chemical modeling based on the understanding of the excitation conditions in today's studies. Note that ALMA will only be able to observe higher-order transitions of the most common dense gas tracers at high redshift. These transitions are likely to be subthermally excited, and thus faint relative to the lower order transitions. Here, again, the lower frequency coverage of the EVLA may prove to be of essence, even though the EVLA will most likely be limited to brighter galaxies than can be observed with ALMA (see, e.g., discussion on the upper HCN limit in the $z=6.42$ quasar J1148+5251 in Chapter 4).

12.2.3 Dynamical Properties of Distant Star-Forming Galaxies

In a three sentence summary, this study of molecular gas of some of the most distant, gas-rich quasars at high spatial and velocity resolution with the VLA has permitted, for the first time, to study the dynamical structure of $z>4$ galaxies down to resolutions of 1.0 kpc (and, with the aid of gravitational lensing, even higher resolution). The three sources in the sample show either compact, dense molecular gas reservoirs, reminiscent of but more extreme than circumnuclear rings in nearby ULIRGs, or extended, disturbed dynamical structure, reminiscent of nearby mergers, or even a combination of both. These systems thus became the prime laboratories to study the coevolution of supermassive black holes and extreme starbursts at early cosmic epochs, and are first observational proof for some of the scenarios that are suggested by recent cosmological simulations at early epochs.

Even though the study of molecular gas at 1 kpc resolution in the most distant galaxies is very time consuming, and currently only possible for a few, very bright sources, they are the key to understanding how early galaxies assemble, and how AGN properties in these systems relate to star formation (and thus, how they evolve). One particular aspect

of these studies is that they do not only constrain the properties of the ISM, but those of the galaxy as a whole (as they are able to predict dynamical masses of the systems). The results for PSS J2322+1944 and BRI 1335-0417 show enough detail to constrain dynamical radiative transfer models of quasar formation in the context of cosmological simulations (see Narayanan et al. 2007 for the first such study based on J1148+5251, one of the two objects that my group observed prior to this thesis work, see discussion above). Numerical simulations show that galaxy mergers are a viable precursor of quasar formation, and that the gas involved in such processes can both fuel nuclear starbursts and feed the growth of a quasar's central supermassive black hole. As the molecular ISM is central to these processes, direct, dynamical observations of molecular gas at high resolution and complementing excitation studies can severely constrain such simulations in a unique and essential way. It thus is important to aspire to improve simulations based on this new CO data. Due to the importance of such observations, they are one of the key science drivers for ALMA, which will be able to do this in more detail, and for many, also fainter galaxies. As mentioned several times before, ALMA observations will take place in higher J transitions of CO and thus may not pick up cold, diffuse molecular gas components. This is why, even in the age of ALMA, the VLA (or, more precisely, its successor/upgrade, the EVLA) will still play a central role in such investigations. Note however that ALMA is perfectly suited for high redshift studies of the main atomic cooling lines of the ISM (i.e., C II N II, and O I), which may offer important complementing information.

There are however a number of issues that can be addressed before both these facilities are fully operational. As described previously, one of the main general diagnostics in studies of dust and molecular gas at high redshifts is the Schmidt-Kennicutt relation, describing the efficiency at which molecular gas is formed into stars under certain physical conditions and at different redshifts. Due to the fact that we now have a number of $z > 4$ systems that are spatially resolved in molecular gas emission, one obvious question occurs: do the FIR dust emission and molecular line emission come from the same areas? As a particular question for AGN systems, is the FIR emission concentrated close to the AGN (indicating that it contributes significantly to the dust heating), or does it indeed mostly come from the more extended area where molecular gas is found, as indicated by the Schmidt-Kennicutt relations? Complementing FIR observations in the systems resolved in CO emission thus have the potential to eliminate (or at least constrain) one of the main biases in studies of star formation at high redshift. Since early 2007, such observations have become possible. Due to the receiver upgrade and the construction of longer baselines, the PdBI can now achieve up to $0.3''$ resolution at 1 mm, which corresponds to FIR wavelengths at $z > 4$. Also, CARMA has become operational, and will offer similar resolutions at 1 mm during the upcoming winter season. Studies of spatially resolved Schmidt-Kennicutt law at high redshift thus are possible now, well before the ALMA era. So one clearly important short-term goal is to use these facilities to complement the high-resolution CO studies with the VLA with high-resolution continuum studies using millimeter interferometers.

Another question that may come to mind is: The peak epoch of quasar activity and star formation is between $z=2$ and 3, so why are high resolution CO observations basically limited to $z > 4$? The selection criterium for the observations presented was basically limited

by the frequency coverage of the current VLA receivers. On a timescale of 2-4 years, a large fraction of the VLA antennas will be equipped with EVLA receivers that cover the frequency range between that of the current receivers, which will enable us to obtain CO observations at basically *any* redshift. Given that there are currently 43 galaxies at $z > 1$ detected in CO emission, of which most will be bright enough to be resolvable with the EVLA, this will open up a large discovery space. As shown above, all systems that were studied so far show clear differences. It thus will be very important to enlarge the sample size to be able to employ any kind of unification scheme to the variety of sources.

Recent studies have shown that such schemes are essential to properly classify the huge number of galaxy types that have been detected in the distant universe, and may significantly overlap. Note that galaxy “types” in the distant universe are commonly defined through the selection technique (e.g., optical brightness, mid-infrared brightness, submillimeter brightness, existence of a Lyman break, existence of Ly α emission, etc.). Consequently, systematic studies of single galaxies have often revealed an overlap between these types (e.g., many mid-infrared bright galaxies are submillimeter-bright, many submillimeter galaxies have AGN and thus are not pure starbursts, etc.). It thus is important to obtain physical quantities, such as the distribution, temperature, and density (and thus mass/abundance) of the gas and dust in such galaxies. If galaxies of different “types” show similar ISM properties, they may not be fundamentally different, even if some selective diagnostics classify them differently.

A simple description of future strategies in high resolution CO observations at high redshift thus may be: extend the sample from quasars to different kinds of galaxies, cover the full redshift range between $z=0$ and (currently) $z=7$, complement molecular gas observations with studies of the dust at comparable resolution, and wait for ALMA to study fainter populations.

12.2.4 A Bright Future for ISM Studies of Galaxies in the Early Universe

The previous sections summarize the results of this thesis, and outline the next steps in the different areas. Systematic future studies will thus imply a number of steps.

The main goal is to build galaxy type-dependent luminosity functions in molecular line and dust continuum emission, and to probe down these luminosity functions at high redshift to the level of normal galaxies instead of being limited to the brightest end. This is an essential ingredient to understanding the star formation history of the universe, in particular the role of the ISM in the complex processes leading to star formation. The properties of star formation in different kinds of galaxies and environments and at different redshifts can be directly tied to the properties and distribution of the ISM. These kind of studies are also essential to understand the connection between star formation and AGN activity/black hole assembly, as the gaseous ISM both fuels the starburst and feeds the ISM. In particular, they have the potential to trace feedback mechanisms, such as are currently proposed to be responsible for coevolution of both, leading to the present day

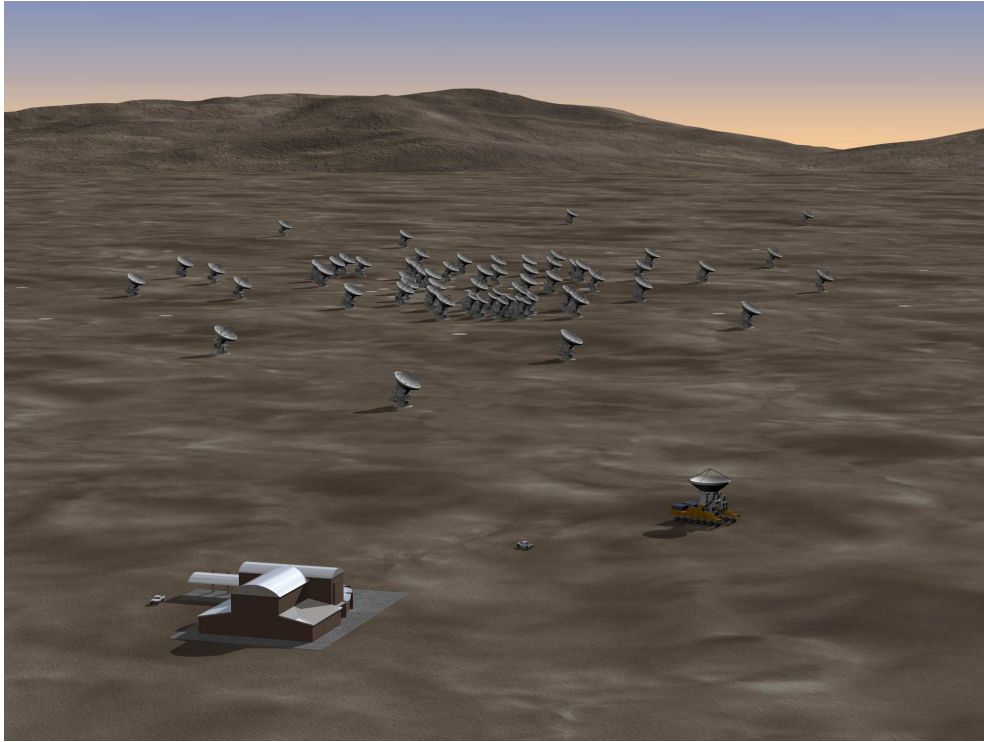


Figure 12.9: Computer-rendered image of ALMA and ACA. Image courtesy of NRAO/AUI, and Computer Graphics by ESO

relation between central black hole mass and bulge mass/velocity dispersion. The dynamics of molecular gas may also be a key to understanding how early galaxies assemble in more detail than possible so far. In particular, they are excellent probes to constrain the merger fractions at all redshifts, which will have important implications for cosmology.

Observationally, this ultimately means that we need to study the composition and distribution of molecular gas reservoirs in galaxies out to large distances. This implies studies of excitation-dependent morphology, revealing temperature, density, and abundance gradients throughout the galaxies. Such studies have to be carried out systematically, and have to be complemented by comprehensive studies of nearby galaxies in the same properties to be able to search for evolutionary traces (and chemical evolution).

The studies in the framework of this thesis aim at providing a basis for such studies. This analysis has shown that with currently existing data and models, some basic questions can already be addressed. However, studying these issues in great detail are long-term goals, that will require substantial amounts of observing time even with future facilities such as the EVLA and ALMA. To make these interferometric studies most efficient (note that interferometers are sensitive and offer excellent spatial resolution, but are hardly survey instruments due to their small field of view at high radio frequencies), samples need to be selected well and in a systematic way.

Flux-limited samples can be obtained in continuum surveys, both wide-field survey and deep, pointed studies. In contrast to most studies in the past, future far-infrared and sub-millimeter/millimeter cameras such as PACS and SPIRE on board Herschel, and LABOCA and SCUBA2 at APEX and the JCMT will have sensitivities and field-of-views to do this much more efficiently, and will reduce the dependence on optical surveys for target selection. Also, studies at multiple FIR to millimeter wavelengths (e.g., at 200, 350, 450, 650, 850, 1100, 1200, 2000, and 3000 μm , as possible with current and future bolometer arrays) will allow to obtain photometric redshifts, in particular for sources that are not detectable in the optical (although it will also be important to observe complete samples of optically or otherwise selected samples, such as a systematic study of the SDSS quasar sample over the whole redshift range). This is important for both obscured sources and galaxies at very high redshift (note that the negative K correction may hold for studies until $z=10$ and beyond, but obtaining optical/IR redshifts at such wavelengths is currently impossible, and will probably remain unfeasible until the launch of JWST). Such photometric redshifts can then be used to search for molecular line emission with wide-band receivers. Due to sensitivity, this will most likely be with ALMA and the EVLA (where the former has the better sensitivity, and the latter has the better $\Delta z/z$).

It also is important to remember that ALMA operates at wavelengths where only higher order transitions of the most common molecular tracers are accessible at high redshift. The “workhorse” bands of ALMA will be at 850 μm and 1 mm. This corresponds to CO($J=6\rightarrow 5$) and HCN($J=8\rightarrow 7$) and higher at $z>7$. CO($J=6\rightarrow 5$) will only be excited in extreme systems (note that the CO spectral line SED of the Milky Way peaks around CO($J=2\rightarrow 1$) and is only weakly excited above CO($J=4\rightarrow 3$)), and HCN($J=8\rightarrow 7$) only in very few galaxies even within the extreme sample (mostly due to its extreme critical density). The standard probe for star-forming regions with ALMA at the highest redshifts thus will likely be the 158 μm fine structure transition of [C II], the main cooling line of the neutral ISM. This implies that it is important to better understand the properties of this line in nearby galaxies, and how it relates to molecular line emission. HIFI on board Herschel will be the optimal instrument to do so (in addition to the FIR lines of N II and O I, which will also be good probes for ALMA, see Chapter 2). On longer timescales, the SKA will become available to largely improve studies at lower wavelengths (the standard radio bands for continuum studies at very high resolution and fields of view, but also the 22 GHz band important for high- z molecular line studies).

There clearly is a bright future for studies of the interstellar medium in the most distant galaxies. However, as studies such as presented in this thesis have shown, we do not have to wait for the next generation of instruments for all of it.

Appendix A

Existing Molecular Line Observations at High Redshift

Since the initial high redshift detection of CO in 1991, the number of sources steadily increased. Many of these galaxies have been studied in more than one CO transition, and some debated systems have been revisited several times. Also, attempts to resolve the CO emission have resulted in an increased number of publications. In addition, studies of molecules different from CO are showing the first results. This summary aims at providing a comprehensive overview over all existing studies as a context for the investigations in this thesis (which are included), and for general reference.

A.1 Inventory of Observations

This chapter provides an overview of all existing molecular gas observations at high redshift, including results from this thesis. Due to similar tracer capabilities, an overview of detected millimeter carbon lines is provided. All tables list the galaxy type and redshift, the telescope used for observations, and the main emission line properties, i.e., the integrated line flux and the width of the line. Sources are listed in order of redshift. Tables A.1, A.2, and A.3 summarize all published observations of carbon monoxide. The realm of CO detections is clearly dominated by the Plateau de Bure Interferometer. This is mostly due to its superior sensitivity and spectral baseline stability (which limits single-dish studies), and due to its greater bandwidth and coverage of CO redshifts relative to the VLA. Note however that the highest redshift CO detection at $z=6.42$ was initially obtained with the VLA. Also, only the VLA currently has the capability to resolve redshifted CO at $0.15''$ resolution, and thus currently is the prime instrument for high resolution studies. Table A.4 lists all detections of molecular tracers different from CO. Note that these galaxies are a subsample of the galaxies detected in CO. If the reported HNC line in APM08279+5255 (Guélin et al. 2007) can be confirmed by observations of an unblended transition, six molecules are currently known in the $z>1$ universe. Also, note that three out of the five detected galaxies in this sample were initially detected by the VLA, as were

three out of the six molecules (counting the $\text{HCN}(J=1\rightarrow 0)$ line in the Cloverleaf as the initial detection, see discussion below). Due to the fact that redshifts are initially known from CO, the limited bandwidth of the VLA is less of a concern for these studies, leading to a higher number of initial detections. Also, due to the higher dipole moments of the molecules in this table relative to CO, the higher order transitions that are redshifted into the millimeter observing windows are usually not highly excited. This eliminates one huge advantage that millimeter telescopes can exploit in CO studies. Still, the most transitions of molecules other than CO have been detected with the PdBI. Table A.5 gives a list of all detections of lines of atomic or singly ionized carbon. Note that, due to the relatively high frequency of the C II line, observations of C^+ are limited to the highest redshifts. However, due to the relative brightness of C II relative to CO, submillimeter telescopes with limited collecting areas like the SMA can also be successfully used for such studies (providing access to somewhat lower redshifts).

There are a few noteworthy cases of diversity in the given lists:

IRAS F10214+4724: This was the first high redshift galaxy to be detected in CO emission (Brown & Vanden Bout 1991). While the detection of the line was quickly confirmed by many different groups using different telescopes, the actual intensity of the line remained subject to debate for several years (Radford et al. 1996). The $\text{CO}(J=3\rightarrow 2)$ lines in F10214 thus is probably the one that has been observed most often among the high z sources. Note that a similar discussion revolved around the strength of the C I lines in this source (Brown & Vanden Bout 1992b; Weiß et al. 2005b).

The Cloverleaf: Barvainis et al. (1997) reported a detection of the $\text{HCN}(J=4\rightarrow 3)$ line in this source. Six years later, Solomon et al. (2003) reported a detection of the $\text{HCN}(J=1\rightarrow 0)$ line in the same source. However, they also reported a non-confirmation of the $\text{HCN}(J=4\rightarrow 3)$ line. Subsequent deep observations with the PdBI show an indication of the line at about one third of the initially reported peak strength (Guélin 2007, private communication). If confirmed, the strength of this line would be comparable to that of the $\text{HCO}^+(J=4\rightarrow 3)$ line (Riechers et al. 2008a, in prep.), in agreement with the $\text{HCN}(J=1\rightarrow 0)/\text{HCO}^+(J=1\rightarrow 0)$ line ratio (Solomon et al. 2003; Riechers et al. 2006b).

Table A.1: All $z > 1$ CO Detections in the Literature ($1.06 \leq z \leq 2.56$)

Source	type	z	transition	I_{CO} (Jy kms $^{-1}$)	line FWHM (kms $^{-1}$)	telescope	refs.
SMM J02396-0134	SMG _L	1.062 ± 0.002	2-1	3.4 ± 0.3	780 ± 60	PdBI	1
MIPS J1428+3526	SB _L	1.3250 ± 0.0002	2-1	5.3 ± 1.2	386 ± 64	NMA/R	2
		1.3247 ± 0.0002	3-2	13.9 ± 4.8	386 ± 104	NMA/R	2
Q0957+561	QSO _L	1.4141	2-1	2.0	160/500	PdBI	3
			2-1	1.2 ± 0.1	160 ± 20	PdBI	4
					280 ± 50		
HR10	ERO	1.439	1-0	0.6 ± 0.1		VLA	5
		1.439 ± 0.001	2-1	1.4 ± 0.1	400	PdBI	6
		1.440 ± 0.001	5-4	1.35 ± 0.3	380	PdBI	6
3C 318	QSO	1.571	2-1	1.19 ± 0.22	200	PdBI	7
SMM J123549+6215	SMG	2.202	3-2	1.6 ± 0.2	600 ± 50	PdBI	8
			6-5	2.3 ± 0.4		PdBI	8
IRAS F10214+4724	QSO _L	2.2867 ± 0.0003	3-2	21 ± 5	200	12m	9
		2.28560 ± 0.00003	3-2	10.4		30m	10
		2.2855 ± 0.0003	3-2	4.1 ± 0.9	230 ± 30	30m	11
			3-2	4.4 ± 0.7	150	45m	12
		2.2858 ± 0.0002	3-2	7.5 ± 2.0	200	NMA	13,14
			3-2	3.5 ± 0.5		PdBI	15
		2.2853 ± 0.0003	3-2	4.8 ± 0.7	250 ± 15	OVRO	16
		2.2854 ± 0.0001	3-2	4.2 ± 0.8	220 ± 30	PdBI	17
		2.2855 ± 0.001	3-2	6.7 ± 1.4	170 ± 30	12m	18
		2.28582 ± 0.00002	4-3	15.5		30m	10
		2.2857 ± 0.0003	6-5	9.4 ± 2.0	240 ± 30	30m	11
SMM J16371+4053	SMG	2.380 ± 0.004	3-2	1.0 ± 0.2	830 ± 130	PdBI	1
SMM J163650+4057	SMG	2.3853 ± 0.0014	3-2	2.3 ± 0.2	840 ± 110	PdBI	19
		2.385	3-2	2.3 ± 0.3	710 ± 50	PdBI	8
		2.383	7-6	1.1 ± 0.2		PdBI	19
			7-6	6.7 ± 0.7		PdBI	8
53W002	RG	2.394 ± 0.001	3-2	1.5 ± 0.3	540 ± 100	OVRO	20
		2.3927 ± 0.0003	3-2	1.20 ± 0.15	420 ± 40	PdBI	21
SMM J163658+4105	SMG	2.450 ± 0.002	3-2	1.8 ± 0.3	870 ± 80	PdBI	1
		2.452	3-2	1.8 ± 0.2	800 ± 50	PdBI	8
			7-6	3.3 ± 0.5		PdBI	8
SMM J123707+6214	SMG	2.490	3-2	0.91 ± 0.09	430 ± 60	PdBI	8
SMM J044307+0210	SMG _L	2.5094 ± 0.0002	3-2	1.4 ± 0.2	350 ± 60	PdBI	19
		2.509	3-2	1.4 ± 0.2	650 ± 40	PdBI	8
			7-6	1.0 ± 0.3		PdBI	8
SMM J16359+6612 A	SMG _L	2.5168 ± 0.0003	3-2	1.2 ± 0.14	500 ± 100	OVRO	22
B			3-2	3.5 ± 0.12		OVRO	22
C			3-2	1.6 ± 0.13		OVRO	22
A		2.51740	3-2	1.67 ± 0.13	220 ± 50	PdBI	23
					220 ± 50		
B		2.51741	3-2	2.50 ± 0.12		PdBI	23
C		2.51744	3-2	1.58 ± 0.17		PdBI	23
B		2.51737	3-2	2.8 ± 0.2	310 ± 20	30m	24
B		2.51732	4-3	4.0 ± 0.4	340 ± 25	30m	24
B		2.51746	5-4	5.1 ± 0.5	295 ± 30	30m	24
B		2.51738	6-5	4.0 ± 0.5	340 ± 35	30m	24
A			7-6	3.3 ± 1.4		PdBI	23
B			7-6	2.5 ± 0.7		PdBI	23
Cloverleaf	QSO _L	2.5585 ± 0.0001	3-2	8.1	326 ± 25	PdBI	25
			3-2	14.4 ± 4.4	352 ± 81	BIMA	26
		2.5579	3-2	9.9 ± 0.6	362 ± 23	30m	27
		2.55784 ± 0.00003	3-2	13.2 ± 0.2	416 ± 6	PdBI	28
			4-3	21.1 ± 0.8	375 ± 16	30m	27
			5-4	24.0 ± 1.4	398 ± 25	30m	27
			7-6	47.3 ± 2.2		PdBI	27
		2.5582 ± 0.0003	7-6	41 ± 4	339 ± 21	OVRO	29
			7-6	50.1 ± 2.8	480 ± 35	PdBI	30
			7-6	38.4	450	PdBI	31

Table A.2: All $z > 1$ CO Detections in the Literature ($2.56 \leq z \leq 4.69$)

Source	type	z	transition	I_{CO} (Jy kms $^{-1}$)	line FWHM (kms $^{-1}$)	telescope	refs.
SMM J14011+0252	SMG $_L$	2.5653 ± 0.0003	3-2	2.4 ± 0.3	200 ± 40	OVRO	32
		2.5652 ± 0.0001	3-2	2.8 ± 0.3	190 ± 11	PdBI	33
		2.5651 ± 0.0002	7-6	3.2 ± 0.5	170 ± 30	PdBI	33
VCV J1409+5628	QSO	2.585 ± 0.001	3-2	2.4 ± 0.7	370 ± 60	OVRO	34
		2.5832 ± 0.0001	3-2	2.3 ± 0.2	311 ± 28	PdBI	35
			7-6	4.1 ± 1.0		PdBI	35
MG 0414+0534	QSO $_L$	2.639 ± 0.002	3-2	2.6	580	PdBI	36
MS1512-cB58	LBG $_L$	2.7265 ± 0.0005	3-2	0.37 ± 0.08	174 ± 43	PdBI	37
LBQS1230+1627B	QSO $_L$	2.741	3-2	0.80 ± 0.26	(tentative)	PdBI	38
RX J0911+0551	QSO $_L$	2.796 ± 0.001	3-2	2.9 ± 1.1	350 ± 60	OVRO	34
SMM J02399-0136	SMG $_L$	2.808 ± 0.002	3-2	3.0 ± 0.4	710 ± 80	OVRO	39
		2.8076 ± 0.0002	3-2	3.1 ± 0.4	1100	PdBI	40
SMM J04135+10277	QSO $_L$	2.846 ± 0.002	3-2	5.4 ± 1.3	340 ± 120	OVRO	34
Cosmic Eye	LBG $_L$	3.0740 ± 0.0002	3-2	0.50 ± 0.07	190 ± 24	PdBI	41
B3 J2330+3927	RG	3.094	4-3	1.3 ± 0.3	500	PdBI	42
SMM J22174+0015	SMG	3.099 ± 0.004	3-2	0.8 ± 0.2	780 ± 100	PdBI	1
MG 0751+2716	QSO $_L$	3.1999	3-2	4.6 ± 0.5	400 ± 50	PdBI	43
		3.200 ± 0.00014	4-3	5.96 ± 0.45	390 ± 38	PdBI	44
		3.1999	4-3	4.2 ± 0.7	390 ± 70	PdBI	43
			8-7	2.2 ± 0.7		PdBI	43
SMM J09431+4700	SMG $_L$	3.3460 ± 0.0001	4-3	1.1 ± 0.1	420 ± 50	PdBI	19
		3.346	4-3	1.1 ± 0.2	400 ± 45	PdBI	8
SMM J13120+4242	SMG	3.408 ± 0.004	1-0	0.42 ± 0.07	1040 ± 190	GBT	45
		3.408 ± 0.002	4-3	1.7 ± 0.3	530 ± 50	PdBI	1
TN J0121+1320	RG	3.520	4-3	1.2 ± 0.4	700	PdBI	46
6C1909+722	RG	3.532	4-3	1.62 ± 0.30	530 ± 70	PdBI	47
4C60.07	RG		1-0	0.24 ± 0.03		VLA	48
		3.791	4-3	2.50 ± 0.43	>1000	PdBI	47
4C41.17	RG	3.7958 ± 0.0008	4-3	1.8 ± 0.2	1000 ± 150	PdBI	49
APM 08279+5255	QSO $_L$		1-0	0.150 ± 0.045		VLA	50
			1-0	0.22 ± 0.05		VLA	51
		3.9122 ± 0.0007	1-0	0.152 ± 0.020	556 ± 55	GBT	52
			1-0	0.168 ± 0.015		VLA	53
			2-1	0.81 ± 0.18		VLA	50,53
		3.9114 ± 0.0003	4-3	3.7 ± 0.5	480 ± 35	PdBI	54
		3.9115 ± 0.001	4-3	3.7 ± 0.4	490 ± 60	30m	55
		3.9118 ± 0.0003	4-3	3.8 ± 0.4	470 ± 17	PdBI	55
		3.9113 ± 0.0008	6-5	7.3 ± 0.7	445 ± 40	30m	55
		3.9109 ± 0.0002	9-8	9.1 ± 0.8		PdBI	54
3.9111 ± 0.0006	9-8	11.1 ± 2.2	480 ± 40	30m	55		
3.9119 ± 0.0003	9-8	12.5 ± 2.4	460 ± 22	PdBI	55		
3.9110 ± 0.0015	10-9	11.9 ± 2.4	480 ± 90	30m	55		
3.9110 ± 0.0015	11-10	10.4 ± 2.1	520 ± 50	30m	55		
PSS J2322+1944	QSO $_L$	4.1192 ± 0.0004	1-0	0.19 ± 0.08	200 ± 70	VLA	56
		4.1173 ± 0.0003	1-0	0.165 ± 0.014	202 ± 17	GBT	52
		4.1184 ± 0.0008	1-0	0.25 ± 0.06	184 ± 46	100m	52
			2-1	0.92 ± 0.30		VLA	56,57
		4.1199 ± 0.0008	4-3	4.21 ± 0.40	375 ± 41	PdBI	58
BRI 1335-0417	QSO	4.1199 ± 0.0008	5-4	3.74 ± 0.56	273 ± 50	PdBI	58
			2-1	0.32 ± 0.06		VLA	59
			2-1	0.44 ± 0.06		VLA	60
		4.4074 ± 0.0015	5-4	2.8 ± 0.3	420 ± 60	PdBI	61
BRI 0952-0115	QSO $_L$	4.4337 ± 0.0006	5-4	0.91 ± 0.11	230 ± 30	PdBI	38
BR 1202-0725	QSO	4.6932 ± 0.0004	1-0	0.124 ± 0.012	329 ± 36	GBT	52
		4.6956 ± 0.0012	1-0	0.22 ± 0.06	522 ± 146	100m	52
			2-1	0.49 ± 0.05		VLA	60
			4-3	1.5 ± 0.3		PdBI	62
		4.695 ± 0.002	5-4	2.7 ± 0.41	220 ± 74	NMA	63
		$4.6916/4.6947$	5-4	2.4 ± 0.3	$190/350$	PdBI	62
		4.6915 ± 0.001	7-6	3.1 ± 0.86	$250-300$	30m	62

Table A.3: All $z > 1$ CO Detections in the Literature ($4.69 \leq z \leq 6.42$)

Source	type	z	transition	I_{CO} (Jy kms $^{-1}$)	line FWHM (kms $^{-1}$)	telescope	refs.
SDSS J0338+0021	QSO	5.0267 ± 0.0003	5–4	0.73 ± 0.09	500	PdBI	64
TN J0924-2201	RG	5.202 ± 0.001	1–0	0.087 ± 0.017	250–400	ATCA	65
		5.202	5–4	1.19 ± 0.27	200–300	ATCA	65
SDSS J0927+2001	QSO	5.7722 ± 0.0006	5–4	0.44 ± 0.07	610 ± 110	PdBI	66
		5.7722 ± 0.0006	6–5	0.69 ± 0.13	550 ± 150	PdBI	66
SDSS J1148+5251	QSO	6.418 ± 0.004	3–2	0.18 ± 0.04		VLA	67,68
		6.4189 ± 0.0006	6–5	0.73 ± 0.076	279	PdBI	69
		6.4192 ± 0.0009	7–6	0.64 ± 0.088		PdBI	69

Notes—An index L at the galaxy type indicates magnification by strong gravitational lensing.

References—(1) Greve et al. 2005; (2) Iono et al. 2006a; (3) Planesas et al. 1999; (4) Krips et al. 2005; (5) Greve et al. 2003; (6) Andreani et al. 2000; (7) Willott et al. 2007; (8) Tacconi et al. 2006; (9) Brown & Vanden Bout 1991; (10) Brown & Vanden Bout 1992a; (11) Solomon et al. 1992a; (12) Tsuboi & Nakai 1992; (13) Kawabe et al. 1992; (14) Sakamoto et al. 1992; (15) Radford et al. 1993; (16) Scoville et al. 1995; (17) Downes et al. 1995; (18) Radford et al. 1996; (19) Neri et al. 2003; (20) Scoville et al. 1997; (21) Alloin et al. 2000; (22) Sheth et al. 2004; (23) Kneib et al. 2005; (24) Weiss et al. 2005aa; (25) Barvainis et al. 1994; (26) Wilner et al. 1995; (27) Barvainis et al. 1997; (28) Weiss et al. 2003; (29) Yun et al. 1997; (30) Alloin et al. 1997; (31) Kneib et al. 1998; (32) Frayer et al. 1999; (33) Downes & Solomon 2003; (34) Hainline et al. 2004; (35) Beelen et al. 2004; (36) Barvainis et al. 1998; (37) Baker et al. 2004; (38) Guilloteau et al. 1999; (39) Frayer et al. 1998; (40) Genzel et al. 2003; (41) Coppin et al. 2007; (42) De Breuck et al. 2003a; (43) Alloin et al. 2007; (44) Barvainis et al. 2002; (45) Hainline et al. 2006; (46) De Breuck et al. 2003b; (47) Papadopoulos et al. 2000; (48) Greve et al. 2004; (49) De Breuck et al. 2005; (50) Papadopoulos et al. 2001; (51) Lewis et al. 2002a; (52) Riechers et al. 2006a; (53) Riechers et al. 2007a; (54) Downes et al. 1999; (55) Weiss et al. 2007; (56) Carilli et al. 2002a; (57) Carilli et al. 2003; (58) Cox et al. 2002; (59) Carilli et al. 1999; (60) Carilli et al. 2002b; (61) Guilloteau et al. 1997; (62) Omont et al. 1996; (63) Ohta et al. 1996; (64) Maiolino et al. 2007; (65) Klammer et al. 2005; (66) Carilli et al. 2007; (67) Walter et al. 2003; (68) Walter et al. 2004; (69) Bertoldi et al. 2003b.

Table A.4: All $z > 1$ Detections of Dense Molecular Gas in the Literature

Source	type	z	transition	I_{CO} (Jy kms $^{-1}$)	line FWHM (kms $^{-1}$)	telescope	refs.
IRAS F10214+4724	QSO $_L$	2.2858 \pm 0.0002	HCN(1-0)	0.05 \pm 0.01	140 \pm 30	GBT	1
			HCN(4-3)	0.10 \pm 0.03	110 \pm 43	PdBI	2
SMM J16359+6612 B Cloverleaf	SMG $_L$	2.5168	HCN(1-0)	0.032 \pm 0.008		VLA	3
	QSO $_L$	2.5569 \pm 0.0006	HCN(1-0)	0.069 \pm 0.012		VLA	4
			HCN(4-3)	2.6 \pm 0.5	436 \pm 103	30m	5
			HCN(4-3)	<1.2 a		PdBI	4
			HCO $^+$ (1-0)	0.055 \pm 0.006		VLA	6
			HCO $^+$ (4-3)	0.80 \pm 0.12	414 \pm 75	PdBI	7
			CN(3-2)	1.37 \pm 0.17	666 \pm 97	PdBI	8
			CS(3-2)	0.09 \pm 0.02		VLA	9
VCV J1409+5628	QSO	2.5832	HCN(1-0)	0.015 \pm 0.005	177 \pm 80	VLA	10
APM 08279+5255	QSO $_L$	3.9121	HCN(5-4)	0.98 \pm 0.12	440 \pm 59	PdBI	11
			HCN(5-4)	0.85 \pm 0.10	400 \pm 40	PdBI	12
			HCO $^+$ (5-4)	0.87 \pm 0.13	490 \pm 80	PdBI	13
			HNC(5-4)	2.3 \pm 1.1	(blended) b	PdBI	14

Notes—An index L at the galaxy type indicates magnification by strong gravitational lensing. Redshifts without error bars are adopted from CO.

a This line was not confirmed and is currently considered not detected.

b Due to blending with another line, this detection is not entirely certain.

References—(1) Vanden Bout et al. 2004; (2) Riechers et al. 2008c, in prep.; (3) Gao et al. 2007; (4) Solomon et al. 2003; (5) Barvainis et al. 1997; (6) Riechers et al. 2006b; (7) Riechers et al. 2008a, in prep.; (8) Riechers et al. 2007a; (9) Riechers et al. 2008b, in prep.; (10) Carilli et al. 2005; (11) Wagg et al. 2005; (12) Weiss et al. 2007; (13) Garcia-Burillo et al. 2006; (14) Guelin et al. 2007.

Table A.5: All $z > 1$ Detections of Millimeter Carbon Lines in the Literature

Source	type	z	transition	I_{CO} (Jy kms $^{-1}$)	line FWHM (kms $^{-1}$)	telescope	refs.
IRAS F10214+4724	QSO $_L$	2.2854	[CI](1-0)	11		30m	1
			[CI](1-0)	1.6 \pm 0.2	160 \pm 30	30m	2
			[CI](2-1)	55		30m	1
			[CI](2-1)	150		12m	1
Cloverleaf	QSO $_L$	2.5578	[CI](1-0)	3.6 \pm 0.4	430 \pm 46	30m	3
			[CI](1-0)	3.9 \pm 0.6	360 \pm 60	30m	2
			[CI](2-1)	5.2 \pm 0.3	368 \pm 25	PdBI	4
SMM J14011+0252	SMG $_L$	2.5653	[CI](1-0)	1.8 \pm 0.3	235 \pm 45	30m	2
APM 08279+5255	QSO $_L$	3.911	[CI](1-0)	0.93 \pm 0.13	386 \pm 67	PdBI	5
PSS J2322+1944	QSO $_L$	4.1199	[CI](1-0)	0.81 \pm 0.12	319 \pm 66	PdBI	6
BR 1202-0725N	QSO	4.6949	[CII]	6.8 \pm 1.1	240 \pm 50	SMA	7
SDSS J1148+5251	QSO	6.4189 \pm 0.0006	[CII]	4.1 \pm 0.5	350 \pm 50	30m	8

Notes—An index L at the galaxy type indicates magnification by strong gravitational lensing. Redshifts without error bars are adopted from CO.

References—(1) Brown & Vanden Bout 1992b; (2) Weiss et al. 2005b; (3) Barvainis et al. 1997; (4) Weiss et al. 2003; (5) Wagg et al. 2006; (6) Pety et al. 2004; (7) Iono et al. 2006b; (8) Maiolino et al. 2005.

A.2 Statistical Analysis and Source Classification

A number of interesting things can be learned by simply looking at the detection counts. The left panels of Figure A.1 show the number of high- z CO (*top*) and HCN (*bottom*) detections versus the year of initial detection. The number of high- z CO detections is rising steadily since the advent of the PdBI in the mid-nineties, in particular since the inclusion of its fifth and sixth antenna. The dip in 2001 is probably explained by the long-term shutdown of PdBI in 2000. The number of initial detections is relatively constant since 2003, with an average of about five new detections per year. The total number of detections as of August 2007 is 43. The number of high- z HCN detections is rising at a rate of about one per year since its initial discovery in 2003 (see above for further discussion), and is currently known in five galaxies, i.e., about 10% of the CO-detected sample. Note that HCO⁺ has been detected in two out of these five galaxies, while CS and CN were detected in one out of the latter. The right panels of Figure A.1 show the distribution of high- z CO (*top*) and HCN (*bottom*) detections in redshift space. The sample of CO-detected high- z galaxies is highly selected and flux-limited. However, note that the distribution peaks at a redshift around $z=2.5$, i.e., in the epoch where most star formation in the universe is believed to occur (see also Solomon & Vanden Bout 2005). Due to the low number of detections and the selection effects involved, the statistical significance of this finding is not very high. This result is still interesting, as the sample should contain galaxies with some of the highest massive star formation rates at every epoch. The same relation for HCN is below any statistical significance, but peaks at the same redshift.

Figure A.2 again shows the redshift distribution of the CO-detected high- z sources, but divided by galaxy type. Quasars are detected over the whole redshift range, and represent 42% of the whole sample. Submillimeter galaxies are only detected in CO below a redshift of 3.5, and represent 33% of the sample. Both populations clearly peak around $z=2.5$, however, the distribution of quasars hints at a selection effect. Radio galaxies represent about 16% of the sample. Only four of the detections (9%) do not fall into these three categories. However, with the recently improved receivers of the PdBI, a larger number of Lyman-break galaxies (LBGs) representing a highly abundant (but not necessarily distinct) population of galaxies in the early universe should become accessible (currently: 2 detections), and may contribute a larger fraction to the sample in the future.

Figure A.3 shows the CO and HCN transitions in which the galaxies in this sample were detected. Due to the fact that many galaxies were detected in more than one transition, the numbers are larger than the actual sample size. The CO distribution clearly peaks at CO($J=3\rightarrow 2$) and CO($J=4\rightarrow 3$). These transitions lie in the 3 mm observing window at redshifts between 2 and 4 (where most sources are found), which is the standard observing window of the PdBI. Most of the HCN detections were obtained in the HCN($J=1\rightarrow 0$) transition, which falls into the 1.3 cm observing window of the VLA at redshifts of 2.3 to almost 4. This is also reflected in Figure A.3, which shows the most commonly observed CO and HCN transitions at different redshifts. The step function basically reflects the movement of the different CO transitions with redshift through the 3 mm observing window. This visualized one of the main selection effects: galaxies that do not have highly excited

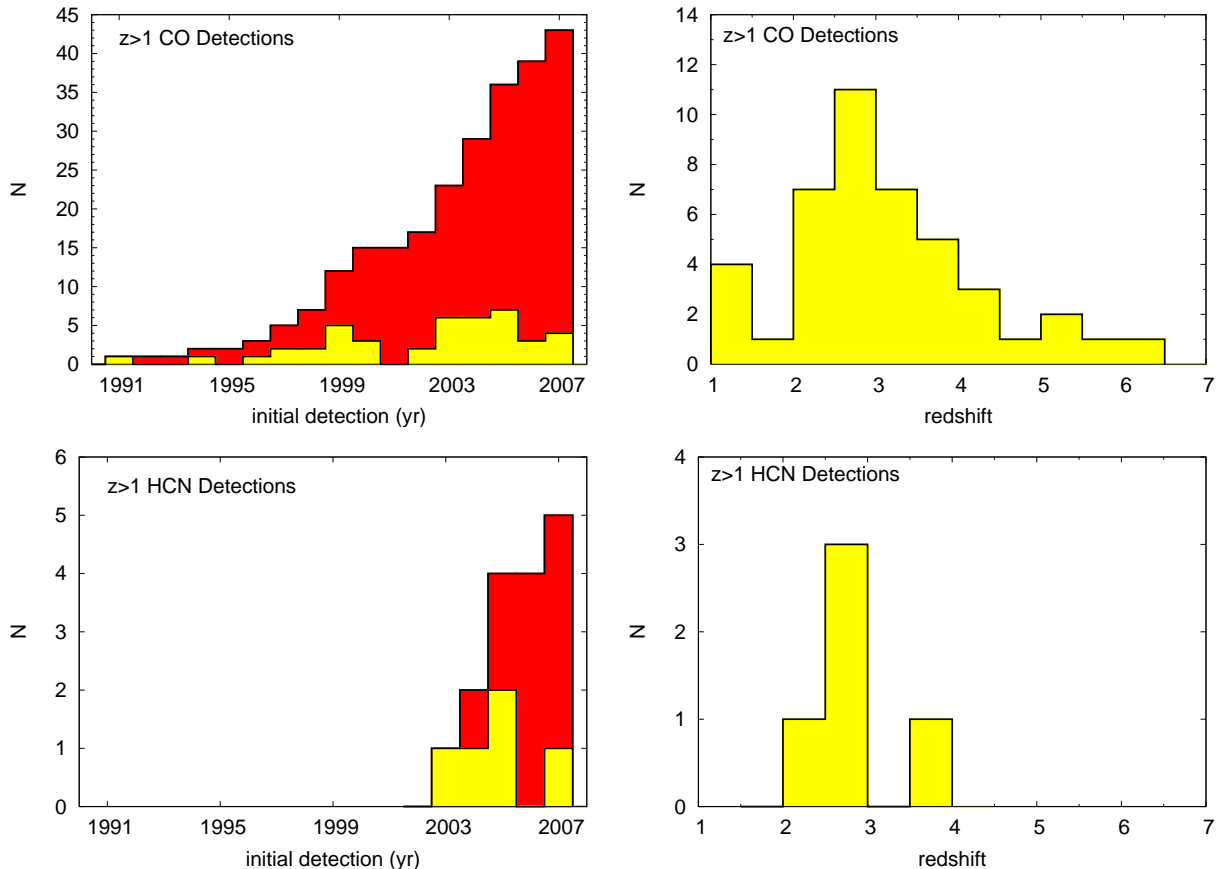


Figure A.1: History of high redshift CO and HCN detections (*left*), and source distribution in redshift space (*right*). *Top left*: The number of $z > 1$ CO detections per year is shown in yellow, and the cumulative number of detections is shown in red. *Bottom left*: Same, but for HCN. *Top right*: Distribution of the high redshift CO detections in redshift space. The size of the redshift bins is $\Delta z = 0.5$. *Bottom right*: Same, but for HCN.

CO ladders are less and less likely to be detected with increasing redshift, even if they exhibit bright CO($J=1 \rightarrow 0$) emission. This effect is even more severe for dense gas tracers like HCN: the only source detected in HCN emission at redshift 4 shows a highly unusual HCN excitation (Weiss et al. 2007). This demonstrates the importance of low-frequency observations of low-order transitions of molecular gas at high redshift: a “blind” search for CO($J=1 \rightarrow 0$) at high redshift may reveal new populations that were missed by searches in higher J CO transitions so far.

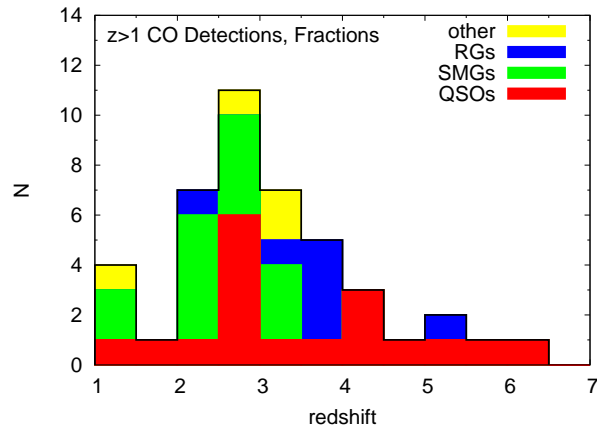


Figure A.2: Source distribution in redshift space for all $z > 1$ CO detections, divided by galaxy type. The size of the redshift bins is $\Delta z = 0.5$.

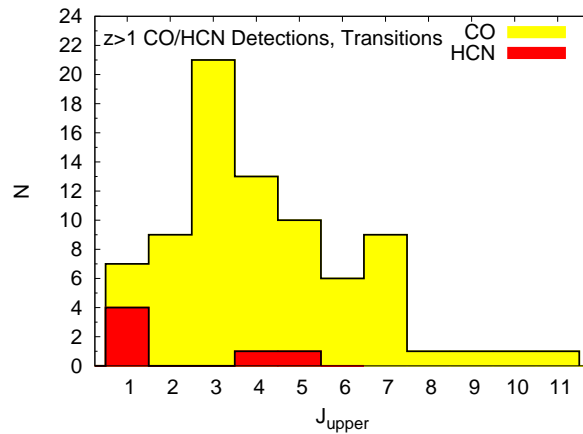


Figure A.3: Detected CO/HCN transitions for all systems detected at $z > 1$. J_{upper} indicates the upper quantum number of the rotational transition. The total number of detections is given for all transitions (i.e., galaxies detected in multiple transitions appear once per transition).

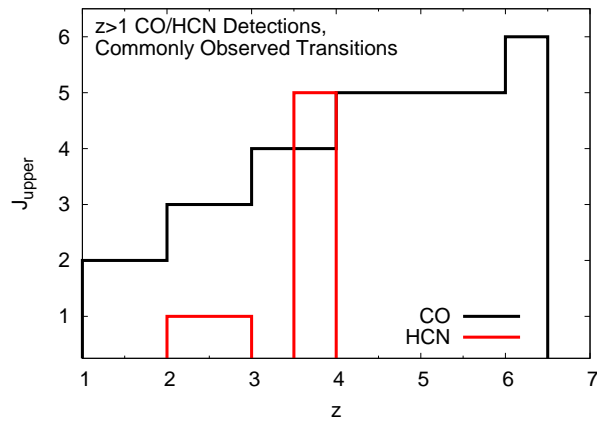


Figure A.4: Most commonly observed CO/HCN transitions for all systems detected at $z>1$ at different redshifts. J_{upper} indicates the upper quantum number of the rotational transition. The size of the redshift bins is $\Delta z=0.5$. The almost linear progression with redshift for the CO detections is set by the most commonly used 3 mm observing window.

Abbreviations

General

AGN	Active Galactic Nucleus
BAL	Broad Absorption Line
BLR	Broad Line Region
CMB	Cosmic Microwave Background
ERO	Extremely Red Object
FF	Filling Factor
FIR	Far-Infrared
FS	Fine Structure
FWHM	Full Width at Half Maximum
FWZI	Full Width at Zero Intensity
GMC	Giant Molecular Cloud
HFS	Hyperfine Structure
HLIRG	Hyperluminous Infrared Galaxy ($L_{\text{IR}} > 10^{13} L_{\odot}$)
IGM	Intergalactic Medium
IR	Infrared
ISM	Interstellar Medium
LIRG	Luminous Infrared Galaxy ($L_{\text{IR}} > 10^{11} L_{\odot}$)
LTE	Local Thermodynamic Equilibrium
LBG	Lyman-Break Galaxy
LVG	Large Velocity Gradient
NLR	Narrow Line Region
QSO	Quasi-Stellar Object
RG	Radio Galaxy
SB	Starburst
SFR	Star-Formation Rate
SMG	Submillimeter Galaxy
ULIRG	Ultraluminous Infrared Galaxy ($L_{\text{IR}} > 10^{12} L_{\odot}$)
UV	Ultraviolet

Telescopes

12 m	NRAO 12 m telescope
30 m	IRAM 30 m telescope
45 m	NRO 45 m telescope
100 m	MPIfR Effelsberg 100 m telescope
ACA	Atacama Compact Array
ALMA	Atacama Large (sub-) Millimeter Array
APEX	Atacama Pathfinder Experiment
ASTE	Atacama Submillimeter Telescope Experiment
ATCA	Australia Telescope Compact Array
BIMA	Berkeley-Illinois-Maryland Association millimeter array
CARMA	Combined Array for Research in Millimeter-wave Astronomy
CCAT	Cornell Caltech Atacama Telescope
CSO	Caltech Submillimeter Observatory
CXO	Chandra X-Ray Observatory
eSMA	Combination of the SMA, the JCMT, and the CSO
EVLA	Expanded Very Large Array
GBT	Green Bank (100 m) Telescope
HERSCHEL	Herschel Space Observatory
HSA	High Sensitivity Array (VLBA + phased VLA + GBT+ Arecibo)
HST	Hubble Space Telescope
JCMT	James Clerk Maxwell Telescope
JWST	James Webb Space Telescope
NMA	Nobeyama Millimeter Array
OVRO	Owens Valley Radio Observatory millimeter array
PdBI	Plateau de Bure Interferometer
Rainbow interferometer	combination of the NMA and the 45 m
SKA	Square Kilometre Array
SMA	Submillimeter Array
SST	Spitzer Space Telescope
VLA	Very Large Array
VLBA	Very Long Baseline Array

Instruments

GISMO	Goddard-Iram Superconducting 2-Millimeter Observer
MAMBO (2)	Max-Planck-Millimeter Bolometer Array (2)
MUSTANG	Multiplexed SQUID/TES Array for Ninety Gigahertz
PACS	Photodetector Array Camera and Spectrometer
SCUBA (2)	Submillimetre Common-User Bolometer Array (2)
SHARC-II	Submillimetre High Angular Resolution Camera II
SPIRE	Spectral and Photometric Imaging Receiver

Institutes and Organizations

AIfA	Argelander-Institut für Astronomie
Caltech	California Institute of Technology
CfA	Harvard-Smithsonian Center for Astrophysics
DFG	Deutsche Forschungsgemeinschaft
ESO	European Southern Observatory
IRAM	Institut de Radioastronomie Millimétrique
MPIA	Max-Planck-Institut für Astronomie
MPIfR	Max-Planck-Institut für Radioastronomie
NAOJ	National Astronomical Observatory of Japan
NRAO	National Radio Astronomy Observatory
NRO	Nobeyama Radio Observatory
NSF	National Science Foundation

Surveys

APM	Automated Plate Measuring machine survey
PSS	Digital Palomar Observatory Sky Survey
SDSS	Sloan Digital Sky Survey

Atoms and Molecules

H	Hydrogen
He	Helium
C	Carbon
N	Nitrogen
O	Oxygen
Mg	Magnesium
S	Sulphur
H ₂	Molecular Hydrogen
CO	Carbon Monoxide
CN	Cyanide Radical
CS	Carbon Monosulfide
H ₂ O	Water
HCN	Hydrogen Cyanide
HNC	Hydrogen Isocyanide
HCO ⁺	Formyl Cation / Oxomethylum
C ₂ H	Ethynyl
H ₂ CO	Formaldehyde (Methanal)
NH ₃	Ammonia
OH	Hydroxyl Radical
SiO	Silicon Monoxide
PAH	Polycyclic Aromatic Hydrocarbons

Units, Constants and Conversions

Boltzmann Constant	$k_B = 1.3806504 \times 10^{-23} \text{ J K}^{-1}$
Newtonian Constant of Gravitation	$G = 6.67428 \times 10^{-11} \text{ m}^3 \text{ kg}^{-1} \text{ s}^{-2}$
Planck Constant	$h = 6.62606896 \times 10^{-34} \text{ J s}$
Reduced Planck Constant	$\hbar = h/2\pi$
Speed of Light	$c = 299,792.458 \text{ km s}^{-1}$
Stefan-Boltzmann Constant	$\sigma_{\text{SB}} = 5.670400 \times 10^{-8} \text{ W m}^{-2} \text{ K}^{-4}$
(Beam) Solid Angle	$\Omega_{(B)}(\text{sterad}) = \frac{\pi \frac{\theta_{\text{maj}}}{2} \times \frac{\theta_{\text{min}}}{2}}{(60 \cdot 60 \cdot 360 / (2\pi))^2} \text{ (arcsec}^2)$
erg	$1 \text{ erg} = 10^{-7} \text{ J}$
Jansky	$1 \text{ Jy} = 10^{-26} \text{ W m}^{-2} \text{ Hz}^{-1}$
Joule	$1 \text{ J} = 1 \text{ W s}$
Electron Volt	$1 \text{ eV} = 1.602 \times 10^{-12} \text{ erg}$
Megaparsec	$1 \text{ Mpc} = 10^6 \text{ pc} = 3.08568025 \times 10^{22} \text{ m}$
Solar Luminosity	$1 L_{\odot} = 3.827 \times 10^{26} \text{ W}$
Solar Mass	$1 M_{\odot} = 1.989 \times 10^{30} \text{ kg}$

Bibliography

- Aalto, S., Booth, R. S., Black, J. H., & Johansson, L. E. B. 1995, *A&A* **300**, 369–+, *Molecular gas in starburst galaxies: line intensities and physical conditions.*
- Aalto, S., Hüttemeister, S., Scoville, N. Z., & Thaddeus, P. 1999, *ApJ* **522**, 165–182, *A New High-Resolution CO Map of the Inner 2.5' of M51. I. Streaming Motions and Spiral Structure.*
- Aalto, S., Polatidis, A. G., Hüttemeister, S., & Curran, S. J. 2002, *A&A* **381**, 783–794, *CN and HNC line emission in IR luminous galaxies.*
- Aalto, S., Spaans, M., Wiedner, M. C., & Hüttemeister, S. 2007, *A&A* **464**, 193–200, *Overluminous HNC line emission in Arp 220, NGC 4418 and Mrk 231. Global IR pumping or XDRs?*
- Alloin, D., Barvainis, R., Gordon, M. A., & Antonucci, R. R. J. 1992, *A&A* **265**, 429–436, *CO emission from radio quiet quasars - New detections support a thermal origin for the FIR emission.*
- Alloin, D., Barvainis, R., & Guilloteau, S. 2000, *ApJL* **528**, L81–L84, *New CO and Millimeter Continuum Observations of the $Z = 2.394$ Radio Galaxy 53W002.*
- Alloin, D., Guilloteau, S., Barvainis, R., Antonucci, R., & Tacconi, L. 1997, *A&A* **321**, 24–28, *The gravitational lensing nature of the Cloverleaf unveiled in CO (7-6) line emission.*
- Alloin, D., Kneib, J.-P., Guilloteau, S., & Bremer, M. 2007, *A&A* **470**, 53–60, *Dust and molecular content of the lensed quasar, MG0751+2716, at $z = 3.2$.*
- Andreani, P., Cimatti, A., Loinard, L., & Röttgering, H. 2000, *A&A* **354**, L1–L5, *CO detection of the extremely red galaxy HR10.*
- Andreani, P., Cristiani, S., Grazian, A., La Franca, F., & Goldschmidt, P. 2003, *AJ* **125**, 444–458, *The Dusty Environment of Quasars: Far-Infrared Properties of Optical Quasars.*
- Athreya, R. M., Kapahi, V. K., McCarthy, P. J., & van Breugel, W. 1997, *MNRAS* **289**, 525–534, *Steep-spectrum radio cores in high-redshift galaxies.*

- Bachiller, R. 1996, *ARA&A* **34**, 111–154, *Bipolar Molecular Outflows from Young Stars and Protostars*.
- Baker, A. J., Harris, A. I., Jewell, P. R., et al. 2005, *Zspectrometer: an Ultra-wideband Spectrometer for Redshift Searches with the Green Bank Telescope*, In *Bulletin of the American Astronomical Society*, Volume 37 of *Bulletin of the American Astronomical Society*, pp. 1315–+.
- Baker, A. J., Tacconi, L. J., Genzel, R., Lehnert, M. D., & Lutz, D. 2004, *ApJ* **604**, 125–140, *Molecular Gas in the Lensed Lyman Break Galaxy cB58*.
- Barnard, E. E. 1919, *ApJ* **49**, 1–24, *On the dark markings of the sky, with a catalogue of 182 such objects*.
- Bartelmann, M. & Loeb, A. 1998, *ApJ* **503**, 48–+, *Effects of Disks on Gravitational Lensing by Spiral Galaxies*.
- Barvainis, R., Alloin, D., & Bremer, M. 2002, *A&A* **385**, 399–403, *A CO survey of gravitationally lensed quasars with the IRAM interferometer*.
- Barvainis, R., Alloin, D., Guilloteau, S., & Antonucci, R. 1998, *ApJL* **492**, L13+, *Detection of CO (3–2) Emission at $Z = 2.64$ from the Gravitationally Lensed Quasar MG 0414+0534*.
- Barvainis, R. & Ivison, R. 2002, *ApJ* **571**, 712–720, *A Submillimeter Survey of Gravitationally Lensed Quasars*.
- Barvainis, R., Maloney, P., Antonucci, R., & Alloin, D. 1997, *ApJ* **484**, 695–+, *Multiple CO Transitions, C i, and HCN from the Cloverleaf Quasar*.
- Barvainis, R., Tacconi, L., Antonucci, R., Alloin, D., & Coleman, P. 1994, *Nature* **371**, 586–588, *Extremely Strong Carbon-Monoxide Emission from the Cloverleaf Quasar at a Redshift of 2.5*.
- Beelen, A., Cox, P., Benford, D. J., et al. 2006, *ApJ* **642**, 694–701, *350 μ m Dust Emission from High-Redshift Quasars*.
- Beelen, A., Cox, P., Pety, J., et al. 2004, *A&A* **423**, 441–447, *Starburst activity in the host galaxy of the $z = 2.58$ quasar J1409+5628*.
- Bell, E. F. 2003, *ApJ* **586**, 794–813, *Estimating Star Formation Rates from Infrared and Radio Luminosities: The Origin of the Radio-Infrared Correlation*.
- Bertoldi, F., Carilli, C. L., Cox, P., et al. 2003a, *A&A* **406**, L55–L58, *Dust emission from the most distant quasars*.
- Bertoldi, F., Cox, P., Neri, R., et al. 2003b, *A&A* **409**, L47–L50, *High-excitation CO in a quasar host galaxy at $z = 6.42$* .

- Bettoni, D., Galletta, G., & García-Burillo, S. 2003, A&A **405**, 5–14, *A new catalogue of ISM content of normal galaxies.*
- Binney, J. & Tremaine, S. 1987, *Galactic dynamics*. Princeton, NJ, Princeton University Press, 1987, 747 p.
- Blain, A. W., Barnard, V. E., & Chapman, S. C. 2003, MNRAS **338**, 733–744, *Submillimetre and far-infrared spectral energy distributions of galaxies: the luminosity-temperature relation and consequences for photometric redshifts.*
- Blain, A. W., Smail, I., Ivison, R. J., Kneib, J.-P., & Frayer, D. T. 2002, Physics Reports **369**, 111–176, *Submillimeter galaxies.*
- Blitz, L. 1996, *CO in the Milky Way*, In W. B. Latter, J. E. Radford Simon, P. R. Jewell, J. G. Mangum, and J. Bally (Eds.), *CO: Twenty-Five Years of Millimeter-Wave Spectroscopy*, Volume 170 of *IAU Symposium*, pp. 11–+.
- Bloemen, J. B. G. M., Strong, A. W., Mayer-Hasselwander, H. A., et al. 1986, A&A **154**, 25–41, *The radial distribution of galactic gamma rays. III - The distribution of cosmic rays in the Galaxy and the CO-H2 calibration.*
- Boger, G. I. & Sternberg, A. 2005, ApJ **632**, 302–315, *CN and HCN in Dense Interstellar Clouds.*
- Bondi, M., Ciliegi, P., Venturi, T., et al. 2007, A&A **463**, 519–527, *The VVDS-VLA deep field. III. GMRT observations at 610 MHz and the radio spectral index properties of the sub-mJy population.*
- Boselli, A., Lequeux, J., & Gavazzi, G. 2002, A&A **384**, 33–47, *Molecular gas in normal late-type galaxies.*
- Bournaud, F. & Combes, F. 2002, A&A **392**, 83–102, *Gas accretion on spiral galaxies: Bar formation and renewal.*
- Brewer, B. J. & Lewis, G. F. 2006, ApJ **637**, 608–619, *Strong Gravitational Lens Inversion: A Bayesian Approach.*
- Brouillet, N., Muller, S., Herpin, F., Braine, J., & Jacq, T. 2005, A&A **429**, 153–159, *HCN and HCO⁺ emission in the disk of M31.*
- Brown, R. L. & Vanden Bout, P. A. 1991, AJ **102**, 1956–1959, *CO emission at $Z = 2.2867$ in the galaxy IRAS F10214 + 4724.*
- Brown, R. L. & Vanden Bout, P. A. 1992a, ApJL **397**, L19–L22, *IRAS F10214 + 4724 - an extended CO emission source at $Z = 2.2867$.*
- Brown, R. L. & Vanden Bout, P. A. 1992b, ApJL **397**, L11–L14, *Forbidden C I emission at $Z = 2.286$ in the protogalaxy IRAS F10214 + 4724.*

- Burke, W. L. 1981, ApJL **244**, L1+, *Multiple Gravitational Imaging by Distributed Masses*.
- Carilli, C. L. 2006, SKA memo **70**, .
- Carilli, C. L., Cox, P., Bertoldi, F., et al. 2002a, ApJ **575**, 145–149, *Imaging Low-Order CO Emission from the $z=4.12$ Quasi-Stellar Object PSS J2322+1944*.
- Carilli, C. L. & Holdaway, M. A. 1999, Radio Science **34**, 817–840, *Tropospheric phase calibration in millimeter interferometry*.
- Carilli, C. L., Kohno, K., Kawabe, R., et al. 2002b, AJ **123**, 1838–1846, *High-Resolution Imaging of Molecular Line Emission from High-Redshift QSOs*.
- Carilli, C. L., Lewis, G. F., Djorgovski, S. G., et al. 2003, Science **300**, 773–775, *A Molecular Einstein Ring: Imaging a Starburst Disk Surrounding a Quasi-Stellar Object*.
- Carilli, C. L., Menten, K. M., & Yun, M. S. 1999, ApJL **521**, L25–L28, *Detection of CO (2-1) and Radio Continuum Emission from the $Z = 4.4$ QSO BRI 1335-0417*.
- Carilli, C. L., Neri, R., Wang, R., et al. 2007, ApJL **666**, L9–L12, *Detection of $1.6 \times 10^{10} M_{\odot}$ of Molecular Gas in the Host Galaxy of the $z = 5.77$ SDSS Quasar J0927+2001*.
- Carilli, C. L., Solomon, P., Vanden Bout, P., et al. 2005, ApJ **618**, 586–591, *A Search for Dense Molecular Gas in High-Redshift Infrared-Luminous Galaxies*.
- Carilli, C. L., Walter, F., Bertoldi, F., et al. 2004, AJ **128**, 997–1001, *Radio Continuum Imaging of Far-Infrared-Luminous QSOs at $z > 6$* .
- Carilli, C. L. & Wang, R. 2006, AJ **131**, 2763–2765, *CO Line Width Differences in Early Universe Molecular Emission-Line Galaxies: Submillimeter Galaxies versus QSO Hosts*.
- Casoli, F., Gerin, M., Encrenaz, P. J., & Combes, F. 1994, A&A **287**, 716–718, *Further support for the presence of water in IRAS 10214+4724*.
- Casoli, F., Sauty, S., Gerin, M., et al. 1998, A&A **331**, 451–462, *Molecular gas in spiral galaxies*.
- Cernicharo, J., Bachiller, R., & Gonzalez-Alfonso, E. 1996, A&A **305**, L5+, *Water emission at 183 GHz from HH7-11 and other low-mass star-forming regions*.
- Cernicharo, J., Goicoechea, J. R., Pardo, J. R., & Asensio-Ramos, A. 2006, ApJ **642**, 940–953, *Warm Water Vapor around Sagittarius B2*.
- Cernicharo, J., Gonzalez-Alfonso, E., Alcolea, J., Bachiller, R., & John, D. 1994, ApJL **432**, L59–L62, *Widespread water vapor emission in Orion*.
- Cernicharo, J., Pardo, J. R., González-Alfonso, E., et al. 1999, ApJL **520**, L131–L134, *Physical Conditions in Shocked Regions of Orion from Ground-based Observations of H_2O* .

- Cernicharo, J., Pardo, J. R., & Weiss, A. 2006, *ApJL* **646**, L49–L52, *A New Water Vapor Megamaser*.
- Chandrasekhar, S. 1960, *Radiative transfer*. New York: Dover, 1960.
- Chartas, G., Brandt, W. N., Gallagher, S. C., & Garmire, G. P. 2002, *ApJ* **579**, 169–175, *CHANDRA Detects Relativistic Broad Absorption Lines from APM 08279+5255*.
- Chartas, G., Eracleous, M., Dai, X., Agol, E., & Gallagher, S. 2007, *ApJ* **661**, 678–692, *Discovery of Probable Relativistic Fe Emission and Absorption in the Cloverleaf Quasar H 1413+117*.
- Chevalier, R. A., Blondin, J. M., & Emmering, R. T. 1992, *ApJ* **392**, 118–130, *Hydrodynamic instabilities in supernova remnants - Self-similar driven waves*.
- Combes, F. 1991, *ARA&A* **29**, 195–237, *Distribution of CO in the Milky Way*.
- Combes, F., Nguyen-Q-Rieu, & Dinh-v-Trung 1997, *A&A* **323**, 357–362, *Search for 183GHz water maser emission in starburst galaxies*.
- Condon, J. J. 1992, *ARA&A* **30**, 575–611, *Radio emission from normal galaxies*.
- Condon, J. J., Anderson, M. L., & Helou, G. 1991, *ApJ* **376**, 95–103, *Correlations between the far-infrared, radio, and blue luminosities of spiral galaxies*.
- Coppin, K. E. K., Swinbank, A. M., Neri, R., et al. 2007, *ApJ* **665**, 936–943, *A Detailed Study of Gas and Star Formation in a Highly Magnified Lyman Break Galaxy at $z = 3.07$* .
- Cox, P., Omont, A., Djorgovski, S. G., et al. 2002, *A&A* **387**, 406–411, *CO and Dust in PSS 2322+1944 at a redshift of 4.12*.
- Curran, S. J., Johansson, L. E. B., Bergman, P., Heikkilä, A., & Aalto, S. 2001, *A&A* **367**, 457–469, *Molecular gas conditions in NGC 4945 and the Circinus galaxy*.
- Dame, T. M., Hartmann, D., & Thaddeus, P. 2001, *ApJ* **547**, 792–813, *The Milky Way in Molecular Clouds: A New Complete CO Survey*.
- Dame, T. M., Ungerechts, H., Cohen, R. S., et al. 1987, *ApJ* **322**, 706–720, *A composite CO survey of the entire Milky Way*.
- De Breuck, C., Downes, D., Neri, R., et al. 2005, *A&A* **430**, L1–L4, *Detection of two massive CO systems in 4C 41.17 at $z = 3.8$* .
- De Breuck, C., Neri, R., Morganti, R., et al. 2003a, *A&A* **401**, 911–925, *CO emission and associated H I absorption from a massive gas reservoir surrounding the $z = 3$ radio galaxy B3 J2330+3927*.

- De Breuck, C., Neri, R., & Omont, A. 2003b, *New Astronomy Review* **47**, 285–289, *CO emission from $z > 3$ radio galaxies*.
- Desert, F.-X., Boulanger, F., & Puget, J. L. 1990, *A&A* **237**, 215–236, *Interstellar dust models for extinction and emission*.
- Di Matteo, T., Colberg, J., Springel, V., Hernquist, L., & Sijacki, D. 2007, *ArXiv e-prints* **705**, *Direct cosmological simulations of the growth of black holes and galaxies*.
- Di Matteo, T., Springel, V., & Hernquist, L. 2005, *Nature* **433**, 604–607, *Energy input from quasars regulates the growth and activity of black holes and their host galaxies*.
- Dickman, R. L. 1978, *ApJS* **37**, 407–427, *The ratio of carbon monoxide to molecular hydrogen in interstellar dark clouds*.
- Downes, D. & Eckart, A. 2007, *A&A* **468**, L57–L61, *Black hole in the West nucleus of Arp 220*.
- Downes, D., Neri, R., Wiklind, T., Wilner, D. J., & Shaver, P. A. 1999, *ApJL* **513**, L1–L4, *Detection of CO (4-3), CO (9-8), and Dust Emission in the Broad Absorption Line Quasar APM 08279+5255 at a Redshift of 3.9*.
- Downes, D. & Solomon, P. M. 1998, *ApJ* **507**, 615–654, *Rotating Nuclear Rings and Extreme Starbursts in Ultraluminous Galaxies*.
- Downes, D. & Solomon, P. M. 2003, *ApJ* **582**, 37–48, *Molecular Gas and Dust at $z=2.6$ in SMM J14011+0252: A Strongly Lensed Ultraluminous Galaxy, Not a Huge Massive Disk*.
- Downes, D., Solomon, P. M., & Radford, S. J. E. 1995, *ApJL* **453**, L65+, *New Observations and a New Interpretation of CO(3-2) in IRAS F10214+4724*.
- Draine, B. T. & Lee, H. M. 1984, *ApJ* **285**, 89–108, *Optical properties of interstellar graphite and silicate grains*.
- Eales, S. A., Alexander, P., & Duncan, W. D. 1989, *MNRAS* **240**, 817–822, *Photometry of Cygnus A at 800 and 1100 microns*.
- Eckart, A., Downes, D., Genzel, R., et al. 1990, *ApJ* **348**, 434–447, *Warm gas and spatial variations of molecular excitation in the nuclear region of IC 342*.
- Eddington, A. S. 1921, *Zeitschrift für Physik* **7**, 351+, .
- Edge, A. C. & Frayer, D. T. 2003, *ApJL* **594**, L13–L17, *Resolving Molecular gas in the Central Galaxies of Cooling Flow Clusters*.
- Egami, E., Neugebauer, G., Soifer, B. T., et al. 2000, *ApJ* **535**, 561–574, *APM 08279+5255: Keck Near- and Mid-Infrared High-Resolution Imaging*.

- Ellis, R. S. 2007, ArXiv Astrophysics e-prints, *Observations of the High Redshift Universe*.
- Ellison, S. L., Songaila, A., Schaye, J., & Pettini, M. 2000, AJ **120**, 1175–1191, *The Enrichment History of the Intergalactic Medium-Measuring the C IV/H I Ratio in the Ly α Forest*.
- Encrenaz, P. J., Combes, F., Casoli, F., et al. 1993, A&A **273**, L19+, *Water at Z=2.286*.
- Evans, A. S., Frayer, D. T., Surace, J. A., & Sanders, D. B. 2001, AJ **121**, 1893–1902, *Molecular Gas in Infrared-Excess, Optically Selected and the Quasars Connection with Infrared-Luminous Galaxies*.
- Evans, II, N. J. 1999, ARA&A **37**, 311–362, *Physical Conditions in Regions of Star Formation*.
- Faber, S. M., Tremaine, S., Ajhar, E. A., et al. 1997, AJ **114**, 1771–+, *The Centers of Early-Type Galaxies with HST. IV. Central Parameter Relations*.
- Fan, X., Carilli, C. L., & Keating, B. 2006, ARA&A **44**, 415–462, *Observational Constraints on Cosmic Reionization*.
- Fan, X., Narayanan, V. K., Lupton, R. H., et al. 2001, AJ **122**, 2833–2849, *A Survey of $z > 5.8$ Quasars in the Sloan Digital Sky Survey. I. Discovery of Three New Quasars and the Spatial Density of Luminous Quasars at $z \sim 6$* .
- Ferrarese, L. & Merritt, D. 2000, ApJL **539**, L9–L12, *A Fundamental Relation between Supermassive Black Holes and Their Host Galaxies*.
- Fixsen, D. J., Bennett, C. L., & Mather, J. C. 1999, ApJ **526**, 207–214, *COBE Far Infrared Absolute Spectrophotometer Observations of Galactic Lines*.
- Flower, D. R. 2001, Journal of Physics B Atomic Molecular Physics **34**, 2731–2738, *The rotational excitation of CO by H₂*.
- Frayer, D. T., Ivison, R. J., Scoville, N. Z., et al. 1999, ApJL **514**, L13–L16, *Molecular Gas in the Z = 2.565 Submillimeter Galaxy SMM J14011+0252*.
- Frayer, D. T., Ivison, R. J., Scoville, N. Z., et al. 1998, ApJL **506**, L7–L10, *Molecular Gas in the Z = 2.8 Submillimeter Galaxy SMM 02399-0136*.
- Fuente, A., García-Burillo, S., Gerin, M., et al. 2005, ApJL **619**, L155–L158, *Photon-dominated Chemistry in the Nucleus of M82: Widespread HOC⁺ Emission in the Inner 650 Parsec Disk*.
- Fuente, A., Martin-Pintado, J., Cernicharo, J., & Bachiller, R. 1993, A&A **276**, 473–+, *A chemical study of the photodissociation region NGC 7023*.

- Gao, Y., Carilli, C. L., Solomon, P. M., & Vanden Bout, P. A. 2007, *ApJL* **660**, L93–L96, *HCN Observations of Dense Star-forming Gas in High-Redshift Galaxies*.
- Gao, Y. & Solomon, P. M. 2004a, *ApJ* **606**, 271–290, *The Star Formation Rate and Dense Molecular Gas in Galaxies*.
- Gao, Y. & Solomon, P. M. 2004b, *ApJS* **152**, 63–80, *HCN Survey of Normal Spiral, Infrared-luminous, and Ultraluminous Galaxies*.
- García-Burillo, S., Graciá-Carpio, J., Guélin, M., et al. 2006, *ApJL* **645**, L17–L20, *A New Probe of Dense Gas at High Redshift: Detection of HCO⁺ (5-4) Line Emission in APM 08279+5255*.
- Gebhardt, K., Bender, R., Bower, G., et al. 2000, *ApJL* **539**, L13–L16, *A Relationship between Nuclear Black Hole Mass and Galaxy Velocity Dispersion*.
- Gebhardt, K., Richstone, D., Ajhar, E. A., et al. 1996, *AJ* **112**, 105–+, *The Centers of Early-Type Galaxies With HST. III. Non-Parametric Recovery of Stellar Luminosity Distribution*.
- Genzel, R. 1991, *Physical Conditions and Heating/Cooling Processes in High Mass Star Formation Regions*, In C. J. Lada and N. D. Kylafis (Eds.), *NATO ASIC Proc. 342: The Physics of Star Formation and Early Stellar Evolution*, pp. 155–+.
- Genzel, R., Baker, A. J., Tacconi, L. J., et al. 2003, *ApJ* **584**, 633–642, *Spatially Resolved Millimeter Interferometry of SMM J02399-0136: A Very Massive Galaxy at $z = 2.8$* .
- Goldreich, P. & Kwan, J. 1974, *ApJ* **189**, 441–454, *Molecular Clouds*.
- Gonzalez-Alfonso, E., Cernicharo, J., Bachiller, R., & Fuente, A. 1995, *A&A* **293**, L9–L12, *183 GHz water emission in W 49N*.
- Gracia-Carpio, J., Garcia-Burillo, S., & Planesas, P. 2007, *ArXiv Astrophysics e-prints*, *Dense molecular gas in a sample of LIRGs and ULIRGs: The low-redshift connection to the huge high-redshift starbursts and AGNs*.
- Graciá-Carpio, J., García-Burillo, S., Planesas, P., & Colina, L. 2006, *ApJL* **640**, L135–L138, *Is HCN a True Tracer of Dense Molecular Gas in Luminous and Ultraluminous Infrared Galaxies?*
- Graham, A. W. & Driver, S. P. 2007, *ApJ* **655**, 77–87, *A Log-Quadratic Relation for Predicting Supermassive Black Hole Masses from the Host Bulge Sérsic Index*.
- Graham, A. W., Erwin, P., Caon, N., & Trujillo, I. 2001, *ApJL* **563**, L11–L14, *A Correlation between Galaxy Light Concentration and Supermassive Black Hole Mass*.
- Greve, T. R., Bertoldi, F., Smail, I., et al. 2005, *MNRAS* **359**, 1165–1183, *An interferometric CO survey of luminous submillimetre galaxies*.

- Greve, T. R., Ivison, R. J., & Papadopoulos, P. P. 2003, ApJ **599**, 839–846, *Gas and Dust in the Extremely Red Object ERO J164502+4626.4*.
- Greve, T. R., Ivison, R. J., & Papadopoulos, P. P. 2004, A&A **419**, 99–107, *Detection of CO $J = 1-0$ in the $z = 3.79$ radio galaxy 4C 60.07*.
- Greve, T. R., Papadopoulos, P. P., Gao, Y., & Radford, S. J. E. 2006, ArXiv Astrophysics e-prints, *Molecular gas in extreme star-forming environments: the starbursts Arp220 and NGC6240 as case studies*.
- Guélin, M., Salomé, P., Neri, R., et al. 2007, A&A **462**, L45–L48, *Detection of HNC and tentative detection of CN at $z = 3.9$* .
- Guelin, M., Zylka, R., Mezger, P. G., Haslam, C. G. T., & Kreysa, E. 1995, A&A **298**, L29+, *Cold dust emission from spiral arms of M 51*.
- Guilloteau, S., Omont, A., Cox, P., McMahon, R. G., & Petitjean, P. 1999, A&A **349**, 363–368, *Dust and CO lines in high redshift quasars*.
- Guilloteau, S., Omont, A., McMahon, R. G., Cox, P., & Petitjean, P. 1997, A&A **328**, L1–L4, *The second detection of CO at redshift larger than 4*.
- Hainline, L. J., Blain, A. W., Greve, T. R., et al. 2006, ApJ **650**, 614–623, *Observing Cold Gas in Submillimeter Galaxies: Detection of CO (1–0) Emission in SMM J13120+4242 with the Green Bank Telescope*.
- Hainline, L. J., Scoville, N. Z., Yun, M. S., et al. 2004, ApJ **609**, 61–68, *A Study of CO Emission in High-Redshift QSOs Using the Owens Valley Millimeter Array*.
- Häring, N. & Rix, H.-W. 2004, ApJL **604**, L89–L92, *On the Black Hole Mass-Bulge Mass Relation*.
- Hartmann, J. 1904, ApJ **19**, 268–286, *Investigations on the spectrum and orbit of delta Orionis*.
- Hasinger, G., Schartel, N., & Komossa, S. 2002, ApJL **573**, L77–L80, *Discovery of an Ionized Fe K Edge in the $z=3.91$ Broad Absorption Line Quasar APM 08279+5255 with XMM-Newton*.
- Helou, G., Soifer, B. T., & Rowan-Robinson, M. 1985, ApJL **298**, L7–L11, *Thermal infrared and nonthermal radio - Remarkable correlation in disks of galaxies*.
- Henkel, C., Chin, Y.-N., Mauersberger, R., & Whiteoak, J. B. 1998, A&A **329**, 443–450, *Dense gas in nearby galaxies. XI. Interstellar $^{12}\text{C}/^{13}\text{C}$ ratios in the central regions of M82 and IC342*.
- Henkel, C., Mauersberger, R., Wiklind, T., et al. 1993, A&A **268**, L17–L20, *Dense gas in nearby galaxies. VI - A large C-12/C-13 ratio in a nuclear starburst environment*.

- Henkel, C., Schilke, P., & Mauersberger, R. 1988, *A&A* **201**, L23–L26, *Molecules in external galaxies - The detection of CN, C₂H, and HNC, and the tentative detection of HC₃N*.
- Hogerheijde, M. R., Jansen, D. J., & van Dishoeck, E. F. 1995, *A&A* **294**, 792–810, *Millimeter and submillimeter observations of the Orion Bar. 1: Physical structure*.
- Hollenbach, D. J. & Tielens, A. G. G. M. 1999, *Reviews of Modern Physics* **71**, 173–230, *Photodissociation regions in the interstellar medium of galaxies*.
- Hopkins, P. F., Hernquist, L., Martini, P., et al. 2005, *ApJL* **625**, L71–L74, *A Physical Model for the Origin of Quasar Lifetimes*.
- Hu, E. M. & Cowie, L. L. 2006, *Nature* **440**, 1145–1150, *High-redshift galaxy populations*.
- Hu, E. M., Cowie, L. L., McMahon, R. G., et al. 2002, *ApJL* **568**, L75–L79, *A Redshift $z=6.56$ Galaxy behind the Cluster Abell 370*.
- Hu, E. M., McMahon, R. G., & Egami, E. 1996, *ApJL* **459**, L53+, *Detection of a LY alpha Emission-Line Companion to the $z=4.69$ Quasar BR 1202\$-0725*.
- Humphreys, E. M. L., Greenhill, L. J., Reid, M. J., et al. 2005, *ApJL* **634**, L133–L136, *First Detection of Millimeter/Submillimeter Extragalactic H₂O Maser Emission*.
- Hunter, S. D., Bertsch, D. L., Catelli, J. R., et al. 1997, *ApJ* **481**, 205–+, *EGRET Observations of the Diffuse Gamma-Ray Emission from the Galactic Plane*.
- Ibata, R. A., Lewis, G. F., Irwin, M. J., Lehár, J., & Totten, E. J. 1999, *AJ* **118**, 1922–1930, *NICMOS and VLA Observations of the Gravitationally Lensed Ultraluminous BAL Quasar APM 08279+5255: Detection of a Third Image*.
- Imanishi, M., Nakanishi, K., & Kohno, K. 2006, *AJ* **131**, 2888–2899, *Millimeter Interferometric Investigations of the Energy Sources of Three Ultraluminous Infrared Galaxies, UGC 5101, Markarian 273, and IRAS 17208-0014, Based on HCN-to-HCO⁺ Ratios*.
- Imanishi, M., Nakanishi, K., Kuno, N., & Kohno, K. 2004, *AJ* **128**, 2037–2047, *Near-Infrared and Millimeter Constraints on the Nuclear Energy Source of the Infrared-luminous Galaxy NGC 4418*.
- Iono, D., Tamura, Y., Nakanishi, K., et al. 2006a, *PASJ* **58**, 957–963, *CO (3-2) and CO (2-1) Detections in a $z = 1.3$ Hyper-Luminous Starburst Galaxy*.
- Iono, D., Yun, M. S., Elvis, M., et al. 2006b, *ApJL* **645**, L97–L100, *A Detection of [C II] Line Emission in the $z = 4.7$ QSO BR 1202-0725*.
- Irwin, M. J., Ibata, R. A., Lewis, G. F., & Totten, E. J. 1998, *ApJ* **505**, 529–535, *APM 08279+5255: an Ultraluminous Broad Absorption Line Quasar at a Redshift $Z = 3.87$* .

- Ivezić, Ž., Menou, K., Knapp, G. R., et al. 2002, AJ **124**, 2364–2400, *Optical and Radio Properties of Extragalactic Sources Observed by the FIRST Survey and the Sloan Digital Sky Survey*.
- Ivison, R. J. 2006, MNRAS **370**, 495–500, *Searching for a gigamaser in APM08279+5255, and other short stories*.
- Iye, M., Ota, K., Kashikawa, N., et al. 2006, Nature **443**, 186–188, *A galaxy at a redshift $z = 6.96$* .
- Jansen, D. J., van Dishoeck, E. F., Black, J. H., Spaans, M., & Sosin, C. 1995, A&A **302**, 223–+, *Physical and chemical structure of the IC 63 nebula. II. Chemical models*.
- Jiang, L., Fan, X., Hines, D. C., et al. 2006, AJ **132**, 2127–2134, *Probing the Evolution of Infrared Properties of $z \sim 6$ Quasars: Spitzer Observations*.
- Kawabe, R., Sakamoto, K., Ishizuki, S., & Ishiguro, M. 1992, ApJL **397**, L23–L26, *Aperture synthesis CO ($J = 3-2$) observations of a protogalaxy candidate IRAS F10214+4724*.
- Kayser, R., Surdej, J., Condon, J. J., et al. 1990, ApJ **364**, 15–22, *New observations and gravitational lens models of the Cloverleaf quasar H1413 + 117*.
- Keeton, C. R. & Kochanek, C. S. 1998, ApJ **495**, 157–+, *Gravitational Lensing by Spiral Galaxies*.
- Kellermann, K. I., Sramek, R., Schmidt, M., Shaffer, D. B., & Green, R. 1989, AJ **98**, 1195–1207, *VLA observations of objects in the Palomar Bright Quasar Survey*.
- Kennicutt, Jr., R. C. 1998a, ApJ **498**, 541–+, *The Global Schmidt Law in Star-forming Galaxies*.
- Kennicutt, Jr., R. C. 1998b, ARA&A **36**, 189–232, *Star Formation in Galaxies Along the Hubble Sequence*.
- Klamer, I. J., Ekers, R. D., Bryant, J. J., et al. 2006, MNRAS **371**, 852–866, *A search for distant radio galaxies from SUMSS and NVSS - III. Radio spectral energy distributions and the z - α correlation*.
- Klamer, I. J., Ekers, R. D., Sadler, E. M., & Hunstead, R. W. 2004, ApJL **612**, L97–L100, *Molecular Gas at High Redshift: Jet-induced Star Formation?*
- Klamer, I. J., Ekers, R. D., Sadler, E. M., et al. 2005, ApJL **621**, L1–L4, *CO (1-0) and CO (5-4) Observations of the Most Distant Known Radio Galaxy at $z=5.2$* .
- Knapp, G. R. & Rupen, M. P. 1996, ApJ **460**, 271–+, *Molecular Gas in Elliptical Galaxies: CO Observations of an IRAS Flux-limited Sample*.

- Kneib, J.-P., Alloin, D., Mellier, Y., et al. 1998, *A&A* **329**, 827–839, *Modelling the Cloverleaf: contribution of a galaxy cluster at $Z \sim 1.7$* .
- Kneib, J.-P., Neri, R., Smail, I., et al. 2005, *A&A* **434**, 819–825, *Molecular gas in a $z \sim 2.5$ triply-imaged, sub-mJy submillimetre galaxy typical of the cosmic far-infrared background*.
- Kneib, J.-P., van der Werf, P. P., Kraiberg Knudsen, K., et al. 2004, *MNRAS* **349**, 1211–1217, *A multiply imaged, submillimetre-selected ultraluminous infrared galaxy in a galaxy group at $z \sim 2.5$* .
- Knudsen, K. K., Walter, F., Weiss, A., et al. 2007, *ApJ* **666**, 156–164, *New Insights on the Dense Molecular Gas in NGC 253 as Traced by HCN and HCO⁺*.
- Koda, J., Sofue, Y., Kohno, K., et al. 2002, *ApJ* **573**, 105–121, *Nobeyama Millimeter Array CO ($J=1-0$) Observations of the H α /Radio Lobe Galaxy NGC 3079: Gas Dynamics in a Weak Bar Potential and Central Massive Core*.
- Kodaira, K., Taniguchi, Y., Kashikawa, N., et al. 2003, *PASJ* **55**, L17–L21, *The Discovery of Two Lyman α Emitters beyond Redshift 6 in the Subaru Deep Field*.
- Kohno, K. 2005, *Prevalence of Compact Nuclear Starbursts in Nearby Seyfert Galaxies*, In S. Hüttmeister, E. Manthey, D. Bomans, and K. Weis (Eds.), *The Evolution of Starbursts*, Volume 783 of *American Institute of Physics Conference Series*, pp. 203–208.
- Kohno, K., Matsushita, S., Vila-Vilaró, B., et al. 2001, *Dense Molecular Gas and Star Formation in Nearby Seyfert Galaxies*, In J. H. Knapen, J. E. Beckman, I. Shlosman, and T. J. Mahoney (Eds.), *The Central Kiloparsec of Starbursts and AGN: The La Palma Connection*, Volume 249 of *Astronomical Society of the Pacific Conference Series*, pp. 672–+.
- Krips, M., Neri, R., Eckart, A., et al. 2005, *A&A* **431**, 879–886, *Q0957+561 revised: CO emission from a disk at $z = 1.4$* .
- Krumholz, M. R. & Thompson, T. A. 2007, *ArXiv e-prints* **704**, *The Relationship Between Molecular Gas Tracers and Kennicutt-Schmidt Laws*.
- Laing, R. A. & Peacock, J. A. 1980, *MNRAS* **190**, 903–924, *The relation between radio luminosity and spectrum for extended extragalactic radio sources*.
- Larson, R. B. 1981, *MNRAS* **194**, 809–826, *Turbulence and star formation in molecular clouds*.
- Lattanzio, J. C. & Boothroyd, A. I. 1997, *Nucleosynthesis of Elements in Low to Intermediate Mass Stars Through the AGB Phase*, In T. J. Bernatowicz and E. Zinner (Eds.), *American Institute of Physics Conference Series*, Volume 402 of *American Institute of Physics Conference Series*, pp. 85–+.

- Ledoux, C., Theodore, B., Petitjean, P., et al. 1998, A&A **339**, L77–L80, *Adaptive optics imaging and integral field spectroscopy of APM 08279+5255: Evidence for gravitational lensing*.
- Lee, M.-Y., Lee, C. W., Kim, H., & Rhee, M.-H. 2006, Journal of Korean Astronomical Society **39**, 1–7, *CO Observations of Barred Spiral Galaxies*.
- Lehar, J., Burke, B. F., Conner, S. R., et al. 1997, AJ **114**, 48–53, *The Gravitationally Lensed Radio Source MG 0751+2716*.
- Lepp, S. & Dalgarno, A. 1996, A&A **306**, L21–L24, *X-ray-induced chemistry of interstellar clouds*.
- Lequeux, J. 2005, *The interstellar medium*. The interstellar medium, Translation from the French language edition of: Le Milieu Interstellaire by James Lequeux, EDP Sciences, 2003 Edited by J. Lequeux. Astronomy and astrophysics library, Berlin: Springer, 2005.
- Lequeux, J., Le Bourlot, J., Des Forets, G. P., et al. 1994, A&A **292**, 371–380, *Results of the ESO-SEST Key Program: CO in the Magellanic Clouds. 4: Physical properties of molecular clouds in the Small Magellanic Cloud*.
- Leroy, A., Bolatto, A. D., Simon, J. D., & Blitz, L. 2005, ApJ **625**, 763–784, *The Molecular Interstellar Medium of Dwarf Galaxies on Kiloparsec Scales: A New Survey for CO in Northern, IRAS-detected Dwarf Galaxies*.
- Lewis, G. F., Carilli, C., Papadopoulos, P., & Ivison, R. J. 2002a, MNRAS **330**, L15–L18, *Resolved nuclear CO(1-0) emission in APM 08279+5255: gravitational lensing by a naked cusp?*
- Lewis, G. F., Chapman, S. C., Ibata, R. A., Irwin, M. J., & Totten, E. J. 1998, ApJL **505**, L1+, *Submillimeter Observations of the Ultraluminous Broad Absorption Line Quasar APM 08279+5255*.
- Lewis, G. F., Ibata, R. A., Ellison, S. L., et al. 2002, MNRAS **334**, L7–L10, *Spatially resolved STIS spectra of the gravitationally lensed broad absorption line quasar APM08279+5255: the nature of component C and evidence for microlensing*.
- Li, Y., Hopkins, P. F., Hernquist, L., et al. 2007, ArXiv e-prints **706**, *Modeling the Dust Properties of $z \sim 6$ Quasars with ART² – All-wavelength Radiative Transfer with Adaptive Refinement Tree*.
- Lisenfeld, U., Braine, J., Duc, P.-A., et al. 2004, A&A **426**, 471–479, *Molecular and ionized gas in the tidal tail in Stephan’s Quintet*.
- Madore, B. F. 1977, MNRAS **178**, 1–9, *Numerical simulations of the rate of star formation in external galaxies*.

- Magorrian, J., Tremaine, S., Richstone, D., et al. 1998, *AJ* **115**, 2285–2305, *The Demography of Massive Dark Objects in Galaxy Centers*.
- Maiolino, R., Cox, P., Caselli, P., et al. 2005, *A&A* **440**, L51–L54, *First detection of [CII]158 μ m at high redshift: vigorous star formation in the early universe*.
- Maiolino, R., Neri, R., Beelen, A., et al. 2007, *A&A* **472**, L33–L37, *Molecular gas in QSO host galaxies at $z > 5$* .
- Mao, R. Q., Henkel, C., Schulz, A., et al. 2000, *A&A* **358**, 433–450, *Dense gas in nearby galaxies. XIII. CO submillimeter line emission from the starburst galaxy M 82*.
- Martín, S., Martín-Pintado, J., Mauersberger, R., Henkel, C., & García-Burillo, S. 2005, *ApJ* **620**, 210–216, *Sulfur Chemistry and Isotopic Ratios in the Starburst Galaxy NGC 253*.
- Martín, S., Mauersberger, R., Martín-Pintado, J., Henkel, C., & García-Burillo, S. 2006, *ApJS* **164**, 450–476, *A 2 Millimeter Spectral Line Survey of the Starburst Galaxy NGC 253*.
- Mauersberger, R. & Henkel, C. 1989, *A&A* **223**, 79–88, *Dense gas in nearby galaxies. I - Distribution, kinematics and multilevel studies of CS*.
- Mauersberger, R., Henkel, C., Wielebinski, R., Wiklind, T., & Reuter, H.-P. 1996, *A&A* **305**, 421–+, *Molecular distribution and kinematics in nearby galaxies. I. NGC 253*.
- Mauersberger, R., Henkel, C., Wilson, T. L., & Harju, J. 1989, *A&A* **226**, L5–L8, *Dense gas in nearby galaxies. II - CS emission from spiral galaxies*.
- McKee, C. F. & Ostriker, J. P. 1977, *ApJ* **218**, 148–169, *A theory of the interstellar medium - Three components regulated by supernova explosions in an inhomogeneous substrate*.
- Meijerink, R. & Spaans, M. 2005, *A&A* **436**, 397–409, *Diagnostics of irradiated gas in galaxy nuclei. I. A far-ultraviolet and X-ray dominated region code*.
- Mooney, T. J. & Solomon, P. M. 1988, *ApJL* **334**, L51–L54, *Star formation rates and the far-infrared luminosity of Galactic molecular clouds*.
- Muñoz, J. A., Kochanek, C. S., & Keeton, C. R. 2001, *ApJ* **558**, 657–665, *Cusped Mass Models of Gravitational Lenses*.
- Narayanan, D., Cox, T. J., Robertson, B., et al. 2006, *ApJL* **642**, L107–L110, *Molecular Outflows in Galaxy Merger Simulations with Embedded Active Galactic Nuclei*.
- Narayanan, D., Li, Y., Cox, T. J., et al. 2007, *ArXiv e-prints* **707**, *The Nature of CO Emission From $z \sim 6$ Quasars*.

- Navarro, J. F., Frenk, C. S., & White, S. D. M. 1997, ApJ **490**, 493–+, *A Universal Density Profile from Hierarchical Clustering*.
- Neri, R., Genzel, R., Ivison, R. J., et al. 2003, ApJL **597**, L113–L116, *Interferometric Observations of Powerful CO Emission from Three Submillimeter Galaxies at $z=2.39$, 2.51, and 3.35*.
- Nguyen, Q.-R., Jackson, J. M., Henkel, C., Truong, B., & Mauersberger, R. 1992, ApJ **399**, 521–532, *A survey for extragalactic HCN and HCO(+)*.
- Ohta, K., Yamada, T., Nakanishi, K., et al. 1996, Nature **382**, 426–428, *Detection of molecular gas in the quasar BR1202 - 0725 at redshift $z = 4.69$* .
- Omont, A. 2007, Reports of Progress in Physics **70**, 1099–1176, *Molecules in galaxies*.
- Omont, A., Cox, P., Bertoldi, F., et al. 2001, A&A **374**, 371–381, *A 1.2 mm MAMBO/IRAM-30 m survey of dust emission from the highest redshift PSS quasars*.
- Omont, A., Petitjean, P., Guilloteau, S., et al. 1996, Nature **382**, 428–431, *Molecular gas and dust around a radio-quiet quasar at redshift 4.69*.
- Ott, M., Witzel, A., Quirrenbach, A., et al. 1994, A&A **284**, 331–339, *An updated list of radio flux density calibrators*.
- Paglione, T. A. D., Jackson, J. M., Ishizuki, S., & Rieu, N.-Q. 1995, AJ **109**, 1716–1723, *First Observations of extragalactic CSJ = 1 goes to 0*.
- Papadopoulos, P., Ivison, R., Carilli, C., & Lewis, G. 2001, Nature **409**, 58–60, *A massive reservoir of low-excitation molecular gas at high redshift*.
- Papadopoulos, P. P., Röttgering, H. J. A., van der Werf, P. P., et al. 2000, ApJ **528**, 626–636, *CO (4-3) and Dust Emission in Two Powerful High-Z Radio Galaxies, and CO Lines at High Redshifts*.
- Peacock, J. A. 1999, *Cosmological Physics*. Cosmological Physics, by John A. Peacock, pp. 704. ISBN 052141072X. Cambridge, UK: Cambridge University Press, January 1999.
- Peacock, J. A., Miller, L., & Longair, M. S. 1986, MNRAS **218**, 265–278, *The statistics of radio emission from quasars*.
- Pentericci, L., Van Reeve, W., Carilli, C. L., Röttgering, H. J. A., & Miley, G. K. 2000, A&AS **145**, 121–159, *VLA radio continuum observations of a new sample of high redshift radio galaxies*.
- Pety, J., Beelen, A., Cox, P., et al. 2004, A&A **428**, L21–L24, *Atomic carbon in PSS 2322+1944, a quasar at redshift 4.12*.

- Phillips, J. A. & Lazio, T. J. W. 1995, ApJL **442**, L37–L39, *Images of HCO(+) (1-0) emission in a molecular cloud near 1E 1740.7 - 2942*.
- Pickett, H. M., Poynter, R. L., Cohen, E. A., et al. 1998, J. Quant. Spectrosc. Radiat. Transfer **60**, 883–890, *Submillimeter, Millimeter, and Microwave Spectral Line Catalog*.
- Planesas, P., Martin-Pintado, J., Neri, R., & Colina, L. 1999, Science **286**, 2493–2495, *Gas-rich galaxy pair unveiled in the lensed quasar 0957+561*.
- Radford, S. J. E., Brown, R. L., & Vanden Bout, P. A. 1993, A&A **271**, L21+, *Distribution of Molecular Gas in the Primeval Galaxy IRAS:F10214+4724*.
- Radford, S. J. E., Downes, D., Solomon, P. M., Barrett, J., & Sage, L. J. 1996, AJ **111**, 1021–+, *Resolution of the Discrepancy in the CO(3-2) Flux of IRAS F10214+4724*.
- Rhoads, J. E. & Malhotra, S. 2001, ApJL **563**, L5–L9, *Ly α Emitters at Redshift $z = 5.7$* .
- Riechers, D. A., Walter, F., Carilli, C. L., & Bertoldi, F. 2007b, ApJL **submitted**, *Observations of Dense Molecular Gas in a Quasar Host Galaxy at $z=6.42$: Further Evidence for a Trend in the $L_{\text{FIR}}/L'_{\text{HCN}}$ Star Formation Diagnostic*.
- Riechers, D. A., Walter, F., Carilli, C. L., & Bertoldi, F. 2007e, ApJL **to be submitted**, *Formation of a Quasar Host Galaxy 1.4 Billion Years After the Big Bang*.
- Riechers, D. A., Walter, F., Carilli, C. L., et al. 2007d, ApJL **to be submitted**, *A Molecular Einstein Ring at $z=4.12$: Imaging the Quasar Host Galaxy of PSS J2322+1944 Through a Cosmic Lens*.
- Riechers, D. A., Walter, F., Carilli, C. L., et al. 2006a, ApJ **650**, 604–613, *CO(1-0) in $z > \sim 4$ Quasar Host Galaxies: No Evidence for Extended Molecular Gas Reservoirs*.
- Riechers, D. A., Walter, F., Carilli, C. L., & Lewis, G. F. 2007c, ApJ **to be submitted**, *Imaging the Molecular Gas in a $z=3.9$ Quasar Host Galaxy at $0.3''$ Resolution: A Central, sub-kiloparsec Scale Star Formation Reservoir in APM 08279+5255*.
- Riechers, D. A., Walter, F., Carilli, C. L., et al. 2006b, ApJL **645**, L13–L16, *First Detection of HCO⁺ Emission at High Redshift*.
- Riechers, D. A., Walter, F., Cox, P., et al. 2007a, ApJ **666**, 778–783, *Detection of Emission from the CN Radical in the Cloverleaf Quasar at $z=2.56$* .
- Riechers, D. A., Weiss, A., Walter, F., Carilli, C. L., & Knudsen, K. K. 2006c, ApJ **649**, 635–639, *A Search for H₂O in the Strongly Lensed QSO MG 0751+2716 at $z = 3.2$* .
- Rodriguez-Franco, A., Martin-Pintado, J., & Fuente, A. 1998, A&A **329**, 1097–1110, *CN emission in Orion. The high density interface between the H II region and the molecular cloud*.

- Rohlfs, K. & Wilson, T. L. 1996, *Tools of Radio Astronomy*. Tools of Radio Astronomy, XVI, 423 pp. 127 figs., 20 tabs.. Springer-Verlag Berlin Heidelberg New York. Also Astronomy and Astrophysics Library.
- Rowan-Robinson, M. 2000, MNRAS **316**, 885–900, *Hyperluminous infrared galaxies*.
- Rusin, D. & Ma, C.-P. 2001, ApJL **549**, L33–L37, *Constraints on the Inner Mass Profiles of Lensing Galaxies from Missing Odd Images*.
- Sakamoto, K., Ishizuki, S., Kawabe, R., & Ishiguro, M. 1992, ApJL **397**, L27–L30, *Molecular gas distribution in a protogalaxy candidate IRAS F10214 + 4724 - A dense compact nucleus and nondetected extra components*.
- Sandage, A. 1994, ApJ **430**, 1–12, *Bias properties of extragalactic distance indicators. 1: The Hubble constant does not increase outward*.
- Sanders, D. B., Mazzarella, J. M., Kim, D.-C., Surace, J. A., & Soifer, B. T. 2003, AJ **126**, 1607–1664, *The IRAS Revised Bright Galaxy Sample*.
- Sanders, D. B., Scoville, N. Z., & Soifer, B. T. 1991, ApJ **370**, 158–171, *Molecular gas in luminous infrared galaxies*.
- Sanders, D. B., Scoville, N. Z., Young, J. S., et al. 1986, ApJL **305**, L45–L49, *Molecular gas in high-luminosity IRAS galaxies*.
- Schmidt, M. 1959, ApJ **129**, 243–+, *The Rate of Star Formation*.
- Schmidt, M. 1963, Nature **197**, 1040–+, *3C 273 : A Star-Like Object with Large Red-Shift*.
- Schmidt, M. 1970, ApJ **162**, 371–+, *Space Distribution and Luminosity Functions of Quasars*.
- Schneider, D. P., van Gorkom, J. H., Schmidt, M., & Gunn, J. E. 1992, AJ **103**, 1451–1456, *Radio properties of optically selected high-redshift quasars. I - VLA observations of 22 quasars at 6 CM*.
- Schulz, A., Henkel, C., Beckmann, U., et al. 1995, A&A **295**, 183–193, *A high resolution CO J = 4-3 map of Orion-KL*.
- Scoville, N. Z., Evans, A. S., Dinshaw, N., et al. 1998, ApJL **492**, L107+, *NICMOS Imaging of the Nuclei of ARP 220*.
- Scoville, N. Z., Frayer, D. T., Schinnerer, E., & Christopher, M. 2003, ApJL **585**, L105–L108, *The Host Galaxies of Optically Bright Quasi-stellar Objects: Molecular Gas in $z < 0.1$ Palomar-Green Quasi-stellar Objects*.
- Scoville, N. Z. & Solomon, P. M. 1974, ApJL **187**, L67+, *Radiative Transfer, Excitation, and Cooling of Molecular Emission Lines (co and Cs)*.

- Scoville, N. Z., Solomon, P. M., & Jefferts, K. B. 1974, ApJL **187**, L63+, *Molecular Clouds in the Galactic Nucleus*.
- Scoville, N. Z., Yun, M. S., Brown, R. L., & Vanden Bout, P. A. 1995, ApJL **449**, L109+, *Extended Molecular Gas in FSC 10214+4724*.
- Scoville, N. Z., Yun, M. S., Windhorst, R. A., Keel, W. C., & Armus, L. 1997, ApJL **485**, L21+, *CO $J = 3-2$ Emission in the Radio Galaxy 53W002 at $z = 2.394$* .
- Seaquist, E. R. & Frayer, D. T. 2000, ApJ **540**, 765–770, *The Distribution of HCO⁺ $J=4-3$ and HCN $J=4-3$ in the Nuclear Region of M82*.
- Sheth, K., Blain, A. W., Kneib, J.-P., et al. 2004, ApJL **614**, L5–L8, *Detection of CO from SMM J16359+6612, the Multiply Imaged Submillimeter Galaxy behind A2218*.
- Shields, G. A., Menezes, K. L., Massart, C. A., & Vanden Bout, P. 2006, ApJ **641**, 683–688, *The Black Hole-Bulge Relationship for QSOs at High Redshift*.
- Shu, F. H., Adams, F. C., & Lizano, S. 1987, ARA&A **25**, 23–81, *Star formation in molecular clouds - Observation and theory*.
- Sijacki, D., Springel, V., Di Matteo, T., & Hernquist, L. 2007, ArXiv e-prints **705**, *A unified model for AGN feedback in cosmological simulations of structure formation*.
- Silk, J. & Rees, M. J. 1998, A&A **331**, L1–L4, *Quasars and galaxy formation*.
- Skatrud, D. D., de Lucia, F. C., Blake, G. A., & Sastry, K. V. L. N. 1983, Journal of Molecular Spectroscopy **99**, 35–46, *The millimeter and submillimeter spectrum of CN in its first four vibrational states*.
- Soifer, B. T., Charmandaris, V., Brandl, B. R., et al. 2004, ApJS **154**, 151–154, *Spitzer Infrared Spectrograph (IRS) Observations of the Redshift 3.91 Quasar APM 08279+5255*.
- Solomon, P., Vanden Bout, P., Carilli, C., & Guélin, M. 2003, Nature **426**, 636–638, *The essential signature of a massive starburst in a distant quasar*.
- Solomon, P. M. & Barrett, J. W. 1991, *The CO - H₂ Mass Conversion Factor*, In F. Combes and F. Casoli (Eds.), *Dynamics of Galaxies and Their Molecular Cloud Distributions*, Volume 146 of *IAU Symposium*, pp. 235–+.
- Solomon, P. M., Downes, D., & Radford, S. J. E. 1992a, ApJL **398**, L29–L32, *Warm molecular gas in the primeval galaxy IRAS 10214 + 4724*.
- Solomon, P. M., Downes, D., & Radford, S. J. E. 1992c, ApJL **387**, L55–L59, *Dense molecular gas and starbursts in ultraluminous galaxies*.
- Solomon, P. M., Downes, D., Radford, S. J. E., & Barrett, J. W. 1997, ApJ **478**, 144–+, *The Molecular Interstellar Medium in Ultraluminous Infrared Galaxies*.

- Solomon, P. M., Radford, S. J. E., & Downes, D. 1990, *ApJL* **348**, L53–L56, *Dense molecular clouds and the ARP 220 starburst*.
- Solomon, P. M., Radford, S. J. E., & Downes, D. 1992b, *Nature* **356**, 318–+, *Molecular gas content of the primaeval galaxy IRAS 10214 + 4724*.
- Solomon, P. M., Rivolo, A. R., Barrett, J., & Yahil, A. 1987, *ApJ* **319**, 730–741, *Mass, luminosity, and line width relations of Galactic molecular clouds*.
- Solomon, P. M. & Sage, L. J. 1988, *ApJ* **334**, 613–625, *Star-formation rates, molecular clouds, and the origin of the far-infrared luminosity of isolated and interacting galaxies*.
- Solomon, P. M. & Vanden Bout, P. A. 2005, *ARA&A* **43**, 677–725, *Molecular Gas at High Redshift*.
- Solomon, P. M. & Wickramasinghe, N. C. 1969, *ApJ* **158**, 449–+, *Molecular and Solid Hydrogen in Dense Interstellar Clouds*.
- Spergel, D. N., Bean, R., Doré, O., et al. 2007, *ApJS* **170**, 377–408, *Three-Year Wilkinson Microwave Anisotropy Probe (WMAP) Observations: Implications for Cosmology*.
- Spergel, D. N., Verde, L., Peiris, H. V., et al. 2003, *ApJS* **148**, 175–194, *First-Year Wilkinson Microwave Anisotropy Probe (WMAP) Observations: Determination of Cosmological Parameters*.
- Springel, V., Di Matteo, T., & Hernquist, L. 2005, *MNRAS* **361**, 776–794, *Modelling feedback from stars and black holes in galaxy mergers*.
- Springel, V., White, S. D. M., Jenkins, A., et al. 2005b, *Nature* **435**, 629–636, *Simulations of the formation, evolution and clustering of galaxies and quasars*.
- Sternberg, A. & Dalgarno, A. 1995, *ApJS* **99**, 565–+, *Chemistry in Dense Photon-dominated Regions*.
- Storrie-Lombardi, L. J., McMahon, R. G., Irwin, M. J., & Hazard, C. 1996, *ApJ* **468**, 121–+, *APM $Z \geq 4$ QSO Survey: Spectra and Intervening Absorption Systems*.
- Strong, A. W., Bloemen, J. B. G. M., Dame, T. M., et al. 1988, *A&A* **207**, 1–15, *The radial distribution of galactic gamma rays. IV - The whole galaxy*.
- Tacconi, L. J., Neri, R., Chapman, S. C., et al. 2006, *ApJ* **640**, 228–240, *High-Resolution Millimeter Imaging of Submillimeter Galaxies*.
- Taniguchi, Y., Ajiki, M., Nagao, T., et al. 2005, *PASJ* **57**, 165–182, *The SUBARU Deep Field Project: Lyman α Emitters at a Redshift of 6.6*.

- Tielens, A. G. G. M. 2005, *The Physics and Chemistry of the Interstellar Medium*. The Physics and Chemistry of the Interstellar Medium, by A. G. G. M. Tielens, pp. . ISBN 0521826349. Cambridge, UK: Cambridge University Press, 2005.
- Townes, C. H. & Schawlow, A. L. 1975, *Microwave Spectroscopy*. New York: Dover, 1975.
- Tremaine, S., Gebhardt, K., Bender, R., et al. 2002, ApJ **574**, 740–753, *The Slope of the Black Hole Mass versus Velocity Dispersion Correlation*.
- Tsuboi, M., Miyazaki, A., Imaizumi, S., & Nakai, N. 1999, PASJ **51**, 479–482, *A Search for the CO ($J = 1-0$) Emission Line toward the Quasar H1413+117*.
- Tsuboi, M. & Nakai, N. 1992, PASJ **44**, L241–L245, *Observations of CO ($J = 1-0$) and ($J = 3-2$) emission lines toward the very high-redshifted galaxy IRAS F10214+4724*.
- Turner, J. L., Ho, P. T. P., & Beck, S. C. 1998, AJ **116**, 1212–1220, *The Radio Properties of NGC 5253 and Its Unusual H II Regions*.
- Usero, A., García-Burillo, S., Fuente, A., Martín-Pintado, J., & Rodríguez-Fernández, N. J. 2004, A&A **419**, 897–912, *Molecular gas chemistry in AGN. I. The IRAM 30 m survey of NGC 1068*.
- van Dishoeck, E. F. 2004, ARA&A **42**, 119–167, *ISO Spectroscopy of Gas and Dust: From Molecular Clouds to Protoplanetary Disks*.
- Vanden Bout, P. A., Solomon, P. M., & Maddalena, R. J. 2004, ApJL **614**, L97–L100, *High-Redshift HCN Emission: Dense Star-forming Molecular Gas in IRAS F10214+4724*.
- Venturini, S. & Solomon, P. M. 2003, ApJ **590**, 740–745, *The Molecular Disk in the Cloverleaf Quasar*.
- Vestergaard, M. 2004, ApJ **601**, 676–691, *Early Growth and Efficient Accretion of Massive Black Holes at High Redshift*.
- Vestergaard, M. & Peterson, B. M. 2006, ApJ **641**, 689–709, *Determining Central Black Hole Masses in Distant Active Galaxies and Quasars. II. Improved Optical and UV Scaling Relationships*.
- Wagg, J., Wilner, D. J., Neri, R., Downes, D., & Wiklind, T. 2005, ApJL **634**, L13–L16, *HCN $J = 5-4$ Emission in APM 08279+5255 at $z = 3.91$* .
- Wagg, J., Wilner, D. J., Neri, R., Downes, D., & Wiklind, T. 2006, ApJ **651**, 46–50, *Atomic Carbon in APM 08279+5255 at $z = 3.91$* .
- Walter, F., Bertoldi, F., Carilli, C., et al. 2003, Nature **424**, 406–408, *Molecular gas in the host galaxy of a quasar at redshift $z = 6.42$* .

- Walter, F., Brinks, E., de Blok, W. J. G., Thornley, M. D., & Kennicutt, R. C. 2005, *First Results from THINGS: The HI Nearby Galaxy Survey*, In R. Braun (Ed.), *Extra-Planar Gas*, Volume 331 of *Astronomical Society of the Pacific Conference Series*, pp. 269–+.
- Walter, F., Carilli, C., Bertoldi, F., et al. 2004, *ApJL* **615**, L17–L20, *Resolved Molecular Gas in a Quasar Host Galaxy at Redshift $z=6.42$* .
- Walter, F. & Heithausen, A. 1999, *ApJL* **519**, L69–L72, *The Discovery of a Molecular Complex in the Tidal Arms near NGC 3077*.
- Walter, F., Taylor, C. L., Hüttemeister, S., Scoville, N., & McIntyre, V. 2001, *AJ* **121**, 727–739, *The Interaction between the Interstellar Medium and Star Formation in the Dwarf Starburst Galaxy NGC 4214*.
- Wang, M., Henkel, C., Chin, Y.-N., et al. 2004, *A&A* **422**, 883–905, *Dense gas in nearby galaxies. XVI. The nuclear starburst environment in NGC 4945*.
- Wang, R., Carilli, C. L., Beelen, A., et al. 2007, *AJ* **134**, 617–627, *Millimeter and Radio Observations of $z \sim 6$ Quasars*.
- Weiß, A., Downes, D., Henkel, C., & Walter, F. 2005b, *A&A* **429**, L25–L28, *Atomic carbon at redshift ~ 2.5* .
- Weiß, A., Downes, D., Neri, R., et al. 2007, *A&A* **467**, 955–969, *Highly-excited CO emission in APM 08279+5255 at $z = 3.9$* .
- Weiß, A., Downes, D., Walter, F., & Henkel, C. 2005a, *A&A* **440**, L45–L49, *Multiple CO lines in SMM J16359+6612 - further evidence for a merger*.
- Weiß, A., Henkel, C., Downes, D., & Walter, F. 2003, *A&A* **409**, L41–L45, *Gas and dust in the Cloverleaf quasar at redshift 2.5*.
- Weiß, A., Neininger, N., Hüttemeister, S., & Klein, U. 2001, *A&A* **365**, 571–587, *The effect of violent star formation on the state of the molecular gas in M 82*.
- Weiß, A., Walter, F., & Scoville, N. Z. 2005c, *A&A* **438**, 533–544, *The spectral energy distribution of CO lines in M 82*.
- Werner, M. W., Gatley, I., Becklin, E. E., et al. 1976, *ApJ* **204**, 420–423, *One arc-minute resolution maps of the Orion Nebula at 20, 50, and 100 microns*.
- White, R. L., Becker, R. H., Fan, X., & Strauss, M. A. 2005, *AJ* **129**, 2102–2107, *Hubble Space Telescope Advanced Camera for Surveys Observations of the $z = 6.42$ Quasar SDSS J1148+5251: A Leak in the Gunn-Peterson Trough*.
- White, R. L., Becker, R. H., Helfand, D. J., & Gregg, M. D. 1997, *ApJ* **475**, 479–+, *A Catalog of 1.4 GHz Radio Sources from the FIRST Survey*.

- Williams, J. P., Blitz, L., & McKee, C. F. 2000, Protostars and Planets IV, 97–+, *The Structure and Evolution of Molecular Clouds: from Clumps to Cores to the IMF*.
- Willott, C. J., Martínez-Sansigre, A., & Rawlings, S. 2007, AJ **133**, 564–567, *Molecular Gas Observations of the Reddened Quasar 3C 318*.
- Wilner, D. J., Zhao, J.-H., & Ho, P. T. P. 1995, ApJL **453**, L91+, *The Molecular Medium of H1413+117: BIMA CO(3-2) and HCO +(4-3) Observations*.
- Wilson, C. D. 1995, ApJL **448**, L97+, *The Metallicity Dependence of the CO-to-H₂ Conversion Factor from Observations of Local Group Galaxies*.
- Wilson, C. D., Harris, W. E., Longden, R., & Scoville, N. Z. 2006, ApJ **641**, 763–772, *Two Populations of Young Massive Star Clusters in Arp 220*.
- Wilson, C. D., Scoville, N., Madden, S. C., & Charmandaris, V. 2000, ApJ **542**, 120–127, *High-Resolution Imaging of Molecular Gas and Dust in the Antennae (NGC 4038/39): Super Giant Molecular Complexes*.
- Winn, J. N., Rusin, D., & Kochanek, C. S. 2004, Nature **427**, 613–615, *The central image of a gravitationally lensed quasar*.
- Woo, J.-H., Treu, T., Malkan, M. A., & Blandford, R. D. 2006, ApJ **645**, 900–919, *Cosmic Evolution of Black Holes and Spheroids. I. The $M_{\text{BH}}-\sigma$ Relation at $z = 0.36$* .
- Wouterloot, J. G. A., Brand, J., Burton, W. B., & Kwee, K. K. 1990, A&A **230**, 21–36, *IRAS sources beyond the solar circle. II - Distribution in the Galactic warp*.
- Wu, J., Evans, II, N. J., Gao, Y., et al. 2005, ApJL **635**, L173–L176, *Connecting Dense Gas Tracers of Star Formation in our Galaxy to High- z Star Formation*.
- Yao, L., Seaquist, E. R., Kuno, N., & Dunne, L. 2003, ApJ **588**, 771–791, *CO Molecular Gas in Infrared-luminous Galaxies*.
- Young, J. S. & Scoville, N. Z. 1991, ARA&A **29**, 581–625, *Molecular gas in galaxies*.
- Yun, M. S. & Carilli, C. L. 2002, ApJ **568**, 88–98, *Radio-to-Far-Infrared Spectral Energy Distribution and Photometric Redshifts for Dusty Starburst Galaxies*.
- Yun, M. S., Carilli, C. L., Kawabe, R., et al. 2000, ApJ **528**, 171–178, *Sensitive Radio Observations of High-Redshift Dusty QSOs*.
- Yun, M. S., Reddy, N. A., & Condon, J. J. 2001, ApJ **554**, 803–822, *Radio Properties of Infrared-selected Galaxies in the IRAS 2 Jy Sample*.
- Yun, M. S., Reddy, N. A., Scoville, N. Z., et al. 2004, ApJ **601**, 723–734, *Multiwavelength Observations of the Gas-rich Host Galaxy of PDS 456: A New Challenge for the ULIRG-to-QSO Transition Scenario*.

-
- Yun, M. S., Scoville, N. Z., Carrasco, J. J., & Blandford, R. D. 1997, *ApJL* **479**, L9+,
Resolution and Kinematics of Molecular Gas Surrounding the Cloverleaf Quasar at $Z = 2.6$ Using the Gravitational Lens.

Curriculum Vitae

Personal Details

Name: Dominik Alexander Riechers
Date of Birth: 22 July 1978
Place of Birth: Hannover, Germany
Citizenship: German
Home Address: Schneidmühlstr. 12, D-69115 Heidelberg, Germany
Work/Mailing Address: Max-Planck-Institute for Astronomy
Königstuhl 17, D-69117 Heidelberg, Germany
Phone: +49-6221-528-315, FAX: +49-6221-528-246
E-mail: riechers@mpia.de
Web Site URL: <http://www.mpia.de/homes/riechers>

Present Occupation

- *PhD Student*
Department for Galaxies and Cosmology
Max-Planck-Institute for Astronomy, Heidelberg, Germany

Future Position

- *Hubble Postdoctoral Fellow* (sponsor: Prof. Nicholas Z. Scoville)
Astronomy Department
California Institute of Technology, Pasadena, CA, USA

Education

- *PhD* in Astronomy (defense scheduled: November 07, 2007)
Max-Planck-Institute for Astronomy & University of Heidelberg, Germany, 2007
Title of PhD Thesis: ‘*The Molecular ISM of Quasar Host Galaxies in the Early Universe*’,
Advisors: Prof. H.-W. Rix (MPIA) and Dr. F. Walter (MPIA)
- *Diploma* in Physics (grade: sehr gut, A)
Max-Planck-Institute for Radioastronomy & University of Bonn, Germany, 2004
Title of Diploma Thesis: ‘*Speckle Interferometry and Radiative Transfer Modeling of Evolved Stars: The OH/IR Star OH 104.9+2.4*’,
Advisor: Prof. G. Weigelt (MPIfR)

- *Student* of Physics & Astronomy, University of Bonn, Germany (October 1998–February 2004)
- *Abitur* (A–levels), majors: Mathematics & Physics (grades: 0.7[A+]/1.0[A]) Jugenddorf-Christophorusschule Königswinter, Germany (June 1997)

Fields of Interest

- Observational Cosmology: Epoch–of–Reionization Science
- The AGN–Starburst Connection in the Context of Galaxy Evolution
- Dust, Atomic and Molecular Gas in High–Redshift Quasars and Starburst Galaxies
- Radiative Transfer and Large Velocity Gradient Modeling

Recent Awards/Honors

- Awarded a Hubble Postdoctoral Fellowship at Caltech (starting November 2007)
- PhD financed through German Science Foundation (DFG) Priority Program 1177: ‘Witnesses of Cosmic History: Formation and evolution of black holes, galaxies and their environment’, via project ‘The Quasar-Starburst Connection’
- Chandra X–Ray Observatory PI grant for Cycle 9 observations (\$35,718) (July 2007)
- Spitzer Space Telescope PI grant for Cycle 4 observations (\$7,725) (May 2007)
- ALMA grant for presenting at the 2006 Global ALMA Conference ‘Science with ALMA: A New Era for Astrophysics’ (June 2006)
- Member of the American Astronomical Society (since 2005)

Attended Conferences, Meetings and Schools

- 77th Annual Scientific Meeting of the Astronomische Gesellschaft: ‘The Sun and Planetary Systems - Paradigms for the Universe’, Freiburg, Germany (2003 September 15-20): *Poster Presentation*
- 4th IRAM Interferometry School, Grenoble, France (2004 November 22-26): *Poster Presentation*
- Ringberg Workshop on Multiwavelength Surveys, Castle Ringberg, Germany (2005 March 28 - April 01)
- 207th Meeting of the American Astronomical Society, Washington, DC, USA (2006 January 08-12): *Poster Presentation*
- ALMA Conference ‘From z-Machines to ALMA: (Sub)Millimeter Spectroscopy of Galaxies’, Charlottesville, VA, USA (2006 January 13-14): *Contributed Talk*
- DFG Summer School (Priority Program 1177) ‘Evolution of galaxies and their large-scale environment’, Bad Honnef, Germany (2006 July 02-07)
- XXVIth General Assembly of the International Astronomical Union, Prague, Czech Republic (2006 August 14-25): *2×Poster Presentation*

-
- ALMA Conference ‘Science with ALMA: a new era for Astrophysics’, Madrid, Spain (2006 November 13-17): *Poster Presentation*
 - 209th Meeting of the American Astronomical Society, Seattle, WA, USA (2007 January 05-10): *PhD Thesis Talk*
 - COSMOS Collaboration Meeting, American Museum of National History, New York City, NY, USA (2007 June 11-14)
 - International Conference ‘Galaxy Growth in a Dark Universe’, Heidelberg, Germany (2007 July 16-20): *Poster Presentation*
 - 80th Annual Scientific Meeting of the Astronomische Gesellschaft: ‘Cosmic Matter’, Würzburg, Germany (2007 September 24-29): *Invited Talk*

Work Experience

- Conducting independent research, MPIA, September 2004–present (PhD Thesis)
- Co-Organizer of the MPIA Galaxy Coffee (weekly seminar), January 2005–September 2006
- Scientific Assistant, MPIA, June–August 2004
- Scientific Assistant, MPIfR, February–March 2004
- Conducting independent research, MPIfR, April 2003–January 2004 (Diploma Thesis)
- Student Assistant, MPIfR, September 2001–March 2003
- Alternative Civilian Service, Franziskus Hospital, Linz, Germany, December 1997–December 1998

Teaching Experience

- Teaching Assistant, Practical Course in Astronomy, Landessternwarte Heidelberg, February 2007
- Public Lecturer, MPIA Guided Institute Tours (several times per year), 2004–2007
- Private Tutor (Math/Physics/Chemistry) for High School Students, 1995–2003

Proposing Experience

- Writing of 40 proposals as PI for Large Observatories: NRAO VLA and GBT, IRAM PdBI and 30 m, ESO VLT, APEX, Spitzer Space Telescope, Chandra X-Ray Observatory, and CARMA; ~70% of these proposals were awarded observing time (additional proposals pending refereeing; 2004–present)
- Participation as Co-I on an additional ~50 proposals (same observatories; 2004–present)

Observing Experience

- Sternwarte Bonn/Hoher List, Daun, Germany (optical): 1999
- MPIfR Effelsberg 100m telescope: 2001–2003
- SAO BTA 6m telescope, Karachevo-Cherkesia, Russia (near-infrared): 2003
- NRAO Very Large Array (VLA): 2004–present
- NRAO Green Bank Telescope (GBT): 2004–present
- IRAM 30m telescope: 2005–present
- ESO Very Large Telescope (VLT): 2005–present
- IRAM Plateau de Bure Interferometer (PdBI): 2005–present
- Combined Array for Research in Millimeter-wave Astronomy (CARMA): 2007–present

Computing Experience

- Operating Systems: Linux, Unix, DOS, Windows, MacOS X, Solaris
- Programming and script languages: Fortran, C, C-shell, latex, (x)html, php
- Other: gnuplot, SuperMongo, IDL, AIPS, aips++/CASA, GILDAS/CLASS, IRAF, MIDAS

Languages

- German (native)
- English (fluent)
- French (good)
- Spanish (basics)

List of Publications

(Visit <http://www.mpia.de/homes/riechers/publications.html> for weblinks and preprints.)

Theses:

- **Riechers, D. A.**, ‘*The Molecular ISM of Quasar Host Galaxies in the Early Universe*’, PhD Thesis, University of Heidelberg, Germany, 2007, submitted (this document)
- **Riechers, D. A.**, ‘*Speckle Interferometry and Radiative Transfer Modeling of Evolved Stars: The OH/IR Star OH 104.9+2.4*’, Diploma Thesis, University of Bonn, Germany, 2004

Refereed Publications (First Author):

- **Riechers, D. A.**, Walter, F., Carilli, C. L., & Bertoldi, F., ‘*Formation of a Quasar Host Galaxy 1.4 Billion Years After the Big Bang*’, 2007, ApJL, to be submitted [PhD Thesis, Chapter 11]
- **Riechers, D. A.**, Walter, F., Carilli, C. L., Brewer, B. J., Lewis, G. F., Cox, P., & Bertoldi, F., ‘*A Molecular Einstein Ring at $z=4.12$: Imaging the Quasar Host Galaxy of PSS J2322+1944 Through a Cosmic Lens*’, 2007, ApJL, to be submitted [PhD Thesis, Chapter 10]
- **Riechers, D. A.**, Walter, F., Carilli, C. L., & Lewis, G. F., ‘*Imaging the Molecular Gas in a $z=3.9$ Quasar Host Galaxy at $0.3''$ Resolution: A Central, sub-kiloparsec Scale Star Formation Reservoir in APM 08279+5255*’, 2007, ApJ, to be submitted [PhD Thesis, Chapter 9]
- **Riechers, D. A.**, Walter, F., Carilli, C. L., & Bertoldi, F., ‘*Observations of Dense Molecular Gas in a Quasar Host Galaxy at $z=6.42$: A Deviant from the ‘Dense Molecular Gas–Star Formation Law’ at Early Cosmic Times*’, 2007, ApJL, submitted [PhD Thesis, Chapter 4]
- **Riechers, D. A.**, Walter, F., Cox, P., Carilli, C. L., Weiss, A., Bertoldi, F., & Neri, R., ‘*Detection of Emission from the CN Radical in the Cloverleaf Quasar at $z=2.56$* ’, 2007, ApJ, 666, 778 [PhD Thesis, Chapter 6]

- **Riechers, D. A.**, Walter, F., Carilli, C. L., Knudsen, K. K., Lo, K. Y., Benford, D. J., Staguhn, J. G., Hunter, T. R., Bertoldi, F., Henkel, C., Menten, K. M., Weiss, A., Yun, M. S., & Scoville, N. Z., ‘*CO(1–0) in $z \geq 4$ Quasar Host Galaxies: No Evidence for Extended Molecular Gas Reservoirs*’, 2006, ApJ, 650, 604 [PhD Thesis, Chapter 3]
- **Riechers, D. A.**, Weiss, A., Walter, F., Carilli, C. L., & Knudsen, K. K., ‘*A Search for H_2O in the Strongly Lensed QSO MG 0751+2716 at $z = 3.2$* ’, 2006, ApJ, 649, 635 [PhD Thesis, Chapter 8]
- **Riechers, D. A.**, Walter, F., Carilli, C. L., Weiss, A., Bertoldi, F., Menten, K. M., Knudsen, K. K., & Cox, P., ‘*First Detection of HCO^+ Emission at High Redshift*’, 2006, ApJ, 645, L13 [PhD Thesis, Chapter 5]
- **Riechers, D.**, Balega, Y., Driebe, T., Hofmann, K.-H., Men’shchikov, A. B., Shenavrin, V. I., & Weigelt, G., ‘*A quasi-time-dependent radiative transfer model of OH 104.9+2.4*’, 2005, A&A, 436, 925
- **Riechers, D.**, Balega, Y., Driebe, T., Hofmann, K.-H., Men’shchikov, A. B., & Weigelt, G., ‘*High-resolution near-infrared speckle interferometry and radiative transfer modeling of the OH/IR star OH 104.9+2.4*’, 2004, A&A, 424, 165 [Diploma Thesis]

Refereed Publications (Co–Author):

- Carilli, C. L., Neri, R., Wang, R., Cox, P., Bertoldi, F., Walter, F., Fan, X., Menten, K., Wagg, J., Maiolino, R., Omont, A., Strauss, M. A., **Riechers, D.**, Lo, K. Y., Bolatto, A., & Scoville, N., ‘*Detection of $1.6 \times 10^{10} M_\odot$ of molecular gas in the host galaxy of the $z = 5.77$ SDSS quasar J0927+2001*’, 2007, ApJ, 666, L9
- Knudsen, K. K., Walter, F., Weiss, A., Bolatto, A., **Riechers, D. A.**, & Menten, K., ‘*New Insights on the Dense Molecular Gas in NGC 253 as Traced by HCN and HCO^+* ’, 2007, ApJ, 666, 156
- Kurk, J. D., Walter, F., Fan, X., Jiang, L., **Riechers, D. A.**, Rix, H.-W., Pentericci, L., Strauss, M. A., Carilli, C. L., & Wagner, S., ‘*Black Hole Masses and Enrichment of $z \sim 6$ SDSS Quasars*’, 2007, ApJ, in press (arXiv:0707.1662)
- Momjian, E., Carilli, C. L., **Riechers, D. A.**, & Walter, F., ‘*High Sensitivity Array Observations of the $z=4.4$ QSO BRI 1335-0417*’, 2007, AJ, 134, 694
- Driebe, T., **Riechers, D. A.**, Balega, Y., Domiciano de Souza, A., Men’shchikov, A. B., Murakawa, K., Ohnaka, K., Schertl, D., Tuthill, P., & Weigelt, G., ‘*High Angular Resolution Infrared Interferometry and Radiative Transfer Modeling of the oxygen-rich AGB star OH 26.5+0.6*’, 2007, A&A, to be submitted

Conference Contributions (First Author):

- **Riechers, D. A.**, Walter, F., Carilli, C. L., Bertoldi, F., & Cox, P., '*High-Resolution Imaging of Molecular Gas in High-Redshift Quasar Host Galaxies*', 2007, to appear in 'Science with ALMA: a new era for Astrophysics', ApSS (ALMA special issue)
- **Riechers, D. A.**, Walter, F., Carilli, C. L., Knudsen, K. K., Lo, K. Y., Benford, D. J., Staguhn, J. G., Hunter, T. R., Bertoldi, F., Henkel, C., Menten, K. M., Weiss, A., Yun, M. S., & Scoville, N. Z., '*CO(1-0) Emission from Quasar Host Galaxies Beyond Redshift 4*', 2007, in 'From Z-Machines to ALMA', eds. A. J. Baker, J. Glenn, A. I. Harris, J. G. Magnum, M. S. Yun, ASP Conf. Ser., 375, 148
- **Riechers, D. A.**, Walter, F., Carilli, C. L., Weiss, A., Bertoldi, F., Menten, K. M., Knudsen, K. K., & Cox, P., '*Dense Molecular Gas at High Redshift: First Detection of Emission from HCO⁺*', 2007, in 'Galaxy Evolution across the Hubble Time', eds. F. Combes & J. Palous, Proceedings of IAU Symp., 235, 424
- **Riechers, D. A.**, Walter, F., Carilli, C. L., Knudsen, K. K., Lo, K. Y., Benford, D. J., Staguhn, J. G., Hunter, T. R., Bertoldi, F., Henkel, C., Menten, K. M., Weiss, A., Yun, M. S., & Scoville, N. Z., '*Detecting Low-Order CO Emission from $z \geq 4$ Quasar Host Galaxies*', 2007, in 'Galaxy Evolution across the Hubble Time', eds. F. Combes & J. Palous, Proceedings of IAU Symp., 235, 423
- **Riechers, D. A.**, '*The Molecular ISM of Quasar Host Galaxies in the Early Universe*', 2006, AAS, 209, 195.06
- **Riechers, D. A.**, Walter, F., Carilli, C. L., Knudsen, K. K., Lo, K. Y., Benford, D. J., Staguhn, J. G., Hunter, T. R., Bertoldi, F., Henkel, C., Menten, K. M., Weiss, A., Yun, M. S., & Scoville, N. Z., '*CO(1-0) Emission in High-Redshift QSOs*', 2005, AAS, 207, 170.16
- **Riechers, D.**, Driebe, T., Balega, Y., Hofmann, K.-H., Men'shchikov, A. B., & Weigelt, G., '*High-resolution near-infrared speckle interferometry and radiative transfer modeling of the OH/IR star OH 104.9+2.4*', 2005, Astron. Nachr., 326, 666
- **Riechers, D.**, Balega, Y. Y., Driebe, T. M., Hofmann, K.-H., Men'shchikov, A. B., Schertl, D., & Weigelt, G. P., '*High-resolution near-infrared speckle interferometry and radiative transfer modeling of the OH/IR star OH 104.9+2.4*', 2004, New Frontiers in Stellar Interferometry, Proceedings of SPIE Volume 5491, 1714
- **Riechers, D.**, Berger, M., Balega, Y., Driebe, T., Hofmann, K.-H., & Weigelt, G., '*High-Resolution Near-Infrared Speckle Interferometry and Radiative Transfer Modeling of the OH/IR Star OH104.9+2.4*', 2003, Astron. Nachr. Suppl. Ser. 3, 324, 136

Conference Contributions (Co–Author):

- Walter, F., **Riechers, D. A.**, Carilli, C. L., Bertoldi, F., Weiss, A., & Cox, P., ‘*High resolution CO imaging of high redshift QSO host galaxies*’, 2007, in ‘From Z-Machines to ALMA’, eds. A. J. Baker, J. Glenn, A. I. Harris, J. G. Magnum, M. S. Yun, ASP Conf. Ser., 375, 182
- Momjian, E., Carilli, C., **Riechers, D.**, & Walter, F., ‘*High Sensitivity Array Observations of the $z = 4.4$ QSO BRI 1335-0417*’, 2007, AAS, 210, 02.12
- Kurk, J. D., Walter, F., **Riechers, D.**, Rix, H.-W., Wagner, S., Pentericci, L., & Fan, X., ‘*Metallicity and Black Hole Masses of $z \sim 6$ Quasars*’, 2006, to appear in Highlights of Astronomy, Vol. 14, ed. K. A. van der Hucht
- Driebe, T., **Riechers, D.**, Balega, Y., Hofmann, K.-H., Men’shchikov, A. B., & Weigelt, G., ‘*High-resolution near-infrared speckle interferometry and radiative transfer modeling of the OH/IR star OH 26.5+0.6*’, 2005, Astron. Nachr., 326, 648

Public Outreach:

- **Riechers, D. A.**, ‘*Molekulares Gas in hoch rotverschobenen Quasaren: Anregung und Zusammensetzung des Treibstoffs für Sternentstehung*’, 2007, to appear as a ‘Scientific Highlight’ in the MPIA Annual Report 2006 [in German]
- **Riechers, D. A.**, Walter, F., & Carilli, C. L., ‘*Detecting CO(1–0) Emission from $z \geq 4$ Quasar Host Galaxies with the GBT*’, 2006, NRAO Newsletter, 109, 6
- **Riechers, D. A.**, & Smolčić, V., ‘*Girl’s day am MPIA*’, 2005, Sterne und Weltraum, 44, 16 [in German]